DEVELOPMENT OF COLLOIDAL ALLOYED NANOCRYSTALS FOR QUANTUM DOT BASED DEVICE APPLICATIONS

A Thesis Submitted to
the Graduate School of Engineering and Sciences of
İzmir Institute of Technology
in Partial Fulfillment of the Requirements for the Degree of

DOCTOR OF PHILOSOPHY

in Chemistry

by
Seçil SEVİM ÜNLÜTÜRK

June 2018
İZMİR

We approve the thesis of **Seçil SEVİM ÜNLÜTÜRK**

Examining Committee Members:

_____
Prof. Dr. Serdar ÖZÇELİK
Department of Chemistry, İzmir Institute of Technology

_____
Prof. Dr. Mustafa M. DEMİR
Department of Materials Science and Engineering, İzmir Institute of Technology

_____
Assoc. Prof. Dr. Mustafa EMRULLAHOĞLU
Department of Chemistry, İzmir Institute of Technology

_____
Assoc. Prof. Dr. İlbeyi AVCI
Department of Physics, Ege University

_____
Dr. Burak GÜLTEKİN
Solar Energy Institute, Ege Unviersity

28 June 2018

_____   _____
Prof. Dr. Serdar ÖZÇELİK   **Prof. Dr. Canan VARLIKLI**
Supervisor, Department of Chemistry   Co-Supervisor, Department of Photonics
İzmir Institute of Technology   İzmir Institute of Technology

_____   _____
Prof. Dr. Ahmet EROĞLU   **Prof. Dr. Aysun SOFUOĞLU**
Head of the Department of Chemistry   Dean of the Graduate School of
                                                                      Engineering and Sciences

ACKNOWLEDGMENTS

ABSTRACT

DEVELOPMENT OF COLLOIDAL ALLOYED NANOCRYSTALS FOR QUANTUM DOT BASED DEVICE APPLICATIONS

Quantum dots (QDs) are very attractive luminescent semiconducting nanoparticles. In this study, our aim was to synthesize Cd and/or Zn based QDs with tunable optical properties by the particle size and the alloy composition.

Colloidal water dispersible Mn-doped and nondoped ZnS_xSe_{1-x} QDs were synthesized by the one-pot aqueous method. Optical measurements indicate that photoluminescent properties are strongly depended on the capping agent. While MPA capped QDs showed an emission peak in the blue region, others did not show any photoluminescence at all. Mn doping up to 10% resulted in no significant effect on the optical spectra. However structural characterizations, EPR and XRD, supported that Mn ions were bounded to the 220 and 311 facets of QD.

$Zn_xCd_{1-x}S_ySe_{1-y}$ quaternary nanoalloys were synthesized by using a modified two-phase approach for the first time in the literature. Optical properties of highly luminescent $Zn_xCd_{1-x}S_ySe_{1-y}$ nanoalloys were tuned from blue to yellow by the particle size, the alloy composition, and thickness of shell layer. The reactivity of the reactants, initial mole ratios, and other reaction parameters was adjusted to control alloy composition and alloy type: homogeneous and gradient. The reaction time controls the size of particles. The PL QE (up to 52%) and lifetimes (about 25 ns) were found similar regardless of core and core-shell nanoalloys. MicroPL measurements were carried out on $Zn_xCd_{1-x}S_ySe_{1-y}$ nanoalloys by fiber spectrometer integrated to confocal microscope. Photobleaching and blue-shifting, about 6 nm, were observed in the microPL spectra. Photobleaching times and rate constants obtained from single exponential decay curves showed that purification and exposure time are strongly effective. Additionally, the power the excitation light is essential that below 11 µW, photobleaching slows down, and at 2 µW there is no photobleaching. Scale-up methods with high-volume batch and flow reactor were used to synthesize CdTe and $Zn_xCd_{1-x}S_ySe_{1-y}$ QDs.

LEFETs were fabricated with TUBITAK support in collaboration with Heidelberg University. PbS QDs were used as emitting material at the bottom contact top-gate unipolar LEFETs in which uniform electroluminescence was obtained.

ÖZET

KUANTUM NOKTA TEMELLİ CİHAZ UYGULAMALARI İÇİN KOLLOİDAL ALAŞIM NANOKRİSTALLERİN GELİŞTİRİLMESİ

Kuantum noktalar (QD) oldukça ilgi çeken ışık yayan yarı iletken nanoparçacıklardır. Bu çalışmada amacımız Cd ve/veya Zn tabanlı QD'lerin sentezi ile optik özelliklerinin parçacık boyutu ve alaşım komposizyonu ile kontrol edilmesidir.

Kolloidal yapıda suda dağılım yapabilen Mn katkılandırılmış ve katkılandırılmamış ZnS_xSe_{1-x} QD'leri sulu sentez yöntemi ile sentezlenmiştir. Optik ölçümler QD'lerin yüzey aktif ligantlarının fotolüminesans özellikler üzerinde etkili olduğunu göstermiştir. MPA kaplı QD'ler mavi bölgede ışıma yaparken diğerlerinde fotolüminesans özellikler gözlenmemiştir. %10 oranına kadar Mn katkılandırılan QD'lerin optik özelliklerinde herhangi bir değişim gözlemlenmezken EPR ve XRD ölçümleri Mn iyonlarının QD'lerin 220 ve 311 yüzeylerine bağlandıklarını göstermiştir.

$Zn_xCd_{1-x}S_ySe_{1-y}$ dörtlü nanoalaşımlar literatürde ilk kez, modifiye iki faz sentez yöntemi ile sentezlenmiştir. Yüksek ışıma özelliklerine sahip QD'lerin optik özellikleri, parçacık boyutu, alaşım kompozisyonu ve kabuk katman kalınlığı kontrolü ile maviden sarıya kadar ayarlanabilmektedir. Reaktantların reaktiviteleri, başlangıç mol oranları ve diğer reaksiyon parametreleri ile alaşım tipi, homojen ya da gradyan olarak kontrol edilebilmektedir. Parçacık boyutu ise reaksiyon süresi ile kontrol edilmektedir. Çekirdek ve çekirdek/kabuk yapısındaki QD'lerin kuantum verimleri (% 52'ye kadar) ve yarı ömürleri (ortalama 25 ns) benzerdir. MikroPL çalışmaları fiber spektrometre bütünleşmiş konfocal mikroskobu kullanılarak tamamlanmıştır. MikroPL spektrumda fotosönümlenme ve 5-6 nm kadar mavi bölgeye kayma gözlenmiştir. Tekil üstel bozunma eğrileri yardımı ile hesaplanan fotosönümlenme hız sabiti ve zamanı, yıkama işlemi ile ışığa maruz kalma süresinin önemini göstermiştir. Ayrıca gönderilen ışık şiddeti ile fotosönümlenme etkilenmiş; 11 µW altında yavaşlarken, 2 µW'da gözlenmemiştir. CdTe ve $Zn_xCd_{1-x}S_ySe_{1-y}$ QD'lerinin yüksek oranlarda sentezi için yüksek hacimli reaktör ve akışlı reaktör sistemi kullanılmıştır.

Işık yayan alan etkili transistörler, TUBITAK desteğiyle Heidelberg Üniversitesi ile iş birliği içinde, PbS QD'ler kullanılarak üretilmiştir. "Alt kontak üst kapı" yapısındaki tek kutuplu LEFET'lerden düzenli bir elektrolüminesans alınabilmiştir.

TABLE OF CONTENTS

LIST OF FIGURES

LIST OF TABLES

CHAPTER 1

INTRODUCTION

1.1. The Aim of This Study

The aim of this study was to synthesize colloidal quantum dots in both aqueous and organic solvents in different synthetic methods. Since QDs are attractive candidates for especially optoelectronic applications, scale-up techniques were investigated in order to increase the reaction yield. Optimized synthetic procedures were proved by optical and structural characterizations. Produced quantum dots were used in quantum dot based light emitting field effect transistors (LEFETs) (in Heidelberg University) and light emitting diodes (LEDs)(only the preliminary studies are exist)

1.2. Quantum Dots

Quantum dots (QDs) which are luminescent semiconductor nanoparticles. Actually, the term "quantum dot" started to be discussed in the 1980s (Reed et al., 1988), and since then it has attracted attention in terms of exhibiting the quantum size effect. As the nanoparticle size decreases below 10 nm, the energy of an electronic transition can gradually increase and the absorption and emission spectra of such QDs undergo a continuous shift throughout the visible region and near-IR region depending on the particle size (Sergey and Vladimir, 2016).

The quantum size effect in semiconductors was experimentally found for the first time by Dingle and coworkers (Dingle et al., 1974). This effect is eventually related to the density of electronic states in semiconductors. They are classified with respect to the number of dimensions as 2D for quantum wells, 1D for quantum wires and 0D for quantum dots. 3D structures are called as bulk structures and do not exhibit quantum confinement effect. According to this theory, increase in the particle size results shifts in the optical spectra (absorption and emission) to the lower energetic regions which means a red shift in the electromagnetic spectrum. This effect is explained by the "particle in a box" theory in quantum chemistry.
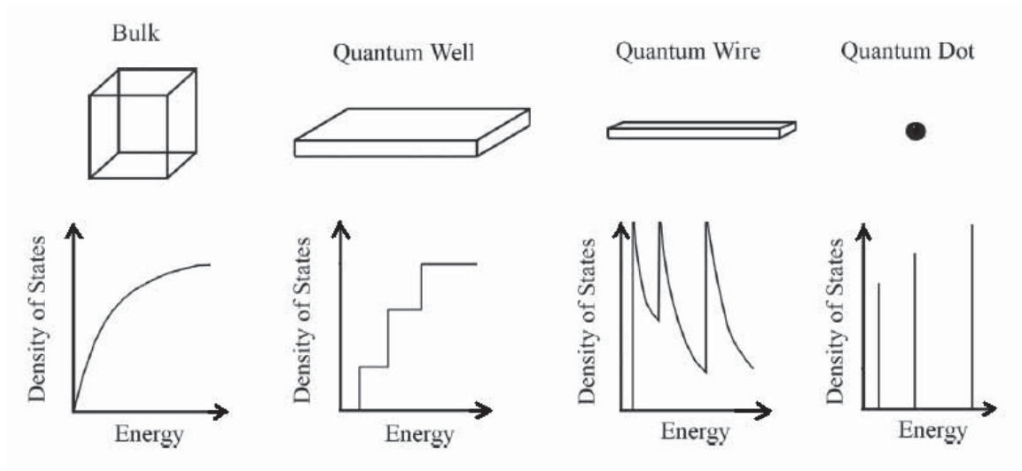
Figure 1.1. The density of states vs. energy for bulk material, quantum well, quantum wire and quantum dot (Source: Xu et al., 2005)

In a bulk semiconductor, in an absorption process, the photon energy exceeds the band gap is followed by the appearance of a free electron in the conduction band and a free hole in the valence band. As a result, they can have any energy within the conduction band for the electron and within the valence band for the hole. The difference is that the masses of these particles are usually much smaller than the mass of an electron freely moving in a vacuum. Since the de Broglie wavelength is inversely proportional with the should be much larger than that in vacuum at the same energies. As the nanoparticle size matches the de Broglie wavelength, the continuous energy spectrum becomes discrete. The energies of these discrete states could be written as :

$$E_n = \frac{n^2 h^2}{8mL^2}$$

(1.1)

where h is the Planck constant, m is the reduced mass and L is the distance between two infinite potential barriers in the particle in a box theory. In the case of QDs, m is the effective mass of electron and hole, L is the particle size in diameter.

Figure 1.2 shows the tunability of QDs by both the particle size and the alloy composition. In the case of Figure 1.2a, CdSe QDs with different particle sizes show different PL emission wavelengths in the visible range of electromagnetic spectrum. Since QDs are binary, we can easily indicate that the composition is the same for each QDs. Even for alloy QDs, keeping the alloy composition the same, optical spectra could

2

be tuned by the particle size. In the same figure (Figure 1.2b) CdSe, CdTe and $CdSe_xTe_{1-x}$ QDs with the same particle size are compared in terms of PL emission wavelength. Although the particle sizes kept constant, the different chemical composition of QDs resulted in different optical properties.
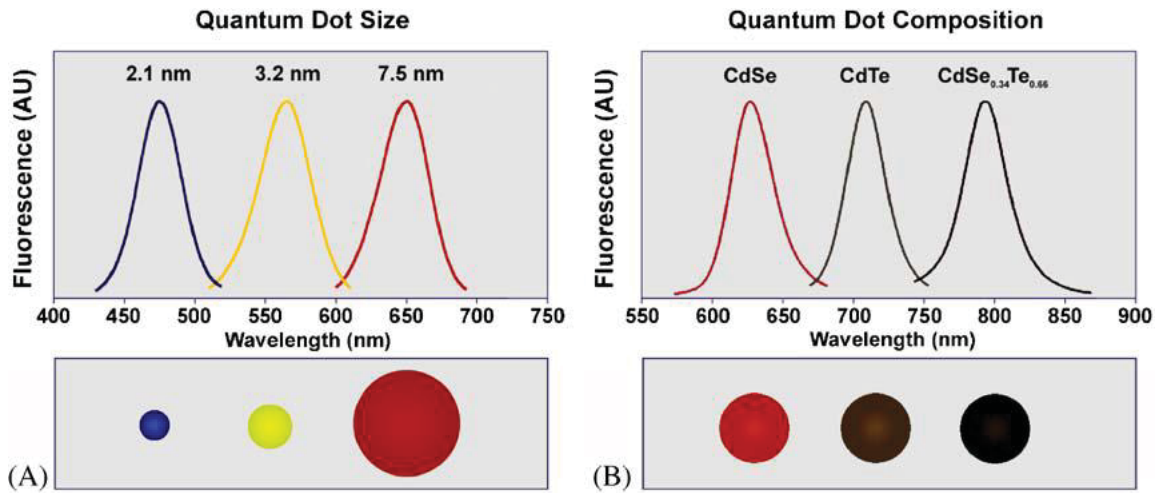
Figure 1.2. Tuning the QD optical parameters by changing the particle size or alloy composition. a) The emission of a CdSe QD which have a different emission wavelength in the visible range (450–650 nm) depending on the nanoparticle size in diameter between 2 and 7.5 nm. The representative particle sizes of these nanoparticles of the constant composition are shown schematically below the corresponding fluorescence spectrum b) Varying the composition of the ternary alloy $CdSe_xTe_{1-x}$, nanoparticles by keeping the particle size the same, the emission maximum may be tuned between 610 and 800 nm. (Source: Bailey and Nie, 2003)

1.3. Types of Quantum Dots

Core type quantum dots could be in binary, ternary and even in quaternary forms. Ternary QDs are one of the most suitable alternatives to binary ones in terms of their similar optoelectronic properties with wider optical properties. In order to enhance the photophysical properties of core ternary QDs, generally, additional inorganic shell coating (like CdS or ZnS) is used (Xie et al., 2009). Another approach for the same purpose is the development of quaternary nanocrystals (Deng et al., 2013).

When we consider alloy (ternary or quaternary) QDs, the optical properties could be tuned not only by the particle size but also the alloy composition. Figure 1.3 represents the various QD types as the core, core/shell, and alloy nanocrystals.

3

Represented core QD could be the binary, ternary or quaternary type. In the core/shell nanocrystals, there is an interface between two different crystal structure (like CdSe and CdTe shown in Figure 1.3 (Bailey and Nie, 2003; Unlu et al., 2013)) Here, the lattice parameters play an important role in terms of photophysical parameters of QD. In the case of alloy nanocrystals cations and/or anions could be placed as homogeneously or gradient. In gradient alloy nanocrystals, the alloy composition of the center and the surface like parts of the nanocrystals vary, but there would not be a certain interface between two crystal structure as in core/shell type QDs.
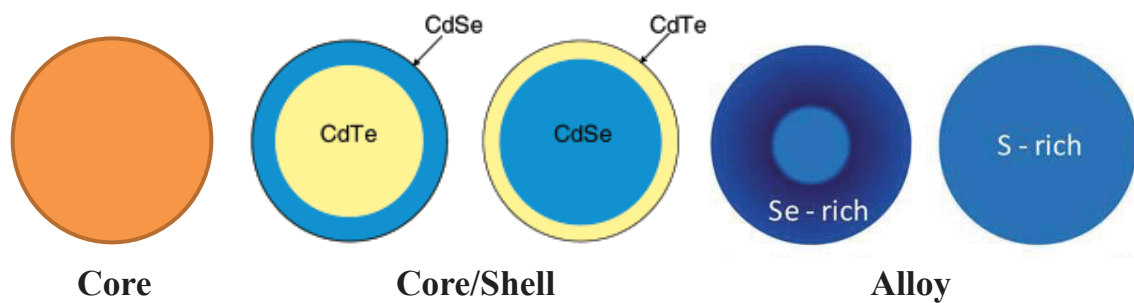
Figure 1.3. Schematic representation of core, core/shell, and alloy quantum dots.(Source: Bailey and Nie, 2003; Unlu et al., 2013)

1.4. Synthesis Methods of QDs

Choosing the proper synthesis method is important to obtain quantum dots with desirable optical and compositional properties. Methods for the synthesis of QDs can be divided into two type of methods as physical (in which there would be no chemical reaction) and chemical methods. One of the most used practical physical methods is the molecular beam epitaxy (MBE) for the QD synthesis. These methods require ultrahigh vacuum conditions in order to deposit atomic or molecular beams on crystalline substrates. Since we prefer to synthesize colloidal QDs in controllable and relatively cheaper methods, MBE is not the scope of this thesis.

Chemical methods for the QD synthesis varies according to the reactants, solvent systems, desired photophysical parameters of QDs etc. Various methods exist in literature, however, most used 5 of them will be discussed in this chapter. There of these methods were used in our Ph.D. study.

1.4.1. Hot Injection Approach

One of the earliest synthesis methods is the hot injection method (in other words organometallic approach) which is the introduction of rapid injection of organometallic precursors into an organic solvent at an elevated temperature. The method provides synthesized QDs in organic solvents, with a bright photoluminescence and discrete optical transitions in which it is required to use very active metal sources like dimethyl cadmium at relatively high reaction temperatures. The requirement of really active reactants at high reaction temperatures make this synthesis method more hazardous than other techniques.
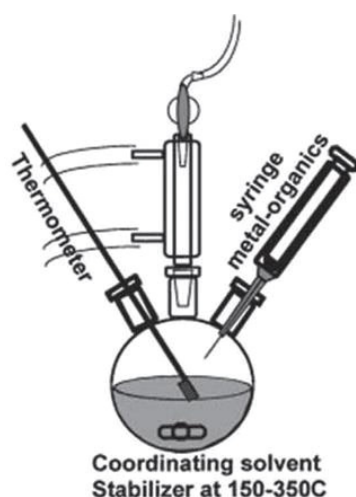
Figure 1.4. Schematic of the synthetic apparatus employed in the preparation of colloidal QDs by the hot-injection method (Source: Waurisch et al., 2011)

Hot injection is firstly developed by Murray et al. in 1993 by CdTe, CdSe, and CdS nanocrystals. The synthesis was based on the pyrolysis (which is the thermal decomposition of the materials at elevated temperatures in an inert atmosphere) of organometallic precursors in an organic solvent. They used dimethyl cadmium as a Cd precursor; and phosphine selenide, phosphine telluride, or bistrimethylsilyl sulfide as the chalcogenide (Se, Te or S) sources. A mixture of trioctylphosphine (TOP) and trioctylphosphine oxide (TOPO) served as the coordinating solvent which also has a high boiling point for the high-temperature synthesis. The resulted QDs have almost perfect crystalline structure, monodisperse, and highly luminescent. The reason is most

probably the high reaction temperatures (300 °C) which annealed out defects and improved crystallinity (Waurisch et al., 2011). Later, Talapin group synthesized highly luminescent CdTe nanocrystals by dimethylcadmium as Cd precursor and different tellurium sources in mixtures of dodecylamine and TOP as the coordinating and size-regulating solvent at 150 ˚C to 220 ˚C reaction temperatures. As a result in the particle size range of 2.5 and 7 nm CdTe nanoparticles with zinc blende crystal structure was obtained (Talapin et al., 2001). In terms of alloy QDs, $Zn_xCd_{1-x}S_ySe_{1-y}$ nanocrystals were also synthesized by the injection of a tri-n-octylphosphine-Se (TOP-Se) precursor into a Cd precursor solution at high reaction temperatures. According to their report, they controlled the optical properties of quaternary QD, by both changing the alloy composition (for the constant particle size), and the particle size (for the same alloy composition).(Deng et al., 2009)

The hot-injection method produces high-quality colloidal QDs, by separating the nucleation and growth in time. Also, annealing of nanoparticles at elevated reaction temperatures allows obtaining defect-free colloidal QDs with a relatively high quantum yield of fluorescence. Size distribution of QDs obtained by this method may reduce under 5% in some cases, too (Protière and Reiss, 2006; Chen et al., 2013). On the other hand, highly reactive metal precursors at relatively high reaction temperatures can not be classified as user-friendly, so we did not prefer to use this technique in our Ph.D. study.

1.4.2. Solvothermal Approach

In a solvothermal approach, the reaction occurs in stainless steel autoclaves. Freshly prepared QD reactants are put stainless steel autoclaves and heated. The reaction temperature is adjusted (approximately in the range of 150-375 ºC) for proper reaction time. This technique was used in literature to synthesize ZnS (Liu et al., 2013), CdS (Aboulaich et al., 2012), CdSe (Liu et al., 2013) and CdTe quantum dots (Yang et al., 2008). Glutathione (GSH) and thioglycolic acid (TGA) capped CdTe QDs were synthesized by the hydrothermal approach in terms of investigation of major reaction parameters like temperature, pH, reactant concentrations and reaction time etc (Yu et al., 2012). Core/shell CdTe/CdSe QDs were also reported with tunable emission spectra

in the range from 62 0nm to 740 nm. The photoluminescence quantum efficiency of synthesized QDs was given as 44.2 % (Wang and Han, 2010)

Given examples shows that reaction temperature, reaction time, types of solvent, surfactant, and precursors could be arranged to get desired nanocrystals. However, it is not possible to control the growth of the nanoparticles during the reaction time by optical spectra and size distribution. Also, it is not proper for the large-scale synthesis for further experiments. These are the reasons that we did not prefer to use this method in our Ph.D. study.

1.4.3. One-Pot Aqueous Synthesis

One-pot aqueous synthesis approach is one the most preferred methods because it is less toxic and cheaper than other methods. Since many practical applications including biomedicine, photovoltaic systems require water-soluble colloidal QDs, this method is very proper to synthesize colloidal QDs which are stabilized with short alkyl ligands. There are three main synthetic routes to hydrophilic colloidal QDs (Brichkin and Chernykh, 2011) . These are could be counted as synthesis in aqueous solutions, replacement of hydrophobic ligands (stabilizing agents) by hydrophilic ones (shorter alkyl ligands and formation of the secondary water soluble layer which surrounds hydrophobic particles in order to make them dispersible in aqueous medium.

Although all these techniques achieve to form colloidal QDs which can be dispersible in aqueous medium, except the first one (synthesis in aqueous solutions) photoluminescence quantum efficiency of QDs are expected to decrease significantly. This is the reason that one-pot aqueous method is the most proper method to synthesize water-dispersible colloidal QDs. Schematic representation of the synthesis procedure of colloidal aqueous phase QDs is shown in Figure 1.5. Rogach group synthesized CdTe QDs with thioglycolic acid (TGA) and mercaptopropionic acid(MPA) as stabilizing agents in an aqueous medium by one-pot aqueous synthesis approach (Rogach et al., 2007). They reported the emission wavelength range between 500 to 800 nm with 40 – 60 % PL QE. They investigated the effect of capping agent in the growth of QDs and the emission decay times (lifetimes in an excited state). Similarly, Lesnyak synthesized blue emitting TGA capped $Zn_xCd_{1-x}Se$ QDs which has emission tunability from UV to blue spectral region (Lesnyak et al., 2008).
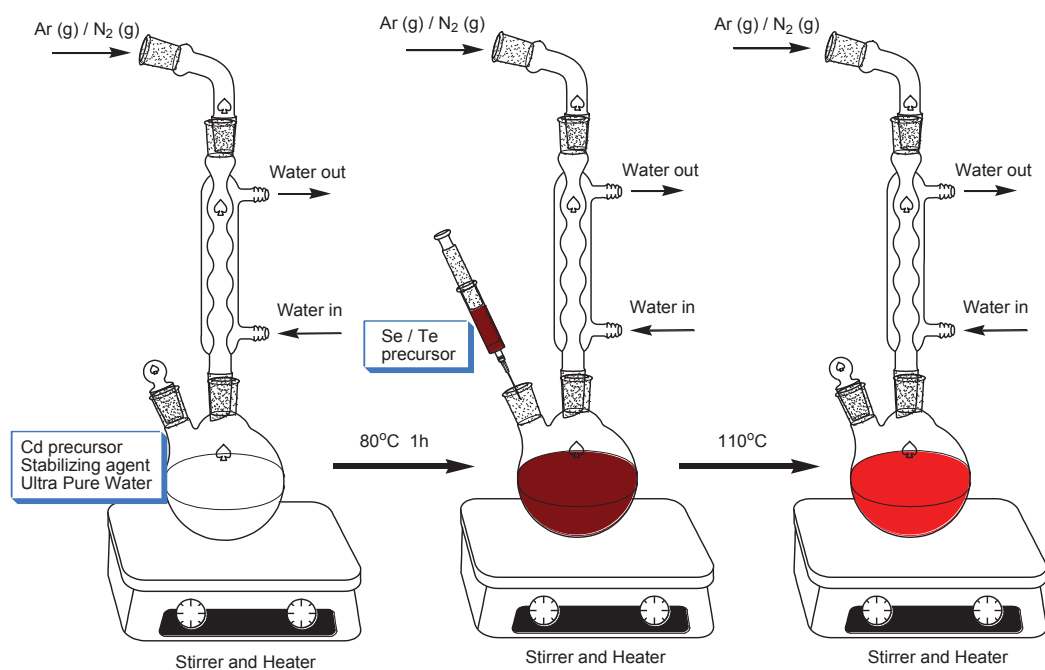
Figure 1.5. Schematic representation of one-pot aqueous synthesis method.

Among these examples, various thiol-substituted ligands are also used as capping agents like mercaptoacetic acid (Koneswaran and Narayanaswamy, 2009) mercaptopropionic acid (Qian et al., 2006), cysteine (Cao et al., 2010), 1-thioglycerol (Zhou et al., 2011), etc. Although its low toxicity and cheaper costs, colloidal QDs synthesized in aqueous medium have a generally broader size distribution and lower PL QE than organic based methods (Yu et al., 2006). Since it is possible to apply additional procedures to improve the photophysical properties of QDs, it is still one of the most preferred techniques in the QD synthesis as mentioned above.

In our Ph.D. synthesis, ZnS_xSe_{1-x} nanocrystals were synthesized by this technique. Detail information about the experimental part exists in the related title.

1.4.4. Two-Phase Approach

The two-phase approach is a more preferable method due to its low toxicity, easy-performing and lower temperature requirement with respect to other methods. Burst et al synthesized 1 - 3 nm thiol-capped gold nanocrystals. They used sodium borohydride to reduce AuCl4 in the presence of an alkanethiol solution (Brust et al.,

1994). Colloidal CdSe and CdS QDs were synthesized by the two-phase approach by Pan group in 2007. They used oil-soluble cadmium myristate (Cd-MA) as cadmium source, and water-soluble chalcogenide precursors as Na_2S, thiourea, NaHSe, Na_2SeSO_3, and selenourea as sulfur and selenium sources, respectively. Since the reactants exist in immiscible two solvents, CdSe nanocrystals were formed in the interface of toluene and water as shown in Figure 1.6. The reaction temperature is between $60 - 90°C$ which is relatively low with respect to other methods. They reported that synthesized CdSe nanocrystals are 1.2-3.2 nm in diameter and have 42 % LP QE at room temperature (Pan et al., 2007).
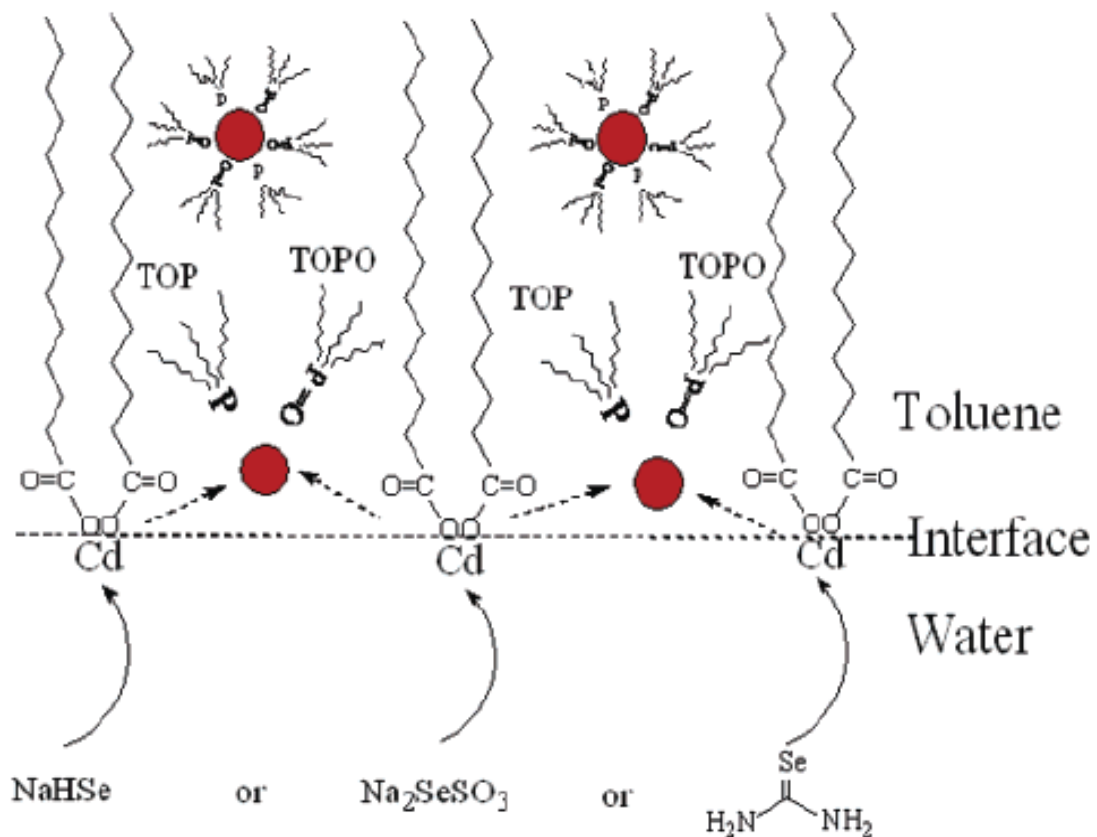
Figure 1.6. The schematic reaction for the mechanism for two-phase synthesis of CdS nanocrystals.(Source: Pan et al., 2007)

Although the two-phase approach has lots of advantages in cost, toxicity and photophysical parameters of QDs (like high PL QE, controllable and monodisperse particle size, narrow FWHM), there are limited studies on this method. In our Ph.D. thesis, we used the two-phase approach in order to synthesize $Zn^xCd_{1-x}S_ySe_{1-y}$

nanocrystals. The schematic representation of the procedure is given in Figure 1.7. The details about the experimental part could be found in the related title.
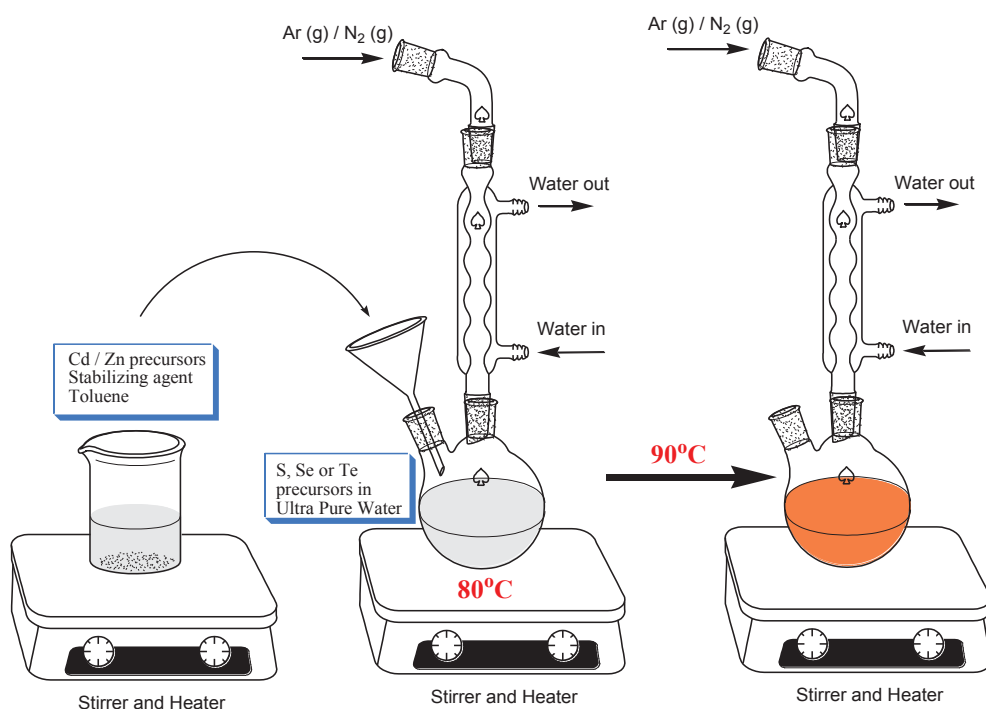
Figure 1.7. Schematic representation of two-phase approach.

1.5. Characterization of Quantum Dots

Characterization of QDs can be divided into two group as optical and structural characterization.

1.5.1. Optical Characterization

The optical properties of the synthesized QDs were measured by using Varian Cary 50 UV-Vis, Varian Cary Eclipse fluorescence spectrometers, and Edinburg FS5 Spectrophotometer. Absorption, PL emission and excitation spectra of QDs, time-correlated single photon counting (TCSPC) – lifetime and photoluminescence quantum efficiency (PL QE) measurements were carried out at room temperature.

Absorbance (optical density – OD) is the logarithmic ratio of initial radiation to transmitted radiation through the sample. Beer's law is applicable for QDs that the absorbance is directly proportional with the concentration of QD, their extinction coefficient (which is specific to the sample) and length of the light path (thickness of the cuvette for solution phase measurements, the thickness of the film for the film samples). Characteristic absorption spectra of QDs is a shoulder rather than a peak. Well defined absorption peaks sign better crystallinity and optical transitions. On the other hand, PL spectra of QDs are like Gaussian-shaped peaks in which narrow FWHM values are desired. FWHM is the width of the PL emission peak at the half maximum intensity. It generally appraises the monodispersity of the QDs.

Generally, the fluorescence emission wavelength shifts to longer wavelength compared to the absorption wavelength. The mechanism is clearly explained in the Jablonski diagram given in Figure 1.8.
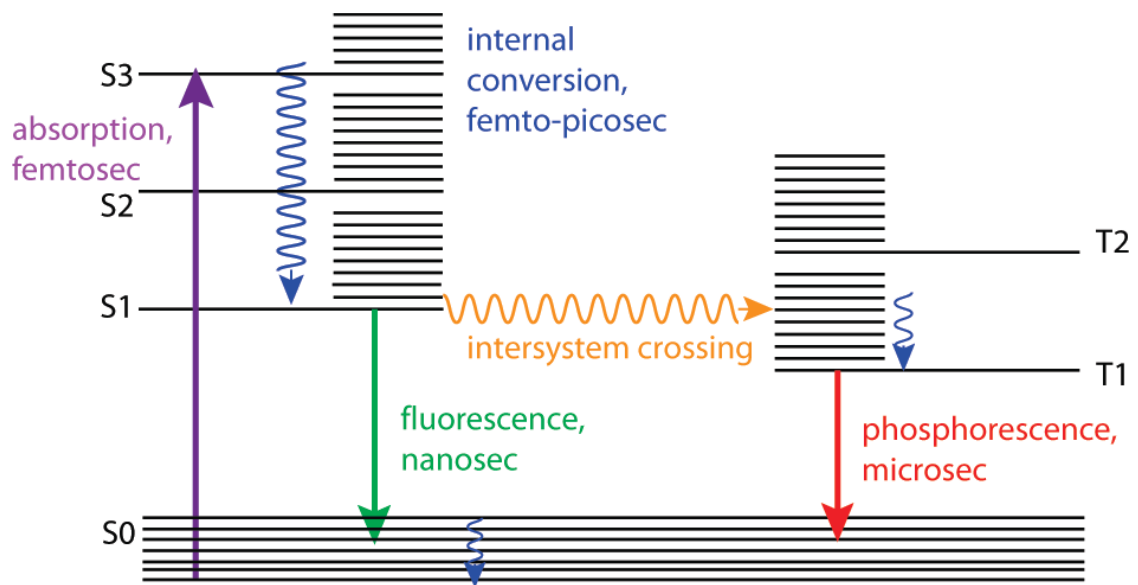
Figure 1.8. Jablonski diagram and a time scale of photophysical processes for organic molecules (Source: Berezin and Achilefu, 2010)

As shown in Figure 1.8, during the absorption process, an electron is excited from the valence band (ground state) of QD to energy levels of the conduction band (excited state). This process is followed by nonradiative vibrational relaxation process which occurs very fast. As a result, electron falls to the lowest excited state in the conduction band. Recombination occurs with the electron in the conduction band and its hole in the valence band. This combination is called as action in which radiative energy

gets out called photoluminescence emission. In other words, the system emits a photon and relaxes to the most stable state - ground state - in the valence band.

The relaxations in the conduction band (just after the absorption process) result in the difference in the energy band gap between absorbed energy and the emitted energy, correspondingly difference in the wavelength in the electromagnetic spectrum. This difference between absorption and emission spectra is called "Stokes shift".

Basically, photoluminescence quantum efficiency (PL QE) is the ratio of the number of emitted photons to the number of absorbed photons. Experimentally, it is possible to calculate PL QE by two different way. One of them is to compare the fluorescence and absorption spectra of both unknown substance and a dye with known quantum yield. That is the reason it is important to choose the proper dye for the calculation. The Absorption and PL spectra of the proper standard dye should overlap with the absorption and PL spectra of the unknown sample (in our case, QD). The PL QE is calculated by the following formula;

$$QY = Q_{ref} \frac{I}{I_{ref}} \frac{OD_{ref}}{OD} \frac{\eta^2}{\eta_{ref}^2} \qquad (1.2)$$

where "QY" is the quantum yield, "I" is the intensity or the area of the emission peak in the emission spectrum (Wavelength vs. Intensity), "OD" is an absorbance at the excitation wavelength, and "η" is the refractive index of the solvent. Subscript "ref" represents the reference dye.

Quantum yield could also be defined as the ratio of radiative and non-radiative processes as shown in the equation below. "k_r" and "k_{nr}" are the rate constants of radiative and non-radiative processes of the sample, respectively (Fery-Forgues and Lavabre, 1999).

$$QY = \frac{k_r}{k_r + \sum k_{nr}} \qquad (1.3)$$

Time-resolved measurements are also an important part of fluorescence spectroscopy. In many cases like the overlap of emission and absorption spectra, time-resolved measurements provide more information than steady-state measurements. Most of these measurements are performed by time-correlated single photon counting

(TCSPC) measurement. The principle of TCSPC is simply, the excitation of the sample by a pulse of light at the specific wavelength and then the measurement of the number of photons with respect to time (Lakowicz, 2006). Lifetime measurements were recorded by FS5, Edinburgh Instruments. Photodynamic information about the synthesized quantum dots was obtained from fluorescence decay traces.

1.5.2. Structural Characterization

Structural characterization of QDs are carried out by using various techniques like X-Ray Diffraction (XRD), Dynamic Light Scattering (DLS), Scanning Transmission Electron Microscopy (STEM), Scanning Electron Microscopy-Energy Dispersive X-Ray Spectroscopy (SEM-EDS), and Transmission Electron Microscopy (TEM), Small angle X-ray Spectroscopy (SAXS), Electron Paramagnetic Resonance (EPR) Spectroscopy in order to reveal information about the chemical composition and crystal structure of the QDs.

XRD is the technique which is based on observing the intensity of scattered X-Ray beam hits the sample. As an output, the lattice parameters and geometry of crystal structure are obtained. Philips X'Pert Pro which is placed in IYTE-MAM was used for the analysis.

Electron Microscopy is a very the other most used technique that capable of providing structural information over a wide range of modification. The Scanning Electron Microscope (SEM) gives information about the morphology and topography of the samples by using electrons rather than light to form an image with approximately between 100 Å and 10 μm resolution. On the other hand, Scanning Electron Transmission Microscope (STEM) can be used to get information about the size and the shape of the QDs due to its higher resolution compared to SEM because of its transmission detector. The most commonly used attachment of SEM is the energy dispersive X-ray detector, EDS. EDS detector allows compositional analysis of the sample from an area, dot or line. The results of EDX analysis are presented as a spectrum and data is given as atomic percent or weight percent. Philips XL 30S FEG Scanning Electron Microscope and Scanning Transmission Electron Microscopy at IYTE-MAM were used for the elemental analysis. The other electron microscope that we used is the Transmission Electron Microscope (TEM). By the help of TEM, the

objects can be seen in the order of a few angstroms. In other words, atoms could be seen. TEM uses a beam of electrons to pass through the crystalline sample. A light source emits electrons then they travel through a vacuum in the column of the microscope. Transmission Electron Microscopy (TEM) at UNAM / Bilkent University was used to analyze the QDs.

The particle size of the QDs is investigated by Dynamic Light Scattering (DLS) Measurements by Malvern Zetasizer Nanoseries -Nano-ZS. Since DLS gives the hydrodynamic diameter of the QDs, the results are generally bigger than the results obtained from TEM or STEM. It is acceptable because TEM measures the hard core of the nanocrystal but DLS measures both the hard core and the hydrodynamic diameter of the nanocrystals (Qian et al., 2007).

1.6. Applications of Colloidal Quantum Dots

Unique properties of colloidal QDs make them very attractive for various applications including light emitting diodes (LEDs), field effect transistors (FETs), solar cells, photovoltaics and biological applications etc. Widely used areas (especially with the scope of this Ph.D. study) LEDs, FETs, and solar cells will be discussed here.

1.6.1. Light Emitting Diodes

QDs are widely used in the optoelectronic applications especially in light emitting diodes as an active layer. In a typical LED, a thin layer of light-emitting QD is sandwiched between the hole transport layer (HTL) and an electron transport layer (ETL), which provide an injection of carriers into the QD for the recombination.

The first study on organic/inorganic electroluminescent device was reported by Alivisatos in 1994. Recombination (light emission) was formed by the injection of holes into p-parapheynlene vinylene (PPV) and the injection of electrons into multilayer CdSe QDs. They obtain red to yellow electroluminescence at relatively low voltages as 4 V (Colvin et al., 1994). The same group improved the efficiency of LED by using CdSe/CdS core/shell type QD with ITO/PPV/CdSe(CdS)/Mg/Ag device structure (Schlamp et al., 1997). From red to green electroluminescence with external quantum

efficiencies of up to 0.22% at brightnesses of 600 cd/m2 and current densities of 1 A/cm2 were obtained. The operating voltages were 4 V and lifetimes were quite long.

At the beginning of 2000, phase segregation between capping agent of QD and the organic layers was used and a 25-fold improvement in luminescence efficiency (1.6 cd A^{-1} at 2,000 cd m^{-2}) was achieved. The device structure that they used was ITO/TPD(35nm)/CdSe/ZnS/TAZ(10nm)/Alq3(40nm)/Mg:Ag/Ag) (Coe et al., 2002). Improvements in the QLEDs were increased and lots of device structures with QDs were studied on specific pure colors (Caruge et al., 2008; Anikeeva et al., 2009; Kang et al., 2015).

In addition to the monochromatic emissions of QD based LEDs, it is also very attractive in devices that emit white light in lighting and display technology. In order to obtain white light, it is required to design three primary colors or two complementary coloring materials. One of the studies that white hybrid organic/inorganic LEDs have been fabricated by using stable red-emitting CdSe/ZnS core-shell quantum dots was reported by Rizzo Group in 2005. The device structure was formed by a host/guest system in which a blue-emitting polymer (PFH-MEH) was used. The green color was provided by Alq_3 and as a result, fairly pure white QLED was fabricated. Device performance was reported as maximum external quantum efficiency up to 0.24% at 1 mA cm^{-2} and 11 V in air atmosphere (Li et al., 2005).
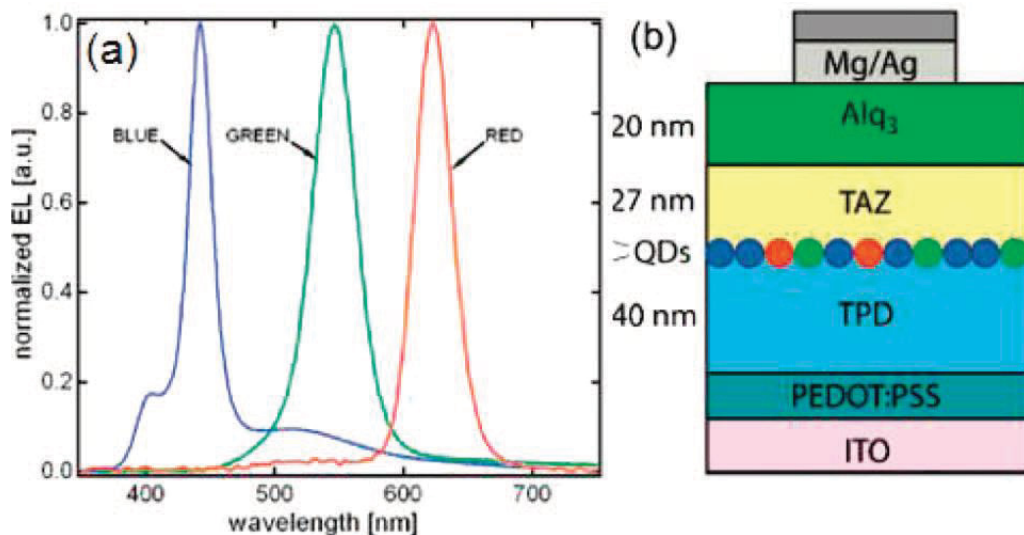
Figure 1.9. White light emitting QLED obtained by a mixture of red, green, and blue QDs. (a) Normalized EL spectra of devices and (b) Device cross section was shown.(Source: Anikeeva et al., 2007)

Anikeeva et al. also reported white QD-LEDs with the emitting balanced mixture of red, green, and blue emitting QDs. The device structure was ITO/PEDOT:PSS/TPD/QDs/TAZ/Alq$_3$ (Figure 36) At an applied voltage of 5 V, the external quantum efficiency of white QD-LED was 0.36% and luminescence efficiency was 0.9 cd A^{-1} (Anikeeva et al., 2007)

After about 25 years of research and development, QLEDs are in the stage of commercialization stage. The results are comparable with commercial LEDs that display and lighting technology embraces the new generation QLEDs nowadays depending on the performance, cost, lifetime, manufacturability, etc of QLEDs.

In our Ph.D. study, the visible range QLED studies have been performing and some preliminary results are achieved by using TOPO and oleic acid capped QDs.

1.6.2. Field Effect Transistors

QDs with precisely controlled particle size, chemical composition, and the optical properties have been explored as the building blocks for field effect transistors (FETs). QD based FETs have lots of advantages like solution processability, low cost etc. However, the performance of QD based FETs strongly depends on the electronic coupling between QDs in which the ligands are the main parameters. Since the long alkyl chain ligands show very poor charge transport properties, ligand exchange procedures or thermal/chemical treatments are required. Before getting into the literature studies on QD based FETs, it would be better to describe the FET basically.

Typical FET has three terminals; gate, drain, and source. The gate terminal controls the opening and closing of a physical gate which permits electrons to flow through or blocks their passage by creating a conductive channel between the source and drain terminals. The source and drain electrodes are usually lithographically patterned. The gate electrode is electrically insulated from the transistor channel with the help of a thin dielectric material". Wide bandgap oxides such as SiO$_2$, Al$_2$O$_3$, and HfO$_2$ and polymers such as PMMA are usually used as the dielectric layers.

By controlling the gate voltage, the current through the semiconductor channel can be easily flipped on and off enabling. Generally, the voltage is applied to the gate electrode and the drain electrode. The source electrode is usually grounded. Basic configurations of QD based field-effect transistor (FETs) are shown in Figure 1.10.
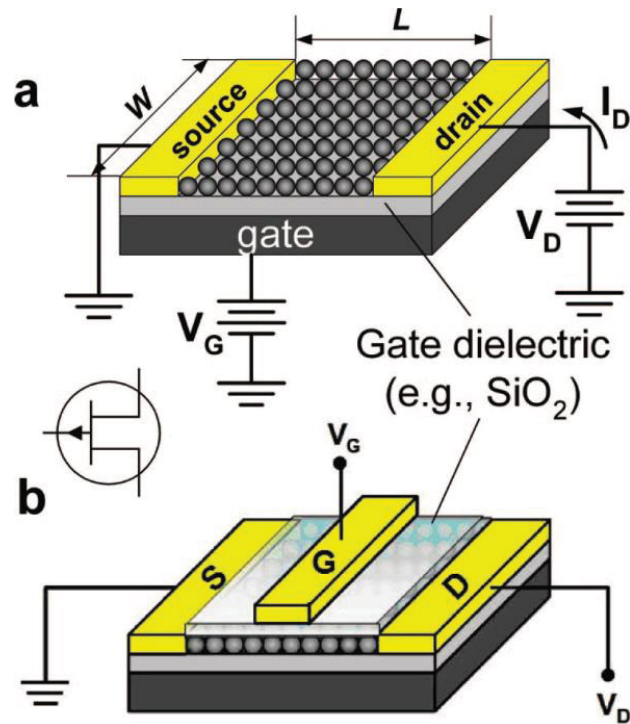
Figure 1.10. Basic configurations of QD based field-effect transistor (FETs) a) Bottom-gated FET, (b) top-gated FET. *L* and *W* show transistor channel length and width, respectively. S, D, and G are the source, drain, and gate electrodes (terminals).(Source: Talapin, 2010)

The first inorganic FETs fabricated using colloidal semiconductor nanoparticles were reported in 1999 by Jacobson and coworkers (Ridley et al., 1999). These devices were performed from pyridine-capped CdSe QDs. However, because of the high annealing temperature (above 250 °C.) there were no QD in the channel of FET after the appealing process. That is the reason the device can not be assigned as QD based FET. QD based FET with close-packed quantum confined QDs were first reported by Talapin et al in 2005 (Talapin and Murray, 2005). oleic acid capped PbSe QDs were used in this study. As they reported, replacement of oleic acid ligand with hydrazine (N_2H_4) resulted the reduction in the interparticle spacing of the conductivity is increased 10 orders of magnitude.

PbSe QDs are also used in FETs by Nozik group (Law et al., 2008; Luther et al., 2008). They chemically treated the PbSe QD films with different amine and thiol ligands. The ones treated with methylamine or pyridine solutions resulted in a significant increase in the conductivity of the devices. 1,2-ethanedithiol treated devices showed ambipolar behavior in the dark but they converted to p-type FETs with 30-60 times higher conductivity after exposure to 300 mW/cm2 broadband illumination (Luther

et al., 2008). This kind of studies points out that the surface ligands are significantly effective on the performance of FETs. Treatments of QD films (simple removal of the surface ligands and their replacement with small molecules is the only one of several processes) is necessary.

Several studies and optimizations on FETs results in significant increases in charge transport/carrier mobilities. For example, using high-k dielectric materials or thinner gate oxides decrease the operating voltage of FETs. HgTe QDs are used in the bottom and top gated FETs by employing high-k dielectric materials as an insulator. As a result, they achieve high field-effect mobility at low gate voltages (Kim et al., 2006). In terms of light emitting field effect transistors (LEFETs) the only study is reported by Zaumseil Group in 2005 (Schornbaum et al., 2015). They used PbS QDs with ionic gel in order to increase the mobility of charge carriers.

Various QD combinations with different ligands and surface modification techniques improve the charge transport properties of QD based FETs and LEFETs. In our Ph.D. study, I had to spend six months in Physical Chemistry Institue at Heidelberg University in order to study LEFETs. The details about this study are under the related title (Chapter 6)

1.6.3. Solar Cells

Colloidal QDs are widely used in solar cells in literature and the progress on this hot topic increases every day. The schematic representation of QD based solar cell is shown in Figure 1.11. The typical output (I-V curve) for the solar cells are also shown in the same figure.

The first inorganic ligand passivated colloidal QD (PbS QDs) photovoltaics was reported in 2011 by Tang et al. 6 % power conversion efficient was achieved by passivating the surface defects and increasing carrier mobilities (Tang et al., 2011). After that, again with PbS QDs, stable QD base solar cells was performed and the power conversion efficiency was improved to 8.55 %. In this study they used ligand exchange procedure for oleic acid capped PbS QDs in order to obtain tetrabutylammonium iodide (TBAI) and 1,2 ethandithiol (EDT) ligands on the surface of QDs (Chuang et al., 2014).
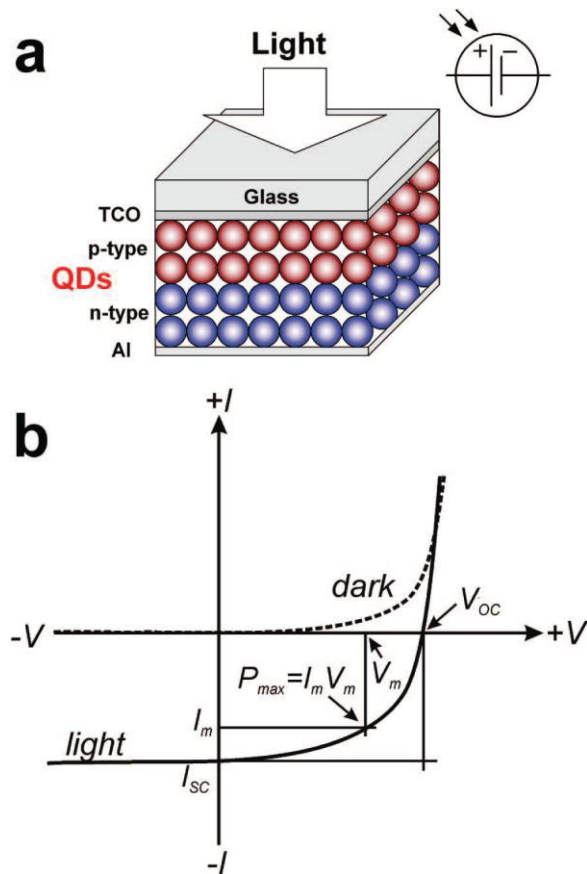
Figure 1.11. (a) The schematic representation of a QD based solar cell with the layers of nanocrystals with n- and p-type conductivity. TCO represents the "transparent conductive oxide". (b) The typical current-voltage (*I-V*) characteristics of a solar cell. Here, V_{oc} is the open-circuit voltage, and I_{sc} is the short-circuit current. The generated electrical power is characterized by its maximum value P_{max}. (Source: Talapin et al., 2010)

CHAPTER 2

SYNTHESIS AND CHARACTERIZATION OF TERNARY ZnS$_x$Se$_{1-x}$ NANOALLOYS

2.1. Introduction

Quantum dots (QDs), with their size-tunable and composition-dependent characteristics, have great potential for many nanoscale optoelectronic applications. Although the QDs of CdTe, CdS, HgSe, HgCdTe have been widely studied by many groups, the potential toxicity of these materials in the biological environment limits their usage. Therefore, synthesis of Cd and Hg-free quantum dots that can be integrated into the existing technology is of importance.

Recently, among the various materials, especially QDs of zinc chalcogenides such as ZnS and ZnSe have attracted tremendous interest. Regardless of the toxicity effect, when compared with others, Zn based QDs have significant advantages in terms of their optical properties in UV-blue region of the electromagnetic spectrum. While ZnS nanocrystals have attraction in optoelectronic devices in terms of high PL emission in UV-blue region (Li et al., 2010; Mandal et al., 2012), ZnSe nanocrystals are widely used as an perfect inorganic passivation shell for another type of quantum dots in order to improve the stability and PL emission by means of its wide band gap and large binding energy (Senthilkumar et al., 2012). Their nanoscale particle size also results in high surface/volume ratio which is significantly required in photocatalytic applications (Mandal et al., 2012; Feng et al., 2014). Moreover, as a ternary compound, ZnS$_x$Se$_{1-x}$ nanoalloys have a great potential to control the energy bandgap and the lattice constants of ZnSe and ZnS binary QDs in one system. Therefore, regarding all properties of the binary system, ZnS$_x$Se$_{1-x}$ nanoalloys also allow tuning the optical properties in a wider range in UV-blue region which make ZnS$_x$Se$_{1-x}$ nanoalloys an attractive choice for optoelectronic applications like LEDs and photodetectors (The European Physical Journal B - Condensed Matter and Complex SystemsChemical Society ReviewsAbdi-Ben Nasrallah et al., 2005; Park et al., 2012).

In addition, further enhancement in the functionalities of QDs can be achieved via doping by foreign atoms. While rare earth elements change the photophysical properties of quantum dots (Pereira et al., 2006), K doping leads to significant increase in the electrical conductivity (Yu et al., 2003), transition metal ion doping leads to high-temperature ferromagnetic nanocrystal aggregates (Schwartz et al., 2003). In addition to these, doping by transition metal atoms is found to be the most efficient way of utilizing magnetic properties in QDs (Lad et al., 2007; Proshchenko and Dahnovsky, 2015).

Studies have revealed that, among the transition metals, especially the incorporation of Mn^{2+} dopants into the Zn based QDs is experimentally easy process due to its similar valence charge and ionic radii (Ma et al., 2013). Mn-doped QDs gain important functionalities such as Stokes-shift-induced reduction in self-quenching, improved thermal conductivity, and enhanced chemical stability (Pradhan et al., 2005). Besides, the location of the Mn ion in the host crystal influences the characteristic features of the quantum dot significantly. As reported by Tsujii et al., upon the doping of ZnS nanocrystals that have no intrinsic magnetism in their ground state most of the Mn ions are coordinated on the surface of the nanocrystal and the amount of Mn ions doped inside the nanocrystal is much smaller than the nominal composition resulting the giant internal magnetization (Tsujii et al., 2003). In addition, several studies showed that in the analysis of the electron paramagnetic resonance (EPR) spectra, the presence of isolated Mn ion as a substitutional atom on Zn sites and as adatom on the surface results in a broad, featureless Lorentzian component line associated with exchange coupled Mn ions (Igarashi et al., 1997; Borse et al., 1999; Beermann et al., 2006; Nistor et al., 2010; Stefan et al., 2011). These are the reasons that, it is essential to understand the location of Mn^{2+} in nanocrystal lattice in terms of determining the final features like exciton-Mn energy transfer rate (Chen et al., 2012) and optical properties (Yang et al., 2006).

Several groups study the correlation of the exact dopant location in order to control the photophysical properties of QDs. Ithurria et al. reported Mn-doped CdS/ZnS core/shell nanocrystals in order to control the Mn ion's radial position in the shell. In this respect, they used photoluminescence spectroscopy to observe and compare the intensity of Mn ion emission (Ithurria et al., 2007). Similarly, Hofman group has studied controlled doping of Mn ion to CdS QDs by the growth of ZnS shell. The correlation of the location of Mn ions was performed by fluorescence spectroscopy, EPR and XRD analysis (Hofman et al., 2017). As it seen, in order to correlate the location of dopant

ion by spectroscopic techniques, getting comparable photoluminescence from the QD is essential. Very recently, Nistor et al. investigated the composition and magnetic properties of the Mn ions in the cubic ZnS quantum dots. The possible factors of the observed collective magnetism as aggregated forms of Mn doping (Nistor et al., 2016), the localization of the Mn ions on the surface of the QDs (Nistor et al., 2015) and the calculations in terms of the interactions related with the number of dopant Mn ions and their locations (Nistor et al., 2016) were investigated.

In this chapter, we focussed on the synthesis of Mn-doped ZnS_xSe_{1-x} nanoalloy QDs at relatively low reaction temperatures in an aqueous medium. Location of the Mn ion is investigated with XRD, PL and SEM-EDS techniques. EPR analysis is done for both solid and liquid samples in order to show the effect of the dipolar interaction of Mn ions in the QD host. Experimental findings are also supported by the state-of-the-art DFT calculations. Both experimental and theoretical findings confirmed each other and result that doped Mn ions are located on the surface of the ZnS_xSe_{1-x} nanoalloys.

2.2. Experimental

The chemicals that are used in the synthesis of ZnS_xSe_{1-x} ternary nanoalloys, zinc chloride, thiourea, manganese chloride, sodium borohydride, sodium hydroxide were purchased from Alfa-Aesar, and thioglycolic acid, selenium powder were purchased from Sigma Aldrich. 2-propanol for purification of nanoalloys was also purchased from Sigma Aldrich.

2.2.1. Synthesis of Se precursor, NaHSe.

NaHSe was synthesized by the procedure as given in our previous study (Unlu et al., 2013). The chemical reaction of the synthesis is also given below.

$$4 \text{ NaBH}_4 + 2 \text{ Se} + 7 \text{ H}_2\text{O} \rightarrow 2 \text{ NaHSe} + \text{Na}_2\text{B}_4\text{O}_7 + 14\text{H}_2 \qquad (2.1)$$

In this synthesis, 1.2 mmol Se powder and 2.5 mmol NaBH$_4$ were mixed with 10 mL ultra-pure water in a reaction flask under Argon atmosphere. When the atmosphere in the flask is inert after 5 minutes, 10 mL ultra-pure water was injected into the flask.

After an hour at room temperature, while Ar gas bubbling, 2.5 ml of clear solution was directly used for the synthesis of colloidal ternary nanoalloys without any further purification. Because of the high sensitivity of NaHSe to the air, it is essential to synthesize it freshly before each experimental trial.

2.2.2. Synthesis of Colloidal ZnS$_x$Se$_{1-x}$ Ternary Nanoalloys.

The alloys were synthesized with a modified one pot aqueous synthesis method (Rogach et al., 2007). 3 mmol ofZnCl$_2$ (or another zinc precursor) was dissolved in 110 ml of ultrapure water. Thioglycolic acid (TGA), mercaptopropionic acid (MPA) or n-acetyl l-cysteine (NAC) were used as capping agents. 6 mmol capping agent was added to the solution indicated Zn precursor for individual reactions. 1.0 M NaOH solution was used to adjust the pH of the medium to the desired value. It is necessary to arrange the pH of the medium to 6 for TGA and NAC, 10 for MPA. The cloudy solution was observed for MPA capped ZnS$_x$Se$_{1-x}$ nanoalloys if the pH was not adjusted to 10. The reaction flask was heated to 80°C at reflux under the nitrogen atmosphere. After one hour, thiourea and freshly synthesized NaHSe were simultaneously injected with different initial mole ratios into the reaction flask as S and Se precursors, respectively; and the reaction temperature was increased to 110°C. Aliquots of the sample were taken at different time intervals and their optical properties were monitored by using UV–Vis spectra. The reaction was stopped after 24 hours by cooling the reaction flask. The excess capping agent, unreacted metal and chalcogen precursors were separated from the nanoalloy particles by precipitation and centrifugation using isopropanol.

2.2.3. Capping ZnS Shell on ZnS$_x$Se$_{1-x}$ Core

In order to coat thioglycolic acid capped ternary ZnS$_x$Se$_{1-x}$ core with inorganic ZnS shell, 1 mmol ZnCl$_2$ and 1 mmol thiourea in 5 mL ultrapure water was added to the nanoalloy dispersion after 20 hours of reaction initiation at 110 °C. 3 mmol thioglycolic acid was also added to Zn and S precursors as an additional capping agent. The reaction was terminated by cooling after 4 hours reaction time following the injection of ZnS shell precursors. Similar purification techniques were used for these core/shell nanoalloys as well.

2.2.4. Synthesis of Colloidal Mn-Doped ZnS_xSe_{1-x} Ternary Nanoalloys.

The same synthesis method was used for the synthesis of Mn^{2+} doped ZnS_xSe_{1-x} nanoalloys. Mn^{2+} stock solutions were prepared at different concentrations, from $MnCl_2$. Different amount of Mn^{2+} solutions were injected into the ZnS_xSe_{1-x} reaction flask at 110 ˚C after 20 hours of reaction time under N_2 atmosphere.

2.2.5. Characterization

Absorption and photoluminescence spectra of the ZnS_xSe_{1-x} and Mn^{2+} doped ZnS_xSe_{1-x} nanoalloys were obtained by Varian Cary Absorption spectrophotometer and Varian Cary Eclipse Fluorescence Spectrometer, respectively. The size of the nanoalloys was measured by Malvern Zetasizer Nano ZS. The X-ray powder diffraction pattern of the nanoalloy was obtained by using a Philips X'pert Pro Materials Research Diffractometer. The grounded samples were placed on a zero-background silicon sample holder. Data were collected by using $CuK\alpha$ (λ= 1.5406 Å) radiation with the 0.02°/seconds scan rate between 10 - 70° for 2Θ values. Composition analysis was carried out by SEM-EDS analysis. Thermal Gravimetric Analysis of ZnSSe nanoparticles was made by using Perkin Elmer Pyris 6 TGA in Ege University Solar Energy Institute. X-band EPR measurements were done by CMS 8400 (Adani) spectrometer provided with a TE102 resonator cavity at a microwave frequency of 9.4 GHz at room temperature. Measurements were performed in quartz sample tubes.

2.3. Results

Alloyed nanocrystals have advantages over binary type nanocrystals in terms of tunability of optical properties not only with the particle size but also the alloy composition. Because of this reason we synthesized ZnS_xSe_{1-x} nanoalloys in an aqueous medium. The formation of the ZnS_xSe_{1-x} nanoparticles was monitored by absorption spectroscopy and DLS measurements while the reaction was in progress. Figure 2.1a shows the absorption spectra of NAC capped ZnS_xSe_{1-x} nanoalloys formed in 5 hours to 24 hours. At the end of 24 hours, the first excitonic peak shifted from 328 nm to 331

nm. Size distributions, determined by DLS measurements, pointed that particle size of the nanoalloys increased from 3 nm to 4 nm. These subtle spectral shifts of the nanoalloy indicate that nucleation and growth of the nanoalloys were almost completed at the time of sampling. Since the exciton radius of ZnS and ZnSe are 2.5 and 3.8 nm, respectively (Wei et al., 2012; Tian et al., 2015), it is expected that optical spectra should have a minimal shift or reached to saturation at the limit of the exciton radius.
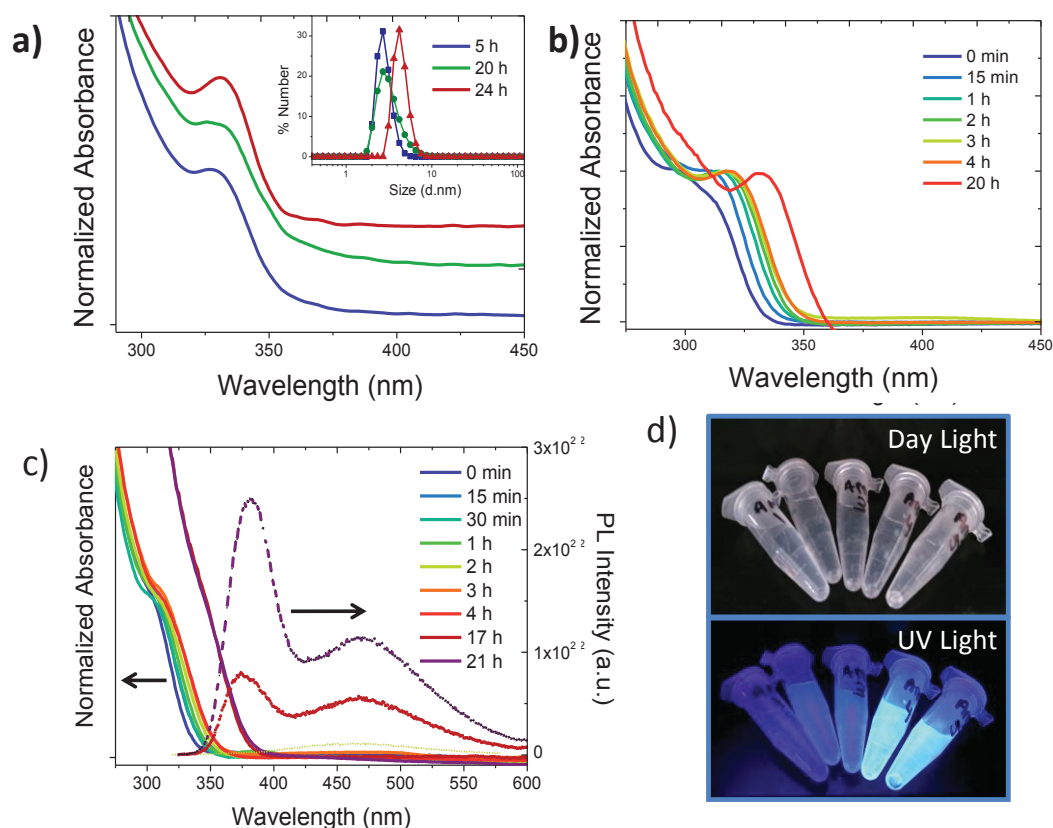
Figure 2.1. Absorption spectra of a) NAC and b) TGA capped ZnS_xSe_{1-x} nanoalloys with respect to reaction time. Inset graph in a) shows the size distribution of nanocrystals obtained from DLS measurements. c) Absorption and PL spectra of MPA capped ZnS_xSe_{1-x} nanoalloys with respect to reaction time. PL emission was seen at longer reaction times. d) Photographs of MPA capped ZnS_xSe_{1-x} nanoalloys under daylight and UV illumination as reaction times increased from left to right.

TGA capped colloidal ZnS_xSe_{1-x} nanoalloys showed similar optical properties as NAC capped nanoalloys seen in Figure 2.1b; a small shift in absorption spectra and no PL emission. However, when MPA was used as the capping agent, ZnS_xSe_{1-x} nanoalloys exhibited PL after 17 hours of reaction time with an intense emission peaked at 380 nm

and a broad spectral feature centered around 470 nm, as depicted Figure 2.1c. Figure 2.1d shows the photographs were taken under daylight and UV illumination, presenting intense PL emission of MPA capped ZnS_xSe_{1-x} nanoalloys. The same findings were observed when $ZnAc_2$ and $ZnNO_3$ were used in different experimental sets. These results indicate that capping agents play a significant role in the PL properties of colloidal ZnS_xSe_{1-x} nanoalloys. The origin of photoluminescence is considered related to capping agent and zinc precursors used. However, it is out of the scope of this study to figure out why PL depends on the type of a capping agent or surface termination by ligands.
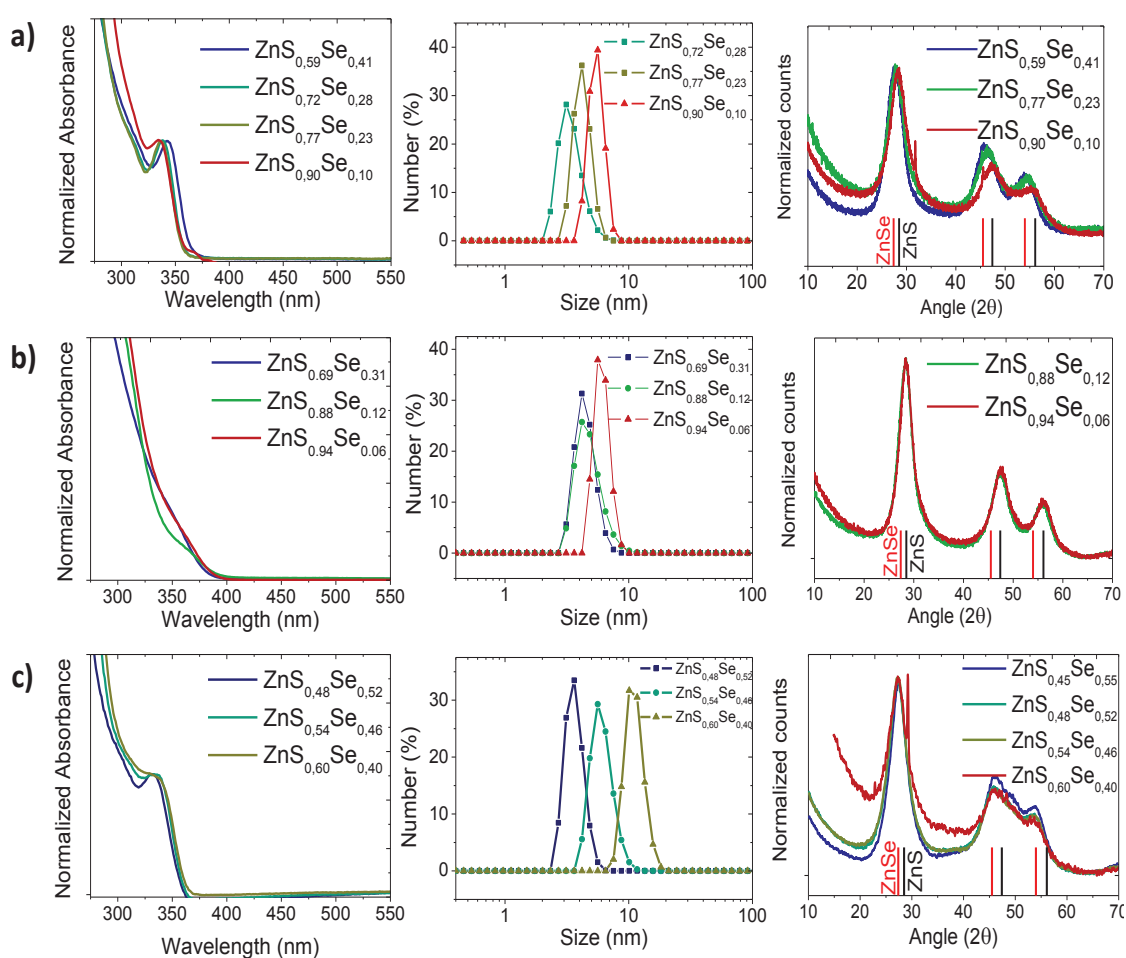
Figure 2.2. Absorption spectra and XRD patterns of the nanoalloys having different capping agents, a) NAC, b) MPA and c) TGA, along with alloy compositions determined by SEM-EDS. The size distribution of nanoalloys was also provided. Reaction time was kept at 20 hours for all samples. Angles in XRD patterns for the binary ZnSe and ZnS bulk structures are shown as red and black lines, respectively.

Spectroscopic properties of ZnS_xSe_{1-x} nanoalloys were mostly determined by absorption spectra, because of the presence of well-defined features of ZnS_xSe_{1-x} nanoalloys with all capping agents and lack of PL from the nanoalloys with different capping agents. The first exciton band in the absorption spectrum of MPA capped nanoalloys is relatively indistinct. Some reports claim that this featureless absorption spectra should stem from the absorption of the host nanocrystal (Zhang et al., 2011), however, we found that the band shape of the absorption spectra was varied when we changed the capping agent. The absorption peak of MPA capped ZnS_xSe_{1-x} nanoalloys was obtained at 357 nm after 24 hours. On the other hand, the first excitonic peak for TGA capped ZnS_xSe_{1-x} nanoalloys was observed at 324 nm at 2 hours and shifted to 332 nm at 20 hours. Capping agents affect the absorption spectra but the reaction rate remains unchanged. The same findings were observed for NAC capped ZnS_xSe_{1-x}nanoalloys.

Because of the concomitant advantages of Mn doping to QDs, we doped Mn ion to colloidally and spectrally stable ZnS_xSe_{1-x} nanoalloys. TGA capped nanoalloys were chosen in the rest of experiments because of better crystallinity inferred from XRD, in Figure 2.2, and the well-defined absorption bands of TGA capped nanoalloys.

Optical properties of nanoalloys can be tuned by both particle size and chemical composition. Since the particle size of the nanoalloys is almost constant during the particles' growth (Figure 2.1), the optical properties of ZnS_xSe_{1-x} nanoalloys can be tuned by controlling the initial mole ratio of S/Se with a specific capping agent. Figure 2.2 represents the spectral and structural properties of the ZnS_xSe_{1-x} nanoalloys with different capping agents, all hydrophilic. The nanoalloy compositions were calculated by SEM-EDS analysis. In all instances, we observed that increasing the initial amount of sulfur (higher S/Se initial mole ratio) led larger particles. It is expected that increasing the amount of sulfur content in the alloy composition, the absorption spectra should shift to the lower wavelengths (blue-shifting) due to lowering the mass of alloy. For the NAC capped ZnS_xSe_{1-x}nanoalloys, it was noted that absorption maximum shifts from 345 nm to 335 nm with an increasing amount of sulfur in the particle, although the size of the particles is getting larger from 3.0 to 5.6 nm. The bigger particle should yield a red-shift, but the alloy composition seems more effective than the particle size on the optical properties, resulting blue-shift. A similar trend was observed for MPA capped ZnS_xSe_{1-x} nanoalloys as well. In the case of TGA capped ZnS_xSe_{1-x}nanoalloys, however, there are marked differences in particle size with different alloy compositions.

The measured hydrodynamic diameters of $ZnS_{0.48}Se_{0.52}$, $ZnS_{0.54}Se_{0.46}$, and $ZnS_{0.60}Se_{0.40}$ nanoalloys are 3.7 nm, 5.7 nm and 10.5 nm, respectively. Because of similar alloy compositions, the size is the determining factor the optical properties, yielding a small but measurable red-shift in the absorption maxima, from 331 nm to 335 nm, instead of expected blue-shift due to the increased amount of sulfur incorporated to the alloy. We note that the particle sizes, in this case, are substantially larger than the exciton sizes of ZnS and ZnSe, even there is a small red-shift; that explain slight red-shift in the spectra.

XRD patterns represented in Figure 2.2 indicates zinc blende cubic structure: 111, 220 and 311 lines observed in the patterns along with the expected peak positions of binary ZnSe and ZnS. Increasing sulfur content in the precursors resulted in shifts in XRD patterns to the higher diffraction angles (according to JCPDS data). Alloy compositions can be calculated from XRD patterns by using Bragg's and Vegard's laws. However, the lattice parameters of zinc blende ZnSe and ZnS binary structures are too close to each other as seen in Figure 2.2, reduces the accuracy of alloy composition, therefore, we calculated alloy compositions by using SEM-EDS instead of XRD patterns.
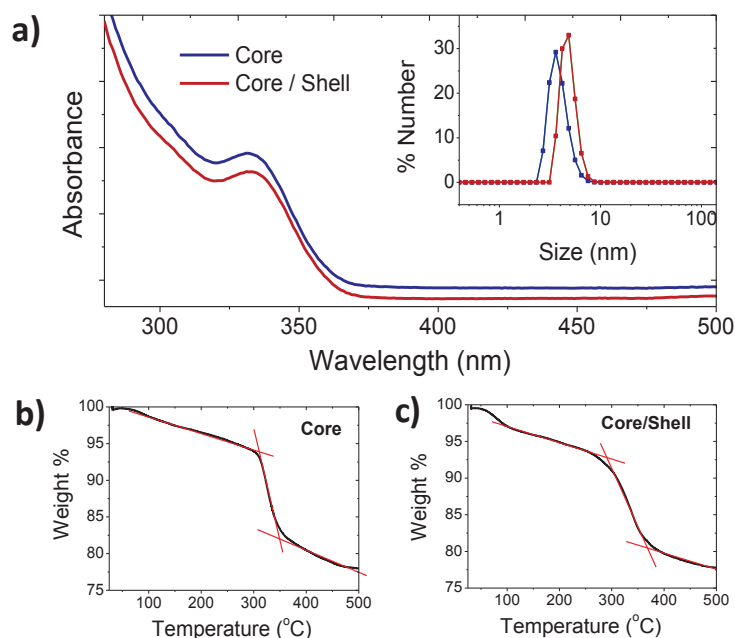
Figure 2.3. a) Absorption spectra and size distribution (inset) obtained of $ZnS_{0.48}Se_{0.52}$ core and core/shell structure for the reaction time. Thermal gravimetric analysis of b) core and c) core/shell structure of $ZnS_{0.48}Se_{0.52}$ nanoalloys. The heating rate was 10°C / minute.

To determine the effect ZnS shell coating on the ZnS_xSe_{1-x} core, the shell layer was grown on the core structure. We observed that ZnS shell did not induce any spectral feature on the absorption spectra and still no photoluminescence emission was obtained. On the other hand, DLS measurements (inset Figure 2.3a) denote an increase in the particle size. While the hydrodynamic diameter of core $ZnS_{0.48}Se_{0.52}$ was 3.5 nm, for core/shell $ZnS_{0.48}Se_{0.52}/ZnS$ structure it was measured as 4.9 nm. The fraction of sulfur in the nanoalloy composition increased according to SEM-EDS analysis due to enlargement of nanoalloys. The findings indicated that the addition of thiourea to form ZnS shell layer was the cause of the increase in the fraction of S content in the nanoalloy. As it is seen in Figure 2.3b and c, both core and core/shell structure of ZnS_xSe_{1-x} nanoalloys have the same amount of capping agent, thioglycolic acid. Decomposition temperature in both core and core/shell structure was around 330°C and approximately 13% weight-loss was determined. This result confirmed that the organic capping agent has no contribution to the sulfur amount in the composition of the nanoalloy. Excess sulfur content proves the further formation of shell layer and indicates that excitons are confined in the core, but not delocalized in the shell layer. This is consistent with the exciton size of ZnS and ZnSe.
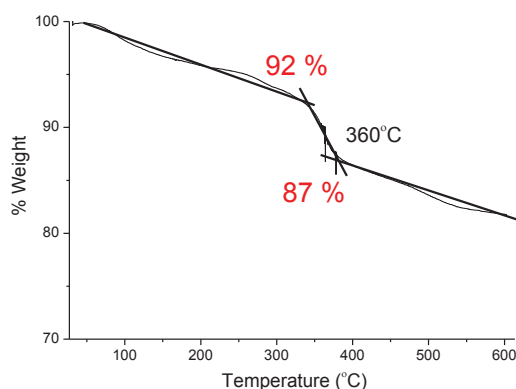
Figure 2.4. The thermal Gravimetric Analysis result of MPA capped ZnS_xSe_{1-x} nanoalloys

The thermal gravimetric analysis was done not only for thioglycolic acid capped nanoalloys but also for mercaptopropionic acid capped ones, as well. For mercaptopropionic acid, the decomposition temperature was around 360°C. Contrary to expectations, the thermal gravimetric analysis showed that only 5% weight loss for mercaptopropionic acid capped nanoalloys (Figure 2.4) although the molecular weight

of mercaptopropionic acid is higher than of thioglycolic acid. This finding points that for the mercaptopropionic acid capped nanoalloys, there may be a lower amount of capping agent on the surface of nanoalloys with respect to thioglycolic acid capped ones. Moreover, thermal gravimetric analysis was used to determine the fraction of sulfur content incorporated into the nanoalloys. Because all capping agents have sulfur in their chemical formula, SEM-EDS analysis provided the total amount of sulfur in both alloy composition of ZnS_xSe_{1-x} and their capping agents (for both mercaptopropionic acid and thioglycolic acid). The results obtained from thermal gravimetric analysis was substracted from the results obtained from SEM-EDS analysis in order to find the exact sulfur amounts in the crystal structure of the ZnS_xSe_{1-x} nanoalloys. Table 2.1 indicates the recalculated alloy compositions obtained from SEM-EDS before and after the thermal gravimetric analysis.

Table 2.1. Alloy compositions of ZnS_xSe_{1-x} nanoalloys with different capping agents determined by SEM-EDS (before and after TG Analysis). Particle size obtained by DLS was given. Data obtained from SEM-EDS analysis were recalculated following the Thermal Gravimetric analysis to eliminate the sulfur content stemming from capping agents.

Capping Agent S:Se initial mole ratio	Alloy Composition by SEM - EDS		Particle Size (nm)
	Raw Data	Recalculated after TG Analysis	
NAC 1:1	$ZnS_{0.59}Se_{0.41}$	--	--
NAC 5:1	$ZnS_{0.72}Se_{0.28}$	--	3.0
NAC 20:1	$ZnS_{0.77}Se_{0.23}$	--	4.0
NAC 50:1	$ZnS_{0.90}Se_{0.10}$	--	5.6
MPA 5:1	$ZnS_{0.69}Se_{0.31}$	$ZnS_{0.67}Se_{0.33}$	--
MPA 20:1	$ZnS_{0.88}Se_{0.12}$	$ZnS_{0.87}Se_{0.13}$	4.0
MPA 50:1	$ZnS_{0.94}Se_{0.06}$	$ZnS_{0.94}Se_{0.06}$	5.5
TGA 1:1	$ZnS_{0.45}Se_{0.55}$	$ZnS_{0.35}Se_{0.65}$	--
TGA 5:1	$ZnS_{0.48}Se_{0.52}$	$ZnS_{0.38}Se_{0.62}$	3.7
TGA 20:1	$ZnS_{0.54}Se_{0.46}$	$ZnS_{0.44}Se_{0.56}$	5.7
TGA 50:1	$ZnS_{0.60}Se_{0.40}$	$ZnS_{0.53}Se_{0.47}$	10.5

To add magnetic susceptibility to $ZnS_{0.48}Se_{0.52}$ nanoalloys, Mn^{2+} ion was doped by varying initial mole ratio of Mn / Zn ions as explained in the experimental part. Figure 2.5 shows UV-Vis, DLS and XRD measurements of Mn^{2+} doped TGA capped $ZnS_{0.48}Se_{0.52}$ nanoalloys. To figure out the optical and structural properties we increased

the initial amount Mn/Zn ratio and found that, increasing the amount of Mn^{2+} was ineffective on particle size and absorption spectra of the nanoalloys. However, SEM-EDS analysis confirmed Mn^{2+}ions doped into ZnS_xSe_{1-x} nanoalloys. By SEM-EDS measurements, the amount of Mn^{2+} ions with respect to Zn ion incorporated into the alloy as an atomic percent was calculated as 2, 4 and 6 % when the initial Mn^{2+} mole percentages were of 2, 5 and 10 %, respectively. The amount of Mn^{2+} ions incorporated was saturated with the initial amount of precursor ratio. This finding was interpreted as limited numbers of sites for Mn^{2+} ions for the incorporation into the lattice. Apparent shifts in 2-theta angles in the XRD patterns particularly for (220) and (311) planes were clearly seen. The shift in the 2-theta for the (311) plane plotted with respect to % Mn^{2+} in the nanoalloy composition. The amount of shift in 2Θ for the (111) plane is minimal and might be distinguishable only when the initial amount is 10%. These findings indicate Mn^{2+} ions are mainly located on the (220) and (311) planes and disturb atomic arrangement in the crystal structure.
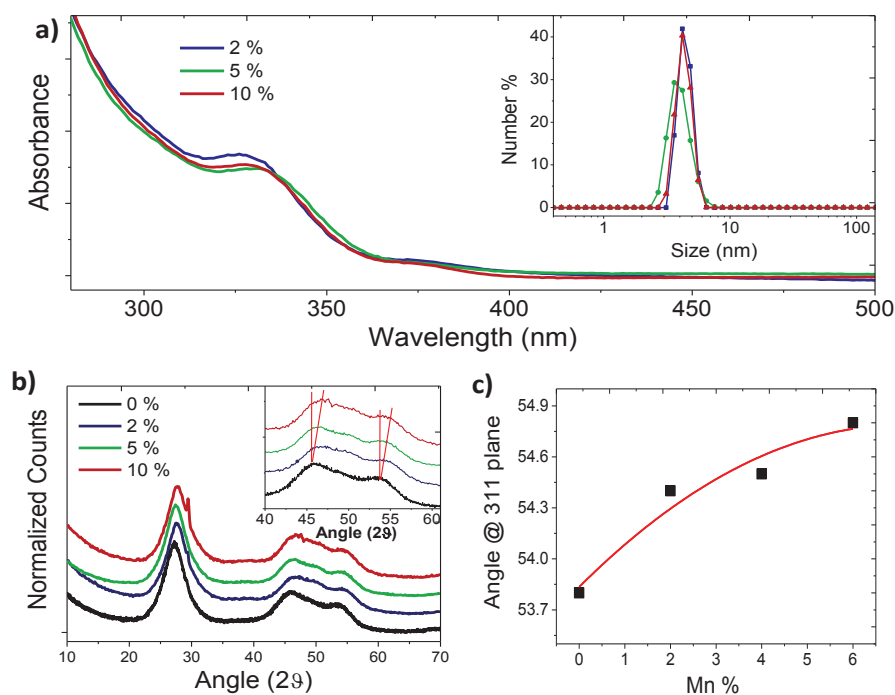
Figure 2.5. a) Absorption spectra with size distribution (inset) and b) XRD pattern of Mn-doped ZnS_xSe_{1-x} nanoalloys with a different initial mole ratio of Mn to Zn ions. Inset indicates the magnified angles for 220 and 311 planes. c) 2Θ-Shifts in 311 plane in XRD patterns as a function of Mn % in the alloy composition determined by SEM-EDS.

XRD and EPR findings point that Mn^{2+} ions preferentially incorporated into (220) and particularly (311) planes. Next, we performed full geometry optimization calculations to investigate how Mn atoms interact with the surfaces of quantum dots. Note that we consider zinc-blende ZnS crystal and its surfaces which are convenient enough to depict the properties of Mn-doped ZnS_xSe_{1-x} nanoalloys.
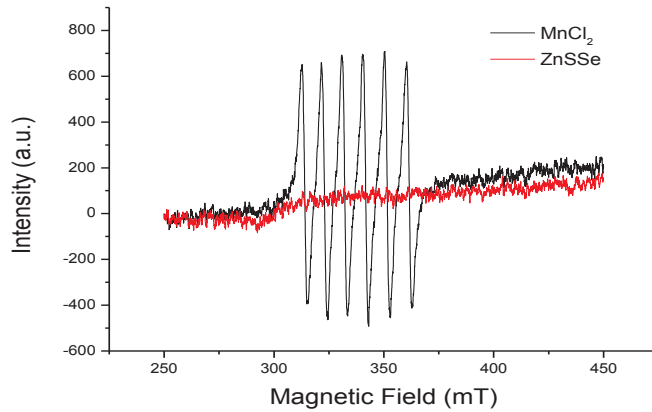
Figure 2.6. EPR spectra of colloidal undoped ZnS_xSe_{1-x} nanoalloys and $MnCl_2$ solution.

EPR measurements were carried out to prove the presence of Mn^{2+} ions incorporated into ZnS_xSe_{1-x} nanoalloys, and to verify findings that Mn^{2+} ions adsorbed on the surface of (311) and (220) planes.
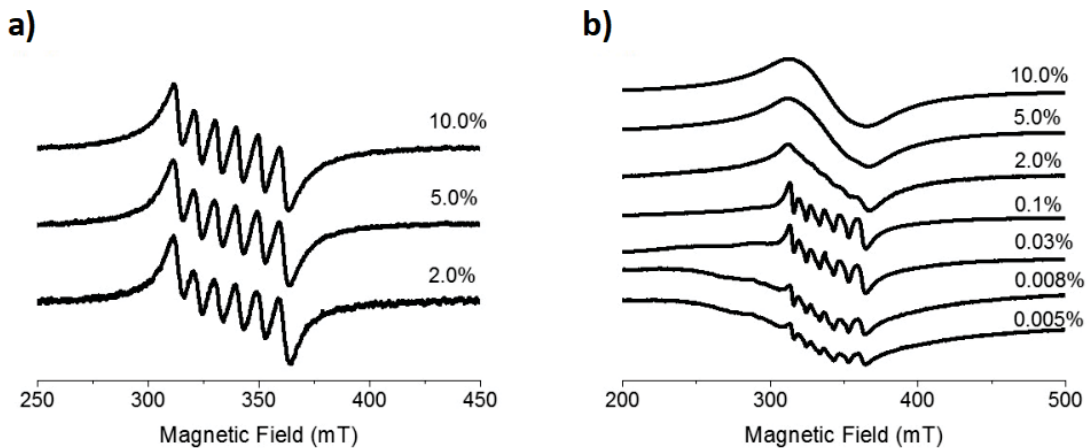
Figure 2.7. EPR spectra of a) colloidal and b) powdered Mn^{2+}doped ZnS_xSe_{1-x} nanoalloys with the different initial amount of Mn^{2+} in atomic percent. Given percentages are for initial Mn / Zn mole ratios. The final % values could not be obtained below 0.1 % At Mn concentrations

The electronic configuration of Mn^{2+} ions ends with $3d^5$ orbital and thus it is paramagnetic. Its electronic ground state is $^6S_{5/2}$ with a nuclear spin number, $I = 5/2$. The hyperfine interaction with Mn^{2+} ion results in six-line splittings in the EPR spectrum according to $2nI + 1$ formula where n is the effective nucleus number. The EPR spectrum of pure $MnCl_2$ with six hyperfine lines is given in Figure 2.6.

Figure 2.7 shows EPR spectra of both colloidal (100 mg/mL in the water) and powdered form of Mn^{2+} doped ZnS_xSe_{1-x} nanoalloys with the different initial amount of Mn^{2+}. For the colloidal form, the EPR signals of samples with 2%, 5% and 10% of Mn^{2+} concentrations were well obtained but below 2% of Mn^{2+} concentration, six hyperfine lines lost its distinction. The normalized spectra of samples with 2%, 5% and 10% of Mn^{2+} show that addition of high concentration of Mn^{2+} ions does not change the line shape of EPR spectrum (Figure 2.8).
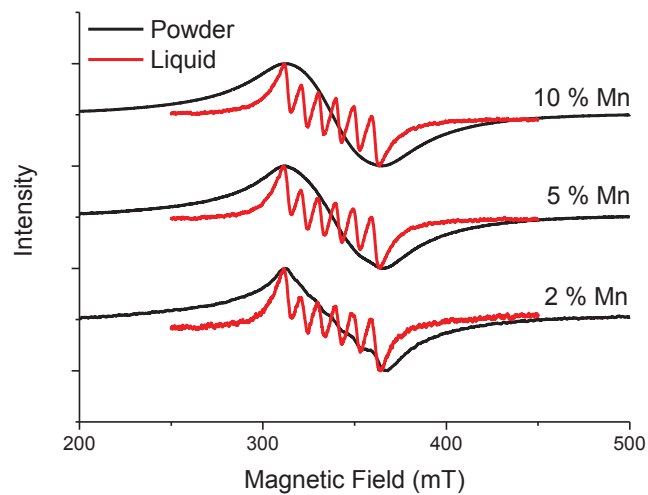
Figure 2.8. EPR spectra of the liquid and powdered Mn doped ZnS_xSe_{1-x} nanoalloys with different initial Mn Atomic %. Given percentages are for initial Mn / Zn mole ratios. The final % values could not be obtained below 0.1 % At Mn concentrations

Figure 2.9a shows the simulation of the EPR spectra of 2% of Mn^{2+} doped ZnS_xSe_{1-x} nanoalloys. The simulation of the spectrum was obtained by the addition of the simulated six line spectrum (C1) and the simulated one broad line spectrum (C2) due to the interacting Mn nuclei (Borse et al., 1999). The six line spectrum is originated from the Mn^{2+} ions located on the surface sites with spin Hamiltonian parameters;

$g= 2.0005$, hyperfine interaction constant $|A_{Mn}|= 85 \times 10^{-4}$ cm^{-1}, and zero field splitting constant $D = 63 \times 10^{-4}$ cm^{-1} (Borse et al., 1999).
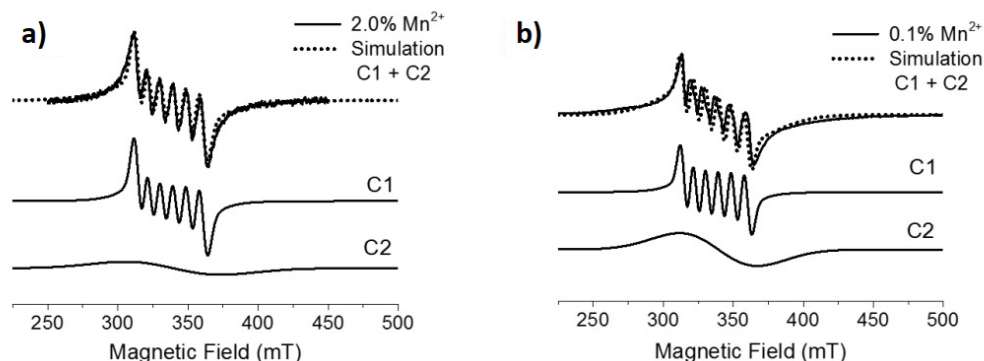
Figure 2.9. Experimental and simulated EPR spectra as the sum of two contributions from surface sites (C1) and dipolar broadened signal (C2) for a) colloidal 2.0% Mn^{2+} and b) powdered 0.1% Mn^{2+} doped ZnS$_x$Se$_{1-x}$ nanoalloys.

On the other hand, the EPR spectrum of the powder form of Mn^{2+} doped ZnS$_x$Se$_{1-x}$ nanoalloy was affected by increasing Mn^{2+} ions (Figure 2.7b). For the powdered samples, below 0.03% Mn^{2+} the broad signal feature due to ferromagnetic Mn is prominent nearby the weak six hyperfine lines (Norberg et al., 2004). Above 0.03% Mn^{2+}, the six hyperfine line pattern of Mn^{2+} ions becomes obvious. Moreover, increasing Mn^{2+} concentration yields a strong dipolar broadened signal due to the interacting Mn nuclei (Borse et al., 1999). Thus, above 2% Mn^{2+} doping the six hyperfine line pattern disappears and a single broad signal remains. Simulation of EPR spectrum of powdered 0.1 % Mn-doped ZnS$_x$Se$_{1-x}$ nanoalloys were obtained by combining two simulated spectra; six line spectrum (C1) with spin Hamiltonian parameters; $g= 2.0005$, hyperfine interaction constant $|A_{Mn}| = 84 \times 10^{-4}$ cm^{-1}, and zero field splitting constant $D = 43 \times 10^{-4}$ cm^{-1} and one broad line spectrum (C2) (Figure 2.9b). Again, the six line spectrum is originated from the Mn^{2+} ions located in surface sites(Borse et al., 1999). Moreover, the magnetic state of Mn-adsorbed surfaces is investigated by means of DFT calculations. Our calculations show that the ground state magnetic moment of each single Mn atom is 5.0 μ$_B$ as a result of its 3d^5 electron configuration. At Mn-free surfaces of the quantum dots, Zn- and S-terminated (111) surfaces have a magnetic moment of 0.2 and 1.3 μ$_B$, respectively, while (220) and (311) surfaces do not possess any magnetization. On the other hand, adsorption of single Mn

atom results in ferromagnetism at all surfaces. For the Zn- and S-terminated (111) surfaces, the magnetic moments are calculated to be 4.0 and 2.8 μ_B, respectively. However, the magnetic moment of the Zn- and S-terminated (220) surfaces are found to be 3.0 and 5.0 μB, respectively. Furthermore, Mn-adsorbed (311) surface has the largest magnetic moment of 6.4 μ_B per Mn atom. It appears that the Mn-induced localized states lead to significant magnetization on the (311), (220) and (111) surfaces.

Furthermore, a significant difference between liquid and powder form was observed for the same atomic percentages. This substantial difference is seen clearly in S4 (in supporting information) that while the hyperfine six line is clearly observable for 2, 5 and 10 % Mn concentration in the liquid sample of EPR spectra, mostly a single broad signal is seen in the EPR spectra of powdered samples.

2.4. Discussion

EPR spectroscopy provides information regarding the location of paramagnetic ions such as manganese. We simulated the room temperature X-band EPR spectra of colloidal and powdered Mn^{2+} ion doped ZnS_xSe_{1-x} nanoalloys and determined similar hyperfine interaction constants $|A_{Mn}| = 85 \times 10^{-4}$ cm^{-1} and 84×10^{-4} cm^{-1}, respectively. These hyperfine interaction constants are attributed to Mn^{2+} ions located on the surface sites (Borse et al., 1999; Nistor et al., 2016). Our findings point that there is a single Mn^{2+} ion adsorbed on the (311) plane. However, EPR spectra of colloidal and powdered Mn^{2+} ion doped ZnS_xSe_{1-x} nanoalloys showed some differences with an increasing Mn concentration. For the powdered samples, the six hyperfine lines disappear upon addition of more Mn ions and a dominant single broad line is observed. On the other hand, the six hyperfine lines are preserved in the EPR spectra of colloidal samples with the same doping concentrations (up to 10% Mn^{2+}). This can be explained by the strong dipolar interactions between Mn^{2+} ions in powdered samples but not in the colloidal samples. When nanoalloys are in powder, the particles are steady and can be very close to each other that facilitates stronger d-d interactions, yielding line broadening in EPR spectra. We propose that in the powder form, particles (individual nanoalloys) are close enough (typically smaller than 1.0 nm) to induce magnetic dipolar broadening, that is confirmed by increased amount of mangenese ions incorporated into the nanoalloys. The local magnetic field created by the presence of an individual Mn^{2+} ion

induce a dipolar interaction with a close by another Mn^{2+} ion within a distance. This interaction, hence the broadening should be proportional with number of magnetic dipole, therefore depends on Mn^{2+} ion concentration; that is what is experimantally observed. However, the same proposal is not valid for the particles in the liquid (colloidal) form: even at the highest Mn^{2+} ion concentration we used (%10) we do not observe any broadening in the EPR spectra. In the aqueous solution the nanoallyed particles are in random motion that prevents particles to come close each other in an ample time to induce magnetic interactions between Mn^{2+} ions incorporated in different particles. We would have observed the broadening in the EPR spectra if the particles come close each other and stay at that distance in an ample time related to the diffusion coefficients of the nanoalloys and the typical measurement time (a few minutes) of EPR spectrometer. Moreover, if there were more than one magnetic moment possible to interact, the experimental finding suggests us that the dipoles might be orthogonal on average, eliminating the dipolar interactions.

Optical and magnetic properties of Mn^{2+} doped QDs with different capping agents are investigated as well. Mn^{2+} doping to both TGA and MPA capped ZnS_xSe_{1-x} nanoalloys did not induce any differences in UV-Vis and PL spectra of the nanoalloys. Since the TGA capped nanoalloys have no PL properties, we confine the discussion considering the PL properties of MPA capped nanoalloys in terms of Mn^{2+} doping. For undoped MPA capped ZnS_xSe_{1-x} nanoalloys there is an intense band-edge excitonic emission peak at 380 nm and a trap state emission around 470 nm most likely attributable to the S^{2-} and Se^{2-} vacancies (Voznyy and Sargent, 2014). We observed that increasing reaction time (forming bigger particle) results in a depression in the intensity of trap state emission which is centered around 470 nm (Figure 2.1c). EPR proved that Mn^{2+} ions are adsorbed on preferentially (311) surface due to lowered interaction energies. As Tachibana et al. reported that these trap states, as the vacancies, decrease exponentially with larger particles. In their study, according to the steady-state and dynamic PL studies, the trap state emission in CdS nanocrystals decreased with increasing nanocrystal size. This result showed vacancies have a relation with the surface area/volume ratio of the QDs (Veamatahau et al., 2015).

When Mn^{2+} ions incorporated into the nanocrystals, characteristic PL emission at around 590 nm is expected to be observed because of strong interaction between electrons in the d orbital of Mn^{2+} ions and s-p orbitals of the host material. Electron transfer between these states causes quenching in characteristic PL emission of host

material (Wu and Yan, 2013). The PL emission originated from Mn^{2+}doping is attributed to the radiative transition from $^4T_1$ (Mn^{2+} ion excited state) to $^6A_1$ (Mn^{2+}ion ground state) (Subha et al., 2013). However if Mn^{2+} ion does not incorporate to the core of nanocrystal, but distributed on the surface of the nanocrystals, the orange-colored PL emission coming from $Mn^{2+}$is not observed (Sooklal et al., 1996; Chen et al., 2000). In our case, Mn^{2+} ion incorporated into the nanoalloy PL emission centered at 380 nm was not affected regardless of the number of manganese ions (increased Mn ion doping) in the nanoalloy. As mentioned above, there are some reports discussing the location of Mn^{2+} on the host material, but according to our literature search, none of them combine EPR and computational analysis approach. We propose that Mn^{2+} ions are not incorporated into the lattice of ZnS_xSe_{1-x} nanoalloy, but they are adsorbed on the surface of the nanoalloys.

2.4.1. Ligand Effects on Growth and Spectral Properties of ZnS_xSe_{1-x} Nanoalloys

There are various methods for the synthesis of quantum dots. The aqueous synthetic route is attractive because of availability of wide variety of capping agents, scalability of reaction, being cost-friendly and requiring less toxic precursors. Also, they are proper for biological applications because of superior aqueous compatibility of biomolecules. Apart from that, using water-dispersible quantum dots in solid films in terms of device applications is more environmental-friendly than organic solvents because of their greater facility and lower cost for solvent waste recycling or disposal (Jing et al., 2016). That is why one pot aqueous synthesis method was preferred for the synthesis of ZnS_xSe_{1-x} nanoalloys (Rogach et al., 2007).

Stabilizing agents are important in terms of regulating the growth of nanocrystal up to macrocrystalline structures and termination of nanocrystal surfaces. Furthermore, they prevent agglomeration of nanocrystals and facilitate dispersion of quantum dots in desired solvents. We used three different thiol capping agents, NAC, TGA, and MPA, that are all hydrophilic. As mentioned in the experimental part, different pH values are used for these different capping agents. For the aqueous synthesis method, pH is obviously an important factor. Hydroxyl ions in the reaction medium favor reacting with transition metals in order to form metal hydroxides. This may result in

precipitation of insoluble metal complexes. According to the Hard Soft Acid Base (HSAB) theory, these hard OH$^-$ ions favor especially the hard cations like Zn, Cd etc (Jing et al., 2016). Especially for Zn-based quantum dots, it is extremely important to adjust pH of medium carefully in terms of formation of $Zn(OH)_2$ complexes and elimination of undesired precipitations (Xu et al., 2010). That is the reason pH values for each capping agent are optimized individually in this study. All the zinc precursors that we used, $ZnCl_2$, $ZnAc_2$ and $Zn(NO_3)_2$ exhibit similar results. Regardless of the zinc precursor, only the MPA capped QDs give specific PL emission. pH values for the different zinc precursors are arranged as considering capping agents. As mentioned in Figure 2.2 before, different capping agents affect both optical and compositional characteristics of the nanoalloys. The growth of nanoalloys could be observed by optical spectra and particle size measurements. However, since the absorption spectra of MPA-capped nanoalloys do not show well-defined band structure and making the analysis difficult, particle size (for similar alloy composition) is used as to distinguish the effect of capping agents. There are many studies involve the comparison of TGA and MPA capping agents in terms of growth (Yuan et al., 2012; Miao et al., 2015). Since both TGA and MPA capping agents have electron withdrawing group, -COOH, the electron density and the strength of the bond between S$^-$ (from capping agent) and metal (from QDs, Zn^{2+} in our case) varies. When the distance between the -S$^-$ and -COOH increase, the electron density of S$^-$ atom increases. As a result of this, the bond between the capping agent and the surface of the quantum dot become more stable and the capping agent binds to the QD surface more tightly. This binding strength effects growth rate of quantum dots directly. In the literature for Zn-based nanocrystals and our study, the growth rate of MPA-capped nanoalloys smaller than TGA-capped nanoalloys. Correspondingly the size of TGA-capped nanoalloys for the same reaction time is longer in than MPA-capped ones. This situation is more complicated when ternary or quaternary type nanoalloys were used. Since we have common cation ternary nanoalloy, it is easy to investigate the effect of different capping agents. However, for the NAC-capped nanoalloys, it could be more complicated since there is more than one functional group in NAC. It means that the growth of nanoalloys could also vary by the effect of pH of the medium (Jiang and Muscat, 2012).

Since the growth of the MPA-capped nanoalloy is better controlled, it is expected to have a PL emission for MPA-capped nanoalloys rather than TGA-capped ones. The spectral difference can be explained by the capping agents. The thermal

gravimetric analysis (TGA) could help to understand how properly the surface of quantum dots is covered. Although the molecular weight of MPA is heavier (additional one more –CH$_2$) than TGA, in TG analysis, the amount of mass loss of TGA-capped nanoalloys was approximately 13% of its total mass, while only 5% loss was observed for MPA-capped nanoalloys. These measurements may remark that a single/few layers of MPA covered the surface of the nanoalloys properly, while multilayer coating of TGA ligand was formed on the surface of the nanoalloys. The significant increase in the hydrodynamic radius of TGA capped ZnS$_x$Se$_{1-x}$ nanoalloys (for various compositions) confirms the formation of multilayer TGA coating. Moreover, the decomposition temperature was higher for the TGA capped nanoalloys, verifying our proposal.

In order to clarify the difference in PL properties of MPA and TGA-capped nanoalloys, some additional explanations in terms of electron delocalizations seem necessary. Electron delocalization could be defined by the help of IUPAC as a concept to describe the pi bonding in organic conjugated systems (Merino et al., 2005). Zhang et al. showed the importance of electron delocalized field in terms of stability of excited electron in the excited state of quantum dots (Chang et al., 2014). It is achieved by using organic capping agent with proper LUMO level to the conduction band (CB) of nanocrystals. The close proximity of LUMO level of organic ligand to CB of QD can provide a region in which an electron delocalized field may exist. Shifts in HOMO levels with one more carbon chain in MPA may result in better electron delocalized field for ZnS$_x$Se$_{1-x}$ nanoalloys. Also, one more carbon in the chain may result in a significant difference in the steric hindrance of the capping agent. The structural form of capping agent affects the efficiency of covering the surface of the nanocrystal.

2.5. Conclusion

We investigated interactions and locations of Mn^{2+} ions doped into ZnS$_x$Se$_{1-x}$ nanoalloys by experimentally (EPR, XRD techniques) and computationally (EPR simulations). We showed that ternary colloidal ZnS$_x$Se$_{1-x}$ nanoalloys can be prepared and doped in aqueous solutions and at low temperature. Optical properties of the nanoalloys can be tuned by alloy composition, particle size, and ligands. The observed UV photoluminescence arises from ZnSSe but no visible emission from manganese ions was observed. Magnetic susceptibility is introduced by the incorporation of Mn^{2+} ions

into the nanoalloys. We found that increased Mn^{2+} concentrations induced no change in particle size and optical properties of doped nanoalloys. We determined that Mn^{2+} ions substitutionally bound to (220) and (311) facets in the zinc blende cubic structure. The substitutionally bound manganese ions strongly interact with each other, resulting in broadening in the EPR spectra for the nanoalloys in the powder and interparticle dipole-dipole magnetic interactions are responsible for induced magnetism. However, when the alloyed particles are in the solution the doped manganese ions cannot interact (observed hyperfine splitting even higher level of doping) with each other due to fast motions of particles in aqueous solutions.

CHAPTER 3

SYNTHESIS AND CHARACTERIZATION OF QUATERNARY $Zn_xCd_{1-x}S_ySe_{1-y}$ CORE AND $Zn_xCd_{1-x}S_ySe_{1-Y}$/ZnCdS CORE/SHELL NANOALLOYS

3.1. Introduction

Semiconductor nanocrystals, in other words quantum dots (QDs) have great attention because of their size-dependent properties and high photoluminescence quantum efficiencies. It is well-known that the tuning of photoluminescence (PL) emission is possible by altering the particle size for binary II−VI QDs such as CdS, ZnS, ZnSe and CdSe (Peng et al., 2000). Owing to this property, these QDs become a great candidate for the use in multicolor bioimaging, biosensing, light-emitting diodes, photovoltaic devices, lasers, and quantum computing devices (Sun et al., 2007; Smith and Nie, 2009). However, in order to obtain various colors in the same device architecture, the large size differences in nanoparticles are required. This could cause many problems in device fabrication processing and also biomolecule conjugations (Bailey and Nie, 2003; Anikeeva et al., 2009). Also, these binary QDs do not have relatively high PL QE in stable blue-green emission region (450 − 530 nm) which is "must-have" region for next-generation displays and white solid-state lighting (Shen et al., 2013).

Therefore several studies have been done in terms of alloyed nanocrystals. For example ZnCdSe ternary nanoalloys were synthesized by Bawendi et all. which resulted that the charge injection is easier in ZnCdSe ternary nanoalloys than binary core/shell CdSe/ZnS nanocrystals. Similarly, improvement in efficiency of solar cells were reported when PbSSe nanocrystals were used rather than PbS or PbSe binary systems. According to these literature examples, alloying different semiconductors becomes an requirement for realizing properties and also new band gaps. However, even for ternary QDs the band gap tunability has a limitation because of the limited configurability in QD composition. That is the reason we have focussed on quaternary colloidal ZnCdSSe

nanocrystals. There are limited number of reports in the literature regarding ZnCdSSe alloys with nanostructures like nanowires (Pan et al., 2010), nanobelts(Pan et al., 2009) and nanodots (Hung et al., 2017). By alloy composition tunability, controlling the ratio of source materials, the band gap of QD (PL emission in electromagnetic spectrum) could be continuously tunable without changing the particle size (Pan et al., 2009).

The first study on $Zn_xCd_{1-x}S_ySe_{1-y}$ QDs were reported by Deng et al in 2009. They used classical hot injection synthesis approach by arranging the relative chemical reactivity of each precursors. PL emission spectra, TEM and TEM-EDS analysis were used to prove the tunability of optical properties of $Zn_xCd_{1-x}S_ySe_{1-y}$ QDs by the particle size and the alloy composition (Deng et al., 2009). Although this study was the first one in terms of the synthesis of quaternary $Zn_xCd_{1-x}S_ySe_{1-y}$ QDs, relatively high temperatures and reactive precursors were needed. Within our knowledge, there is no study on colloidal $Zn_xCd_{1-x}S_ySe_{1-y}$ QDs synthesis at low temperatures (below 100 ˚C)

3.2. Sythesis of Quaternary Colloidal $Zn_xCd_{1-x}S_ySe_{1-y}$ Nanocrystals by Two Phase Method

3.2.1. Preperation of Precursors

Trioctylphosphine oxide (TOPO) capped colloidal quaternary $Zn_xCd_{1-x}S_ySe_{1-y}$ alloy nanocrystals were synthesized by modified two phase approach which was developed from our previous study (Unlu et al., 2013) for the first time in the literature. In this method, Cadmium myristate and zinc myristate were used as cadmium and zinc precursor, respectively. In order to synthesize Cadmium myristate (zinc myristate), Cadmium oxide (CdO) (Zinc oxide((ZnO)) reacted with myristic acid at relatively high temperatures as 250°C for 15 minutes. When the reaction finished, brown color of the solution turns to optically clear product which is Cadmium myristate or zinc myristate occurs after the chemical reaction. Chemical equation of the synthesis of CdMA and ZnMA are given below.

$$CdO(s) + 2\ CH_3(CH_2)_{12}COOH(s) \rightarrow (CH_3(CH_2)_{12}COO)_2Cd(s) + H_2O(g) \quad (3.1)$$

$$ZnO(s) + 2\ CH_3(CH_2)_{12}COOH(s) \rightarrow (CH_3(CH_2)_{12}COO)_2Zn(s) + H_2O(g) \quad (3.2)$$

Recrystallization techniques was used to purify the CdMA and ZnMA. Vacuum filtration is used to obtain pure solid cadmium and zinc precusors in order to use them for quantum dot synthesis.

Figure 3.1. Experimental set-up for the synthesis of CdMA and ZnMA

Thiourea $(NH_2)_2CS$, and NaHSe is used as sulfur and selenium precursors, respectively. Thiourea is a commercially available chemical. However, since NaHSe is highly air sensitive compound, it is essential to synthesize NaHSe freshly. The chemical reaction for the shynthesis of NaHSe is given below.

$$4\ NaBH_4(s) + 2\ Se(s) + 7\ H_20(l) \rightarrow 2\ NaHSe(aq) + Na_2B_4O_7(s) + 14\ H_2(g) \qquad (3.3)$$

3.2.2. Synthesis of $Zn_xCd_{1-x}S_ySe_{1-y}$ Nanocrystals

$Zn_xCd_{1-x}S_ySe_{1-y}$ nanocystals are synthesized at 90°C under an inert atmosphere (Ar or N_2 atmoshpere). NaHSe and thiourea was injected into 80 mL ultrapure water under reflux for 1 hour. At the same time CdMA, ZnMA and capping agent, (trioctylphophine oxide, TOPO or oleic acid, OA) are dissolved in toluene. After 1 hour refluxing aqueous phase, organic phase is injected into the reaction flask. Nucleation of the quantum dots starts in the interface of two system (organic/toluene phase and aqueous phase). Since the capping agent has the long alkyl chains, quantum dots pass to

the organic phase, toluene. The chemical equation of the nucleation of QDs is given in equation 3.4.

$$xCdMA + (1-x)ZnMA + y(NH_2)_2CS + (1-y)NaHSe \rightarrow Zn_xCd_{1-x}S_ySe_{1-y} \text{ (toluen)} \quad (3.4)$$
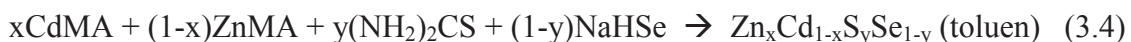
In the synthesis of collodial quaternary $Zn_xCd_{1-x}S_ySe_{1-y}$ nanocrystals, total of 1 mmol of metal cation (total mole of zinc and cadmium precursors) and 1 mmol of chalcogenides (total mole of S and Se precursors) are used. The initial molar amounts of the metals and the chalcogenides can be adjusted according to the desired optical properties or the alloy (product) composition. The initial mole ratios are significantly effective in terms of alloy composition and the particle size. For this purpose, when arranging the amounts of initial Zn and Cd precursors, the starting mole ratios are changed by keeping the amounts of S and Se constant. Similarly, the amounts of S and Se are changed while the quantities of Zn and Cd remain constant in another experimental set. In this way, adjustments between 0 and 1 for the x and y values of the alloy composition of the quaternary $Zn_xCd_{1-x}S_ySe_{1-y}$ nanocystals can be controlled by initial mole ratios. It is very important to keep the nanocrystal particle size (determined by DLS and SAXS measurements) constant for the modification and control of the alloy composition. Thus, when the particle size is fixed, the alloy composition is varied. On the other hand, while the alloy composition (made by SEM-EDS measurements) is kept constant, the growth of the particle (size) is controlled by the reaction duration (growth time).

The synthesized quaternary colloidal alloy nanoparticles are purified in order to get rid of unreacted precursors (reactants) which could be cadmium myristate, zinc myristate, capping agent (trioctyl phosphine oxide), NaHSe or thiourea. For this purpose, solution contains $Zn_xCd_{1-x}S_ySe_{1-y}$ nanocrystals were transffered to a beaker and ethanol was added to the reaction medium. After addition of ethanol, quantum dots start to precipitate. Precipitated quantum dots were collected by centrifugation at 6000 rpm for 30 minutes. After centrifugation, the upper liquid is decantad as waste while the nanoparticles are allowed to dry at room temperature. Quantum dots could be stored as powdered or solution phase. Solution phase quantum dots could be prepared with desired organic solvents with desired concentrations. For optical and structural characterization, both powdered and redispersed QDs are used. The initial molar amounts of cations and chalcogenides are provided in the Table 3.1.

Table 3.1.Reaction parameters of $Zn_xCd_{1-x}S_ySe_{1-y}$ nanocrystals

#	Initial mol amounts (mmol)				Reaction duration (minutes)	Reaction Temperature (^{o}C)	Reaction volume (mL)*
	Cd	Zn	S	Se			
1	0.20	0.80	0.83	0.04	10 - 240	90	160
2	0.20	0.80	0.83	0.08	10 - 120	90	160
3	0.20	0.80	0.83	0.17	10 - 240	90	160
4	0.33	0.66	0.83	0.04	10 - 240	90	160
5	0.33	0.66	0.83	0.08	10 - 180	90	160
6	0.33	0.66	0.83	0.17	10 - 240	90	160
7	0.50	0.50	0.83	0.04	10 - 240	90	160
8	0.50	0.50	0.83	0.08	10 - 120	90	160
9	0.50	0.50	0.83	0.17	10 - 240	90	160
10	0.66	0.33	0.83	0.04	10 - 240	90	160
11	0.66	0.33	0.83	0.08	10 - 180	90	160
12	0.66	0.33	0.83	0.17	10 - 240	90	160
13	0.80	0.20	0.83	0.04	10 - 240	90	160
14	0.80	0.20	0.83	0.08	10 - 180	90	160
15	0.80	0.20	0.83	0.17	10 - 240	90	160

* Total reaction volume includes 80 mL toluene and 80 mL ultra pure water.

3.3. Synthesis of The $Zn_xCd_{1-x}S_ySe_{1-y}$/ZnCdS Core/Shell Type Nanocrystals

In order to grow ZnCdS shell layer on the quaternary $Zn_xCd_{1-x}S_ySe_{1-y}$ core nanoalloy, relevant precursors are added to the unpurified reaction medium. Depending on the amount of chemicals to be added, the thickness of the shell layer ZnCdS and thus the optical properties of the nanocrystals are expected to change. The following equation is used to assess how the amounts of chemicals affect to the shell thickness (Smith et al., 2008).

$$n_{shell} = \frac{n_{QD} \ x \ D_{core} \ x \ N_A \ x \ V_{shell}}{MW_{core}} \qquad (3.5)$$

In this equations, n_{shell}, n_{QD}, D_{core}, and V_{shell} state for the number of shell layer, number of quantum dots in the solution, density of the core structure and the volume of shell, respectively. MW of core is shown as MW_{core}, N_A is the Avagadro's number. In order to find the volume of the shell, the following equation is also used.

$$V_{shell} = \frac{4}{3}\pi[(r_c + \ m \ x \ d_{ML})^3 - r_c{}^3] \qquad (3.6)$$

Here, r_c is the radious of the core which is assumed as spherical. "M" value in d_{ML} states the number of layers in the shell.

In order to synthesize $Zn_xCd_{1-x}S_ySe_{1-y}$ / ZnCdS core / shell type nanoalloys, sulfur, zinc, cadmium precursors for the shell layer and the additional capping agents are preperad individually. While thiourea is dissolved in water, zinc myristate, cadmium myristate and TOPO (with specific ratios) are dissolved in toluene. These two different solutions are added to the reaction medium which containing nucleated and growing nanoparticles at 90 ° C. The reaction is continued at 90 ° C and under argon or nitrogen atmosphere. When the predetermined particle size or absorption/emission wavelength is reached, the reaction is quenched by cooling the reaction flusk, nanocrystal growth is stopped, and the products (colloidal core/shell nanoparticles) are purified with the similar steps as mentioned for the core nanoalloys. Core alloy composition is choosen with Cd/Zn initial mole ratio as 2 and an S/Se initial mole ratio as 5 for the further shell growth experiments. The same synthesis procedure have been repeated many times and it has been determined that the quaternary alloy nanocrystals are reproducibly synthesized. According to the results obtained from the SEM-EDS analysis, it was determined that the alloy composition of the nanocrystal of the core structure (with given initial mole ratios - Table 3.1 experimetnal set #2) is $Zn_{0.2}Cd_{0.8}S_{0.7}Se_{0.3}$. The total amount of initial cations in the alloy nanocrystals was assumed as 0.25 mmol (for a 20 mL reaction volume), and the amount of these chemicals to be added to the shell layer was determined using this molar amount. The total amount of cations in initial chemicals determined for this purpose were 0.1 mmol, 0.2 mmol, 0.5 mmol and 1.0 mmol for each 20 mL QD solutions were prepared. In the

first experimental set, the initial Cd/Zn molar ratio of $Zn_xCd_{1-x}S$ shell alloy composition was adjısted as 2.0. This ratio was then changed to 1.0 for the same core structure, the alloys were re-synthesized and the results were re-evaluated.

Table 3.2. Experimental design of the core shell nanocrystals

Sample *	TOTAL initial cation amount (mmol)**		Shell/ Core Cation Mole Ratios	Reaction Duration (mins) ***	Reaction Temperature (C)	Reaction Volume (mL)	
	Core	Shell				Core	Shell
Core	0.25	0.0	0.0	300	90	20	-----
C / S – 1	0.25	0.1	0.4	300	90	20	20
C / S – 2	0.25	0.2	0.8	300	90	20	20
C / S – 3	0.25	0.5	2.0	300	90	20	20
C / S – 4	0.25	1.0	4.0	300	90	20	20
C / S – 5	0.25	0.05	0.2	300	90	20	20
C / S – 6	0.25	0.1	0.4	300	90	20	20
C / S – 7	0.25	0.2	0.8	300	90	20	20
C / S – 8	0.25	0.5	2.0	300	90	20	20

* While the Cadmium / Zinc initial mole ratio of the shell layer is adjusted as 2 for the samples which are C/S – 1,2,3 and 4, it is adjusted to 1 for the samples called C/S – 5,6,7 and 8.

** "TOTAL initial cation amount of core" is the amount of initial Cd+Zn moles for 20 mL reaction volume. "TOTAL initial cation amount of shell" is the amount of added Cd+Zn moles.

*** At the 120th minute of the reaction time, the shell precursors (thiourea, CdMA, ZnMA and capping agent TOPO were added to the reaction medium with a predetermined volume.

3.4. Results

3.4.1. Optical Characterization of The Colloidal $Zn_xCd_{1-x}S_ySe_{1-y}$ Nanocrystals
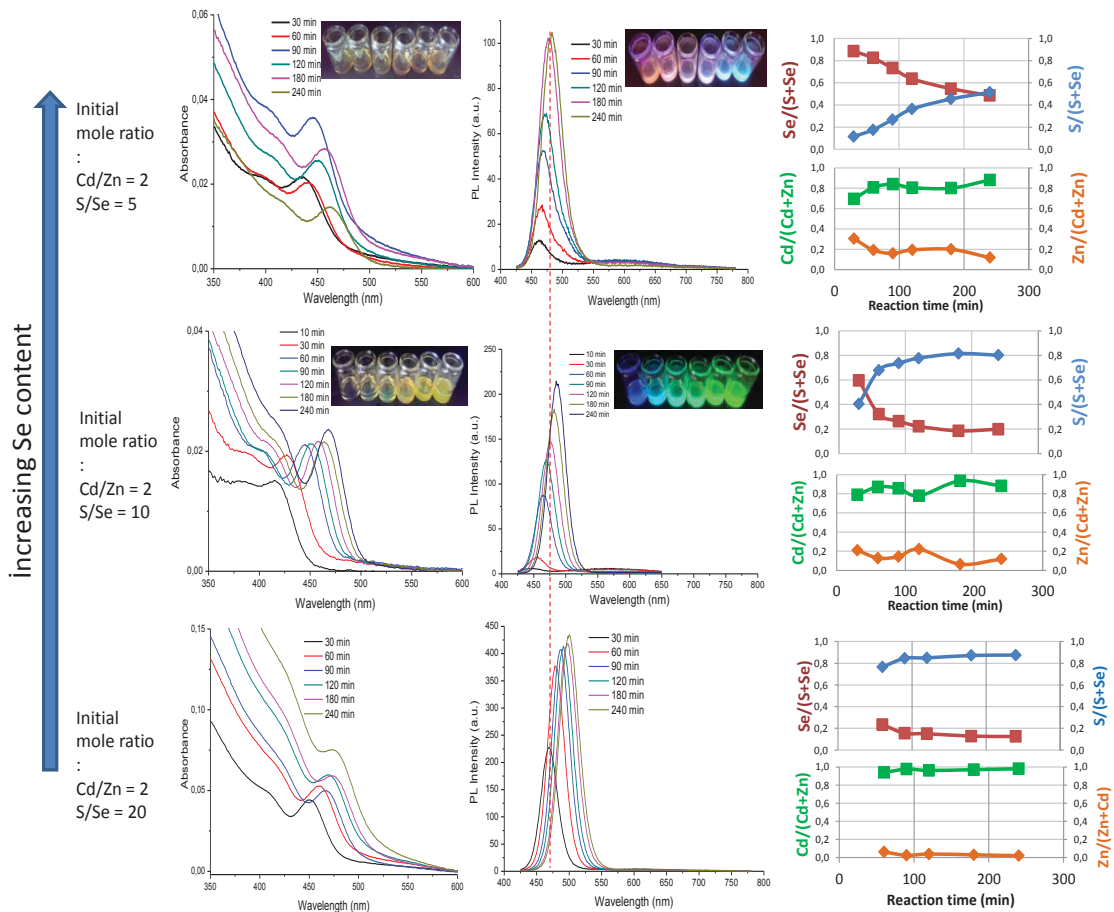
Figure 3.2. Absorption and PL spectra of $Zn_xCd_{1-x}S_ySe_{1-y}$ nanocrystals with the initial mole ratio Cd/Zn = 2 with respect to changing S/Se initial mole ratios. Red dash line is shown the PL blue shift with respect to increasing S/Se initial mole ratio. Photographs shows the images under daylight and UV light. In the right side, SEM-EDS results are shown for the purified samples which are taken in different reaction times.

The UV-Vis absorption and photoluminescence spectra of the colloidal $Zn_xCd_{1-x}S_ySe_{1-y}$ alloy nanocrystals, whose synthesis parameters detailed in Table 3.1, are given in Figure 3.2 and Figure 3.3. The initial S/Se mole ratios were varied from 5 to 20 while the initial Cd/Zn mole ratio was kept constant at 2.0.

When we increased the initial S/Se mole ratio from 5 to 20, $Zn_xCd_{1-x}S_ySe_{1-y}$ nanocrystals emit green / turquoise colors, instead of purple / blue. The absorption and photoluminescence spectra were determined to be shifted about 50-60 nm to the blue region. The alloy composition of the samples was determined by SEM-EDS analysis after purification steps. The findings showed that increasing the initial amount of sulfur, the amount of sulfur in the alloy composition (chemical composition of product) was increased. These results indicate that the alloy composition and thus the optical properties of $Zn_xCd_{1-x}S_ySe_{1-y}$ nanoalloys can be controlled by varying the initial mole ratios of the chalcogenides depending on their reactivities. Different precursors with different reactivites results further optical properties, too.
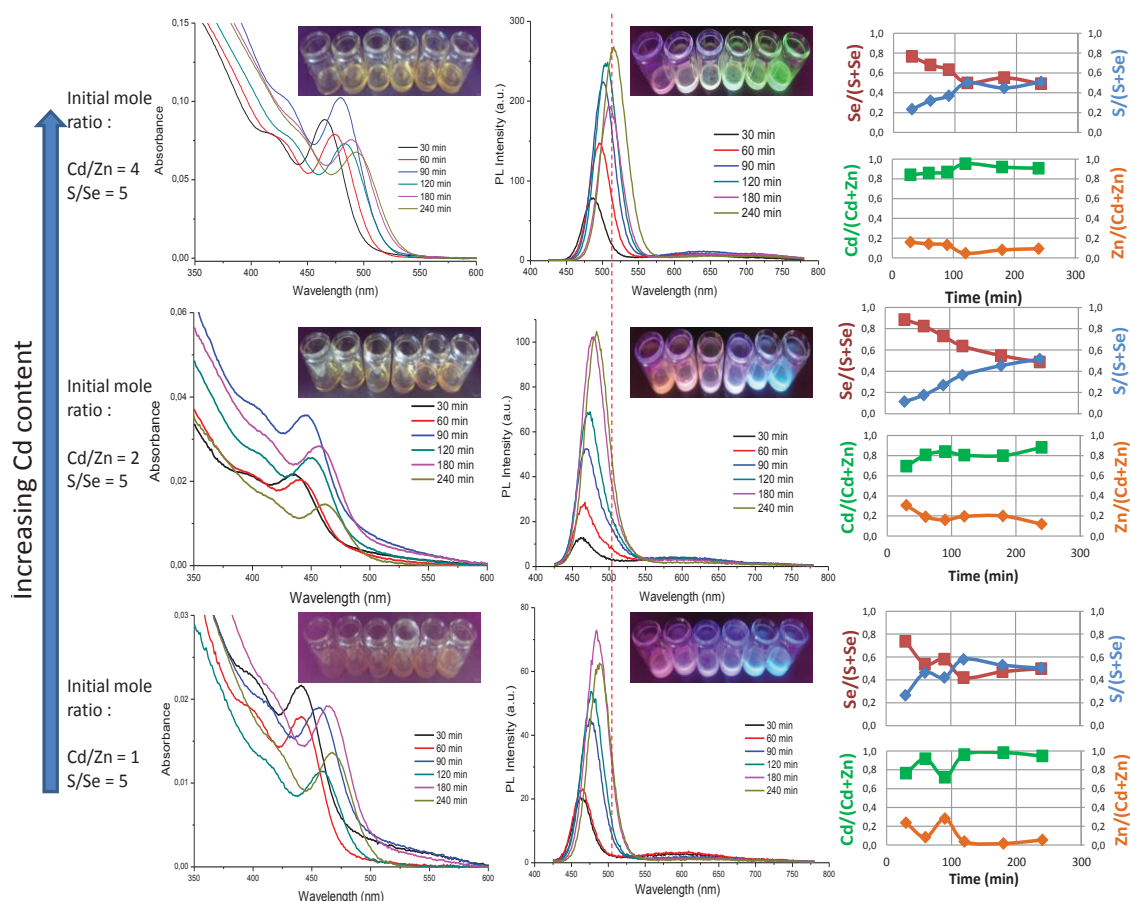
Figure 3.3. Absorption and PL spectra of $Zn_xCd_{1-x}S_ySe_{1-y}$ nanocrystals with the initial mole ratio S/Se = 5 with respect to changing Cd/Zn initial mole ratios. Red dash line is shown the PL blue shift with respect to increasing S/Se initial mole ratio. Photographs shows the images under daylight and UV light. In the right side, SEM-EDS results are shown for the purified samples which are taken in different reaction times.

Table 3.3. Alloy compositions and the optical properties of quaternary type $Zn_xCd_{1-x}S_ySe_{1-y}$ nanocrystals with respect to initial mole ratios and reaction duration.

Initial mole ratios				Alloy composition (SEM-EDS)	Reaction duration (minutes)	λ_{Abs} (nm)	λ_{PL} (nm)	Stokes shift (nm)
Zn	Cd	S	Se					
0.33	0.66	0.83	0.17	$Zn_{0.31}Cd_{0.69}S_{0.11}Se_{0.89}$	30	434	462	28
				$Zn_{0.19}Cd_{0.81}S_{0.18}Se_{0.82}$	60	440	465	25
				$Zn_{0.16}Cd_{0.84}S_{0.27}Se_{0.73}$	90	446	468	22
				$Zn_{0.19}Cd_{0.81}S_{0.36}Se_{0.64}$	120	450	471	21
				$Zn_{0.20}Cd_{0.80}S_{0.45}Se_{0.55}$	180	457	479	22
				$Zn_{0.12}Cd_{0.88}S_{0.51}Se_{0.49}$	240	462	483	21
0.33	0.66	0.83	0.08	-	10	415	444	29
				$Zn_{0.21}Cd_{0.79}S_{0.40}Se_{0.60}$	30	427	455	28
				$Zn_{0.13}Cd_{0.87}S_{0.68}Se_{0.32}$	60	444	465	21
				$Zn_{0.14}Cd_{0.86}S_{0.74}Se_{0.26}$	90	451	469	18
				$Zn_{0.22}Cd_{0.78}S_{0.78}Se_{0.22}$	120	458	475	17
				$Zn_{0.06}Cd_{0.94}S_{0.81}Se_{0.19}$	180	463	483	20
				$Zn_{0.12}Cd_{0.88}S_{0.80}Se_{0.20}$	240	468	486	18
0.33	0.66	0.83	0.04	-	30	451	468	17
				$Zn_{0.06}Cd_{0.94}S_{0.77}Se_{0.23}$	60	461	477	16
				$Zn_{0.02}Cd_{0.98}S_{0.85}Se_{0.15}$	90	466	486	20
				$Zn_{0.04}Cd_{0.96}S_{0.85}Se_{0.15}$	120	469	491	22
				$Zn_{0.02}Cd_{0.97}S_{0.87}Se_{0.13}$	180	473	497	24
				$Zn_{0.06}Cd_{0.98}S_{0.88}Se_{0.12}$	240	475	500	25
0.20	0.80	0.83	0.17	$Zn_{0.16}Cd_{0.84}S_{0.23}Se_{0.77}$	30	465	487	22
				$Zn_{0.14}Cd_{0.86}S_{0.32}Se_{0.68}$	60	475	497	22
				$Zn_{0.13}Cd_{0.87}S_{0.37}Se_{0.63}$	90	479	500	21
				$Zn_{0.05}Cd_{0.95}S_{0.50}Se_{0.50}$	120	482	506	24
				$Zn_{0.08}Cd_{0.92}S_{0.45}Se_{0.55}$	180	489	510	21
				$Zn_{0.09}Cd_{0.91}S_{0.51}Se_{0.49}$	240	493	516	23
0.50	0.50	0.83	0.17	$Zn_{0.24}Cd_{0.76}S_{0.26}Se_{0.74}$	30	440	463	23
				$Zn_{0.08}Cd_{0.92}S_{0.46}Se_{0.54}$	60	442	465	23
				$Zn_{0.28}Cd_{0.72}S_{0.42}Se_{0.58}$	90	456	476	20
				$Zn_{0.04}Cd_{0.96}S_{0.58}Se_{0.42}$	120	458	478	20
				$Zn_{0.02}Cd_{0.98}S_{0.53}Se_{0.47}$	180	463	484	21
				$Zn_{0.05}Cd_{0.95}S_{0.50}Se_{0.50}$	240	468	489	21
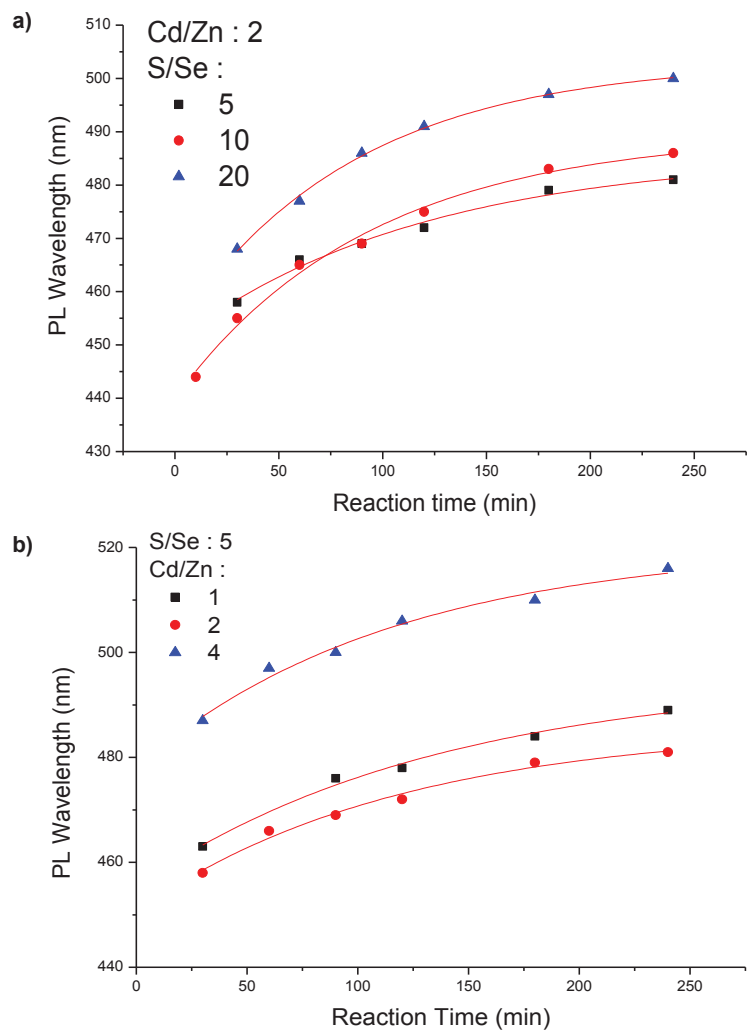
Figure 3.4. The growth kinetic of $Zn_xCd_{1-x}S_ySe_{1-y}$ nanocrystals for a) constant Cd/Zn initial mole ratio as 2 with varying S/Se mole ratio, b) constant S/Se initial mole ratio as 5 with varying Cd/Zn mole ratio.

The reaction kinetics were studied using the UV-Vis absorption and photoluminescence spectra. The graphs given in Figure 3.4 give information about the reaction kinetics. If the variation of the PL maximum wavelength with respect to reaction time is ploted, it is clearly seen that the PL wavelength shifts to the red region for each different cation and anion amounts. However, the rate of the red shift slows down after a certain period of time. The same red shift could be observed in the absorption spectra, too. The slowing of the change in the PL wavelength indicates that the growth of alloy nanocrystals has reached the stopping point. After this poing both the particle size and the optical properties does not change significantly as they do in the earlier reaction times.

Table 3.4. Growth constants of the ZnCdSSe nanocrystals. (The growth kinetics are given in Figure 3.4)

Sample	Growth constants
$Zn_{0.12}Cd_{0.88}S_{0.51}Se_{0.49}$	118.2
$Zn_{0.12}Cd_{0.88}S_{0.80}Se_{0.20}$	93.9
$Zn_{0.06}Cd_{0.98}S_{0.88}Se_{0.12}$	86.5
$Zn_{0.05}Cd_{0.95}S_{0.50}Se_{0.50}$	135.8
$Zn_{0.09}Cd_{0.91}S_{0.51}Se_{0.49}$	115.9

The change in PL QE over the reaction time is also given in Figure 3.5. When the particles are small, PL quantum yield is as low as 1-2%, reaching values of 40-45% after about 100 minutes reaction time. The particle size was measured by SAXS technique. It was determined that the PL quantum yields are relatively low when the particle size of the nanoalloy are small.
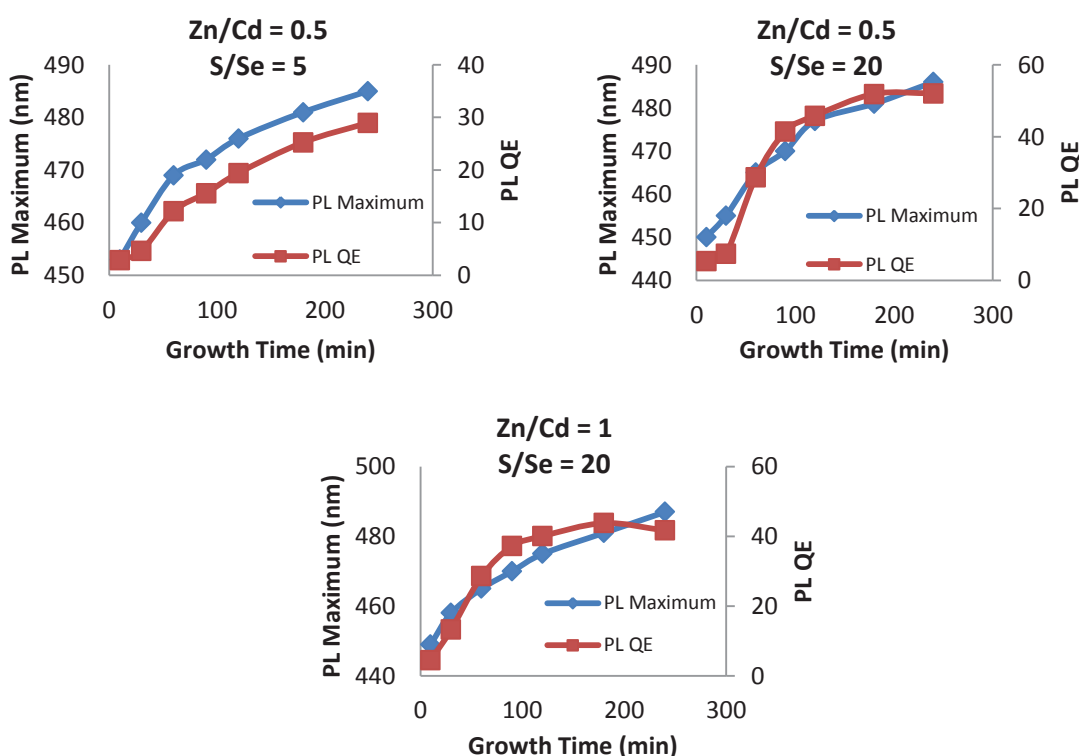
Figure 3.5. Growth kinetics of $Zn_xCd_{1-x}S_ySe_{1-y}$ nanocrystals in terms of PL max shift and PL QE.

The reason of this could be explained as the following: When the nanocrystals are small, some of the alloys' atoms are on the particle surface without any capping agent protection. Since these cappig agents, TOPO and oleic acid act as a protective layer, small nanoparticles are vulnerable to environmental influences. The environmental effects are transmitted to the inorganic atoms by the interaction of the solvent molecules (toluene) present in the environment with the organic ligands. The crystal structure of the alloy is open to the environmental influences, it can not protect the excitonic (electron-hole pair) structure that create the PL emission. This can lead to a low PL quantum yield. As seen in the figures (Figure 3.5), as the reaction time increases, the PL quantum yields of $Zn_xCd_{1-x}S_ySe_{1-y}$ alloy nanoparticles increase and the highest quantum yield reached is about 40%.
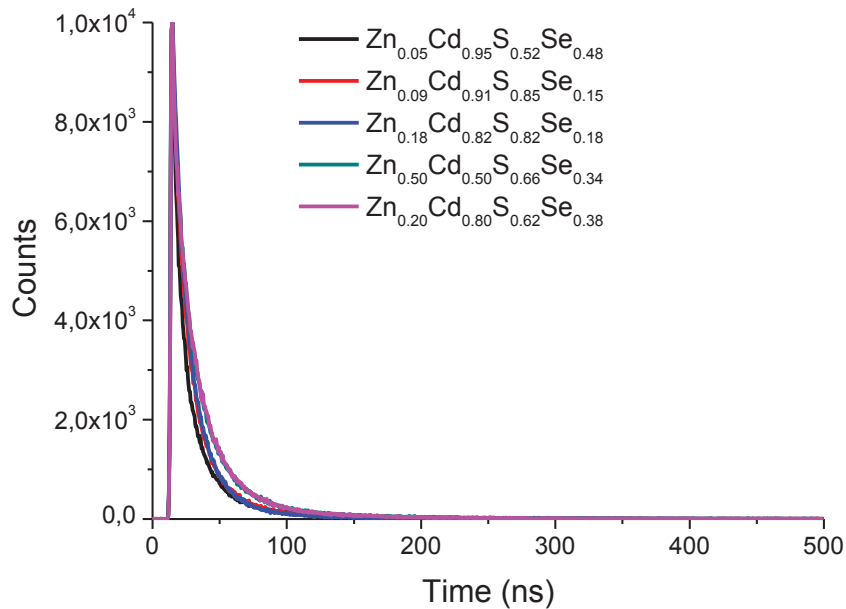
Figure 3.6. Lifetime decays of the $Zn_xCd_{1-x}S_ySe_{1-y}$ nanoalloys with different alloy compositions. Table shows the lifetime values of different processes with relative percentages.

Another important optical parameter is photoluminescence lifetime. The PL lifetimes of $Zn_xCd_{1-x}S_ySe_{1-y}$ nanocrystals were measured by the TCSPC system. Alloy nanocrystals were excited with 368 nm laser. The typical decay curve which is observed in all over the nanocyrstals is shown inFigure 3.6. The analysis software of the TCSPC system yielded (1/e times of the max. intensity) the lifetimes which are given in theFigure 3.6. It has been determined that $Zn_xCd_{1-x}S_ySe_{1-y}$ alloy nanoparticles have three

different decay times. This results suggest that three different photophysical processes occur at the excited states (excitonic energy level). The fastest decay time is 15 ns with 35% of contribution, while the slowest is 95 ns with 8% of contribution. The weighted average PL lifetime is estimated to be 27 ns. Similar decay curves were observed for the alloyed nanocrystals with different alloy compositions, but with similar average lifetimes. These results show that PL lifetimes are independent of the alloy compositions. This result shows that even though the composition of the alloy can be tuned, it is not feasible to control photon dynamics in the excitonic levels during the lifetime of the excitonic processes. In other words, if the alloy composition is effective on photodynamic phenomena, the time resolution of the present measurement system would be insufficient to measure fast processes that occur.

Table 3.5. Lifetimes of the $Zn_xCd_{1-x}S_ySe_{1-y}$ nanoalloys with different alloy compositions. Each nanoalloy has three exponential process. The contributions of each process are given with the corresponding lifetime values of that process.

Sample	τ_1 (ns)	$\%_1$	τ_2 (ns)	$\%_2$	τ_3 (ns)	$\%_3$	τ_4 (ns)	$\%_4$	$\tau_{average}$ (ns)	χ^2
$Zn_{0.05}Cd_{0.95}S_{0.52}Se_{0.48}$	3.8	13.6	13.3	52.7	36.2	24.6	127.9	9.1	28	1.1
$Zn_{0.09}Cd_{0.91}S_{0.85}Se_{0.15}$	6.5	20.3	16.3	58.4	41.7	16.7	143.7	4.6	24	1.1
$Zn_{0.18}Cd_{0.82}S_{0.82}Se_{0.18}$	8.0	26.7	17.5	62.1	59.5	9.7	444.1	1.5	25	1.2
$Zn_{0.20}Cd_{0.80}S_{0.62}Se_{0.38}$	2.1	2.3	14.5	56.6	28.1	41.7	101.3	10.4	30	1.2
$Zn_{0.50}Cd_{0.50}S_{0.66}Se_{0.34}$	1.5	1.4	11.0	26.5	23.2	57.6	86.1	14.6	29	1.0

3.4.2. Structural Characterization of The Colloidal $Zn_xCd_{1-x}S_ySe_{1-y}$ Nanocrystals

Transmission electron microscopy (TEM) analysis was performed to understand the particle sizes, monodispersity and the shapes of the quaternary $Zn_xCd_{1-x}S_ySe_{1-y}$ alloy nanoparticles. As it can be seen in Figure 3.7, $Zn_xCd_{1-x}S_ySe_{1-y}$ nanocrystals are monodisperse and spherical as expected. This observation which proves the SAXS and DLS analysis, indicated that the nanocrystals had a single-size distribution in terms of the particle size.
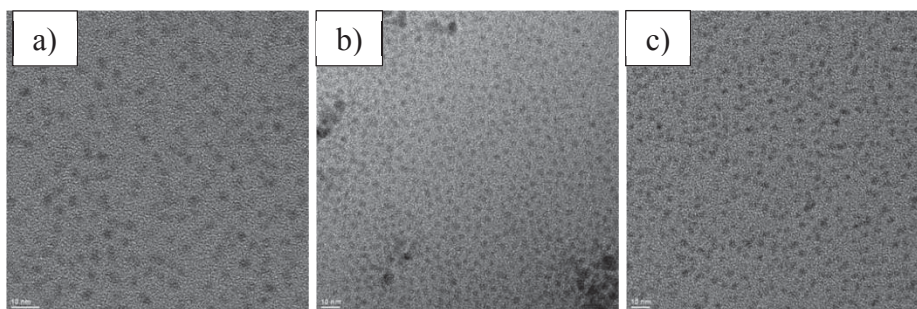
Figure 3.7. TEM images of a) $Zn_{0.12}Cd_{0.88}S_{0.89}Se_{0.11}$, b) $Zn_{0.12}Cd_{0.88}S_{0.80}Se_{0.20}$, c) $Zn_{0.13}Cd_{0.87}S_{0.87}Se_{0.13}$ nanoalloys.

The shape of the nanocrystals have been observed to be spherical. The TEM analysis shows that the average size of the particle is about 3 nm. TEM results were found to be consistent with SAXS measurements (the results are given later).
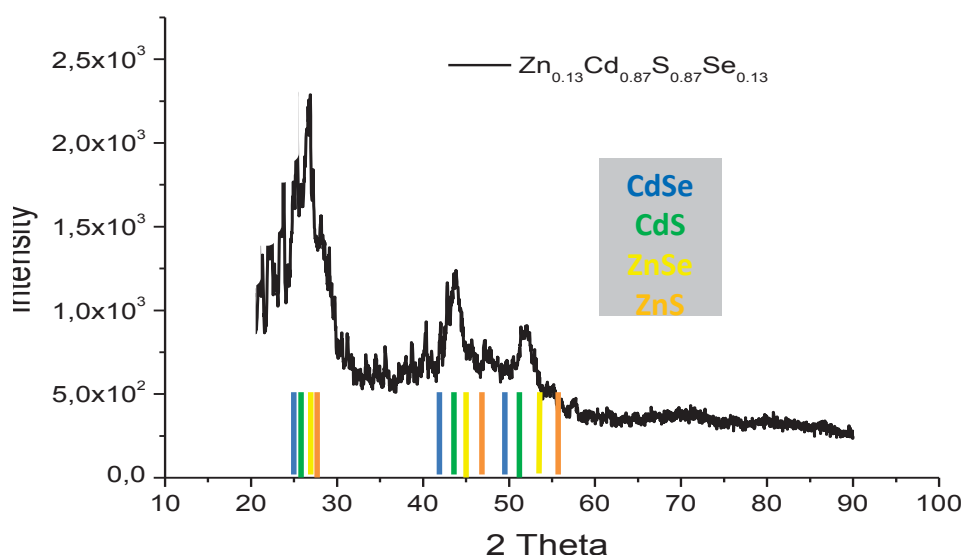
Figure 3.8. XRD difractogram of $Zn_{0.13}Cd_{0.87}S_{0.87}Se_{0.13}$ nanocrystals. The colored lines refers to (111), (220) and (311) planes of CdSe, CdS, ZnSe and ZnS binary nanocrystals.

XRD plays an important role in the structural characterization of $Zn_xCd_{1-x}S_ySe_{1-y}$ alloy nanocrystals. Figure 3.8 shows the XRD pattern of the $Zn_{0.13}Cd_{0.87}S_{0.87}Se_{0.13}$ nanoalloy composition. The blue, green, yellow, and orange lines shown in Figure 3.8 represent the diffraction angles of the corresponding binary crystal structures (CdSe, CdS, ZnSe, and ZnS) which are forming the ZnCdSSe nanocrystals corresponding to

the "zinc blende" structure. The peak values of the synthesized quaternary colloidal alloys are between the peaks of the parent binary structures. The peaks in the XRD pattern obtained are closer to the CdS binary structure that supports the analyses deduced from SEM-EDS: the alloy composition is Cd and S richer.

The optical and structural characteristics of the synthesized quaternary alloy $Zn_xCd_{1-x}S_ySe_{1-y}$ nanocrystals are given above. The most important issue in alloy nanoparticle synthesis is that optical properties (such as λ_{abs} and λ_{PL}) can be controlled by both alloy composition and the particle size.

$$E_n = \frac{n^2 h^2}{8mL^2} \qquad (3.7)$$

The simple equation 3.7 shows the particle size and the effect of the alloy composition (over mass) on the UV-Vis absorption wavelength or PL wavelength. Although this equation is derived from the "particle-in-a box" model, which is the most simple quantum mechanical model, it is very useful in explaining the optical properties of nanocrystals. The first case to demonstrate experimentally is to show that the particle size can be kept constant and the chemical composition of the formed nanoparticles can be adjusted by varying the initial mole ratios. The other is to control the particle size by the reaction time, keeping the nanocrystal alloy composition constant. Both cases have been examined here, we proved/performed that alloy composition and the particle size can control the optical properties of the colloidal alloy.

Figure 3.9 depicts that the photoluminescence spectra can be tuned by the particle size by keeping the alloy composition of $Zn_xCd_{1-x}S_ySe_{1-y}$ similar but different particle sizes. The particle size distributions obtained by SAXS measurements are shown as proving that the particle size varied by the reaction time. The photoluminescence spectra of the nanoalloys were shifted form 512 nm to 541 nm; while the particle is grown from 3.3 nm to 4.1 nm. During the growth of the reaction, negligable alloy composition changes were determined. The SAXS measurements for this experimental set, which is generally considered as homogeneous growth, determined that the particles size increases significantly. Thus, it has been shown that optical properties are controlled by the particle size with the same chemical alloy composition (keeping them same in the experimental uncertainty). It is foreseen that the small changes in the alloy composition will have negligible effect on the optical

properties. The accuracy of this prediction can only be achieved with energy filtered high resolution transmission electron microscopy (HR-TEM) measurements, but we do not have that facilities.
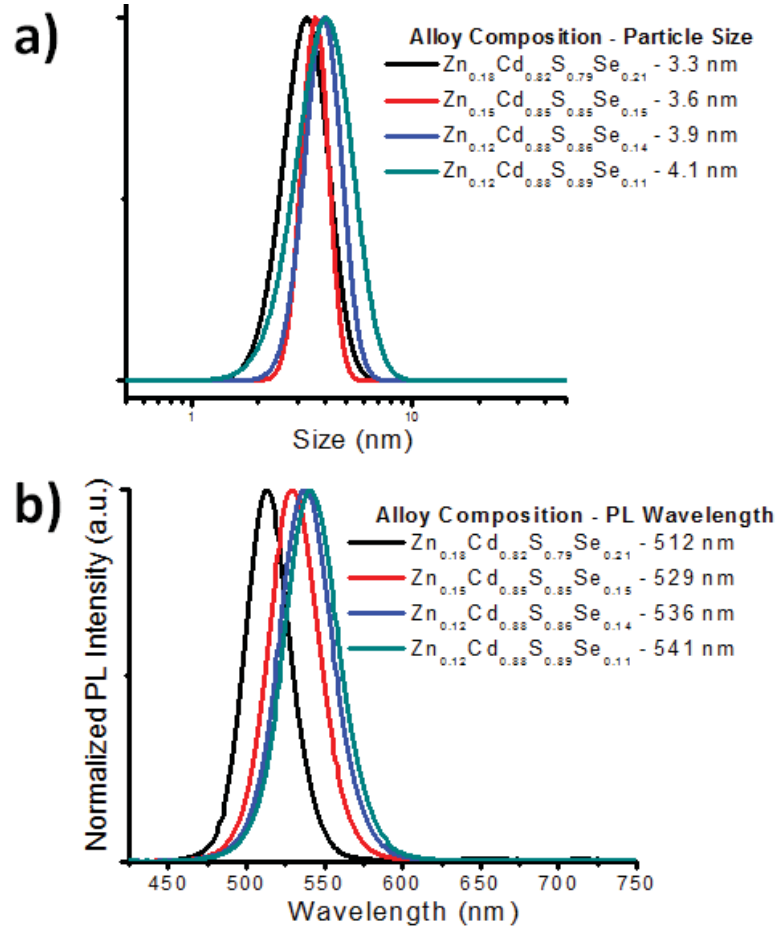
Figure 3.9. a) PL spectrum and b) size distribution obtained from SAXS measurements of $Zn_xCd_{1-x}S_ySe_{1-y}$ nanoalloys which has the similar alloy composition but different particle size.

It is shown in Figure 3.10 that the PL emission spectra of the $Zn_xCd_{1-x}S_ySe_{1-y}$ nanoalloys can be tuned by the alloy composition, whose particle size is fixed between 3.2 nm and 3.4 nm according to SAXS measurements. It proved that the particle size was very close to each other, but the composition of the alloy - particularly the Zn and Cd ratios - is controlled by adjusting the initial mole ratios. The changes in this alloy composition causes shift in the photoluminescence spectra of the alloyed nanocrystals. The alloy compositions given in the Figure 3.10 were obtained as a result of SEM-EDS analysis. As expected, depending on the increase in the amount of Cd in the alloy and

keeping the particle size and the S/Se mole ratio constant, the PL spectra shifts to larger wavelengths (to the red). The PL wavelengths increased from 493 nm to 526 nm when the amount of Zn:Cd changed from 0.50:0.50 to 0.05: 0.95 in selected samples with a constant S/Se ratio confirmed by SEM-EDS analysis. The amount of Cd in the alloy composition (the product) has increased about twice but the increase in amount of Se is only 1/4 compared to its initial value.
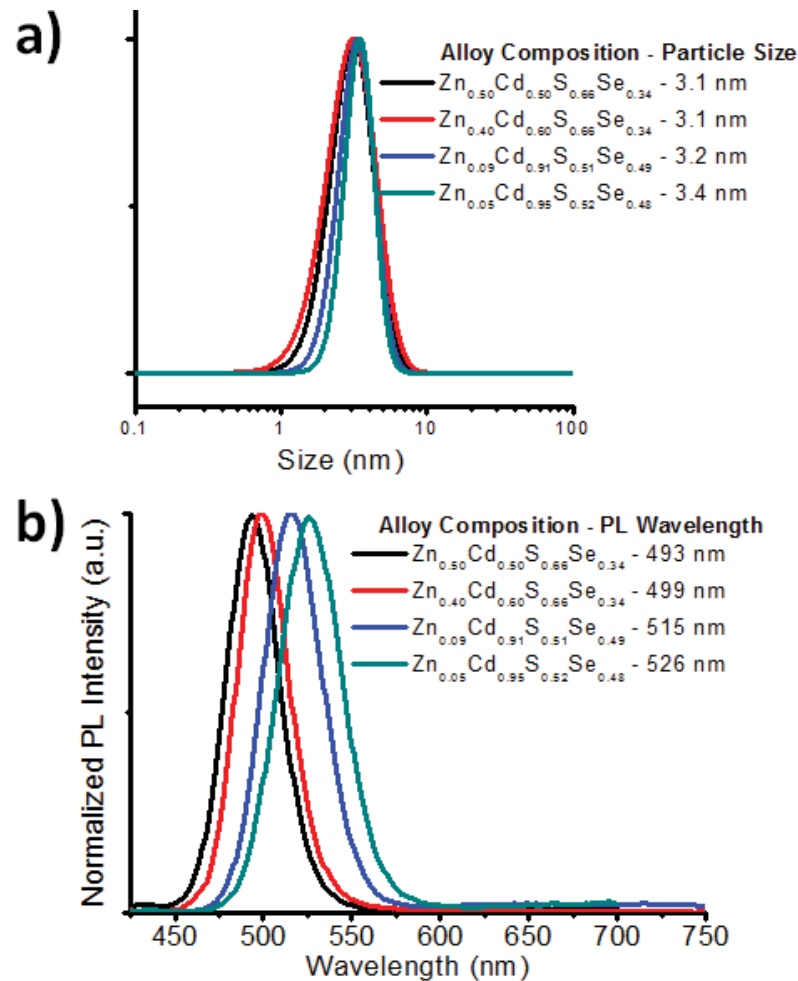
Figure 3.10. a) PL spectrum and b) size distribution obtained from SAXS measurements of $Zn_xCd_{1-x}S_ySe_{1-y}$ nanoalloys which has the similar particle size but different alloy composition.

It is proved here that both the particle size and the alloy composition could be arranged in order to control the optical properties independently. An important point to note is that such controls are extremely difficult in quaternary nanoalloys. It is often desirable to select the precursors that form the nanoalloys have similar reactivity to each other. While the metal cations used in our studies have similar chemical

structures/reactivities, the anion sources have different structures and their reactivity varies considerably. To compensate for this, the S/Se mole ratios were varied from 5 to 20. These values are based on the results of our previous study (Unlu et al., 2013). In general, selenium sources are more reactive than sulfur sources, so sulfur content is significantly higher than selenium content and the difference between reactivities is tried to be balanced. As far as we concern, it is not easy to find or synthesize sulfur and selenium sources with similar reactivities. Such resources may be prepared, but it is considered that it will require completely different optimizations.

3.4.3. Optical and Structural Characterization of Core / Shell - $Zn_xCd_{1-x}S_ySe_{1-y}/Zn_xCd_{1-x}S$ - Quaternary Nanocrystals

Core / shell type $Zn_xCd_{1-x}S_ySe_{1-y}$ / $Zn_xCd_{1-x}S$ nanocrystals were synthesized by the addition of excees amount of Zn – Cd and S precursors after 2 hours reaction time into the reaction flask contains core $Zn_xCd_{1-x}S_ySe_{1-y}$ nanocrystals. First sampling after shell addition was done in 150th minutes as a total reaction time (30th minutes after shell addition). Detail information about shell labels were introduced in Table 3.2.

In Figure 3.11 absorption and photoluminescence emission spectra of core and core / shell type $Zn_xCd_{1-x}S_ySe_{1-y}$ and $Zn_xCd_{1-x}S_ySe_{1-y}$ / $Zn_xCd_{1-x}S$ nanocrystals were shown. Increasing the amount of shell / core cation initial ratio results red shift (shifts to the higher wavelengths – lower energy region) in the electromagnetic spectrum. This results clearly show that optical properties of these nanocrystals were directly dependent to the thickness of the shell layer. While the nanocrystals with the core composition as $Zn_{0.17}Cd_{0.83}S_{0.69}Se_{0.31}$ absorb the light at 483 nm after 5 hours reaction time, core / shell type nanocrystals absorb light at 487 nm, 495 nm, 510 nm and 533 nm with the increase in the shell layer, respectively. Similarly photoluminescence emission maximums of these nanocrystals were shifted from 503 nm to 506 nm, 515 nm, 529 nm and 555 nm, with repect to increasing shell layer. Figure 3.12 also shows the red shift in photoluminescence emission spectra of core and core / shell type nanocrystals in terms of reaction time, more specifically.
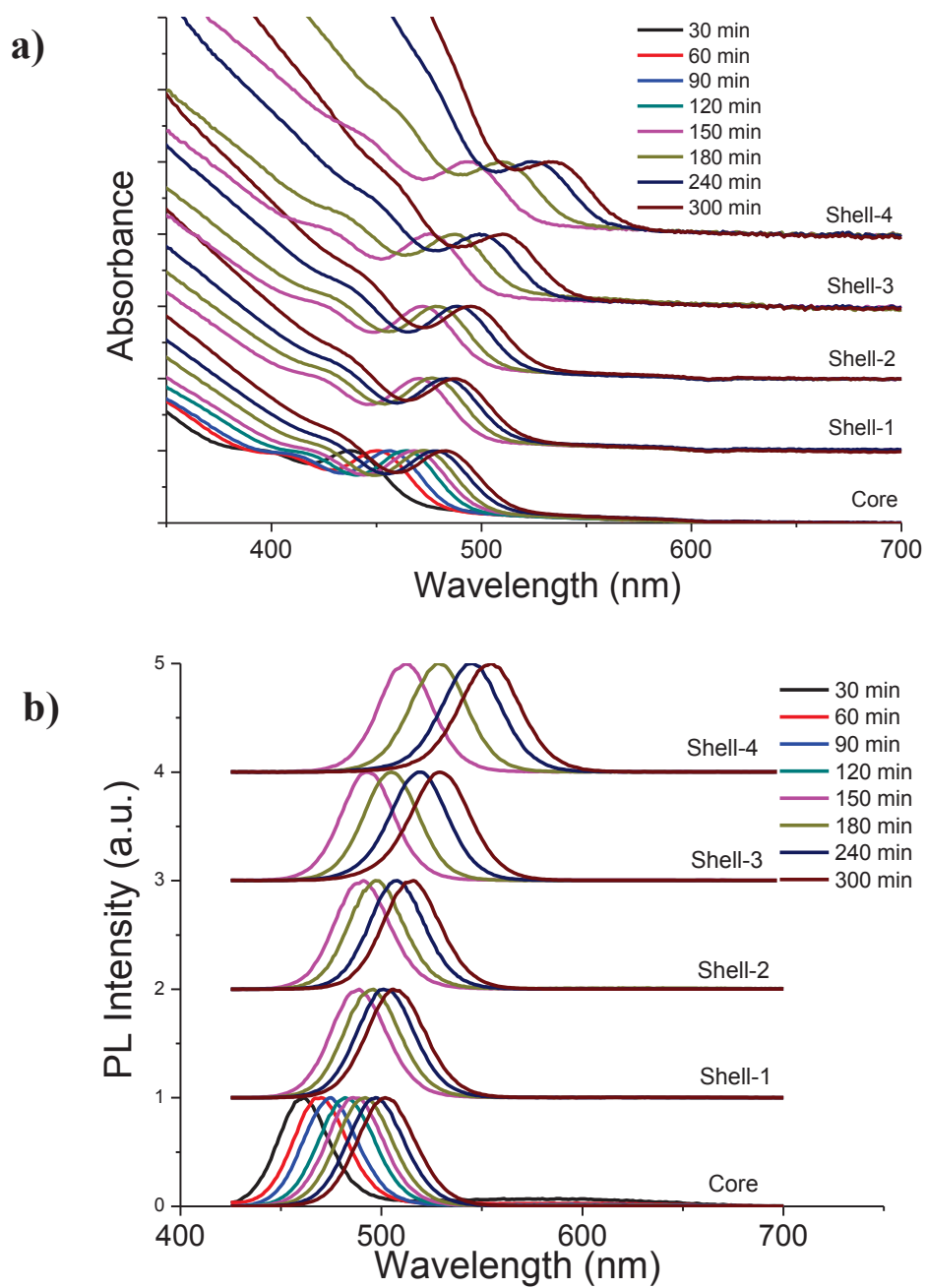
Figure 3.11 Absorption and PL spectra of $Zn_xCd_{1-x}S_ySe_{1-y}$ / $Zn_xCd_{1-x}S$ Core / shell nanocrystals with respect to different ZnCdS shell layers. Images shows the nanocrystals under day light and UV light. From left to right shell layer increases. The first tube on the left side is the core nanocrystals.
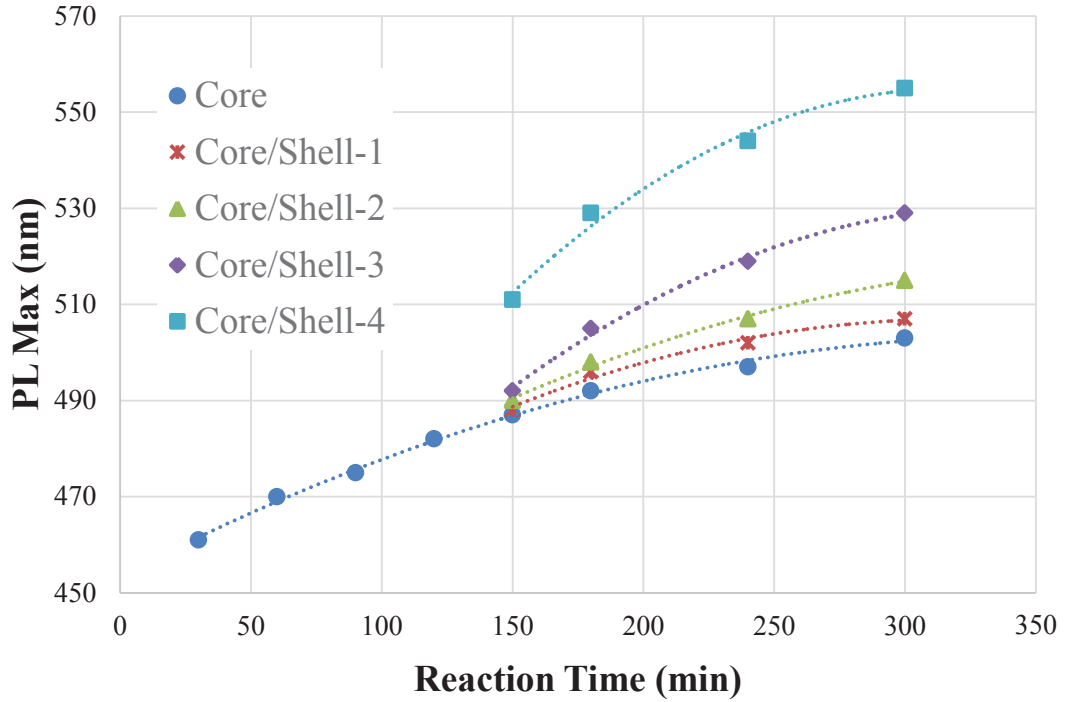
Figure 3.12. PL maximum wavelengths variation of core and core / shell type $Zn_xCd_{1-x}S_ySe_{1-y}$ and $Zn_xCd_{1-x}S_ySe_{1-y}$ / $Zn_xCd_{1-x}S$ nanocrystals in terms of reaction time

SEM-EDS analysis of the purified core and core / shell type $Zn_xCd_{1-x}S_ySe_{1-y}$ and $Zn_xCd_{1-x}S_ySe_{1-y}$ / ZnCdS nanocrystals show that, increasing shell layer (increasing the amount of initial shell precursors in the reaction) causes the increase in sulfur content in the final alloy composition. However, it is required to use HR-TEM-EDX or EF-HR-TEM to determine the individual alloy composition of the core and the shell parts.

Table 3.6. Lifetimes of the core/shell $Zn_xCd_{1-x}S_ySe_{1-y}$/ZnCdS nanoalloys with different Shell thicknesses. Each nanoalloy has three exponential process. The contributions of each process are given with the corresponding lifetime values of that process

Sample	τ_1 (ns)	$\%_1$	τ_2 (ns)	$\%_2$	τ_3 (ns)	$\%_3$	$\tau_{average}$ (ns)	χ^2
Core	6,21	17,21	18,28	73,02	77,62	9,77	22,0	1,111
Core/Shell-1	7,05	23,77	17,93	68,63	71,26	7,6	19,4	1,181
Core/Shell-2	7,50	30,74	17,89	60,66	69,35	8,6	19,1	1,188
Core/Shell-3	6,22	40,04	17,19	51,5	81,45	8,46	18,2	1,25
Core/Shell-4	6,39	20,33	20,08	63,39	71,55	16,28	25,7	1,228

Lifetime of the core/shell nanoalloys were also investigated as shown in the Table 3.6. Altohugh there are some variations in the average lifetimes values. However, since all the lifetime decays are three exponential and the contributions of each processes are similar, we can assume that all the core/shell structures have similar tren in terms of lifetime and these small variatons are negligable.

Figure 3.13 is a kind of summary of photophysical characteristics of core and core / shell type $Zn_xCd_{1-x}S_ySe_{1-y}$ and $Zn_xCd_{1-x}S_ySe_{1-y}$ / $Zn_xCd_{1-x}S$ nanocrystals. Given two graphs show the photoluminescence emission maximum, photoluminesncence quantum efficiency and full width at half maximum (FWHM) values in terms of shell / core initial concentration ratios. Results are also given in Table 3.2. As expected, increasing initial shell content, causes red shift in the optical spectra. While the PL max is shifting to the higher wavelengths, PL QE % of nanocrystals is increasing at first but then it starts to decrease. Even so, the PL QE % of the nanocrystals were calculated around 50%. Besides, FWHM of the nanocrystals does not change significantly, lies around 30 – 34 nm. On the contrary, shell-4 which has the highest initial shell content shows the lowest PL QE % as 20 % and the highest FWHM value as 36 nm. This results show the limitations of additional shell amount for this specific composition and our shell precursors. It may be stem from the surface defects and corresponding nonradiative transitions. As is known, increasing nonradiative transitions causes the reduce in photoluminescence quantum efficiencies.
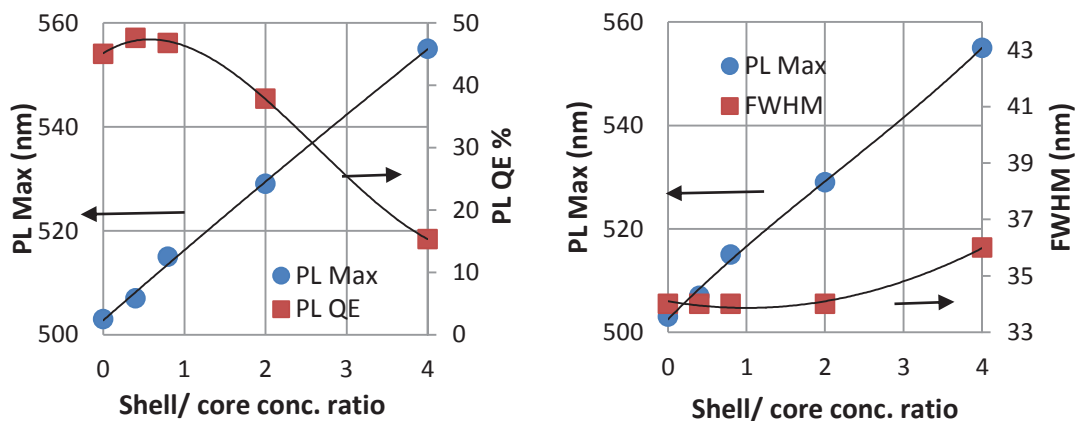
Figure 3.13. Relationship of shell / core concentration ratio of core / shell type $Zn_xCd_{1-x}S_ySe_{1-y}$ / ZnCdS nanocrystals with PL emission maximum, PL quantum efficiency and band width.

As mentioned in Table 3.2, Cd/Zn initial mole ratio in shell content was also changed from 2 to 1 in order to find out the most optimum condition for core / shell type nanocrystals. Shell 5 to Shell 8 in the corresponding table indicates the mentioned experimental sets. In this set shell / core initial concentration ratio was not increased to 4, because of the observed negative effects of thick shell layer in previous results.

The results are similar with the first expermemental sets (From Shell-1 to Shell-4) but there are some deviations. The photophyscal parameters like photoluminescence shift and shell thickness, photoluminescence quantum efficiencies with respect to shell / core initial concentration ratio are summarized in Figure 3.14 and Figure 3.15.
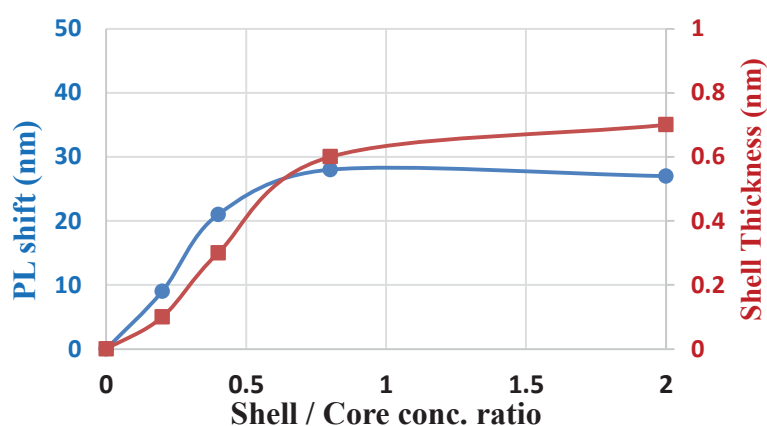
Figure 3.14. Relationship between shell / core initial concentration ratio of core / shell type $Zn_xCd_{1-x}SySe1_{-y}$ / $Zn_xCd_{1-x}S$ nanocrytals with PL maximum shift and shell thickness obtained from SAXS analysis. (Shell thikness = Total size of core / shell nanocrystals – Size of core nancrystals)

The size of the nanocrystals were obtained by the SAXS analysis. In order to obtained the shell thickness, we substract the size of the core nanocrystal from the total size of the core / shell type nancrystals. HR-TEM analysis is required to obtaine direct thickness of the shell layer. SAXS measurements showed that, the size of the core nanocrystals was 3 nm in diameter. Increasing the shell content during the reaction, causes increase in shell thicknesses up to 0.7 nm. Also the photoluminescence spectra shifts to the higher wavelentghs (lower energy region) with respect to initial shell / core concentration ratio. After the point in which the initial shell / core concentration ratio was 0.8, the increase in both shell thickness and photoluminescence red shift decelerates. This results are clearly seen in Figure 3.14.
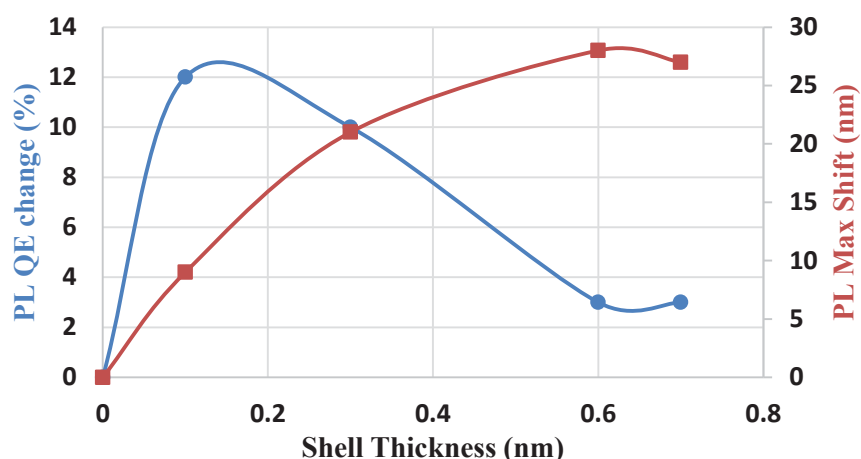
Figure 3.15. Relationship between the shell thicknes of core / shell type $Zn_xCd_{1-x}S_ySe_{1-y}$ / $Zn_xCd_{1-x}S$ nanocrytals with PL maximum shift and phottlumienscence quantum efficincy chagen. shell thicknesses obtained from SAXS analysis. (Shell thikness = Total size of core / shell nanocrystals – Size of core nancrystals)

In Figure 3.15, change in photoluminescence quantum efficiency and PL maximum shift with respect to shell thickness was also shown. PL QE % was calculated by using Coumarine 102, as a reference dye. Also integrated sphere was used in order to find the absolute quantum efficincy of nanocrystals. These values are higher than the ones which calculated with the reference dye, but the trend in reducing with respect to shell thickness was identical. As it is seen that, after 0.2 nm shell thickness, PL QE % starts to reduce significantly. Similar results were also obtained from the first experimental sets. The reason of this reducing in PL QE % may be again the surface defects formed on the formed new shell layers.

3.5. Conclusion

In this chapter, core and core / shell - $Zn_xCd_{1-x}S_ySe_{1-y}$ and $Zn_xCd_{1-x}S_ySe_{1-y}$/ZnCdS colloidal quaternary nanocrystals were synthesized by two phase approch at relatively low temperatures (90°C). According to our knowledge, this is the first study in the literature in terms of synthesis technique of quaternary nanoalloys. We controlled the optical properties of nanoalloys by both the particle size and the alloy composition. In order to achieve such a control on the optical properties the initial mole ratios of the precursors, reaction volume, duration, temperature and shell layer thickesses were

controlled carefully. According to the TEM and SAXS analysis, the particle size is found out as 3-4 nm in diameter. The alloy compositions are determined by SEM-EDS as varying between $0.05 < x,y < 0.90$ for $Zn_xCd_{1-x}S_ySe_{1-y}$ nanoalloys. The absorption and PL spectrum, lifetime, PL QE and FWHM were tuned by the aforementioned reaction parameters. We prove that it is possible to obtain high quality quaternary QDs emitted in the visible range controlling the experimental parameters in two phase synthesis approach.

CHAPTER 4

MICROSPECTROSCOPIC PHOTOLUMINESCENCE PROPERTIES OF COLLOIDAL QUANTUM DOTS

4.1. Introduction

Colloidal semiconductor nanocrystals have received much attention over the past decades due to their unique optical properties which are tunable by both the particle size and alloy composition. Especially quaternary QDs like $Zn_xCd_{1-x}S_ySe_{1-y}$ are a great candidate in the use of biological and optical application because of their ability to cover the whole visible range in the electromagnetic spectrum. However fundamental optical properties like spectral diffusion and fluorescence intermittency (blinking – on/off behavior of QDs) are very critical in these kind of applications For example, fluctuations of the fluorescence intensity which is called blinking is attributed to the photo-induced charging of QD because of the electron transfer to the trap states. Since this behavior decrease the number of generated photons, it degrades performance of optoelectronic devices (Zhu et al., 2013).

Many interesting photophysical parameters like blinking, photobleaching etc. could not be observed in the ensemble of quantum dots with relatively broad size distributions (>5 %) (M. et al., 2002). That is why few studies exist in the literature in terms of single particle QD properties (Lee and Osborne, 2007; Pshenay-Severin et al., 2015). These examples showed that experimental parameters like humidity, measurement temperature, capping agents etc. affect the results significantly. Controlled experiments in the various atmospheric conditions are created (M. et al., 2002; Pechstedt et al., 2010) in order to investigate the effect of oxygen. Since surface of the QDs are able to influenced by the interaction of oxygen and water molecules, the existance of these molecules generates photooxidation reactions. Photobleaching – reduction in intensity of PL emission and blue shift are observables related to photooxidation reactions. CdSe/ZnS nanoparticles showed 29 nm blue shift as a results of photooxidation reaction (M. et al., 2002). Similarly 15 nm blue shift was observed for the same nanoparticles when 3W/cm^2 power was applied for 5000 second (Cordero

et al., 2000). The possible explanation of the blue shifts is either decreasing in particle size or changes in alloy composition. XPS analysis was used to prove that the alloy composition was changed for nanoparticle CdSe/ZnS. They reported that $CdSeO_x$ and ZnO are formed in the presence of oxygen initiating photooxidation reactions (Pechstedt et al., 2010). Hoyer reported that the particle size of CdSe nanoparticles decreases after photooxidation reaction because of the SeO_2 formation; observing blue shift (Hoyer et al., 2011).

4.2. Experimental Set-up

Microspectroscopic measurements were carried out by using a set-up equipped with confocal fluorescence microscope and integrated fiber-optic CCD spectrometer. The high-pressure Hg lamp from Olympus with 100 W out-power was used to excite the samples. The Hg lamp spectrum is given in Figure 4.1a. As it is seen, although the mercury lamp appears as white light to the human eye, in fact, there are intense lines at 365, 405 and 546 nm. The excitation wavelength can be selected using appropriate excitation filters. The excitation, emission and dichroic filters (Figure 4.1b) are used to excite the samples in 365 nm.
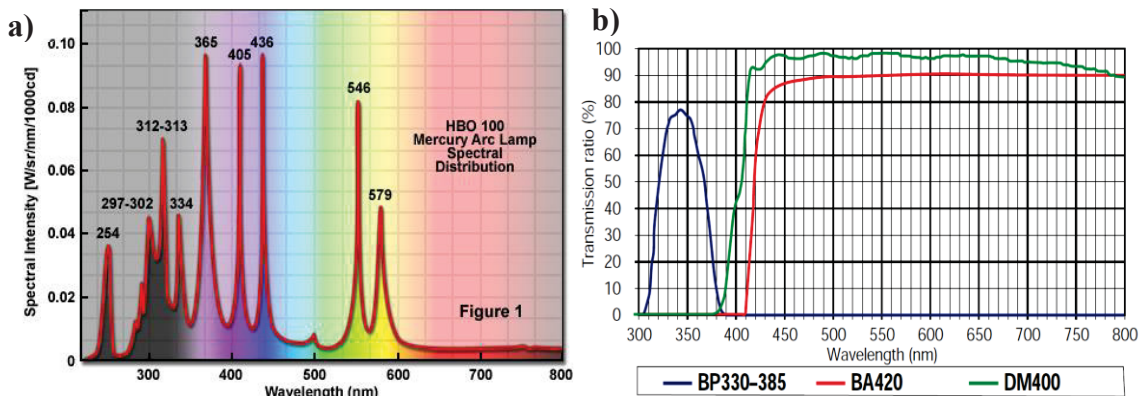
Figure 4.1. The spectrum of a) Hg lamb and b) excitation, emission and dichroic filters used for μPL measurements

Microphotoluminescence (μPL) from nanoalloys are collected by the fiber spectrometer. Fiber diameter used in fiber spectrometer is 300 μm. At this point, the μPL spectra of the nanoalloys were collected through the objective (40x) from the exact

center of the microscope image. The system was calibrated by Rhodamine doped polymeric microspheres with a diameter of 1.0 μm. The calibration procedure is as follows: Microspheres with a diameter of 1.0 μm are centered to the field of view of the observation area by fine movements of the microscope table. Since the microspheres are 1.0 μm in diameter, microspheres are easily identified with the imaging software and the PL spectra are collected by the fiber-spectrometer. At the end of this calibration, it was determined that the μPL spectra and their intensities were collected from a region with a diameter of 10 μm, no μPL emission outside of 10 μm was observed.
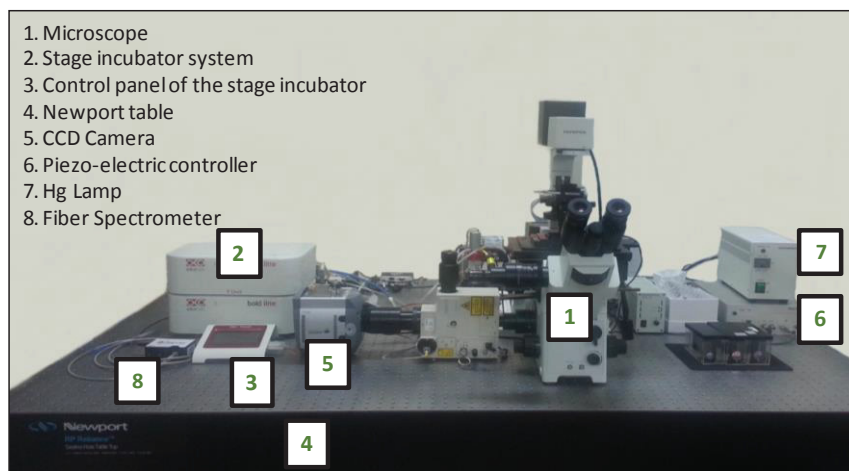
Figure 4.2. The confocal microscope in our laboratory. The confocal microscope consist of stage incubator system and its control panel, CCD camera, piezo-electriccontroller, Hg lamp and fiber spectrometer used for μPL measurements. The whole system is placed on Newport table to prevent enviromental vibrations.

The fiber spectrometer is connected to the confocal microscope system. The whole system (ANDOR) in our laboratory is shown in Figure 4.2.

Fiber spectrometer is connected to the confocal microscope as shown in Figure 4.3. The other side of the fiber is connected to the Ocean Optics "Flame" brand spectrometer through SMA connection. The fiber spectrometer connected by the USB cable to computer uses the Ocean View software (provided by Ocean Optics). It is possible to collect and save the instantaneous μPL spectra and intensities with the help of this set-up. Since the integration time – time to collect the number of photons

incoming from sample – is directly proportional to the µPL intensity collected, it is essential to arrange the integration time especially in kinetic studies.
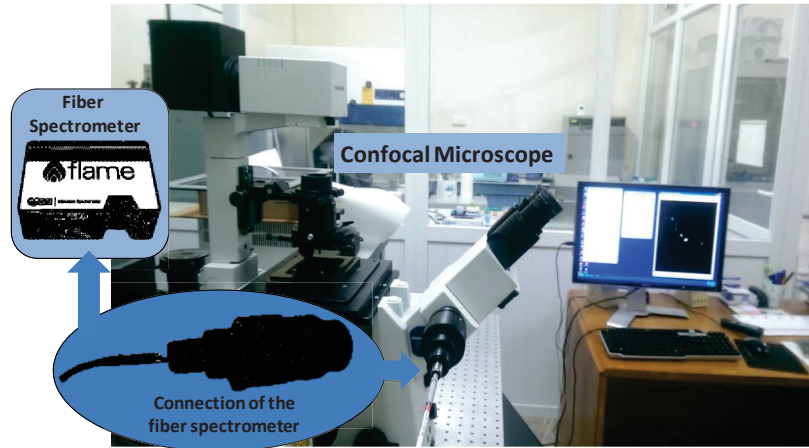
Figure 4.3. The connection of the fiber spectrometer to the confocal microscope.

In our studies 100x and 40x objectives are used. It is crucial to determine the photon flux for the current set-up. As shown in Figure 4.1b, with the help of the appropriate filters, 365 nm line of Hg lamp was used as the excitation source for the µPL measurements. The power of this excitation source measured from the output of the objectives was 68 µW. The equation below is used to obtain the number of photons per second.

$$E = \frac{hc}{\lambda} = \frac{(6.63x10^{-34}J.s)(\frac{3x10^8m}{s})}{365x10^{-9}m} = 5.45x10^{-19}J/photon \qquad (4.1)$$

Here, "E" is the energy in J/photon, "h" is the plank constant, "c" is the speed of light and "λ" is the wavelength of the excitation light. According to the calculations, 365 nm light has $5.5x10^{-19}$ Joule/photon energy. The following equation is used to calculate the number of photons per second. Here, "P" is the power in Watt (Joule/second) and "t" is the time in second. The calculations showed that the light with the power 68 µW has $1.2x10^{14}$ photons per second.

$$\frac{number\ of\ photons}{t} = \frac{P}{E} = \frac{68x10^{-6}J/s}{5.45x10^{-19}J/photon} = 1.2x10^{14}photon/s \quad (4.2)$$

The images obtained from the confocal microscope were collected with 40x objective as mentioned before. According to the calculations, the length of 1 pixel with 40x objective and the microscope system is 0.28 μm. The image size (area) that obtained on the screen is 145 (0.28 μm x 512) x 145 μm. The size of the area illuminated is approximately two times of the area appeared on the screen. Therefore, the true beam diameter is 290 μm, and the area of the beam is calculated as 6.6×10^{-4} cm^2 (by using πr^2).

The photon flux is defined as the number of photons falling into 1 cm^2 area per second. In this case, if we consider that the number of 1.2×10^{14} photons falling to 6.6×10^{-4} cm^2 area within one second, the photon flux is 1.8×10^{17} photons/cm^{2}s. The area measured with fiber spectrometer is a circle with 10 μm in diameter. The spatial resolution of the confocal microscope in the x-y plane is approximately 3x3 or 4x4 pixel (when 100x objective used). If only one nanoparticle is present in this resolution and the particle diameter is taken as 3 nm (which is obtained from SAXS measurements for $Zn_xCd_{1-x}S_ySe_{1-y}$), the number of photons on a nanoparticle is approximately 10^3 photons/particle. This number of photon may induce linear optical processes (single exciton or even multi-exciton processes) in the nanoalloys.

4.3. Microspectroscopic Measurements of The Nanoalloys in The Solution and Film Phases

The film phase of $Zn_xCd_{1-x}S_ySe_{1-y}$ nanoalloys show red shift in the optical spectra by comparing the solution phase. As shown in Figure 4.4, nanoparticles in the solution phase show the maximum emission peak at 531 nm. In the film phase spectra this value shifted to 537 nm. There is no change in peak characteristic and full width at half maximum (FWHM) (33 nm). Since these kinds of shifts and increase in FWHM values are observable due to clusters/agglomerations in the samples, it seems that the lack of such observations in our case indicates almost no agglomeration and high stability of $Zn_xCd_{1-x}S_ySe_{1-y}$ nanocrystals in the film phase.

The film phase $Zn_xCd_{1-x}S_ySe_{1-y}$ nanoalloys show the red shift in optical spectra by comparing the solution phase. As shown in Figure 4.4, nanoparticles in the solution phase show the maximum emission peak at 531 nm. In the film phase spectra this value shifted to 537 nm. There is no change in peak characteristic and full width at half

maximum (FWHM) (33 nm). Since these kind of shifts and increase in FWHM values are observable due to clusters/agglomerations in the samples, it seems that the lack of such observations in our case indicates less agglomeration and high stability of $Zn_xCd_{1-x}S_ySe_{1-y}$ nanocrystals in film phase.
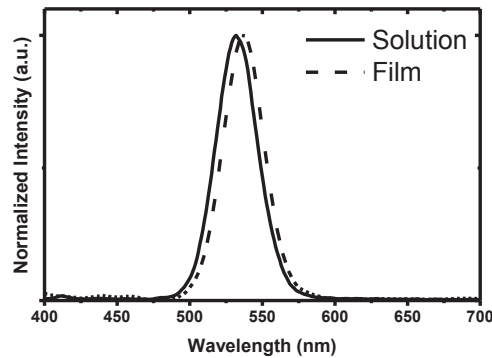
Figure 4.4. The emission spectra of $Zn_xCd_{1-x}S_ySe_{1-y}$ nanoalloyed particles in the solution as well as the film phase

4.4. Connecting the Fiber Spectrometer to The Confocal Microscope
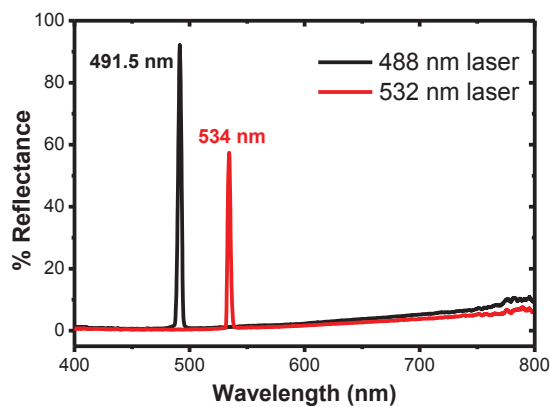
Figure 4.5. Reflectance measurements of the test laser used. Measurements are done by fiber spectrometer

To test the fiber spectrometry and alignment, laser light sources with known wavelengths were used. Reflections from the lasers were measured by the fiber spectrometer. By the help of this set-up spectrum in Figure 4.5 was obtained. The fiber spectrometer works as expected, but a small difference than the expected wavelength (2 nm) is measured. The expected sensitivity and slit spacing for fiber spectra are 20 and

200 micrometers and corresponding spectral resolutions - 2 and 10 nm. These are thought to be unaffected in terms of the success of our study.

After the collection of the emission spectrum by the fiber spectrometer and the correlation of the wavelengths are done by reference lasers, the reflectance probe is removed and the "transmission" mode fiber is directly connected to the confocal microscope. In order to test how much light can be collected locally with the fiber from the microscope view, the study given in Figure 4.6 is done. For this study, $Zn_xCd_{1-x}S_ySe_{1-y}$ nanoalloys are drop-casted on glass substrates. After they dried and the film is formed, the samples are analyzed by confocal microscope. The emitting objects in the image were analyzed by bringing the emitting objects to the center of the image appearing at different locations that are marked in the Figure 4.6. For example, the intensity is higher in the spot labeled as 1 compared to spot area 2 and 3, respectively. Collected PL intensity by fiber spectrometer for the specific regions in the image showed direct proportionality with the density of the nanoparticles, as expected. When 100x objective is used with 512 x 512 pixels, one side of the microscope image is approximately 150 μm. In this case, the fiber spectrometer is able to collect the PL count from a spot area which has maximum 5 μm in diameter. This significant limitation allows taking microspectroscopic measurements from the prepared samples with a spatial resolution of -/+ 10 μm.
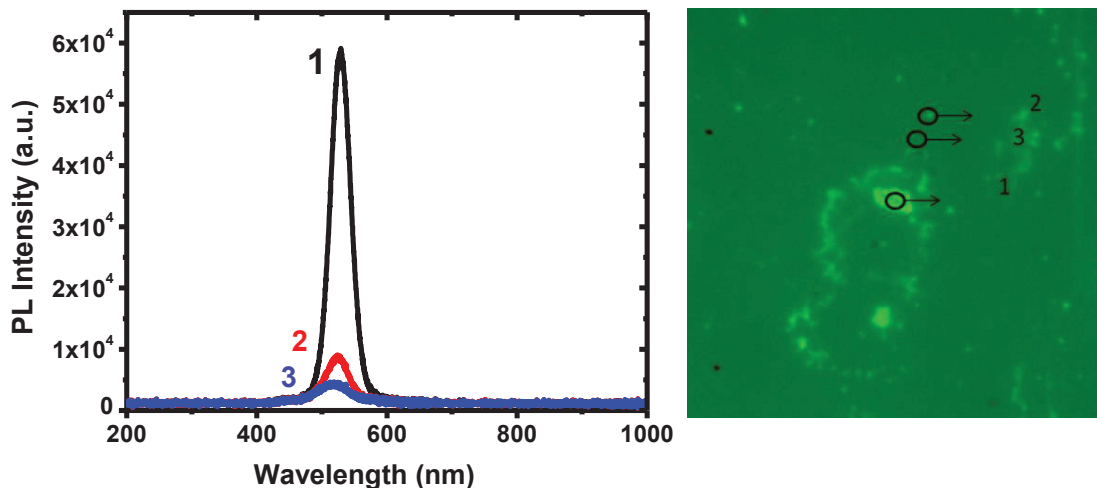
Figure 4.6. The local emission spectra of confocal microscope image obtained by fiber spectrometer. 40x objective is used. Given image has 512x512 pixels and each pixel is approximately 0.3μm. The area of the image is 150x150 μm^2.

4.5. Collecting PL Spectra From Different Types of Quantum Dots by Fiber Spectrometer

a) Brigh Field   **b)** Fluorescence Image   **c)** Merged Image
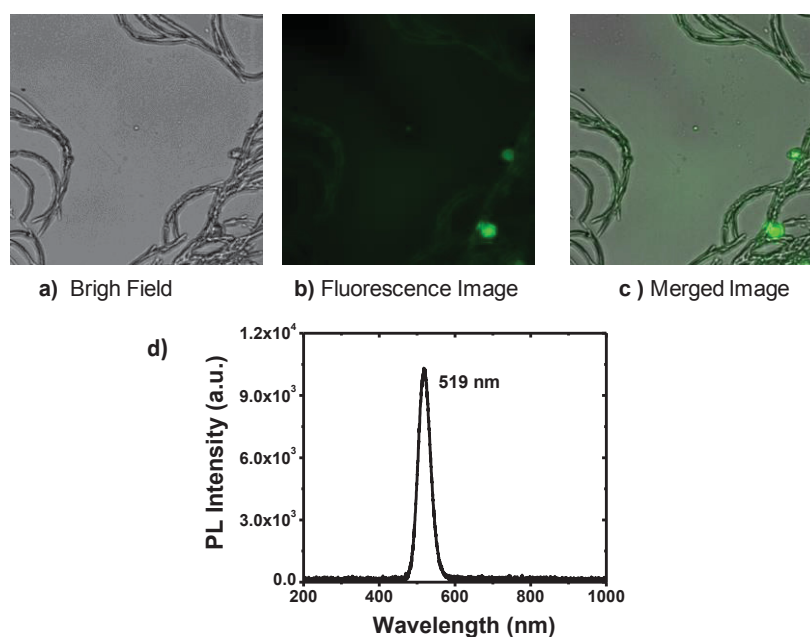
Figure 4.7. a) Bright field b) Fluorescence (Hg lamp excitation) and c) merged images of drop-casted $Zn_xCd_{1-x}S_ySe_{1-y}$ nanoalloys. Images are obtained from confocal microscope d) PL spectrum of the related sample. Spectrum is obtained by fiber spectrometer from the center of the image. 40x objective is used. The integration time of the fiber spectrometer is 100ms.

$Zn_xCd_{1-x}S_ySe_{1-y}$ nanoalloys were coated on a cleaned microscopic slide by drop casting technique. White light is used to obtain bright field images as shown in Figure 4.7a. The white light was turned off and the Hg lamp was turned on in order to excite the samples at 365 nm by adjusting the appropriate filter set (Figure 4.7b.). The image is colored by the ImageJ program. These two images can also be combined with the image analysis program ImageJ and shown in Figure 4.7c as a merged image. The fiber spectrometer, as mentioned before, collects the emission only from the center of the image. Emission spectrum shown in Figure 4.7d is obtained from the small nanoparticle cluster at the center of the images. The emission spectrum shows maximum PL peak at 519 nm with very high signal-to-noise ratio. The FWHM is measured as 35 nm. This value is similar to the solution phase FWHM values of nanoparticles.

a) Brigh Field   **b)** Fluorescence Image   **c)** Merged Image
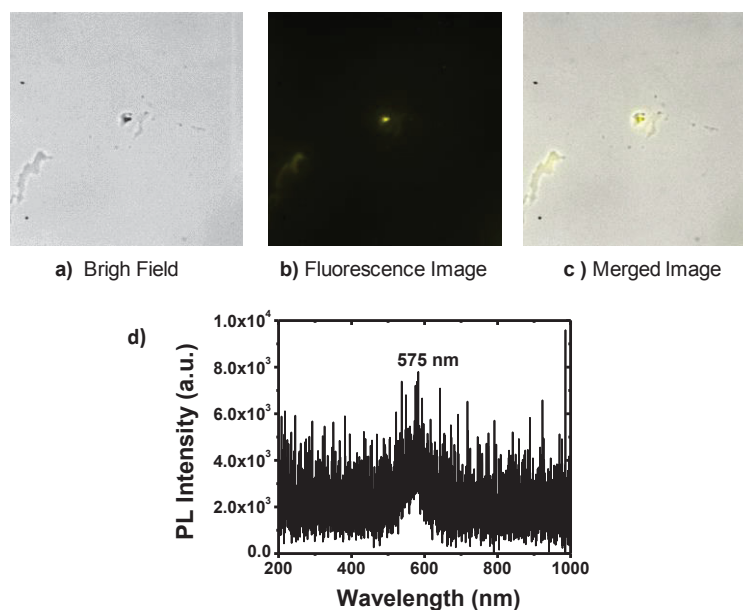
Figure 4.8. a) Bright field b) Fluorescence (Hg lamp excitation) and c) merged images of drop-casted CdTe nanoalloys. Images are obtained from confocal microscope d) PL spectrum of the related sample. Spectrum is obtained by fiber spectrometer from the center of the image. 40x objective is used. The integration time of the fiber spectrometer is 10 s.

Since the emission spectrum was obtained with TOPO coated $Zn_xCd_{1-x}S_ySe_{1-y}$ nanoalloys by the fiber spectrometer successfully, the same study with different nanoparticles was repeated to test whether or not similar results could be obtained. Water-dispersible TGA capped CdTe and ZnCdTe nanoparticles coated with a drop casting technique. However the results did not show expected PL spectrum as TOPO capped $Zn_xCd_{1-x}S_ySe_{1-y}$ nanocrystals. The results for CdTe are shown in Figure 4.8. The emission peak of the CdTe nanoparticles from the center of the image, has very low signal-to-noise ratio at 575 nm. In contrast to $Zn_xCd_{1-x}S_ySe_{1-y}$ nanoalloys, the integration time of the fiber spectrometer is much higher (100ms for $Zn_xCd_{1-x}S_ySe_{1-y}$ nanoalloys and 10s for CdTe nanoparticles). Nevertheless, the signal-to-noise ratio is still significantly lower than the TOPO capped $Zn_xCd_{1-x}S_ySe_{1-y}$ nanoalloys. The same situation is also observed with the ZnCdTe nanoalloys which are shown in Figure 4.9.

The reason of high signal-to-noise ratios in emission spectra for $Zn_xCd_{1-x}S_ySe_{1-y}$ nanoalloys by comparing with CdTe and ZnCdTe nanoparticles could be explained by photoluminescence quantum efficiencies. Since $Zn_xCd_{1-x}S_ySe_{1-y}$ quaternary nanoalloys have relatively high PL emission quantum efficiencies, it is expected to observe PL emission from fiber spectrometer, easily. Another reason could be the fast photobleaching processes of TGA capped CdTe and ZnCdTe nanoparticles during the

Hg lamp excitation. Since the 10 second integration time was not suitable for the microscopic measurements and kinetic studies planned within the scope of this study, the following studies were carried out entirely with $Zn_xCd_{1-x}S_ySe_{1-y}$ core and $Zn_xCd_{1-x}S_ySe_{1-y}$/ZnCdS core/shell nanoalloys.

a) Brigh Field   b) Fluorescence Image   c) Merged Image
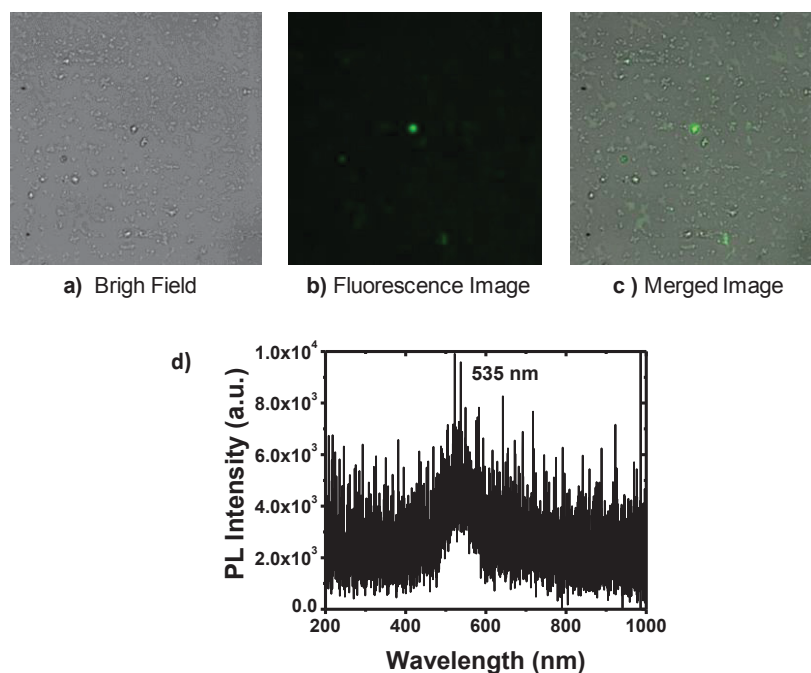
Figure 4.9. a) Bright field b) Fluorescence (Hg lamp excitation) and c) merged images of drop-casted ZnCdTe nanoalloys. Images are obtained from confocal microscope d) PL spectrum of the related sample. Spectrum is obtained by fiber spectrometer from the center of the image. 40x objective is used. The integration time of the fiber spectrometer is 10 s.

4.6. Investigation of The Photobleaching of Nanoparticles by Fiber Spectrometer

The quaternary alloy nanoparticles synthesized in our laboratory exhibit long-term colloidal stability at room temperature and atmospheric conditions (oxygenated environment) for years. In other words, there is neither agglomeration and/or precipitation in the nanoparticle solution, and no change in optical properties is observed. Durability is even in the order of year, in case of environmentally protected conditions (oxygen-free, thermally stable around room temperature or less, and dark places) from light and temperature factors in nitrogen or argon atmospheres. Before the

microspectroscopic studies started, the photostability of the nanoalloys was measured on a fluorescence spectrometer with a Xe lamp excitation. As shown in Figure 4.10 there are no quenching or photobleaching in neither solution phase nor the film phase samples. The excitation light source is set to 365 nm and bandwidths of the spectrometer for both excitation and emission are 5.0 nm. The wavelength of the collected light was selected to be 531 nm and 536 nm for the solution and film phases, respectively, considering the spectra given in Figure 4.4.
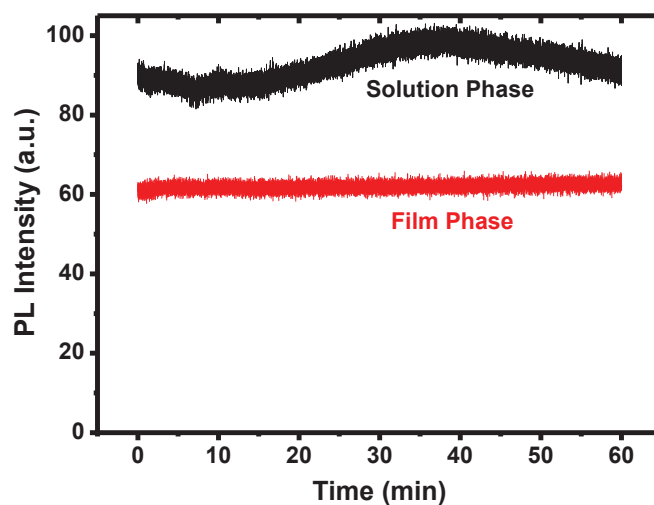
Figure 4.10. Photostability measurements of $Zn_{0.2}Cd_{0.8}S_{0.6}Se_{0.4}$ nanoalloys both in the solution and the film phase. The excitation wavelength is 365 nm. The emission wavelength is 531 nm and 536 nm for the solution and film phase, respectively. Observation time is 60 min for each study.

When alloy nanoparticles are coated onto glass substrates, the films are quite thick and not homogeneous. Since this is not desired, the spin coating technique is used to coat the QDs. First, the glass substrate was cleaned with distilled in water, then in acetone and finally in isopropanol in an ultrasonic bath. $Zn_{0.2}Cd_{0.8}S_{0.6}Se_{0.4}$ nanocrystals coated by spin coating at 5000 rpm for 1 minute. QDs without any purification process were used for the photobleaching studies. The average concentration of the nanoparticles in the reaction medium was 0.125 g / mL. The coated and dried substrates are placed on a different carrier glass substrate for the microscopic analysis. Images and μPL emission spectra were taken with the help of confocal microphotoluminescence set-up. (Figure 4.11).
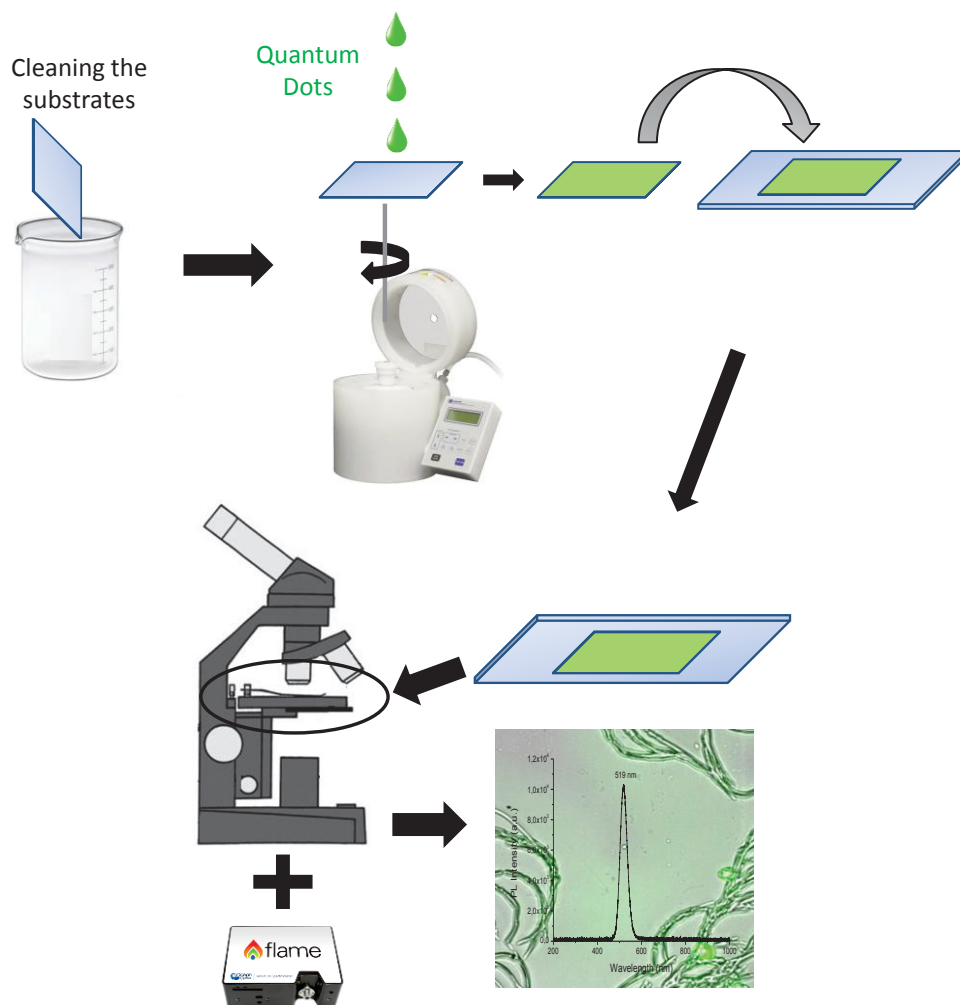
Figure 4.11. Schematic representation of coating the quantum dots on glass substrates and their microPL measurements

When the power of the excitation light is increased, the intensity of emitted light also increases linearly. The emission spectra shown in Figure 4.12 show the relation of PL intensity and the power of the incident light for the ZnCdSSe/ZnCdS core/shell nanoparticles having two different shell layer thicknesses. 365 nm light with various powers ranging from 2 μW to 68 μW is used to excite the samples. The graphs attached to the right side of the emission spectra show a linear relationship between the intensity of emission and the power of the excitation light source. The nanoparticles used here belong to the nanocrystals with shell/core initial cation ratios = 2 and 4, respectively, named core/shell - 3 and - 4 (Table 3.2). It was observed that the emission intensity is higher in samples with larger shell layer thickness. However, it is not easy to conclude a certain result without determining film thicknesses and reanalysis of the same QDs.
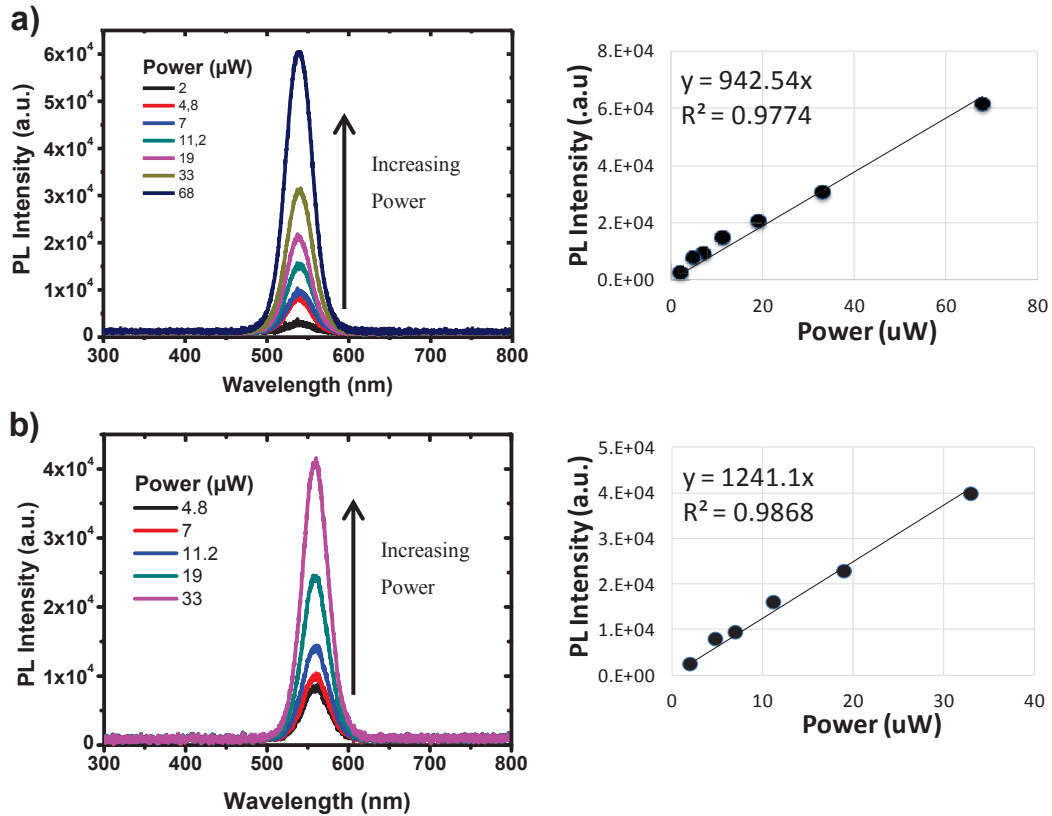
Figure 4.12. PL intensity of nanoparticles with respect to the power of the light source. The shell thickness of the samples in (b) is higher than (a). In order to prevent the saturation of the spectrometer, the integration time is arranged individually.

Although no photobleaching is observed for the alloy nanoparticles in the fluorescence spectrometer, it is observed that the PL intensity decreases with time under the continuous excitation of 11-68 mW with Hg lamp in the confocal microscope. This is a typical photobleaching or photoquenching process and this is related to the number of photons fall on the sample used to excite the nanoalloys. It was also determined that the collected emission spectra were shifted to the blue region of 5-6 nm (high energy region of the spectrum)

Alloy $Zn_xCd_{1-x}S_ySe_{1-y}$ nanoparticles which were coated on glass substrates were continuously excited with 68 μW and 365 nm excitation light up to 25 seconds while microphotoluminescence spectra were continuously recorded with the fiber spectrometer at the exposure time of 1st, 7th, 15th and 25th seconds. The photobleaching time was calculated by plotting the μPL emission intensity at 536 nm with respect to the exposure time.
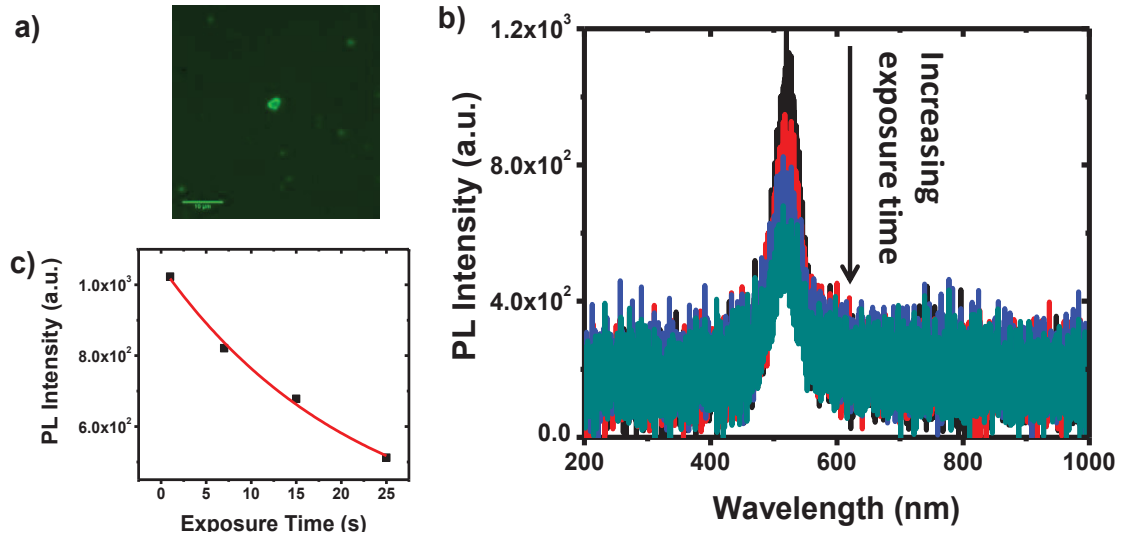
Figure 4.13. a) Confocal microscope image of spin-coated $Zn_{0.2}Cd_{0.8}S_{0.6}Se_{0.4}$ nanoalloys in which Hg lamp is used as excitation light source. QDs are taken from the reaction medium. b) PL spectra from the center of the image in (a) by fiber spectrometer at different exposure times. b) The kinetic decay of photobleaching of the QDs with respect to the exposure time. 100x objective is used for the imaging. The scale bar is 10μm. The integration time is 100 ms and the maximum exposure time is 25s. Power of the excitation light source is 68μW

We may analyse time dependent photobleaching behavior of the quaternary $Zn_xCd_{1-x}S_ySe_{1-y}$ nanoalloys using their decay kinetics according to the change in the photoluminescence intensity obtained from microphotoluminescence spectra: (Lakowicz, 2006). Equation 4.3 represents the single exponential decay for the general photobleaching reaction.

$$I(t) = I_0 \exp(-\frac{t}{\tau}) \qquad (4.3)$$

In this equation I_0 is the photoluminescence intensity at time 0 (initially – before the exposure of the excitation light), and the τ is the decay time. However in our case, since a kind of photobleaching reaction occurs, it is better to call it as "photobleaching time". The inverse of the photobleaching time gives the "photobleaching rate constant, k_p"

$$\tau = \frac{1}{k_p} \qquad (4.4)$$

The photobleaching time can be calculated and convenient to fit the data to single exponential decay model.

According to the data in Figure 4.13, the photobleaching time is calculated as 21.7 seconds. If we consider the µPL photoemission spectra, it was observed that the emission intensity decreases visually within 25 seconds, which confirms the result obtained from the equation given above. The photobleaching rate constant is also calculated as 0.046 s^{-1}. The above equations and the calculations are used to calculate the quaternary $Zn_xCd_{1-x}S_ySe_{1-y}$ nanoalloy photobleaching parameters in the following sections.

In Figure 4.14 similar study is done with $Zn_{0.2}Cd_{0.8}S_{0.6}Se_{0.4}$ nanoalloys without purification and spin coated on a microscopic cover glass (0.17 mm of thickness). According to the kinetic equations, the rate constant is calculated as 0.051 s^{-1}. Calculated photobleaching time is 19.7 s. The only difference from the study shown in Figure 4.13 is the exposure time (25 vs 37 seconds) of the incident light. The difference between the rate constants and photobleaching times are negligible (less than 10%).
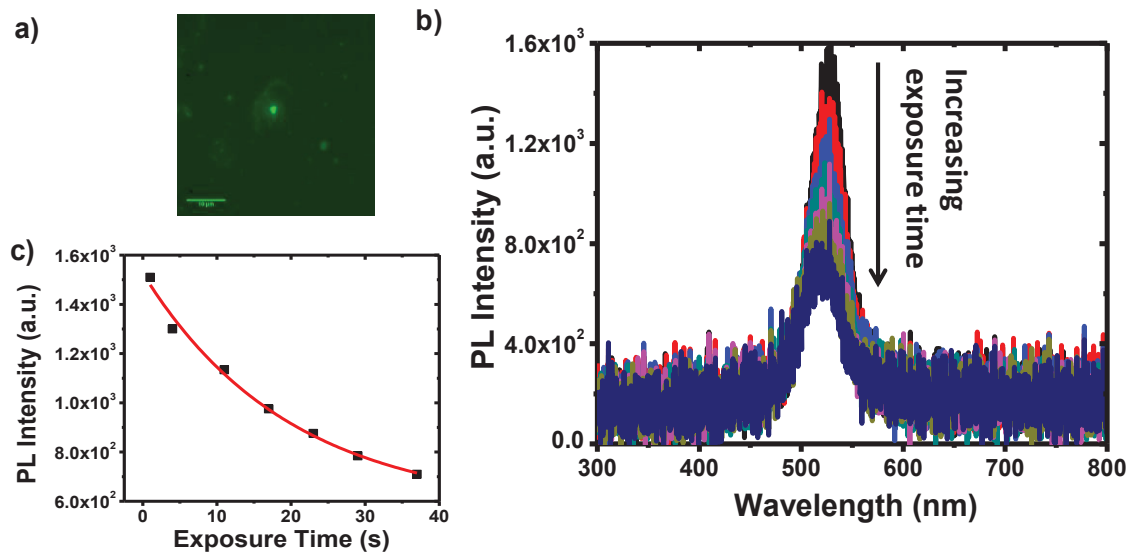
Figure 4.14. a) Confocal microscope image of spin-coated $Zn_{0.2}Cd_{0.8}S_{0.6}Se_{0.4}$ nanoalloys in which Hg lamp is used as excitation light source. QDs are taken from the reaction medium. b) PL spectra from the center of the image in (a) by fiber spectrometer at different exposure times. b) kinetic decay of photobleaching of the QDs with respect to the exposure time. 100x objective is used for the imaging. The scale bar is 10µm. The integration time is 100 ms and the maximum exposure time is 37s. Power of the excitation light source is 68µW
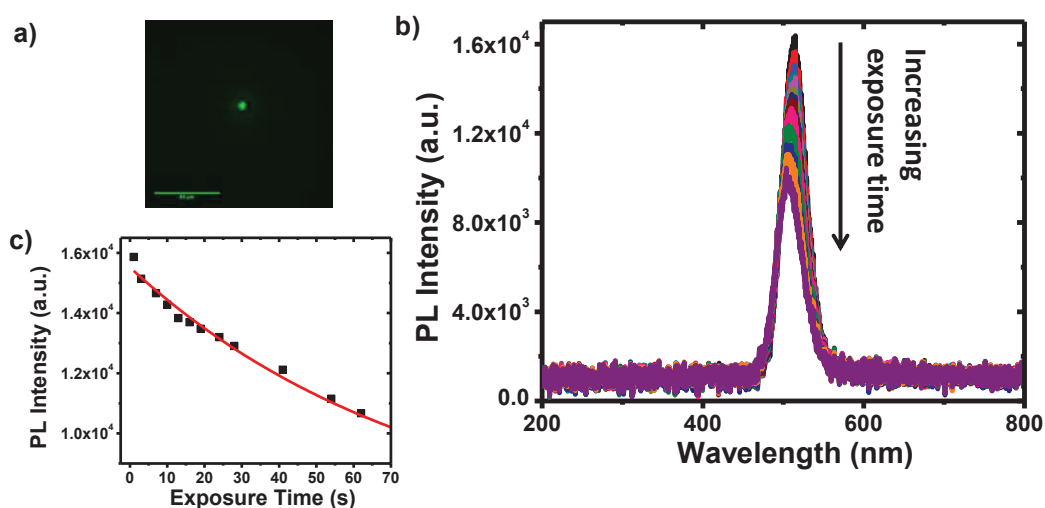
Figure 4.15. a) Confocal microscope image of spin-coated and puried $Zn_{0.2}Cd_{0.8}S_{0.6}Se_{0.4}$ nanoalloys in which Hg lamp is used as excitation light source. b) PL spectra from the center of the image in (a) by fiber spectrometer at different exposure times. c) The kinetic decay of photobleaching of the QDs with respect to the exposure time. 40x objective is used for the imaging. The scale bar is 50μm. The integration time is 1 s and the maximum exposure time is 80 s. Power of the excitation light source is 68μW.

Since the previous alloy nanocrystal films are prepared from unpurified/reaction medium QDs, the films include excess/unreacted organic ligands (trioctyl phosphine oxide-TOPO or oleic acid-OA). In order to understand the effect of organic ligands in photobleaching processes, nanoparticles are purified by centrifugation technique. Purified nanoparticles were redispersed in toluene. The final concentration is 0.01 mg/mL. QDs are coated at 5000 rpm for 1 minute. Figure 4.15 and Figure 4.16 show the results of μPL measurements obtained from these films. In both experiments, the same QD is used with the same experimental procedure. In these examples, the integration time of the spectrometer was set at 1s, as a result the PL intensities are higher than the previous examples in which integration time was shorter. The photobleaching rate constants obtained from Figure 4.15 and Figure 4.16 are 0.013 s^{-1} and 0.010 s^{-1}, respectively. The photobleaching times were calculated as 78.5 s and 98.6 s. In comparison with the unpurified QDs, the rate of the photobleaching is about 4 times slower in the purified nanoalloys. These results indicate that presence of unreacted organic ligands increases photobleaching during the excitation. When the unreacted

organic ligands were removed from the medium, photobleaching was still observed in the alloy nanoparticles. In the discussion part (Title as "4.7. Discussion on Microspectroscopic Studies of ZnCdSSe Nanocrystals"), the mechanisms of photobleaching reactions like chemical interactions between excitons and environmental factors: photochemistry will be examined.
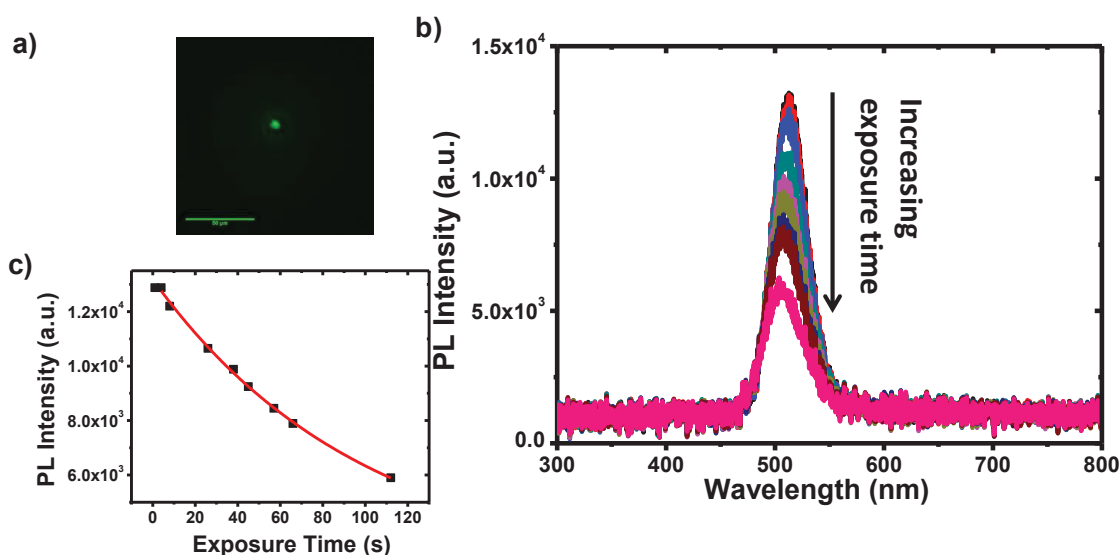
Figure 4.16. a) Confocal microscope image of spin-coated pure $Zn_{0.2}Cd_{0.8}S_{0.6}Se_{0.4}$ nanoalloys in which Hg lamp is used as excitation light source. b) PL spectra from the center of the image in (a) by fiber spectrometer at different exposure times. c) The kinetic decay of photobleaching of the QDs with respect to the exposure time. 40x objective is used for the imaging. The scale bar is 50μm. The integration time is 1 s and the maximum exposure time is 112s. Power of the excitation light source is 68μW

It is understood from the data in Figure 4.17 and Figure 4.18 that the photobleaching coefficient and the photobleaching time are directly related to the exposure time. In Figure 4.17, samples $Zn_{0.2}Cd_{0.8}S_{0.6}Se_{0.4}$ coated at 5000 rpm are prepared. Figure 4.17b shows the emission intensities are related to the exposure times. The relationship is plotted in Figure 4.17c. The exponential slope of the decay is quite different then previous decays. Since the single exponential decay fit still gives better results (χ^2 values is closer to 1) the same equations are used to fit and to obtain the rate constant and photobleaching time values. It is estimated that the rate constant is 7.8×10^{-3} s^{-1} and the photobleaching time is 127.6 s.
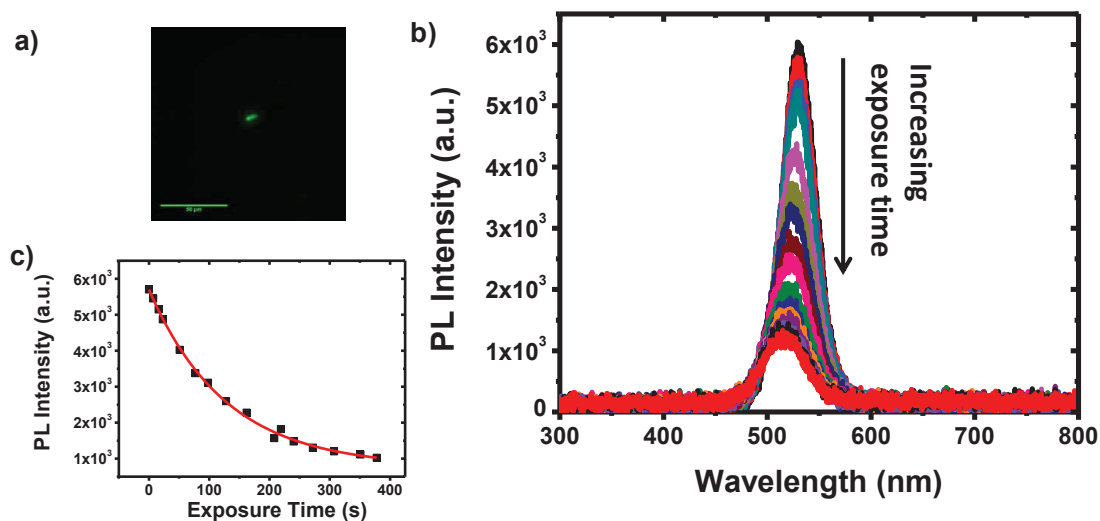
Figure 4.17. a) Confocal microscope image of spin-coated pure $Zn_{0.2}Cd_{0.8}S_{0.6}Se_{0.4}$ nanoalloys in which Hg lamp is used as excitation light source. QDs are coated at 5000 rpm for 1 minutes b) PL spectra from the center of the image in (a) by fiber spectrometer at different exposure times. c) The kinetic decay of photobleaching of the QDs with respect to the exposure time. 40x objective is used for the imaging. The scale bar is 50μm. The integration time is 100 ms and the maximum exposure time is 438 s. Power of the excitation light source is 68μW

The experiments were repeated by increasing the integration time from 100 ms to 1s. Although the integration time is not expected to affect the microspectroscopic analysis, it needs to be proven. All the other experimental parameters were kept constant, the only difference was the integration time which is set as 1 s rather than 100 ms. As shown in Figure 4.18, shows the PL spectra and the kinetic decay of photobleaching of QDs with respect to exposure time for the given QD in the image. The rate constant of this process is measured as 6.8×10^{-3} s^{-1} and the photobleaching time is 148 s.

As is known, the film thicknesses are inversely proportional with the rotation time per second of the spin coater. Up to now, relatively high rpm values (5000 rpm) was used in order to arrange as less number of nanoparticle is present in the "spot" (high rpm values will cause the separation of all the nanoparticles from each other). The same microspectroscopic measurements were performed again at 2000 rpm, 3500 rpm and 5000 rpm for the examination of the effect of rotation speed on the photobleaching rate constant and time. The exposure time is increased up to 600 seconds. Figure 4.19 and

Figure 4.20 show the microspectroscopic studies of $Zn_{0.2}Cd_{0.8}S_{0.6}Se_{0.4}$ nanoalloys coated at 3500 rpm and 2000 rpm, respectively. Since the exposure time is extended to the longer time ranges in regards of previous examples, the difference in slope is more pronounced. The decay is not single exponential anymore. It means that there would be two or more photobleaching processes and related rate constants and times. The photobleaching constants for the sample coated at 3500 rpm (Figure 4.19) are calculated: 0.026 s^{-1} and 5.9×10^{-3} s^{-1} for fast and slow photobleaching processes (early exposure times in the decay and after 200 seconds), respectively. Photobleaching times are 39 s and 170 s, for the same order. On the other hand, the sample coated with 2000 rpm (Figure 4.20), showed single exponential decay as seen in previous examples (coating with 5000 rpm). The photobleaching rate constant is calculated as 8.9×10^{-3} s^{-1} and the photobleaching time is 112 s. These results show that the photobleaching times and rate constants vary with the thickness of the films (which is the result of different rotations speeds in spin coater). It can be considered that the film thicknesses will change the total number of nanoalloys in the unit area. In this case, it can be assumed that the photobleaching constants will vary with the number of nanoparticles.
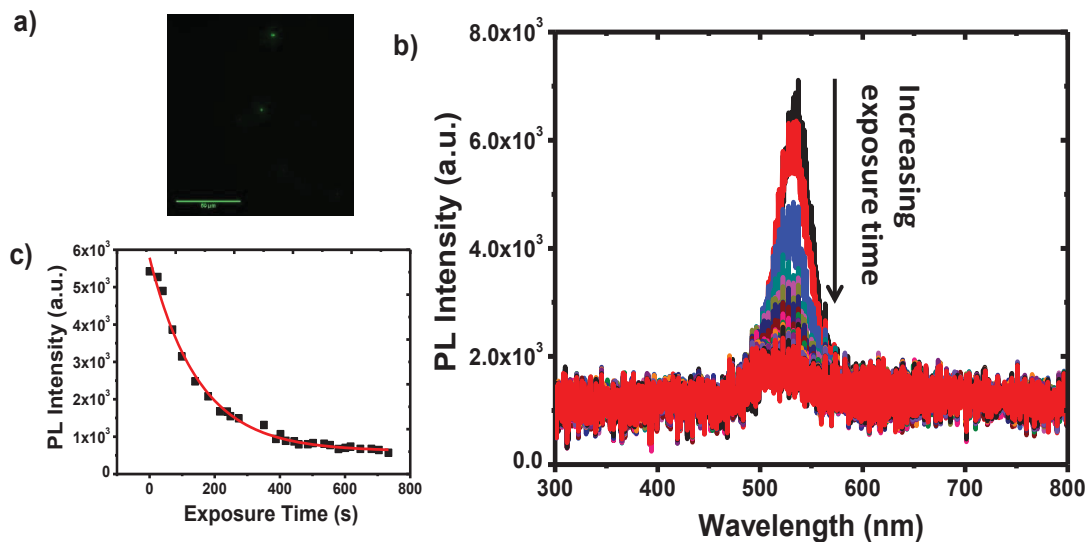
Figure 4.18. a) Confocal microscope image of spin-coated pure $Zn_{0.2}Cd_{0.8}S_{0.6}Se_{0.4}$ nanoalloys in which Hg lamp is used as excitation light source. QDs are coated at 5000 rpm for 1 minutes b) PL spectra from the center of the image in (a) by fiber spectrometer at different exposure times. c) The kinetic decay of photobleaching of the QDs with respect to the exposure time. 40x objective is used for the imaging. The scale bar is 50μm. The integration time is 100 ms and the maximum exposure time is 733 s. Power of the excitation light source is 68μW
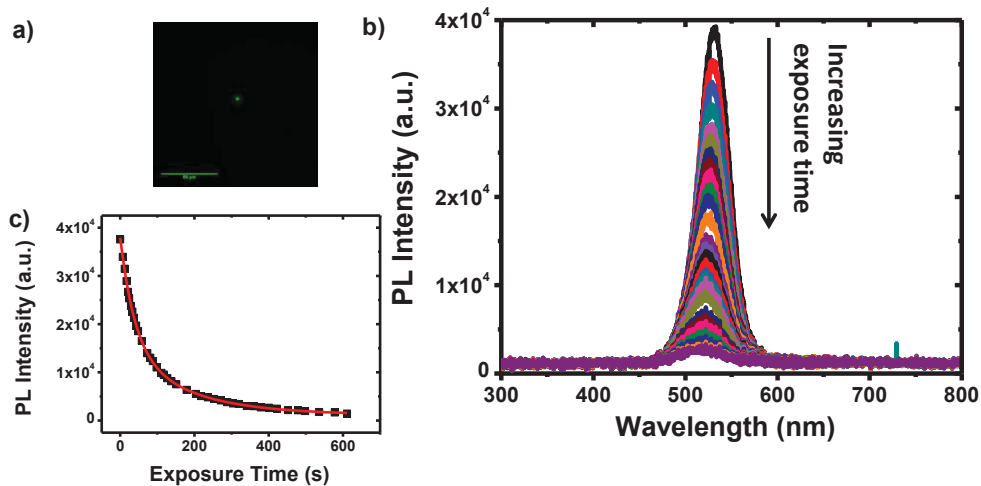
Figure 4.19. a) Confocal microscope image of spin-coated pure $Zn_{0.2}Cd_{0.8}S_{0.6}Se_{0.4}$ nanoalloys in which Hg lamp is used as excitation light source. QDs are coated at 3500 rpm for 1 minutes b) PL spectra from the center of the image in (a) by fiber spectrometer at different exposure times. c) The kinetic decay of photobleaching of the QDs with respect to the exposure time. 40x objective is used for the imaging. The scale bar is 50μm. The integration time is 1 s and the maximum exposure time is 611 s. Power of the excitation light source is 68μW
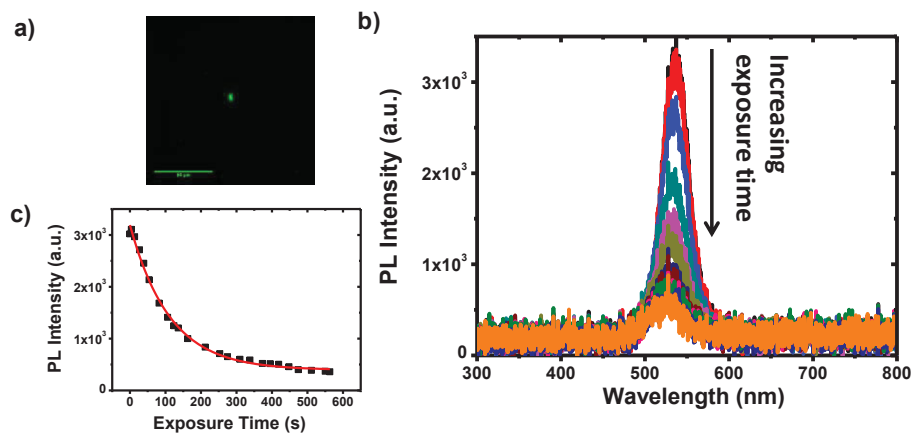

Figure 4.20. a) Confocal microscope image of spin-coated pure $Zn_{0.2}Cd_{0.8}S_{0.6}Se_{0.4}$ nanoalloys in which Hg lamp is used as excitation light source. QDs are coated at 2000 rpm for 1 minutes b) PL spectra from the center of the image in (a) by fiber spectrometer at different exposure times. c) The kinetic decay of photobleaching of the QDs with respect to the exposure time. 40x objective is used for the imaging. The scale bar is 50μm. The integration time is 1 s and the maximum exposure time is 595 s. Power of the excitation light source is 68μW
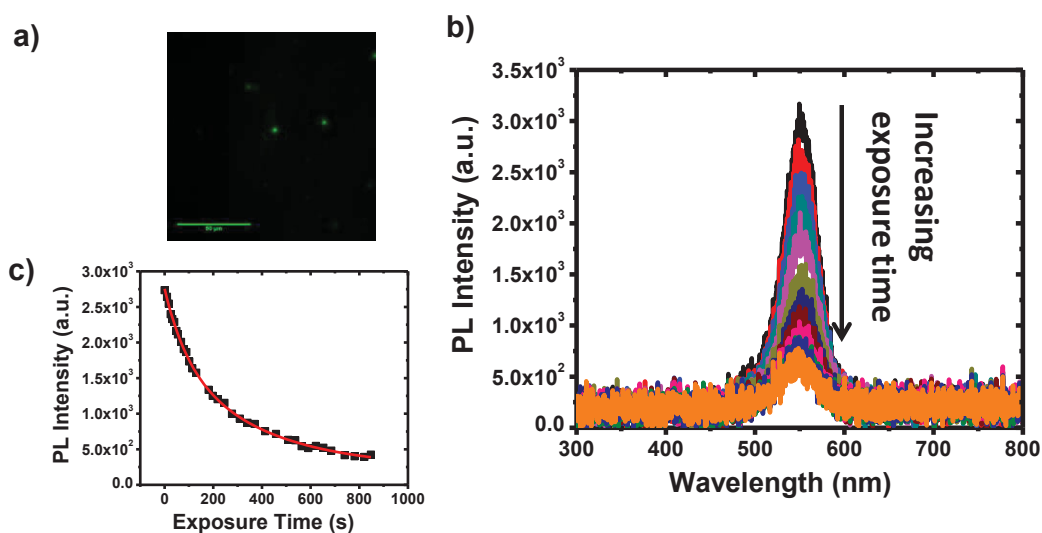
Figure 4.21. a) Confocal microscope image of spin-coated pure ZnCdSSe / ZnCdS (Core/shell-4) nanoalloys in which Hg lamp is used as excitation light source. QDs are coated at 5000 rpm for 1 minutes (Shell/Core initial mole ratios is 4) b) PL spectra from the center of the image in (a) by fiber spectrometer at different exposure times. c) The kinetic decay of photobleaching of the QDs with respect to the exposure time. 40x objective is used for the imaging. The scale bar is 50μm. The integration time is 100 ms and the maximum exposure time is 821 s. Power of the excitation light source is 68μW

In order to investigate the effect of the inorganic shell on the surface of alloy nanoparticles in terms of the photobleaching, core/shell nanoalloys are also studied. Nanoalloy samples named Core / shell-3 and Core / shell-4 are used for this study. The detailed information about these nanoalloys is given in Table 3.2 The results of microspectroscopic studies of these samples are shown Figure 4.21, Figure 4.22 and Figure 4.23.

In Figure 4.21, microspectroscopic emission spectra and photobleaching decays of the "core / shell-4" sample are given. In this study, the exposure time is extended to approximately 15 minutes and the integration time is set to 100 ms. Biexponential decay curve is obtained. The photobleaching constants are measured as 0.011 s^{-1} and 2.7 x 10^{-3} s^{-1}. The photobleaching time values are 93 s and 370 s. In Figure 4.22, the integration time is increased to 1.0 s for the same sample. The photobleaching rate constant was measured as 8.0x10^{-3} s^{-1} and 1.5x10^{-3} s^{-1}. The photobleaching times are estimated as 126 s and 667 s, respectively. It is also observed that the final peak position in the emission spectra is shifted to blue region according to the initial value for 5nm.
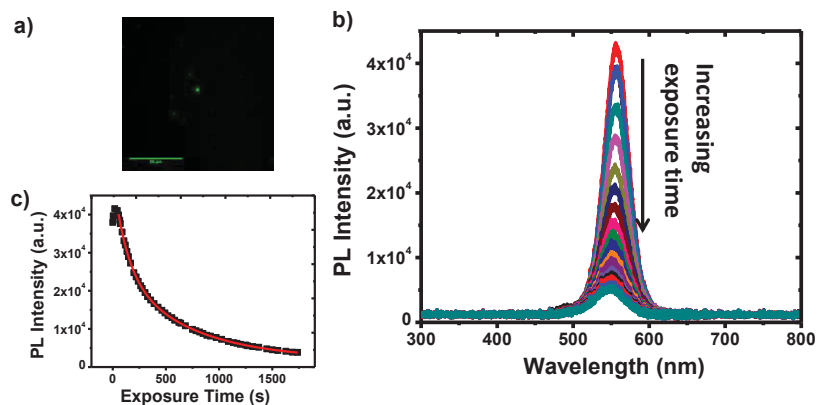
Figure 4.22. a) Confocal microscope image of spin-coated pure ZnCdSSe / ZnCdS (Core/shell-4) nanoalloys in which Hg lamp is used as excitation light source. QDs are coated at 5000 rpm for 1 minutes (Shell/Core initial mole ratios is 4) b) PL spectra from the center of the image in (a) by fiber spectrometer at different exposure times. c) The kinetic decay of photobleaching of the QDs with respect to the exposure time. 40x objective is used for the imaging. The scale bar is 50μm. The integration time is 1 s and the maximum exposure time is 1738 s. Power of the excitation light source is 68μW
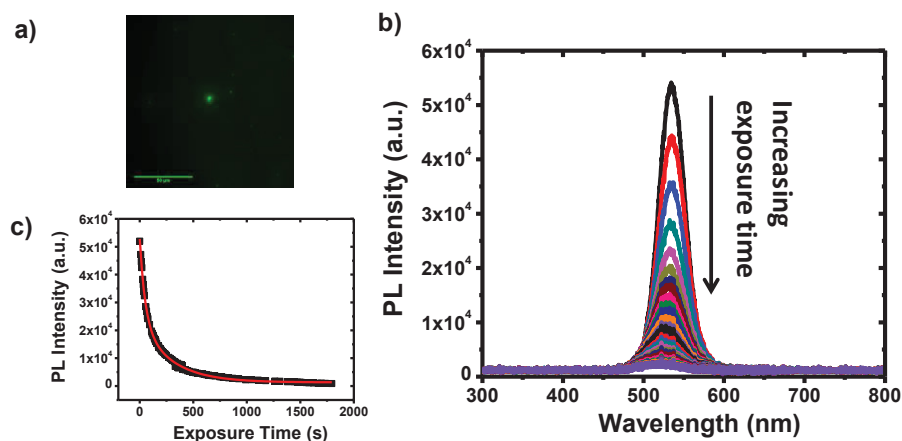

Figure 4.23. a) Confocal microscope image of spin-coated pure ZnCdSSe / ZnCdS (Core/shell-3) nanoalloys in which Hg lamp is used as excitation light source. QDs are coated at 5000 rpm for 1 minutes (Shell/Core initial mole ratios is 2) b) PL spectra from the center of the image in (a) by fiber spectrometer at different exposure times. c) The kinetic decay of photobleaching of the QDs with respect to the exposure time. 40x objective is used for the imaging. The scale bar is 50μm. The integration time is 1s and the maximum exposure time is 1794 s. Power of the excitation light source is 68μW

As can be seen, in ZnCdSSe/ZnCdS core/shell alloy nanoparticles also have two different photobleaching rate constants. Figure 4.23 indicates a study of the core/shell-4 structure which has a thicker shell layer than core/shell-3. As a result the PL peak max is in the higher wavelenghts as expected (The details are given under the title "3.4.2. Optical and Structural Characterization of Core / Shell - $Zn_xCd_{1-x}S_ySe_{1-y}/Zn_xCd_{1-x}S$ - Quaternary Nanocrystals"). The photobleaching constant is 0.020 s^{-1} and 3.5×10^{-3} s^{-1}, and the photobleaching times are 51 s and 289 s, respectively. The rate constants are closer to the ones for the core nanoalloys. It can be seen from Figure 3.13 that the photophysical parameters such as the FWHM and the photoluminescence quantum efficiencies are better in core/shell-3 structure than core/shell-4 structure. As in solution phase, core/shell-3 nanoalloys gave better results in the film phase, too.
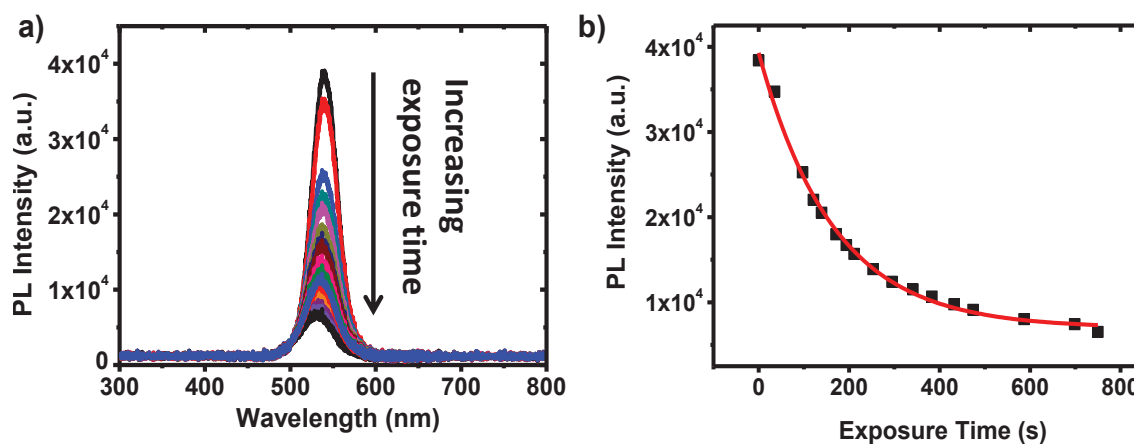
Figure 4.24. a) PL spectrum obtained by fiber spectrometer of spin-coated pure ZnCdSSe/ZnCdS core/shell nanoalloys (initial shell/core mole ratio = 2)(Core/Shell-3) b)decay of the PL intensity with respect to the exposure time. QDs are coated at 5000 rpm. Integration time is 1 s. Maximum exposure time is 750 s. Power of the excitation light source is 33μW

So far in this study, the power of the excitation light is always set to 68μW which is the highest power available. From the linear relationship of the source power and PL intensity, we examined the photobleaching decay of core/shell nanoalloys. In this case, the nanoalloys are excited with the same Hg lamp but lower power is used. The analysis of nanoparticles with a shell layer thickness of up to 2 (roughly 2), called core/shell – 3, are done with 33 μW power of excitation source. Photobleaching curves of nanoparticles excited with 33μW are shown in Figure 4.24. As can be seen, the excitation power was reduced by half, and photobleaching decay curved yielded similar

results with the power of 68 µW. The calculated photobleaching time is 165 s and the rate constant is 6.1×10^{-3} s^{-1}.
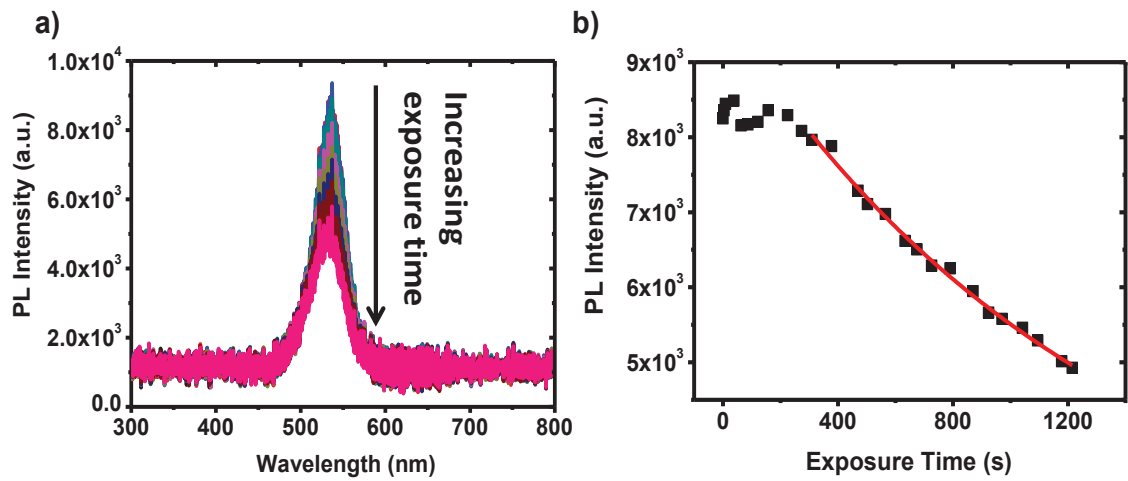
Figure 4.25. a) PL spectrum obtained by fiber spectrometer of spin coated pure ZnCdSSe/ZnCdS core/shell nanoalloys (initial shell/core mole ratio = 2)(Core/Shell-3) b)decay of the PL intensity with respecto to exposure time. QDs are coated at 5000 rpm. Integration time is 1 s. Maximum exposure time is 1215 s. Power of the excitation light source is 11µW
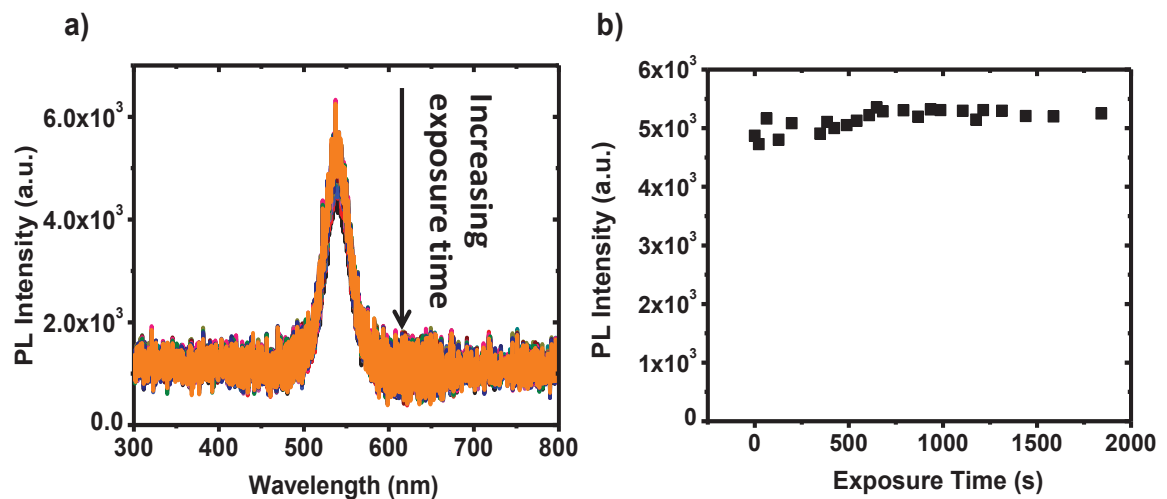
Figure 4.26. a) PL spectrum obtained by fiber spectrometer of spin coated pure ZnCdSSe/ZnCdS core/shell nanoalloys (initial shell/core mole ratio = 2)(Core/Shell-3) b)decay of the PL intensity with respecto to exposure time. QDs are coated at 5000 rpm. Integration time is 1s. Maximum exposure time is 1800 s. Power of the excitation light source is 2µW

When the excitation light intensity is further reduced to 11 µW, the photobleaching tendency changes considerably. The nanoparticles, which have always been quenched in the first 200s, have not shown any photobleaching effect for the first 200 seconds. However, after 200 second exposure time, the photobleaching starts. The rate constant is found as 7.7×10^{-4} s^{-1} and the photobleaching time is 1306 s. Figure 4.25 indicates the PL spectra and photobleaching decays for the study.

As the power of excitation light decreases, the observed photobleaching in nanoparticles also decreases. The results in Figure 4.26 were obtained when the excitation power was reduced to the lowest possible intensity of 2µW. Despite the prolongation of the exposure time to half an hour, no photobleaching effect was observed.

Figure 4.27 shows the relationship between power of the excitation light and the photobleaching rate constant. As expected, increasing the power of the excitation light results increase in the photobleaching rate constant. Since we did not observe any photobleaching at 2µW, we assume the photobleaching rate constant as zero in the graph. Table 4.1 summaries the all measurement parameters and the calculated photobleaching rate constant and time.
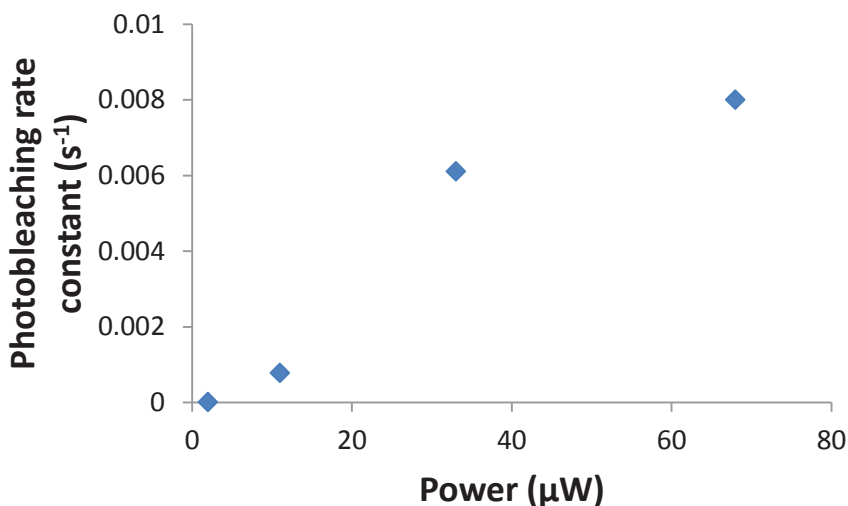
Figure 4.27. Power of the excitation light with respecto to photobleaching rate constant. Since there is no photobleaching at power 2 µW, it is assumed as zero. Increasing the power of excitation results increase in the photobleaching rate constant.

Table 4.1. A summary of photoblocking studies. Alloy composition, shape numbers, photobase, velocity constants and photobleaching time are given in relation to the shapes. In addition, the measurement times and excitation times as well as the specimens are indicated.

Alloy Composition	Figure	Rotation speed (rpm)	Power of excitation light (μW)	Exposure time (second)	Integration time (second)	Photobleaching rate constant (s^{-1})	Photobleaching time (second)	Note
$Zn_{0.2}Cd_{0.8}S_{0.6}Se_{0.4}$	Figure 4.13	5000	68	25	0.1	0.046	21.Tem	Reaction medium
$Zn_{0.2}Cd_{0.8}S_{0.6}Se_{0.4}$	Figure 4.14	5000	68	37	0.1	0.051	19.Tem	Reaction medium
$Zn_{0.2}Cd_{0.8}S_{0.6}Se_{0.4}$	Figure 4.15	5000	68	80	1.0	0.013	79	Pure
$Zn_{0.2}Cd_{0.8}S_{0.6}Se_{0.4}$	Figure 4.16	5000	68	112	1.0	0.010	99	Pure
$Zn_{0.2}Cd_{0.8}S_{0.6}Se_{0.4}$	Figure 4.17	5000	68	600	0.1	7.8×10^{-3}	128	Pure
$Zn_{0.2}Cd_{0.8}S_{0.6}Se_{0.4}$	Figure 4.18	5000	68	600	1.0	6.8×10^{-3}	148	Pure
$Zn_{0.2}Cd_{0.8}S_{0.6}Se_{0.4}$	Figure 4.19	3500	68	600	1.0	0.026 5.9×10^{-3}	39 170	Pure

(cont. on next page)

Table 4.1. (cont.)

Alloy Composition	Figure	Rotation speed (rpm)	Power of excitation light (μW)	Exposure time (second)	Integration time (second)	Photobleaching rate constant (s^{-1})	Photobleaching time (second)	Note
$Zn_{0.2}Cd_{0.8}S_{0.6}Se_{0.4}$	Figure 4.20	2000	68	600	1.0	8.9×10^{-3}	112	Pure
$Zn_{0.2}Cd_{0.8}S_{0.6}Se_{0.4}/ZnCdS$ (Ç/K – 3)	Figure 4.21	5000	68	900	0.1	0.011 2.7×10^{-3}	93 370	Pure
$Zn_{0.2}Cd_{0.8}S_{0.6}Se_{0.4}/ZnCdS$ (Ç/K – 3)	Figure 4.22	5000	68	1800	1.0	8.0×10^{-3} 1.5×10^{-3}	125 667	Pure
$Zn_{0.2}Cd_{0.8}S_{0.6}Se_{0.4}/ZnCdS$ (Ç/K – 4)	Figure 4.23	5000	68	1800	1.0	0.020 3.5×10^{-3}	51 289	Pure
$Zn_{0.2}Cd_{0.8}S_{0.6}Se_{0.4}/ZnCdS$ (Ç/K – 3)	Figure 4.24	5000	33	750	1.0	6.1×10^{-3}	165	Pure
$Zn_{0.2}Cd_{0.8}S_{0.6}Se_{0.4}/ZnCdS$ (Ç/K – 3)	Figure 4.25	5000	11	1200	1.0	7.7×10^{-4}	1306	Pure
$Zn_{0.2}Cd_{0.8}S_{0.6}Se_{0.4}/ZnCdS$ (Ç/K – 3)	Figure 4.26	5000	2	1245	1.0	-----	-----	Pure

4.7. Discussion on Microspectroscopic Studies of ZnCdSSe Nanocrystals

Photobleaching studies on ZnCdSSe nanocrystals are done in order to calculate photobleaching time and rate constants by fiber spectroscopy integrated confocal microscopy. Effect of film preparation technique, purification of QDs, the power of the incident light were investigated individually. The results showed that, regardless of the rotation time per second of the spin coater, spin coating technique is better than drop casting in terms of separating QDs from each other. The existence of excess organic ligands in the film medium, reduce the bleaching time significantly. Purification procedures reduced the photobleaching rate constants by 4 times. Power of the excitation light is proportional with the emission intensity that collected from the samples by fiber spectrometer. When the power of excitation light is varied between 11 – 68 μW, the photobleaching constants were significantly changed. The PL emission maximum was blue shifted about 5 nm. At 11 μW power intensity, the first 200 seconds photobleaching is not observed but then a linear decrease in PL intensity is obtained. If 2 μW power intensity is used, there is no photobleaching observed, QDs have spectrally stable.

In general, photobleaching depends on the excitation power intensity, exposure time and molecular environmental factors. The most important molecular environmental factor is the existence of the oxygen molecule. Although the ground state of oxygen is a triplet ($^3O_2$), the excited form is singlet ($^1O_2$). Singlet oxygen has very long half-life (it depends on the solvent, however the smallest one is about 20 microseconds) (Hurst et al., 1982) and initiates the photochemical processes. Since nanoparticles can act as a molecule, they can react with singlet oxygen and photobleaching can be initiated. Power of excitation light, exposure time and other molecular environmental factors affect the photobleaching time and rate constant.

Photobleaching and blue shifting in alloy nanocrystals may stem from the photochemical reaction occurred between singlet oxygen and nanoparticles. We tried to carry out our measurements under argon or nitrogen atmosphere, however, our facilities did not allow to isolate the experimental set up sufficiently. That is the reason, we propose that photobleaching/photooxidation occurs mainly because of the molecular

environmental factors – singlet oxygen. Figure 4.28 explains the molecular mechanism of the photobleaching and blue shifting in electromagnetic spectrum as we proposed.
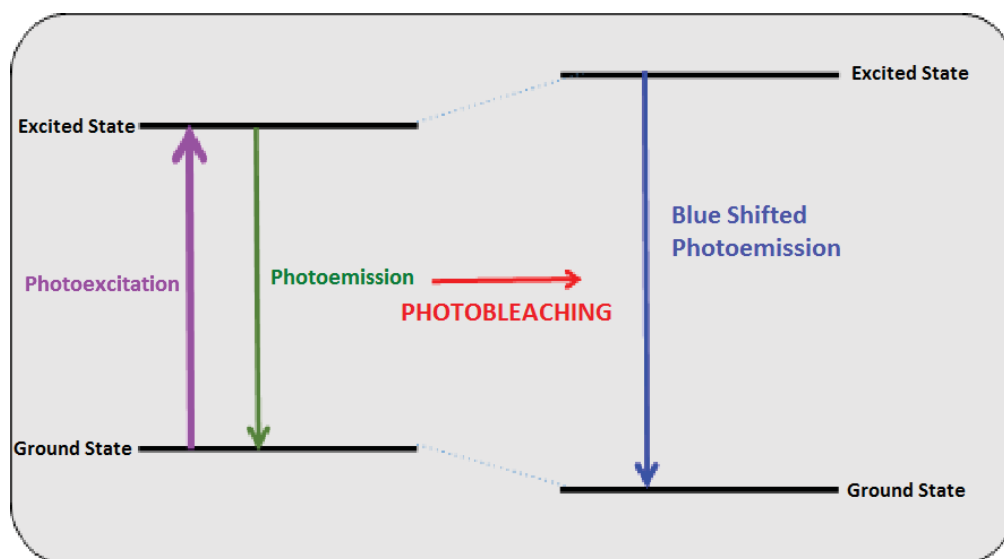
Figure 4.28. Molecular mechanism of the photobleaching and blue-shifted emission in ZnCdSSe nanoalloys. After photobleaching process, a decrease in the particle size or change in the alloy composition results increase in the band gap and blue shifting in the electromagnetic spectrum

Photodegradation occurs in the nanoalloys which are exposed to the photoexcitation and then photobleaching. Zinc and cadmium oxide-based compounds can be formed and as a result, the alloy composition may change. Since cadmium is more electronegative than zinc, cadmium atoms will be more reactive to singlet oxygen. That is the reason total alloy composition will be more zinc-rich than non-photobleached nanocrystals. Increasing zinc amount in the alloy compositions results in a blue-shift in the electromagnetic spectrum. Another reason for the blue shift may be explained by decrease in particle size. If zinc and cadmium atoms leave the nanocrystal structure because of the photobleaching process, the particle size will decrease and the band gap of the nanocrystals will increase (decreasing the number of atoms, results increase in the band gap of the nanocrystals). As a result of this increase in the band gap, blue shift in the electromagnetic spectrum is expected. These hypothesis needs to be proved by XPS and solid-state NMR techniques. Since we do not have these facilities yet, verification of these hypothesis has to be postponed to the near future Nevertheless, literature studies support our ideas. Several studies on CdSe/ZnS binary core/shell nanocrystals shows blue shifting because of photobleaching processes (M. et

al., 2002; Pechstedt et al., 2010; Hoyer et al., 2011). van Sark and Peschstedt designed controlled experiments in the air (nitrogen+oxygen), nitrogen, argon atmosphere and humidity to show that blue shift occurs because of the photooxidation reactions (M. et al., 2002; Pechstedt et al., 2010). Peschstedt used XPS to prove that $CdSeO_x$ and ZnO are formed in photooxidation reactions (Pechstedt et al., 2010). In Hoyer's study, SeO_2 compounds are formed in photooxidation reactions and as a result, the particle size of CdSe nanoparticles decreases. Since the excitons are confined in narrower volume, energy band gap increases and blue shifting in the electromagnetic spectrum is observed (Hoyer et al., 2011).

Van Sark et al. reported that, CdSe/ZnS nanoparticles with 5 nm particle size show 29 nm blue shift after 60 seconds and $20kW/cm^2$ power photoexcitation. The same nanocrystals with 3 – 5 nm particle size showed 15 nm blue shift after 5000 second $3W/cm^2$ power photoexcitation (Cordero et al., 2000). The same study reported that small nanoparticles undergo photodegradation faster than larger ones. Oxygen molecules can diffuse the exciton regions of smaller QDs and photobleaching can be initiated easily.

In our study, we observed 6 nm blue shift after 1800 second and $0.1\ W/cm^2$ (68 μW) power photoexcitation. According to the solution phase SAXS measurements given in chapter 3, difference in the PL spectra is more significant than the particle size This knowledge let us to propose that 6 nm blue shift should result in small differences in particle size

As we mentioned in the previous chapter, in our studies shell layer is approximately 0.8 – 1.0 nm which cause 30 nm red shift in optical spectra. If we assume that the relationship between the particle size and shift is linear, after 1800 seconds and $0.1\ W/cm^2$ photoexcitation process we expect 0.2 nm decrease in particle size of blue shifted nanocrystals. On the other hand, if the particle size is kept constant (3.2 – 3.4 nm) and alloy composition is changed as $0.05 < x,y < 0.90$, increase in Zn content resulted in 30 nm blue shift in optical spectra. It means that, if the particle size does not decrease by photobleaching process, the zinc content in the alloy composition should increase to observe blue shifting. In this process, we propose that cadmium and oxygen react to form new oxide compounds. If the unpurified samples are used in this experiment, excess/unreacted zinc atoms can diffuse to the nanocrystal structure, too. Sulfur or selenium can also react with oxygen, however, these hypothesises should be proved by XPS, solid-state NMR or HRTEM analysis.

Figure 4.29. . Schematic representation of blue shifting. After photoexcitation, photobleaching occurs and the particle size decreases. As a result, microspectroscopic photoemissions (based on excitons) shifts to blue region. The deductions for the particle size are based on SAXS measurements. The gray region on the QD represents the oxidized region after photobleaching. The organic ligands on the surface of the nanoalloys are oleic acid or TOPO, but in order to reduce the complexity of the image, there are not shown

As we mentioned in the previous chapter, in our studies shell layer is approximately 0.8 – 1.0 nm which cause 30 nm red shift in optical spectra. If we assume that the relationship between the particle size and shift is linear, after 1800 seconds and 0.1 W/cm^2 photoexcitation process we expect 0.2 nm decrease in particle size of blue shifted nanocrystals. On the other hand, if the particle size is kept constant (3.2 – 3.4 nm) and alloy composition is changed as $0.05 < x,y < 0.90$, increase in Zn content resulted in 30 nm blue shift in optical spectra. It means that, if the particle size does not decrease by photobleaching process, the zinc content in the alloy composition should increase to observe blue shifting. In this process, we propose that cadmium and oxygen react to form new oxide compounds. If the unpurified samples are used in this experiment, excess/unreacted zinc atoms can diffuse to the nanocrystal structure, too.

Sulfur or selenium can also react with oxygen, however, these hypothesises should be proved by XPS, solid-state NMR or HRTEM analysis.

.

4.8. Conclusion

In this chapter, we have focussed on the photoexcitation and photobleaching processes of $Zn_xCd_{1-x}S_ySe_{1-y}$ quaternary nanoalloy nanocrystals which are synthesized in our laboratory. The measurements are carried out by fiber spectrometer integrated confocal microscope. Several parameters were investigated and as a result, we found out that if the power of the excitation is enough ($\geq$ 11 μW) nanoalloys undergoes photobleaching – the intensity of μPL spectrum decreases and blueing. Monoexponential decay curves are obtained for the intensity of μPL spectrum with respect to the exposure time. According to the related decay rate equations, photobleaching time and rate constants are determined.

CHAPTER 5

SCALE-UP SYNTHESIS OF QUANTUM DOTS

5.1. Introduction

Quantum dots (QDs) are exhibiting special optical properties by adjusting various particle size, shape and the alloy composition of the nanoparticles. In terms of these properties, they have gained a great attention in various areas in which using high-quality QDs is essential. High-quality QDs are required to have uniformity in particle size, shape, alloy composition and perfect crystal structure in order to obtain good optical properties for applications (Yin and Alivisatos, 2005). Futhermore, these applications also require scaled-up manufacturing (rate of kg/day) of QDs with the same quality and properties especially for the production on the industrial usage (Nightingale and de Mello, 2010). That is the reason, large-scale synthesis methods are needed to be improved in order to synthesize high-quality QDs at the rate of kg/day.

In the last decades, several studies are reported in terms of large-scale QD synthesis. Kang et al.synthesized $AgInS_2/ZnS$ core/shell nanocrystals in the presence of gelatin and TGA by using a commercial electric pressure cooker (may be considered as batch reactor). As a result, the multigram scale of water-soluble $AgInS_2/ZnS$ nanocrystals is produced with relatively lower costs (Kang et al., 2015). The same group also reported the synthesis of CISe and AISe cores and their corresponding core/shell nanoparticles in which the reaction yield was approximately 3 g per one batch and the cost of produced nanocrystals was reported as 2.2-2.5 \$/g (Kang et al., 2015).

Large-scale QD synthesis in flow reactors started in 2003 by Alivisatos and Bawendi group using CdSe nanocrystals (Chan et al., 2003; Yen et al., 2003). Alivisatos reported that green chemistry could be applied by using low cost and lesser amount of solvent, at 180-220 $^\circ$C reaction temperatures with a flow rate of 2 µL/minutes. On the other hand, Bawendi used 240 – 320°C reaction temperatures and 2-30 µL/minutes flow rates. They also investigated the number of particles, the particle size and the reaction yield with respect to reaction temperature and residence time. In order to increase the particle size to $6x10^{18}$ particle/L and to decrease the FWHM of PL spectra, supercritical

hexane is used in the reproducible synthesis of CdSe QDs (Marre et al., 2008). Core/shell CdSe/ZnS and CdS/ZnS nanocrystals were also synthesized at 140° C in a flow reactor with 9 mL/hour flow rates. However, in the shell addition part, the reaction temperature was increased to 280° C which is quite high (Yang et al., 2009). Moghaddam et al. synthesized CdSe QDs from selenium oxides in the flow reactor having 1 mm diameter stainless steel tubings. The reaction yield is reported as 167 mg CdSe in 87 minutes with particle size of 3-6 nm and 20-30% PL QE (Moghaddam et al., 2013).

Flow chemistry was also performed in multichannel flow reactors in order to synthesized various nanocrystals like CdSe, CdTe and their alloy CdSeTe nanocrystals at 175° C. 145 gram QD were produced in a reactor consisting of 5 channels in parallel with 1 mm PTFE tubings (Nightingale et al., 2013). Similarly, CdSe, CdS, ZnS and ZnSe core and CdSe/ZnS core/shell type nanocrystals were synthesized in a reactor with a 10 ml volume and running at a flow rate of 2.5 gram/hour. At the end of 2 hours, 5 grams of QD were produced and as an application white-QLED studies were performed (Yang and Tuan, 2014). Huang et al. also synthesized aqueous CdTe nanocrystals with a serious of experiments demonstrating high monodispersity and significantly narrow FWHM values (Huang et al., 2018). Among these are CuInSe (Kim et al., 2014), CdHgTe(Kershaw et al., 2017), ZnO(Zukas and Gupta, 2017) and Pb based nanocrystals (Zhang and Xia, 2014; Lignos et al., 2017) and InP nanocrystals (Baek et al., 2011; Kim et al., 2012; Ippen et al., 2015; Xie et al., 2015) synthesized in flow reactor.

Maeda group published an article in which they pointed out that the particle size and the quantum yield of the synthesized nanocrystals can vary with the reaction parameters like reaction temperature, reactant concentrations and initial mole ratios etc.. That is the reason, optimization has to be done and it is very important in order to scale up techniques for the nanocrystals. Considering the high-volume reactors (typically 500 Liters) especially for the industrial scale (which is approximately 1 kg/day), it would be very expensive in terms of solvent requirements. Almost 1 tone solvent would be necessary in order to synthesize 1 mg/ml QD solution (Zhang et al., 2012). In 2013, Mello group also emphasized the importance of flow reactors in terms of technical difficulties of batch reactors and scientific/technological difficulties in the production of kilogram/day scale (Nightingale and deMello, 2013). Literature studies are summarized in Table 5.1.

Table 5.1. Summary of the literature studies about the synthesis of Quantum Dots by flow reactor

QD	FWHM	QY %	Particle size	Product Yield	Flow Rate	Temperature	Reference
CdSe	28	--	2.44 nm, 2.52 nm, 2.64 nm, 2.69 nm	--	2 µL/min	180 - 210 °C	(Chan et al., 2003)
CdSe		28 – 51 %	1.5 2.7 nm	--	2 – 30 µL/min	180 – 320 °C	(Yen et al., 2003)
CdSe	41 – 49 nm (in squalana) 25 – 27 nm (in hexane)	--	4.5 nm (in squalana) 4 nm (in hexane)	--	--	210 – 270 °C	(Marre et al., 2008)
CdS/ZnS	25 – 33 nm	Blue: 41 % Cyan: 58 % Green: 70 % Yellow: 78 % Orange: 76 % Red: 61 %	4.4 nm (CdS – Blue) 2.4 nm (CdSe – Green) 3.4 nm – 4.0 nm (Core/Shell Orange – Red)	--	4.47 mL/h (core) 8.94 mL/h (Core/Shell)	285 °C (Nucleation) 260 °C (Growth) 140 - 160°C (Shell growth)	(Yang et al., 2009)

Table 5.1 (cont.)

QD	FWHM	QY %	Particle size	Product Yield	Flow Rate	Temperature	Reference
CdSe	30 nm	11 – 28 %	3 – 6 nm	167 mg/87 min	1.25 mL/min (4 nm partic5le size – 28 % QY)	240 – 260 °C	(Moghaddam et al., 2013)
CdTe CdSe CdSeTe	43 nm (CdTe) 4 nm (CdSe) 90 nm (CdSeTe)	--	≈ 2.5 nm	3.7 g CdTe 1.5 g CdSe 2.1 g CdSeTe 145 g/day CdTe	3 – 5 ml/min	Up to 300 °C	(Nightingale et al., 2013)
CdSe	32 nm	15 %	2.45 – 2.73 nm 2.9 nm (XRD) 3 nm (Abs)	5 g	2.5 g/h	200 – 270 °C	(Yang and Tuan, 2014)

5.2. High-Volume Reactor

5.2.1. Experimental Design
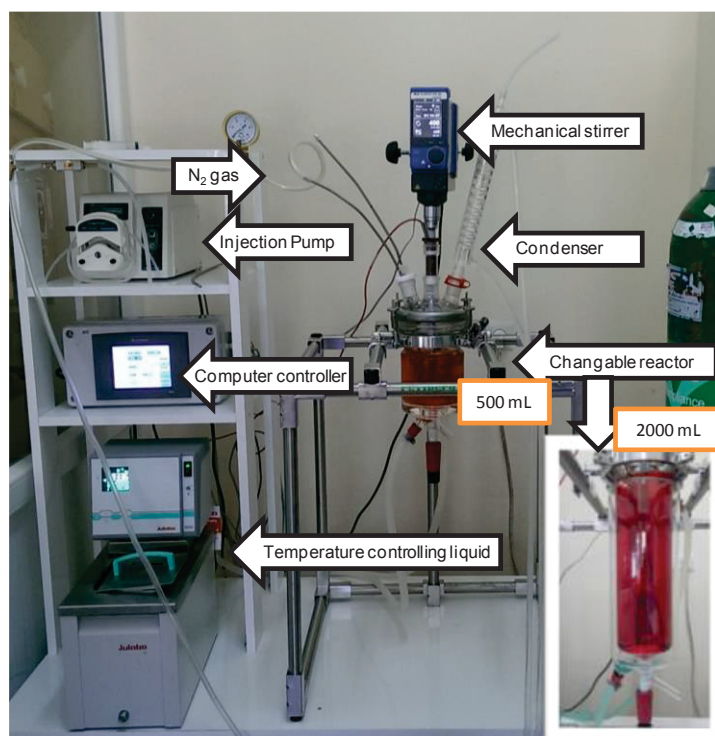
Figure 5.1. Computer controlled high volume reactor and its accessories. 2000 mL reaction vessel is also shown as inset image.

High volüme reactor was designed for the scale up synthesis of QDs in our laboratory. Reaction temprature controller, special glass cover for the reaction vessel were designed specifically according to our knowledge from batch system. The large volume batch reactor system was designed and constructed by using parts listed as follows: a mechanical stirrer (IKA Eurostar 60), reaction vessels (Lenz brand glass reaction vessels with a volume of 500 mL, 1000 mL, and 2000 mL), peristaltic injection pump, liquid (water, oil or antifreeze) tank for the reaction temperature control, and computer controller. The details about the each part are given in the following paragraphs.

The peristaltic pump ensures reproducible test conditions by adjusting injection and pumping speed, both during sample and reactant injection. Similarly, the IKA Eurostar 60 mechanical stirrer is much more effective than the magnetic stirrers used in

standard 100 or 250 mL glass reaction flasks and provides a homogeneous reaction medium with up to 1200 rotation per minute. There are 500 mL, 1000 mL, and 2000 mL Lenz brand glass reaction vessels. The entrances in the lower and upper parts of the reaction chambers, allow the inlet and outlet of the liquid to heat and fix the reaction temperature. Water could be used as a heating liquid for the reactions with a reaction temperature as low as $100\,^{\circ}$C, or oils with a high boiling point or antifreeze mixture for higher reaction temperatures. The Julabo SE temperature control unit recirculates the liquid in the reaction chamber by the thermostat/thermometer immersed in the reactor environment. The digitally readable temperature value on the unit's display is also adjusted by the computer-controlled microprocessor Ultrasonic V570 display. The microprocessor also controls the mixing speed of the mechanical mixer and the injection / pumping speed of the peristaltic pump device.
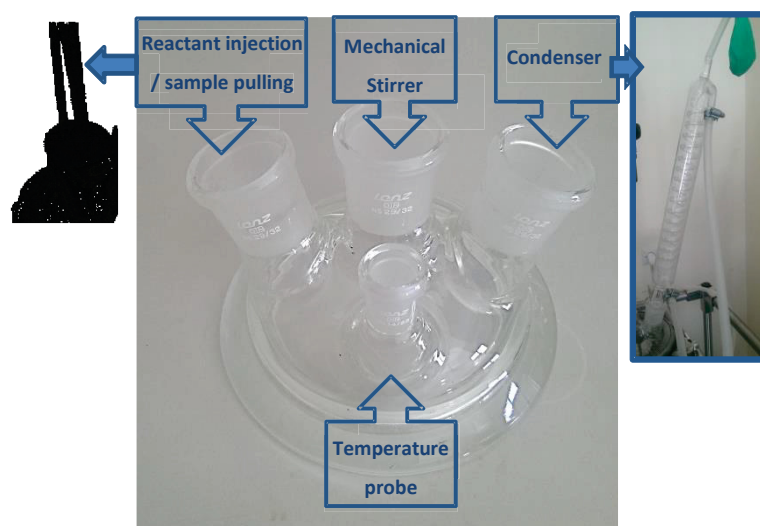
Figure 5.2. Specially designed glass cover for the reaction chamber. The insets are for, reactant insertion, sample extraction, gas inlet, mechanical mixer, temperature control probe inlet and condenser

The reaction chamber is mounted on a rigid mechanical accent so that it does not shake during mixing. The reaction chamber is placed on this accent and closed with a specially designed glass cover. The silicone ring added between the cap and the reaction chamber helps to provide a physicochemically closed system within the chamber. The special design cover of the glass reaction chambers is shown in Figure 5.2. Each entry on the glass reaction chamber cover is designed for a different purpose. The smallest inlet belongs to the probe which provides the inlet temperature control. The other inlets

are designed for the condenser, mechanical stirrer and sample injection and extraction. Argon or nitrogen gas atmosphere is also provided by the sample injection inlet. The long, curved/looped condenser shown in Figure 5.2 is conveniently selected to prevent the solvent evaporation from the medium at high temperatures. The balloon which is connected at the end is necessary for the protection of the closed system and also for controlling the gas outlet. The specially designed Teflon cover shown on the left side in has 3 holes on it. These holes are designed for sample extraction, reactant injection, and gas entry.

5.2.2. Test Experiments for The High-Volume Reactor

5.2.2.1. Synthesis of TGA Capped CdTe Nanocrystals

The large-volume reactor installed in our laboratory has been tested to synthesize CdTe nanocrystals in an aqueous medium using a one-pot aqueous synthesis approach. Water dispersible TGA coated CdTe nanoparticles were first produced in a 500 mL reaction vessel. The optical properties of the nanoparticles were compared with the nanoparticles synthesized in a 100 mL reaction volume in traditional 250 mL reaction flasks.

For the purpose of testing a computer controlled large volume reactor, thioglycolic acid (TGA) capped CdTe nanocrystals were synthesized. The reason for the choice of CdTe nanoparticle production in aqueous media is that it is easy to synthesize these nanoparticles, that the precursors are relatively cheaper, and the reaction temperature is relatively lower (100 ° C) than most of the quantum dot synthesis techniques. It is also relatively easy to control. The amount of chemicals required in the 500 mL reaction chamber is calculated according to the same initial mole ratios of the classical batch reaction flasks. 2.29 g of $CdCl_2$ as a Cd precursor was dissolved in 440 mL of ultrapure water and this mixture was stirred by the addition of 1.68 mL of TGA. The pH of the resulting cloudy solution was set to 11.0 by slowly adding 1 M NaOH solution. At this pH, it was observed that the cloudy solution became completely transparent. This solution was stirred at 80 °C under nitrogen or argon atmosphere at 400 rpm for 1 hour. NaHTe used as Te precursor was prepared by the reaction given in the equation 5.1.

$$4 \text{ NaBH}_4 \text{ (s)} + 2 \text{ Te (s)} + 7 \text{ H}_2\text{0 (l)} \rightarrow 2 \text{ NaHTe (aq)} + \text{Na}_2\text{B}_4\text{O}_7 \text{ (s)} + 14 \text{ H}_2 \text{ (g)} \quad (5.1)$$

As seen in the chemical equation above, Te powder (0.09 g) was reduced with NaBH$_4$ (0.06 g) and NaHTe (aq) was obtained. This reaction carried out in a nitrogen or argon atmosphere in 10 mL of ultrapure water, and was stirred at 60°C until the end of the hydrogen gas evolution (observed by eye as end of bubling). The reaction takes approximately 1 hour. All of the resulting NaHTe (aq) solution was rapidly added to the solution containing the cadmium – TGA mixture in the reactor vessel. At the same time, the reaction temperature is increased to 90°C. The nucleation of nanocrystals is followed by their growth. The optical properties and the particle size of the resulting nanoparticles were monitored by samples taken during certain periods of time along the reaction. When the nanoparticles reach the desired particle size / PL emission, the reaction is terminated by decreasing the reaction temperature. For this purpose, the circulation of water (or the other liquid used for the heating) in the heater chamber is stopped. The absorption and emission spectra of CdTe nanoparticles synthesized in a 500 mL reaction chamber of the high-volume reactor are given in Figure 5.3.
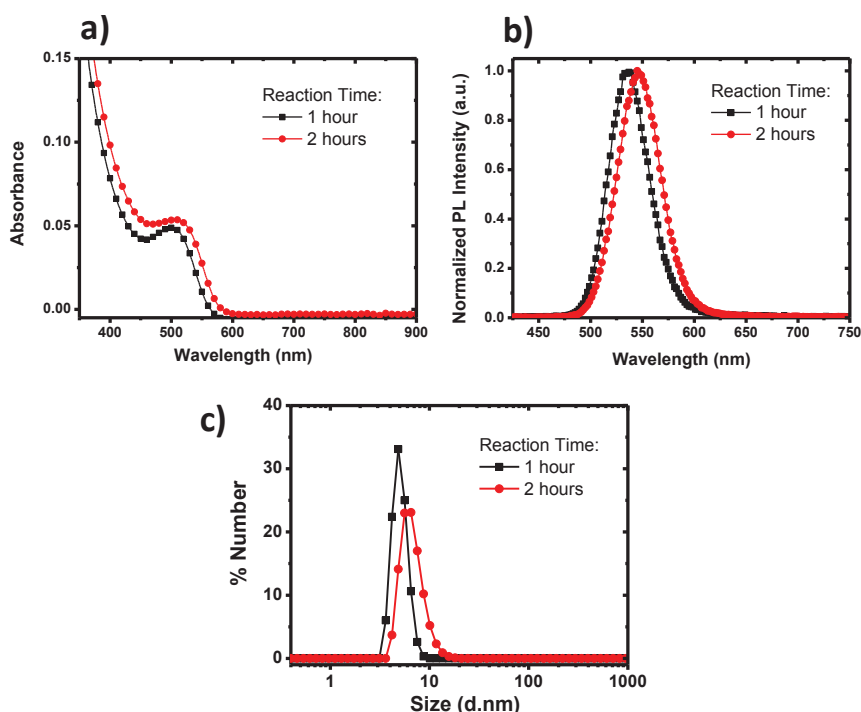
Figure 5.3. a) Absorption and b) emission spectrum of CdTe nanocrystals synthesized in a reactor with 500 mL reaction vessel. c) Particle size obtained by DLS measurements is given.

In binary structures, the optical properties can be solely adjusted by the particle size. As the particle size of the CdTe nanocrystals produced in the reactor increased, the absorption and emission spectra were shifted to the red region (high wavelength - low energy region). According to the spectrum given in Figure 5.3, the shift in the absorption wavelength of the nanoparticles is from 500 nm to 512 nm and for the emission wavelength, it is from 536 nm to 546 nm during the 2 hours reaction. The red-shift is related to the increase in the hydrodynamic diameters of the nanocrystals from 5.0 nm to 6.0 nm. As the nanoparticle grew, there was no change in the chemical composition of the CdTe (Since it is a binary QD, the change in the composition is also not expected). Spectral and particle size data of CdTe nanocrystals produced in a large volume reactor were compared with the characteristics of CdTe nanoparticles synthesized in a 110 mL volume in a 250 mL glass reaction flask in our laboratory.
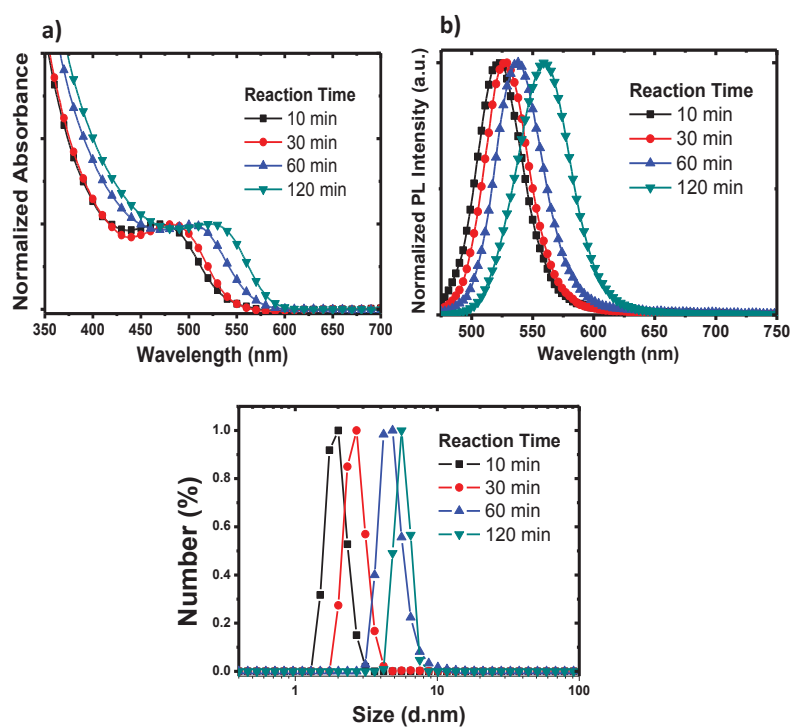
Figure 5.4. a) Absorption and b) Emission spectrum of CdTe nanocrystals synthesized in 250 mL reaction flask as classical batch synthesis.c)Particle sizes obtained by DLS measurements are given

Figure 5.4 shows spectroscopic data on CdTe nanoparticles synthesized using the same starting materials and initial molar ratios with a magnetic stirrer in round bottom glass-reaction flask. According to this data, the absorption wavelength of nanoparticles shifted from 470 nm to 523 nm in the 2 hours reaction time. Similarly, the

emission spectra shifted from 523 nm to 559 nm. Since the redshifts stem from the increase in the particle size, DLS measurements proved the particle size increase from 2.0 nm to 5.6 nm as expected. We concluded that the spectra and the characteristic wavelength values are comparable in two different batch system. As a result of the repeated experiments, it was determined that it is possible to produce nanoparticles in a controlled high-volume reactor. Calculations showed that 0.2 mg/mL reaction yield could be obtained in a typical CdTe synthesis. It means that approximately 100 mg of QD is obtained at 500 mL reaction. If the number of nanoparticles in 1 mL is considered to be roughly 10^{14}, approximately 10^{16} nanoparticles are obtained in a 500 mL reaction. The quantum yields of the synthesized CdTe nanoparticles were determined to be about 30%, as synthesized in the standard 100 mL reactor.
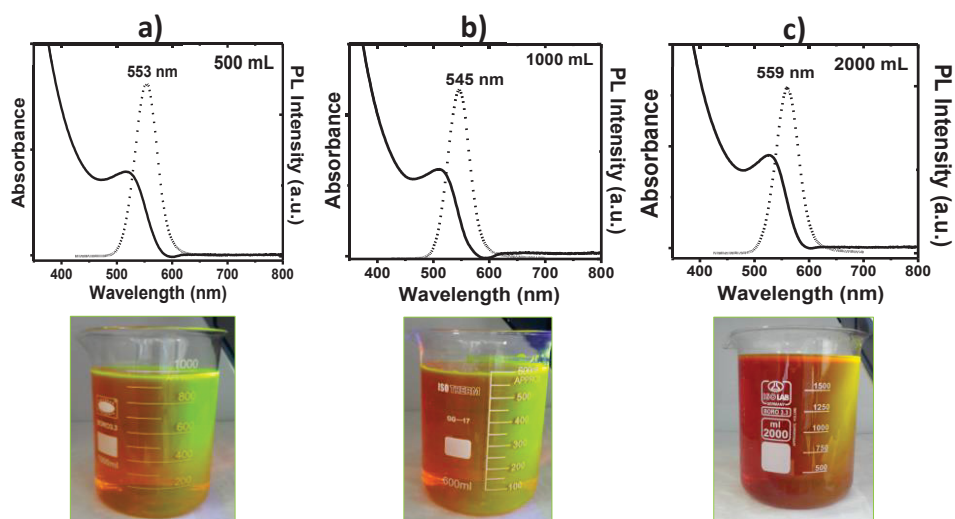
Figure 5.5. Absorption and emission spectrum of TGA capped CdTe nanocrystals which are synthesized in 500 ml, 1000 ml and 2000 ml reaction vessels of high volume reactor. Images belong to the corresponding spectrum

Figure 5.5 shows the absorption and emission spectra of TGA capped CdTe nanoparticles synthesized in a 500 mL, 1000 mL and 2000 mL reaction chamber of a computer controlled reactor. As expected, peak characteristics are similar for all reaction volumes. The irregular spectral shift between the absorption and emission wavelengths are due to the minor changes in the reaction times / the particle size. The PL half-widths (FWHM) of the nanoparticles ranged from 45 to 50 nm which are similar to a glass-250 ml reaction flask. Tests on different reaction volumes have resulted successfully that the spectral characteristics of nanoparticles are reproducible.

The narrow FWHM in the apparent absorption and the PL emission spectra indicates that the nanoparticles are optically in high quality. Figure 5.6 shows the images of nanoparticles synthesized in different volume reactors under daylight and UV-light (365 nm) excitation. CdTe nanoparticles synthesized in large volumes remain stable for as long as in CdTe nanoparticles synthesized under standard conditions and do not exhibit any agglomeration or change in optical properties.

Figure 5.6. Images of TGA capped CdTe nanocrystals which are synthesized in 500 ml, 1000 ml and 2000 ml reaction vessels of high volume reactor.

5.2.2.2. Synthesis of TGA Capped CdTe/CdS Nanoparticles

As in TGA capped CdTe nanoparticles, core/shell structures such as TGA capped CdTe/CdS nanocrystals were also synthesized in a computer controlled, high-volume reaction vessel reactor.
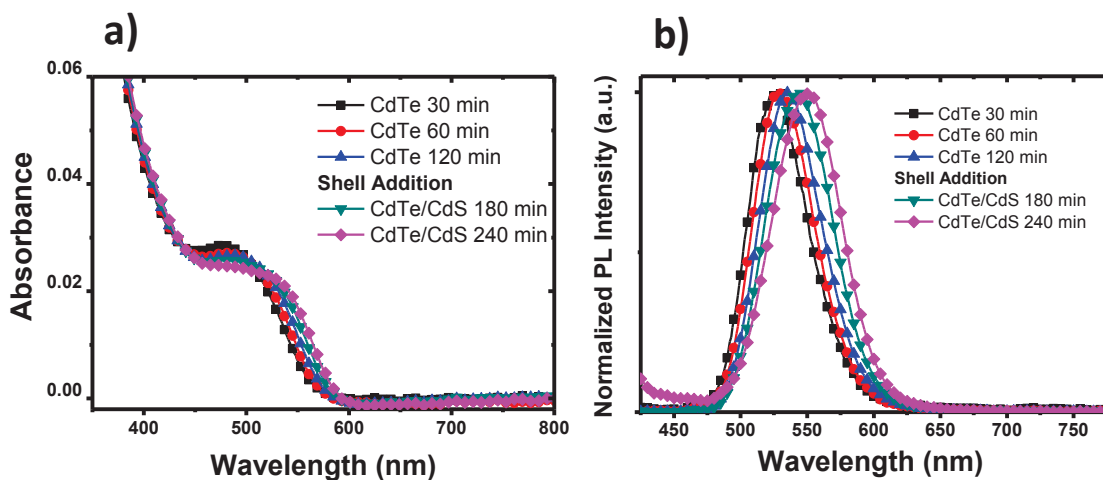
Figure 5.7.a) Absorption and b) PL emission spectra of CdTe/CdS nanocrystals which are synthesized in 500 ml reaction vessel of the high-volume reactor.

Core type CdTe nanocrystals were prepared as given in the previous section, and at 150th minutes of the reaction, thiourea and cadmium chloride were added as shell precursors to initiate shell formation. Due to the taken samples at certain time intervals, a red shift was observed in the electromagnetic spectrum, depending on the duration of the reaction and the addition of the amount of shell precursors. It has been shown that the nanocrystals produced have the same spectral properties as the nanocrystals synthesized in the glass-250 ml reaction flask. These results demonstrate that core/shell nanoparticles can also be synthesized in the reactor.

5.2.3. Synthesis of $Zn_xCd_{1-x}S_ySe_{1-y}$ Quaternary Alloy Colloidal Nanocrystals in The High-Volume Reactor

Synthesis of the large-scale alloy nanoparticles is relatively difficult in standard glass-250 ml reaction flasks in terms of several practical difficulties such as mixing speed, heating homogeneously and keeping the reaction temperature constant. On the other hand, 250 ml glass reaction flasks are suitable for the development of "the synthesis chemistry of the nanocrystals" as we included in previous chapters. In an attempt to produce large-scale QDs, all the optimized reaction parameters are kept the same except the reactor volume. It was aimed to set the production parameters (technology) in volumes of 500 mL, 1000 mL, and 2000 mL by leaving the concentrations of precursors constant. At the specification of production parameters, the optical properties of the nanocrystals like photoluminescence quantum yield, spectral wavelengths, and FWHM values are selected as optimization criteria to compare the reactor parameters in standard low volume and computer controlled high volume batch type reactors. The fact that the optical properties are highly sensitive (especially photoluminescence spectroscopy can detect an emission from a single molecule) makes it possible to determine the smallest structural changes occurred in the alloy nanoparticles during the synthesis or the production steps. These observations help to determine the variations that will occur in the reaction medium and thus optimization. The production results of the synthesis of quaternary alloy colloidal $Zn_xCd_{1-x}S_ySe_{1-y}$ nanocrystals in the computer controlled large-scale reactor which was designed, installed and tested with production of CdTe nanocrystals in our laboratory, are given below.
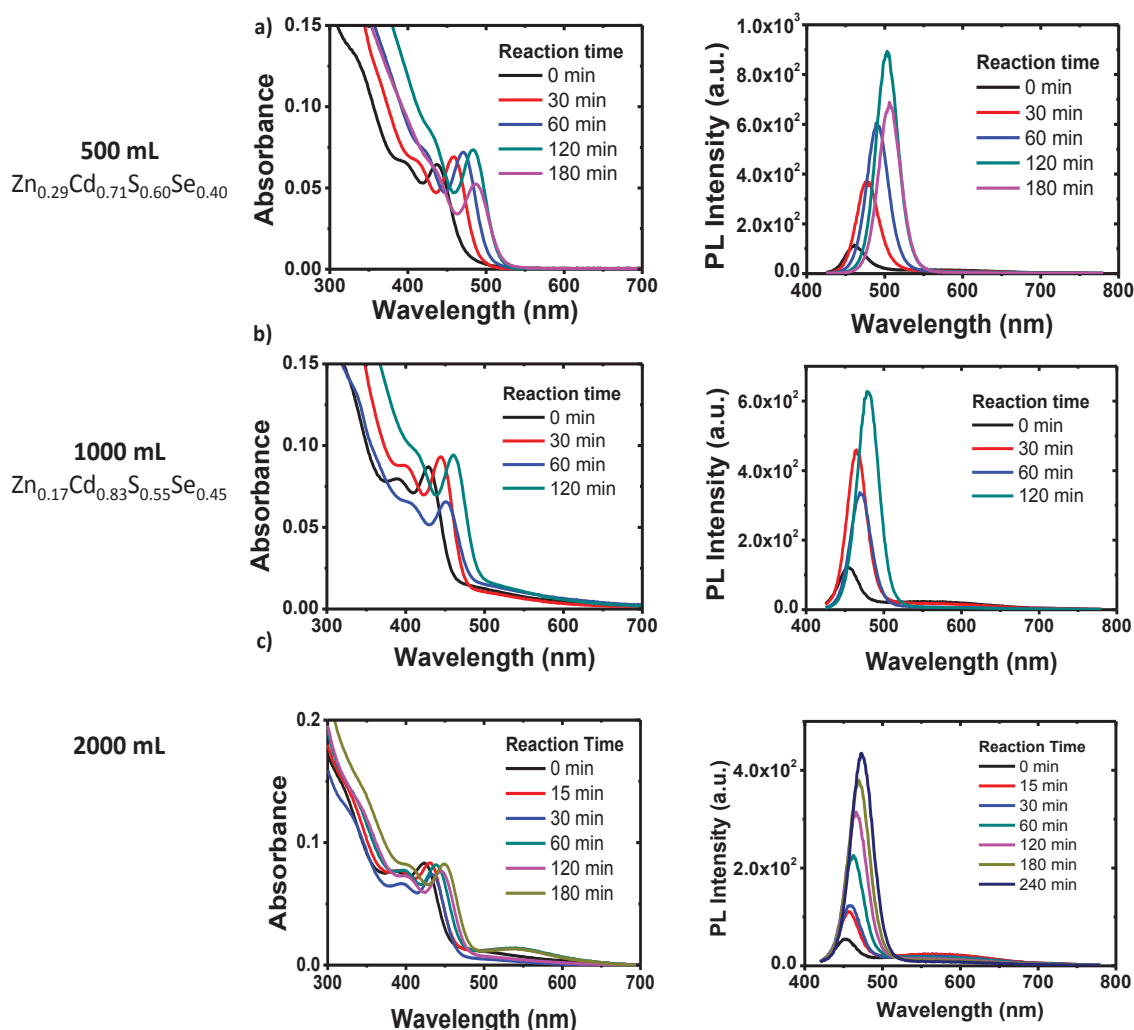
Figure 5.8. Absorption and PL emission of $Zn_xCd_{1-x}S_ySe_{1-y}$ nanocrystals in a) 500 ml, b) 1000 ml and c) 2000 ml reaction vessels of high-volume reactor. The excitation wavelength is 400 nm and the solvent is toluene. .the alloy compositions given in the left side of the image are obtained by SEM-EDS analysis.

Figure 5.8 shows the spectral results of $Zn_xCd_{1-x}S_ySe_{1-y}$ quaternary nanoalloys which were synthesized in different reaction volumes as 500 ml, 1000 ml and 2000 ml reaction vessels. The results show the similarities in peak positions and the characteristics as expected. As can be seen, during the 3 hours reaction, the absorption wavelength shifts from 437 nm to 487 nm and the photoluminescence wavelength shifts from 461 nm to 506 nm for the smallest volume, 500 ml. It was determined that the $Zn_xCd_{1-x}S_ySe_{1-y}$ alloy nanocrystals produced in the large-scale reactor reached a quantum yield of 54% at 120th minutes. During the reaction, the FWHM of the samples remained constant at 32-34 nm.

Table 5.2. Optical parameters like absorption and emission wavelengths, photoluminescence quantum efficiencies and FWHM values for $Zn_xCd_{1-x}S_ySe_{1-y}$ nanocrystals with respect to reaction volumes 100ml, 500 ml, 1000 ml and 2000 ml. The reaction in 100 ml carried out in standard 250 mL glass reaction flask

	Reaction Volume (mL)	Reaction time (minutes)	λ_{abs} (nm)	λ_{em} (nm)	PL QE (%)	FWHM (nm)
Standard 250 mL glass reaction flask	**100 mL**	10	420	453	3	30*
		30	434	460	5	31
		60	447	468	12	31
		90	451	472	16	32
		120	456	475	19	33
		180	461	482	25	34
		240	464	485	29	35
High Volume Reactor	**500 mL**	0	437	461	16	34
		30	457	476	40	34
		60	471	490	49	32
		120	483	503	54	33
		180	487	506	53	33
	1000 mL	0	429	454	11	30
		30	444	465	33	30
		60	451	471	32	30
		120	460	480	41	33
	2000 mL	0	423	453	10	34
		15	431	456	15	32
		30	434	460	17	31
		60	438	462	22	31
		120	445	466	29	32
		180	449	470	31	30
		240	453	473	---	35

* FWHM value for the 10th minute reaction time in 250ml glass reaction flask has trap states. The FWHM value is taken for the first intense emission peak.

Similarly, absorption and photoluminescence spectra of quaternary alloys in 1000 mL and 2000 mL reaction vessels are also given, respectively. The absorption wavelengths of synthesized alloy nanoparticles in the 1000 mL reaction chamber range from 429 nm to 460 nm, while the photoluminescence spectra are between 454 nm and 480 nm. Quantum yields again reached the highest value (41%) at 120th minutes. The FWHM values are similarly between 30 and 33 nm. The reaction of the synthesized

quaternary alloys in the 2000 mL reaction vessel was extended to 4 hours. The growth rate in the 2000 mL reactor is slower than the nanocrystals produced in smaller reaction vessels. The reason of this is most probably the mechanical stirrer is not long enough for 2000 ml vessel. The UV-Vis absorption wavelengths of the nanoparticles produced in the 2000 mL reactor range from 423 nm to 453 nm. The wavelength of the radiation shifts from 453 nm to 473 nm. Quantum yields are slightly lower than 31%. FWHM values also range from 31 nm to 35 nm. Table 5.2 gives the photophysical properties of $Zn_xCd_{1-x}S_ySe_{1-y}$ nanocrystals for different reaction volumes in th high volume ractor and the standard 250 ml reaction flask.. These results show that $Zn_xCd_{1-x}S_ySe_{1-y}$ nanocrystals can be produced in a large scale reactor.

As shown in Table 5.2 for the high volume reactor, increasing the reaction volume results decrease in the reaction growth rates. However in 250 mL reaction flask, the growth of the nanocrystals does not fit to the results obtained from high-volume reactor. Since the reaction temperature control is not proper in 250 ml reaction flask as it is in high volume reactor, difference in the results are expected. Stirring bar and the mechanical stirrer difference also results significant differences in the growth of the nanocrystals. (Since this is a two-phase approach, the QDs are formed in the interface. That is the resason mixing is crucial.)
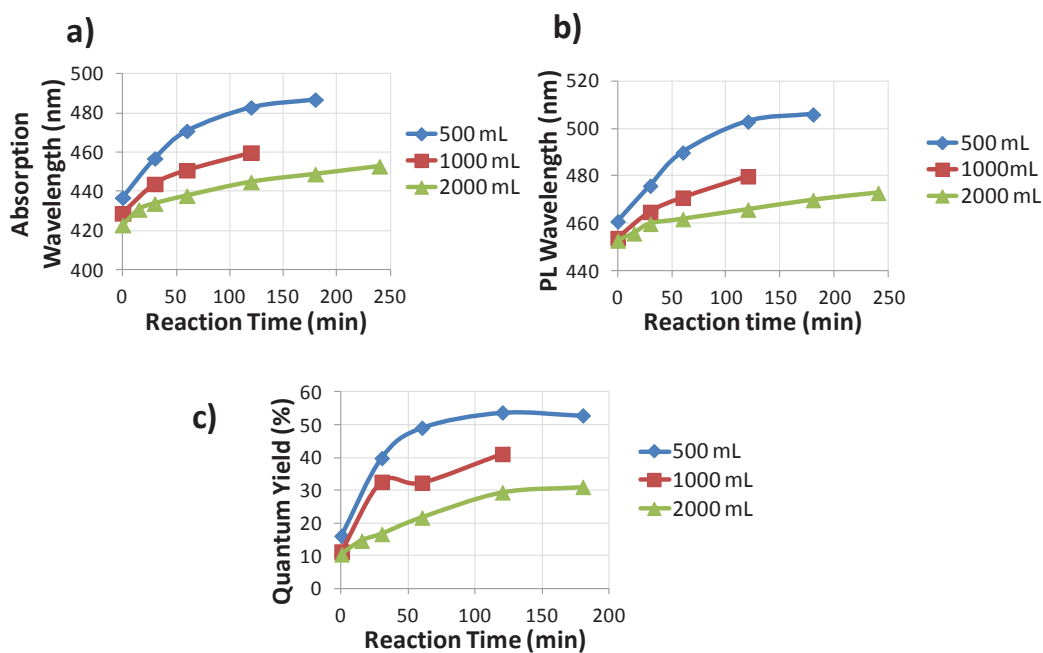
Figure 5.9. a) Absorption and b) PL wavelength shifts and c) photoluminescence quantum efficiency of $Zn_xCd_{1-x}S_ySe_{1-y}$ nanocrystals synthesized in different reaction volumes with respect to reaction time.

In Figure 5.9, variations in wavelengths and quantum yields with reaction time are given in a high-volume reactor. Because of the differences between the 250 ml reaction flask and the high-volume reactor that is mentioned, we did not indicate the classical batch reaction results. As the reaction volume increased, the reaction rate slows down because of the reduction in diffusion rate constants of the precursors in the larger volumes. Since the growth of the nanocrystals depends on the variation in the reaction volume, optimization is required for each volume of the reactor.

We have already mentioned that the $Zn_xCd_{1-x}S_ySe_{1-y}$ nanocrystals diffractogram gives the information of "zinc blende" structure of the nanoparticles which are synthesized in classical batch reactors (Figure 3.8). The XRD patterns of nanocrystals synthesized in the 500 mL and 1000 mL reaction vessels of the large volume reactor are shown in Figure 5.10. Similarly, "zinc blende" nanoparticles with a cubic structure, as expected, support the composition of the nanoalloys obtained from SEM-EDS analysis. Focussing on the angles of the binary bulk structures provides the Cd − S rich alloy composition. A little bit left shift in the angles in 1000 ml reaction vessel indicates the increase of Cd content in the composition. These results show that (i) the SEM-EDS supports the XRD analysis, and (ii) the nanocrystals synthesized in the standard glass reaction flasks do not show significant optical and structural differences with the computer controlled high volume reactor.
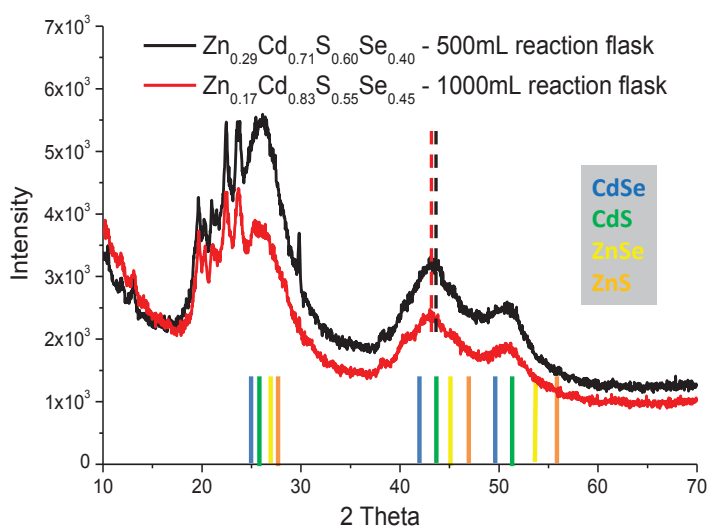
Figure 5.10. XRD pattern of ZnCdSSe nanocrystals synthesized in 500 ml and 1000 ml reaction vessel of the high-volume reactor. The alloy compositions are obtained by SEM-EDS analysis. The lines in different colors represent the angles of binary CdSe, CdS, ZnSe and ZnS bulk structures

5.3. Flow Reactor

5.3.1. Experimental Design
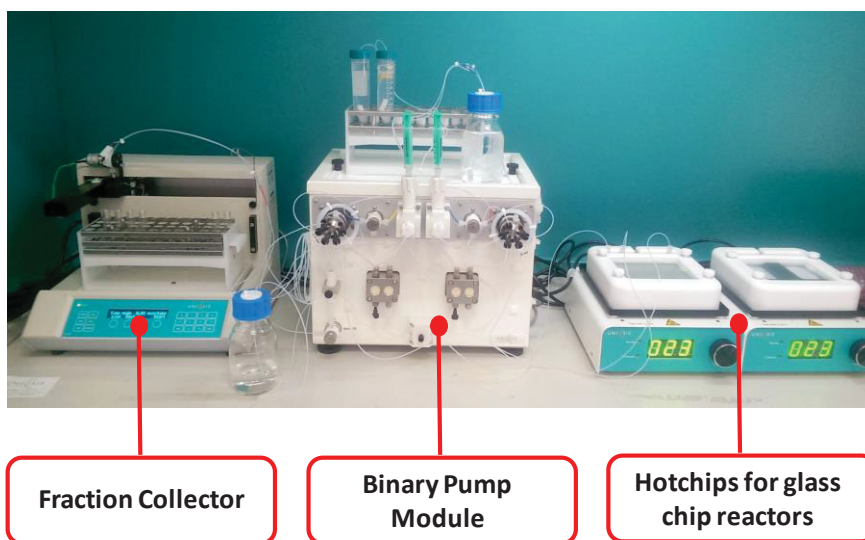
Figure 5.11. Flow reactor system in our laboratory.

Large-scale QD synthesis will also be achieved in laboratory by flow chemistry. For this purpose Flow system purchased from the Uniqsis firm is shown Figure 5.11. This system is controlled by FlowControl software which allows chemists to program and automate sequences of flow chemistry experiments with an unprecedented degree of freedom and flexibility. The system is configured as follows: HPLC pumps, glass chip reactors with different volumes, fraction collectors and sampling robots. Chemically resistant PTFE pumping modules are used. The product could be collected either using a fraction collector (shown in Figure 5.11) or directly to a single vessel. All the accessories are connected to binary pump module by LAN connection. The whole system is connected and controlled by FlowControl software through by WiFi or LAN cable, too. The optional Wifi connection enables to run the system outside of the fume hood.

Reagents (for the test experiments they are called reagent A and reagent B) are given to the pumps by filtrated tubings. The flow rate and residence time of the experiment are controlled by the software. Either 2mL or 20 mL glass chip reactors could be used for the experiments. Volume option of the glass chip could be chosen

according to either test experiments or general reaction time of the synthesis (20 mL glass chip could be preferred for the reactions which require longer reaction time) The reaction temperatures are provided by hot chips which are also controlled by the software.

Flow reactor was recently installed in laboratory and therefore only CdTe nanocrystals are presented in this part of the chapter as test experiments of the flow system.

5.3.1.1. Test Experiments for The Flow Reactor

Cd and Te precursors in aqueous solutions were prepared as standard CdTe synthesis. The initial mole ratios are kept constant. $CdCl_2$ – TGA solution is prepared in 250 mL vessel of flow reactor. The pH of the solution is arranged to 11 by 1.0 M NaOH solution. At the same time, NaHTe solution prepared in 100 mL sealed capped vial under N_2 atmosphere. Since NaHTe is very sensitive to air, it is very important to be careful about preventing oxidation of Te. If not, it is not possible to form CdTe QDs. Besides that, it is very risky in terms of lacking the tubes and pumps by oxide forms of Te.

In the first trial of the CdTe synthesis, 0.3 M Cd and 0.035 M Te precursors are prepared. The reaction temperature was arranged for 90 ^{o}C by adjusting the temperature of the hot chips. Since the approximate reaction duration for the CdTe synthesis is 60 minutes in the classical batch system, we arranged the residence time as 60 minutes by adjusting the flow rate of the pumps. Two of the 20 ml glass chip reactors are connected to each other in order to increase the pathway of the product/QD. Fraction collector is not used in these trials. The product is directly collected into the vessel for further optical optimization.

As shown in Figure 5.12 absorption and PL spectra of the synthesized CdTe nanocrystals have relatively comparable characteristics like standard CdTe nanocrystals which are synthesized in a batch system. QDs absorb the light at 456 nm and emit 534 nm with 78 nm Stokes' shift. The FWHM of the PL peak is 55 nm. TCSPC measurements are also performed to calculate the lifetime of CdTe nanocrystals. For the first trial, 14 ns is calculated for CdTe nanocrystals. Although the results are successful, the concentration of the produced QDs is significantly diluted. Since the total volume of

the reaction will be the sum of reactant A (CdCl₂) and reactant B (NaHTe), it is also expected that the total concentration will be the half of the standard QD solutions. That is the reason, for the further experiments, the precursors were prepared 2 times more concentrated. Cd and Te precursors are prepared as 0.6 M and 0.07 M, respectively. In order to provide the controlled experiment set, only the residence time is changed and the other parameters kept constant.
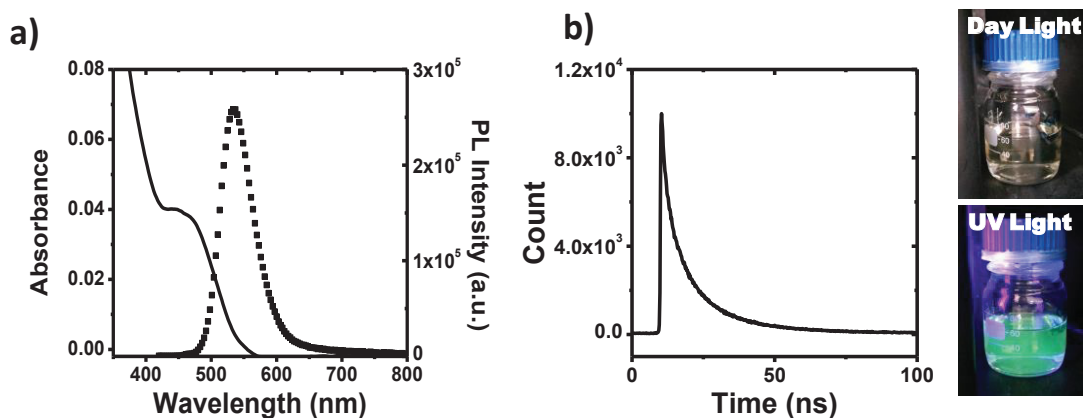
Figure 5.12. a) Absorption and PL spectra of CdTe nanocrystals from the first trial in the flow system. b) TCSPC measurements performed with 450 nm laser. Residence time is 60 minutes. Images in the right side of the figure indicates the QD solution under daylight (upper) and UV illumination (lower).
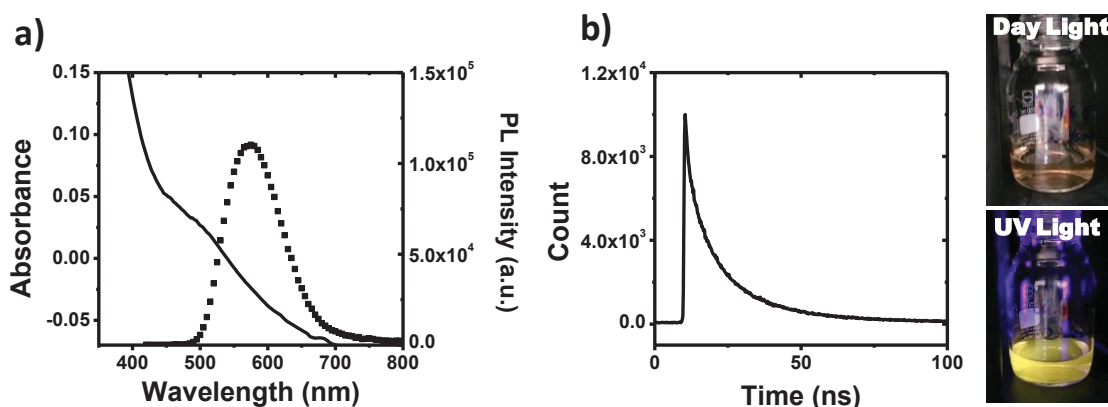
Figure 5.13. a) Absorption and PL spectra of CdTe nanocrystals synthesized in the flow system. b) TCSPC measurements performed with 450 nm laser. Residence time is 60 minutes. Images in the right side of the figure indicates the QD solution under daylight (upper) and UV illumination (lower).
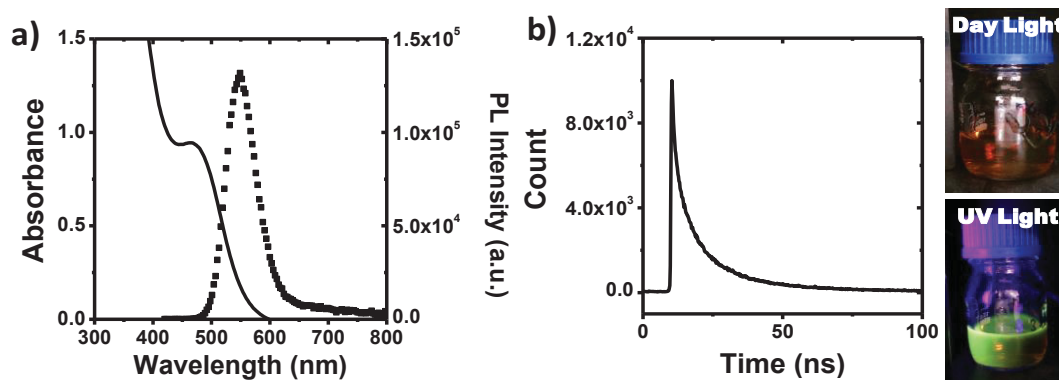
Figure 5.14. a) Absorption and PL spectra of CdTe nanocrystals synthesized in the flow system. b) TCSPC measurements performed with 450 nm laser. Residence time is 30 minutes. Images in the right side of the figure, indicates the QD solution under daylight (upper) and UV illumination (lower).
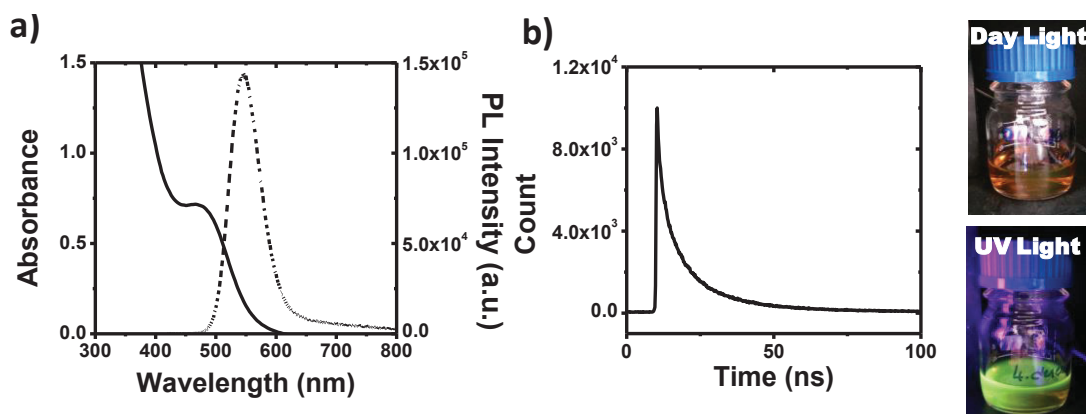
Figure 5.15. a) Absorption and PL spectra of CdTe nanocrystals synthesized in the flow system. b) TCSPC measurements performed with 450 nm laser. Residence time is 15 minutes. Images in the right side of the figure indicates the QD solution under daylight (upper) and UV illumination (lower).

Figure 5.13, Figure 5.14 and Figure 5.15 show the experimental set with different residence time. Since the reactant concentrations are increased two times, the number of nanoparticles are also increased in the produced QD solution (This comment depends on the observation – the color of the solution. Elemental analysis is required to prove this comment). On the other hand it is possible to assume the concentration of the CdTe QDs by their absorbance and extinction coefficient. By the help of the study reported by Yu et al. approximate extinction coefficient could be used to calculate the concentrations (Yu et al., 2003). According to the calculations the concentrations are 4 µM, 10 µM, 80µM, and 70 µM, respectively. As expected the first experimental set has

significantly lower concentration. The reason of the low concentration in the second experimental set is because of the quality of QDs as will be mentioned in the next paragraph. TCSPC measurements are showed that all the produced QDs in the flow reactor have similar lifetimes around 14 – 18 ns with three-exponential processes. All the processes have similar contributions with similar lifetimes. On the other hand, CdTe QDs synthesized in classical 250 ml reaction flask has lifetime around 30 ns. The details on the TCSPC results are given in Table 5.3.

Table 5.3. The lifetime values and relative percentages of each processes for synthesized CdTe QDs in flow reactor

Sample	τ_1 (ns)	% Rel$_1$	τ_2 (ns)	% Rel$_2$	τ_3 (ns)	% Rel$_3$	$\tau_{average}$ (ns)	χ^2
0*	8.19	14.38	24.62	71.35	85.46	14.27	30.9	1.09
1	1.51	5.64	8.07	49.33	22.05	45.03	14.0	1.02
2	2.12	5.59	11.06	55.55	30.14	38.85	18.0	1.07
3	1.43	6.72	8.66	51.30	26.96	41.98	15.9	1.16
4	1.74	8.22	8.98	54.16	27.57	37.62	15.4	1.05

*Sample number - 0 represents the results from the standard glass 250 ml reaction flask.

The absorption and PL spectra of the CdTe nanocrystals showed some trends in terms of nanocrystal growth rates. Increasing the concentration of the reactants with the same reaction parameters results in a significant red shift in the optical spectra. This result indicates that the growth rate is increased significantly when the reactant concentration is doubled. However, the FWHM of the PL spectra of the CdTe nanocrystal (exp. Number 2 in table Table 5.4) is undesirably larger than the typical values. The reason is most probably the long residence time for the current concentrations. In order to solve this problem, residence time is decreased by 30 minutes and then 15 minutes. The results did not show significant differences in terms of optical properties. All the experimental design and the optical parameters that obtained after the synthesis of QDs are given in Table 5.4. Table also indicates the results from classical 250 ml reaction flask. As we mentioned before, the difference between the reaction parameters/conditions affects the results significantly. For example while the Stokes shift of CdTe QDs synthesized in the classical batch reactor is 40 nm, it is approximately 70m for the flow reactor. Also the FWHM and lifetime values

remark the nessesity of tdhe further experiments and optimization for the synthesis in flow reactor. Even so, CdTe QDs were synthesized in the flow reactor with the comparable results in literature.

Table 5.4. Experimental design of CdTe nanocrystals for flow reactor. The optical characterization of synthesized CdTe nanocrystals is also given.

#	Reaction Parameters					Optical Characterization			
	$CdCl_2$ (mmol /100mL)	NaHTe (mmol /100mL)	Reactor Temp (C)	Residence Time (min)	Reactor Volume (mL)	Abs (nm)	PL (nm)	FWHM (nm)	Lifetime (ns)
0*	3	0.35	110	60	110	480	520	40	30.9
1	3	0.35	90	60	20+20	456	534	55	14.0
2	6	0.7	90	60	20+20	495	570	90	18.0
3	6	0.7	90	30	20+20	467	548	55	15.9
4	6	0.7	90	15	20+20	470	546	55	15.4

*Sample number - 0 represents the results from the standard glass 250 ml reaction flask.

5.4. Conclusion

In this chapter, scaled-up QD synthesis was achieved in the high-volume reactors and in the flow reactor. Both of the systems are tested by the synthesis of CdTe nanocrystals. The results are comparable with the standard synthesis methods in the classical reaction flasks. $Zn_xCd_{1-x}S_ySe_{1-y}$ nanocrystals were also synthesized in the high-volume reactors. Alloy compositions are analyzed and the optical properties are investigated that, increasing the reaction volume, the growth rate of the nanocrystals are a little bit slowed down. Although the high-volume reactor is sufficient enough for the reaction volumes up to 2000 mL, the speed of mixing and the keeping the reaction temperature homogeneously in the reaction vessel are challenged. That is the reason the synthesis of the QDs with high-quality, monodisperse and narrow FWHMs could be obtained by the flow reactors. Since the flow reactor in our laboratory is activated for the synthesis of QDs at the beginning of May 2018, only test experiments with CdTe nanocrystals could be performed. The concentration of the reactants, residence time, flow rate, the reaction temperature and reactor volume are some of the parameters that could be arranged during the synthesis.

CHAPTER 6

THE DESIGN AND THE CHARACTERIZATION OF HIGH-QUALITY QUANTUM DOT BASED FIELD-EFFECT TRANSISTORS

6.1. Introduction

Quantum Dots (QDs) are luminescent semiconductor nanocrystals which have typically 1-100 nm size in diameter. This nanoscale size can lead to the quantum confinement effect, which results in interesting optical and electronic properties(Yun et al., 2016). If the radius of a particle is above the exciton Bohr radius of the material, particle starts to show bulk properties. In the range (below the exciton Bohr radius) size and the composition of the nanoparticles are the main factors to control the optical and electronic properties of nanoparticles. Thanks to these properties, QDs are very promising materials in order to serve as building blocks for next-generation thin films electronic and optoelectronic devices like photovoltaics(Sevim et al., 2014), solar cells(Chuang et al., 2014), light-emitting diodes(Dai et al., 2014) and transistors(Zhao et al., 2016). In recent years, QDs with IR range absorption and emission have been widely focussed on because of their large band-gaps, ambipolar features, relatively high charge carrier mobilities etc(Jo et al., 2014). PbS is one of the most studied colloidal quantum dots in this kind of applications, like solar cells(Yuan et al., 2015). For the devices like LEDs, solar cells etc., understanding of charge transport properties is very important. Field effect transistors are the most proper devices to investigate charge transfer characteristics of semiconductors. The field effect transistors (FETs) are based around the concept that charge on a nearby object can attract charges within a semiconductor channel. Besides, light emitting field effect transistors could combine the switching properties of transistors and light emitting properties of light emitting diodes. In a typical FET, there are three electrodes. The source and drain electrodes are in contact with the semiconducting layer. Gate electrode should be insulated from the semiconducting layer. Here dielectric is used as an insulator between the gate electrode

and thesemiconducting layer. As shown in Figure 6.1c the distance between the source and the drain electrode is defined as channel length, L, and the total width as channel width, W. While, source-drain voltage, V_{ds} refers to the potential difference between the source and drain; gate voltage, V_g refers the potential difference between source and gate. The currents related to these potential differences are called as drain current I_{ds} and gate current or gate leakage, I_g, respectively.
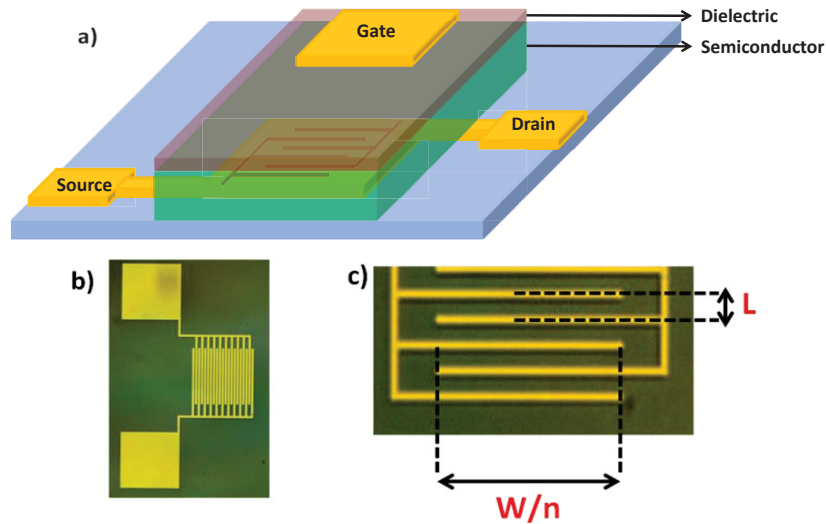
Figure 6.1. a) The architecture of bottom contact top gate field effect transistor b) The design of the FET that is used c) Channel length (L) and width (W/n) are shown. "n" represents the number of channels in the transistor

6.2. Experimental

6.2.1. Film Phase Studies

5 different PbS quantum dots were brought to Heidelberg University in order to study QD based field effect transistors. All the QDs have organic capping agents on their surfaces which helps them to disperse easily in organic solvents like toluene. Since these QDs are binary type, the only thing that can change the optical spectra is the particle size. The difference in the optical spectra shows that size of these QDs is different and they can be calculated by the formula given in a study of Henz at. all. (Moreels et al., 2009) Since there was no significant effect of particle size on output and transfer characteristics of the transistors (Schornbaum et al., 2015) we could say that the

exact particle size of PbS quantum dots is not critical for our study. That is the reason, we can roughly estimate that the particle sizes are around 4 – 10 nm. Figure 6.1 shows the absorption and PL spectra of these QDs. The absorption spectrum was taken by Varian Cary 5000 absorption spectrometer with a Si and PbS detector for different wavelength regions. For the PL measurements, liquid nitrogen-cooled one-dimensional InGaAs line camera from PI Acton was used. 785 nm laser light source was used for the excitation. After all the measurements, data were corrected with the ideal spectrum of halogen light source from Ocean Optics, HL-2000.
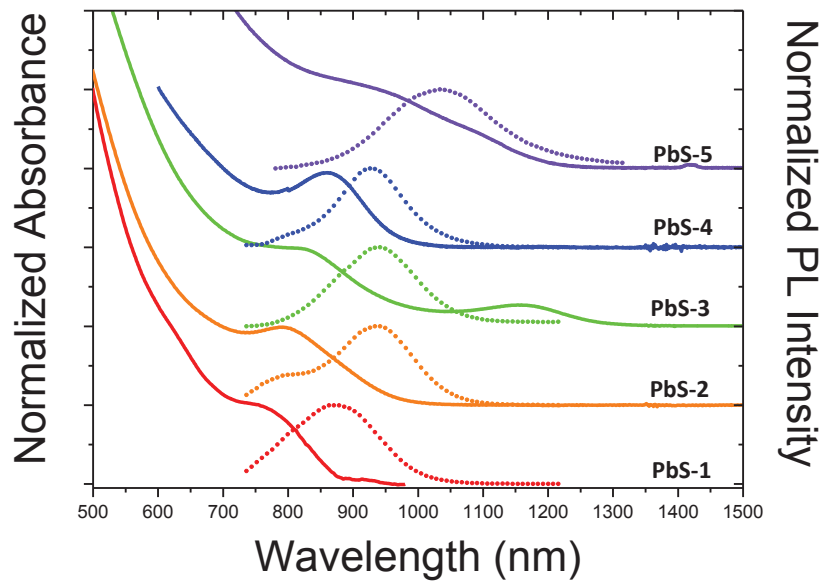
Figure 6.2. Absorption and PL spectra of different PbS quantum dots in solution phase. The solid lines represent the absorption, dash lines represent the PL spectra of QDs.

Since the detector for the LEFET measurements is convenient in the range of 900 – 1600 nm, the quantum dot which emits in the longer wavelength was chosen. Further experiments were done with PbS-5.

Photoluminescence quantum efficiency and lifetime measurements were also done. For the PL QE measurements integrating sphere from LabSphere with a Spectralon coating was used. The same light source was directed to the entrance of the integrated sphere. All the data was corrected by dividing the spectral data of tungsten-halogen lamp, SLS201 from Thorlabs. The results showed that proposed QD is in high-quality enough. QDs are purified from excess precursors by adding acetone and

isopropanol in 1:1 ratio. After centrifugation precipitated QDs were collected and redispersed in toluene.

QD films were obtained by spin coating technique. Different concentrations and different spinning rates were tried. In order to increase the conductivity of the films, ligand exchange technique was used. Long alkyl ligands were replaced with a short alkyl ligand capping agent, mercaptopropionic acid – MPA with the following procedure.

6.2.2. Ligand Exchange:
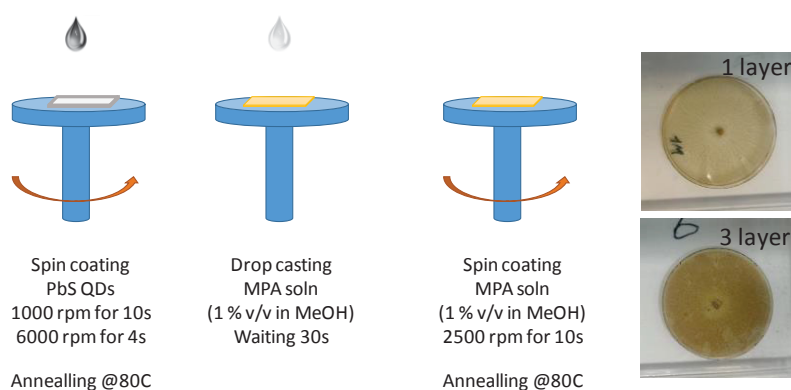
Figure 6.3. Spin coating steps for the ligand exchange procedure. The images show the difference in the color of the films with respect to number of layers – film thickness

As shown in the figure above, spin coating was done step by step for the ligand exchange procedure. QD in toluene was spin coated at1000 rpm for 10s following 6000 rpm for 4s. This increase in the spinning rate helps to remove excess material in the edges of the substrates. After annealing at 80°C for 10 mins, MPA solution in methanol was drop cast on QD film. Waiting for 30 seconds gives sufficient time to MPA ligands to diffuse into QD film and exchange the ligands. Then spin coating was done at 2500 rpm for 10s. Washing with methanol is also required to remove excess MPA ligands on the surface of the film. After annealing at 80°C for 2 minutes, the films are ready for the further coatings.

Ligand exchange is also required in order to achieve the desired thickness of the films. Because after this procedure the surface of the film becomes more hydrophilic and it makes the coating of another organic layer possible. In another case, if the surface

does not become hydrophilic, the solvent involves the organic content can wash the previous layer out. The thickness of the films was measured by a profilometer. The results showed that thickness of the film increase directly proportional. Figure 6.4 shows the film thicknesses obtained from profilometer. The measurements were taken after each ligand exchange procedures. The thickness of the QD films before the ligand exchange also gave the similar results with the 1L coating. Since all these coatings are done outside the glovebox, the morphology of the films was not good enough and small deviations in the thickness measurements are expected. However, the coatings including the ligand exchange steps for the transistor fabrication were done in the glovebox.
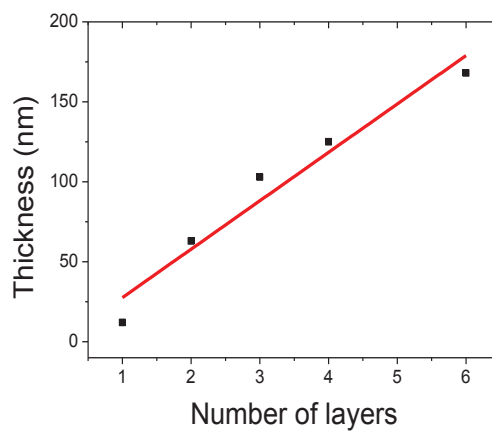
Figure 6.4. The thickness of the films with respect to the number of coatings. The measurements were taken after each ligand exchange procedure. The data was obtained by a profilometer.

6.2.3. Fabrication of FETs and LEFETs;

In this part, we mainly focussed on the fabrication of field effect transistors (FETs) and getting light emission from these FETs. First of all the proper substrates were prepared in a clean room by the photolithography technique. Pre-cleaned substrates were spin-coated by standard double-layer photo-resist materials, LOR5B and S1813. After lithography, the lift-off process was applied with the adapted developer. Before these substrates were used for the transistors, just before the semiconductor coating, they were cleaned with isopropanol and acetone in a sonicator for 30 minutes and dried.

Bottom contact top gate FETs were fabricated. The schematic illustration of the transistors is shown in Figure 6.5 with estimated layer thicknesses.
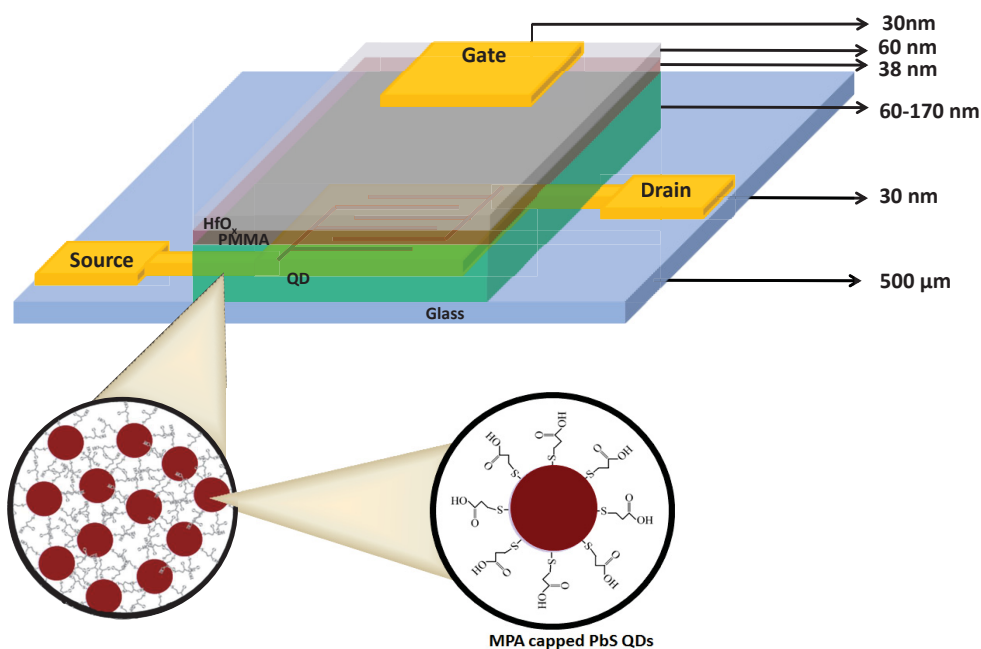
Figure 6.5. Schematic illustration of PbS based bottom contact top gate field effect transistors

Prepared substrates were cleaned in an ultrasonic bath with isopropanol for 10 mins. After cleaning steps PbS QDs were spin coated in the glove box. Different thicknesses were tried to achieve the highest efficiency from the transistors. After ligand exchange procedures, PMMA layer was also spin coated. 12mg/ml electronic grade PMMA solution in n-butylacetate was used with 2000 rpm for 60 seconds. Then the substrates annealed for 30 minutes on the hot plate at 80°C in the glovebox. The estimated thickness of the PMMA layer is 38 nm according to the optimization studies from Dr. Zaumseil's group. HfO_x is coated by Atomic Layer Deposition (ALD) technique. Approximately 60 nm HfO_x were deposited on PMMA layer. For this procedure, 500 alternating cycles of Tetrakis(dimethylamido)hafnium(IV) (TDMAH) (98+ % (99.99+ %-Hf, < 0.2 % Zr) PURATREM - Strem Chemicals) and deionized water were deposited at 100°C under vacuum. During the one cycle, firstly deionized water is purged for 0.015 seconds and then after 60 seconds waiting, TDMAH is purged for 0.15s. After another 60 seconds waiting, the next cycle starts. When the HfO_x deposition is completed, transistors were placed into the thermal evaporator inside the

glovebox. For this deposition, special masks were used depends on the transistors' design. Ag gate is deposited on top of the transistors with 30 nm thickness. Here the evaporation rate is recorded as 0.1 A/s for the first 5 nm, 0.3 A/s up to 15 nm and then 0.5A/s constantly.

In another batch, single wall carbon nanotubes (SWNT) were also used with PbS QDs as a semiconductor layer. First of all SWNT solution was prepared. Since solvents like toluene or xylene increase the selectivity and provide better solubility for SWNT, toluene is used as a solvent (Jakubka et al., 2012). Synthesized (by Dr. Zaumseil's Group) SWNTs were redispersed in toluene in a vial with vigorous stirring at 80°C. In order to obtain pure SWNT solution, in every 10 minutes, the solvent was changed. This procedure was done 4 times. It could be done more than 4 times, but it may cause to decrease the solubility of the SWNTs by removing necessary polymers. After changing the solvent for the last time, toluene is added again, and dispersion is sonicated 30 minutes. Instead of ultrasonication techniques, shear-force-mixing could also be used. Due to relatively strong pi-pi interactions between SWNTs, bundles could be formed and solubility could decrease (Bergin et al., 2009). That is the reason SWNT dispersion was prepared just before the printing procedure. In order to be sure about the concentration and absence of the metallic character of SWNTs, UV-Vis spectra should be taken.

Schematic illustration of the transistors is shown in Figure 6.6 All the layers are coated with the same techniques as before. SWNT are printed by an Aerosol jet printer (AJP). The approximate thickness of the SWNT is 20 nm. The QD film thickness is varied between 10 nm to 170 nm. In one of the trials having the thinnest QD layer, long alkyl chains remain on the surface of the QDs.
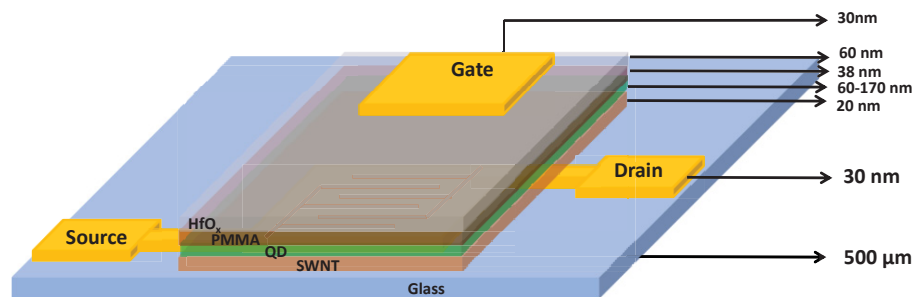
Figure 6.6. Schematic illustration of PbS-SWNT based bottom contact top gate field effect transistors

Choosing the correct dielectric is important in terms of low drive voltages and it could be achieved by high-capacitance dielectrics like HfO_2, Al_2O_3, ZrO_2 etc. However, deposition of these high-k materials by atomic layer deposition techniques are not suitable for top-gated FETs. Because this deposition should be done on the semiconductor layer and it results in irreversible damages (Luzio et al., 2014). Low-k materials like PMMA are also used as dielectrics. However, they also have some disadvantages like low breakdown strength and high probability of pinholes (Held et al., 2015). Also, they require relatively thicker films due to high leakage currents. That is the reason, many groups started to study on hybrid dielectrics in order to combine the advantages of both high-k and low-k materials. These advantages can be count as high permittivity, high breakdown strength, mechanical flexibility, and easy processability etc. (Ortiz et al., 2010). Zaumseil et all. used PMMA and HfO_x bilayer for top-gated FETs and obtained relatively high efficiencies in FETs in their study (Held et al., 2015). That is the reason, in this project we used the same hybrid dielectric structure for the proposed FETs.

6.3. Characterization of FETs and LEFETs;

Transfer and output characteristics of the transistors were carried out with Agilent 4155C semiconductor parameter analyzer in the glovebox. The measurements were controlled with Labview program.

Capacitance measurements were done by Agilent E4980A Precision LCR Meter with the ped structures in each transistor. Peds have different areas as 0.06, 0.03 and 0.015 cm^2. After all, peds are measured and calculated in order to find the accurate capacitance value for the mobility calculations. First of all, the lowest adequate frequency value which resulted in constant capacitance values with the DC voltage. Here, 20 V is used for our quantum dots to be sure that the transistors are "on" state in this DC voltage. For all the transistors, the frequency was chosen as 1 kHz. After that, capacitance measurements were done with a bias range of -20 V to +20 V.Since the whole area (both transistors and peds for the capacitance measurements) was coated with the same layer thicknesses, there is no problem for the QD based transistor, but in QD + SWNT based transistors capacitance values might differ to some extent. Because the SWNTs are coated via aerosol jet printer only to the channels, not to the peds. That

is the reason mobility values do not represent the accurate values but they might be classified as in the range.

Mobility calculations were done by the help of following equations. The absolute values for charge carrier mobilities are not the immediate scope of this study, nevertheless, mobilities were calculated roughly.

For the linear regime;

$$\mu_{lin} = \frac{dI_{ds,lin}}{dV_g} \cdot \frac{L}{WCV_{ds}} \tag{6.1}$$

For the saturation;

$$\mu_{sat} = \frac{d^2 I_{ds,sat}}{dV_g^2} \cdot \frac{L}{WC} \tag{6.2}$$

Here, "$I_{ds,lin}$" and "$I_{ds,sat}$" represents the drain-source current for linear and saturation regime, respectively. V_g is gate voltage, L is the channel length and W is the channel witdh. C is the capacitance of the transistors and it should ne measured as explained in the previous paragrapgh.

Electroluminescence characterization of FETs was done by Keithley 2612A source meter via the Labview program in the air. Acton SpectraPro SP2358 spectrometer was used as a detector.

As mentioned in the previous title, for the rest of this study PbS-5 QD was used because of its higher wavelengths emission properties and better dispersibility in toluene. Other PbS nanocrystals were also prepared and some trials were done, but the best results were obtained with this PbS nanocrystals. Photoluminescence emission was also affected by the ligand exchange procedures. As shown in Figure 6.7, before the ligand exchange procedures, the emission wavelength was around 1050 nm for both liquid and film phase measurements. The small amount of redshifting in film phase measurements was expected. However, it was observed that there was a significant red shift in photoluminescence emission after the ligand exchange that the PL maximum was shifted around 100 nm and it was obtained at around 1150 nm. However, the difference of the red shift for the number of ligand exchanged layers were found as negligible.
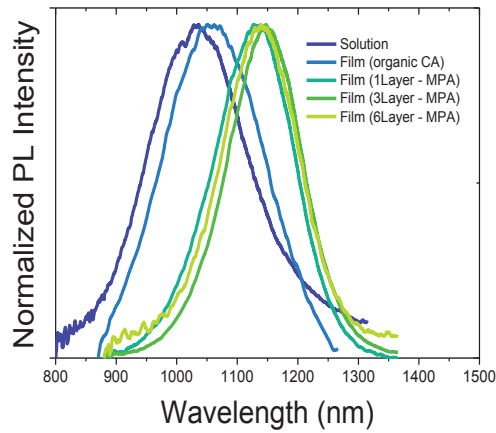
Figure 6.7. PL emission of PbS-5 QDs. From left to right, liquid phase, film phase before ligand exchange and film phase after ligand exchange procedures were shown.

A lifetime of the quantum dots is quite long. The average lifetime of PbS quantum dots was measured with 785 nm excitation source up to 1μs in solution phase and 200 ns in film phase. Photoluminescence quantum efficiencies are around 80% in the solution phase. All the quantum dots with different particle sizes show the similar trends.
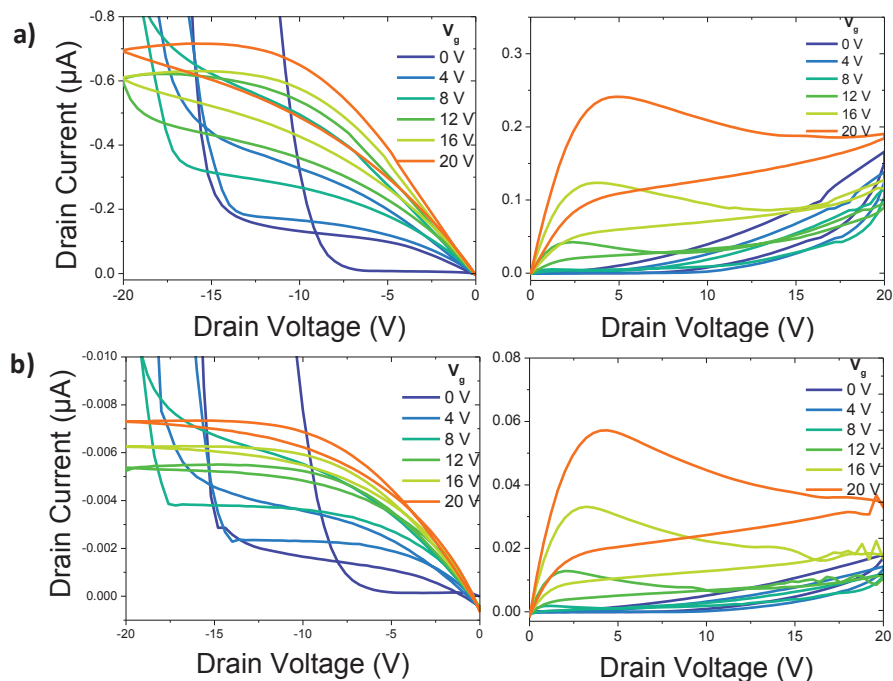
Figure 6.8. Output characteristics of 2 layers QD based FETs at negative (-20 – 0V) and positive (0 – 20V) gate voltages for a field effect transistor with channel length a) 5μm and b) 40μm. The estimated thickness of the QD layer is 63 nm.

Output characteristics of first-generation field effect transistors were shown in Figure 6.8. Here the thickness of the QD film is estimated as 63 nm according to the previous measurements in profilometer. Electrical measurements were done for both 5µm and 40 µm channel length. The characteristics of the curves did not show significant differences depending on the channel length but the drain current decreased with the increase in channel length as expected. The shape of the curves for positive drain voltages (right side in the figure) is interesting because generally, the output curves do not have any reduction in drain current after a top point. Generally drain current increase linearly with the drain voltage at smaller drain voltages. This is called linear regime. When drain voltage increases, the channel starts to pinch-off. More increase in drain voltage results in an expansion in depletion region more and the pinch-off starts to move through the channel. In that point, drain current saturates and becomes independent of drain voltage (Zaumseil and Sirringhaus, 2007).
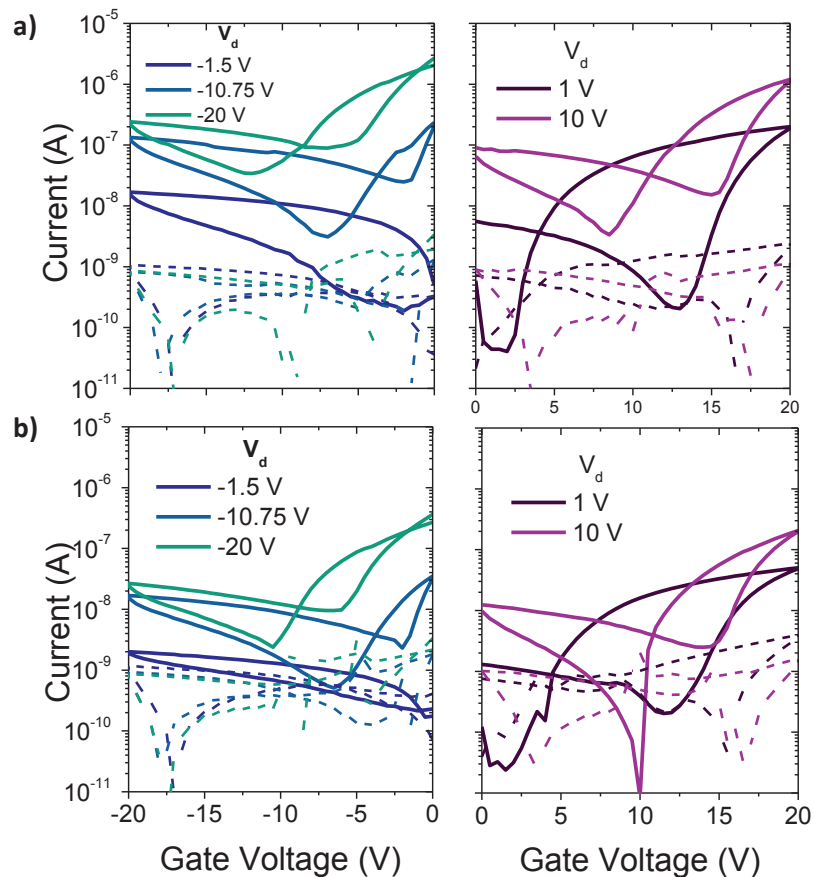
Figure 6.9. Transfer characteristics of 2 layers QD based FETs at negative (-20 – 0V) and positive (0 – 20V) gate voltages for a field effect transistor with channel length a) 5µm and b) 40µm. The estimated thickness of the QD layer is 63 nm. Dash lines represent the gate leakage.

Figure 6.9 represents the transfer characteristics of the same FETs for both positive and negative drain voltages. It is clearly seen that the electron transport is higher than the hole transport – the current in electron injection is higher than hole injection. However, both of them are very low. There is also a significant difference in drain current for the forward and backward scan. This means that there is a large hysteresis. Since there may be lots of shallow and deep trap states in lead chalcogenides like PbS and PbSe, hysteresis like this is also expected (Schornbaum et al., 2015). Shallow states could be defined as trap states which are close to one of the band edges – does not matter conduction or valence bands. On the other hand, deep trap states are the trap states which are in the middle of the band gap.
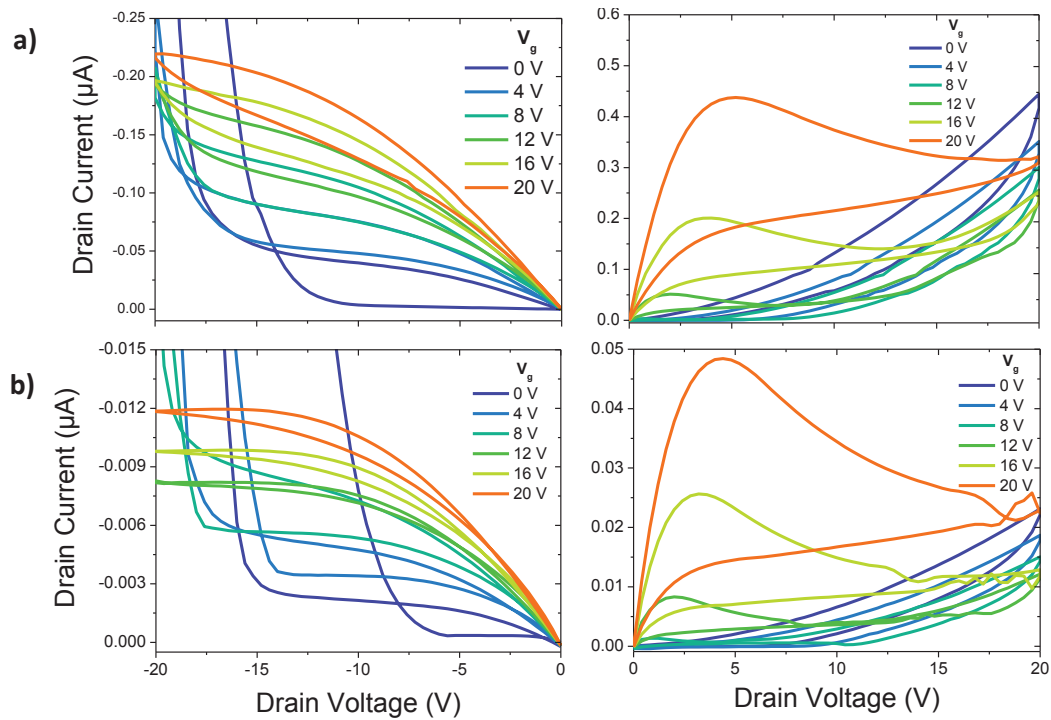
Figure 6.10. Output characteristics of 4layer QD based FETs at negative (-20 – 0V) and positive (0 – 20V) gate voltages for a FETs with channel length a) 5µm and b) 40µm. The estimated thickness of the QD layer is 125 nm.

Figure 6.10 and Figure 6.11 represent the output and transfer characteristics for the same type of field effect transistor with thicker QD films. Here, the approximate film thickness of the semiconductor layer is 125 nm. Much thicker QD film around 170 nm is also applied as semiconductor layer but the curves did not show significant differences. The unusual behaviors in output characteristics were the same, decrease without any saturation in drain current. On the other hand, transfer characteristics

showed that increasing the QD film thickness results in some increase in both hole and electron transport.
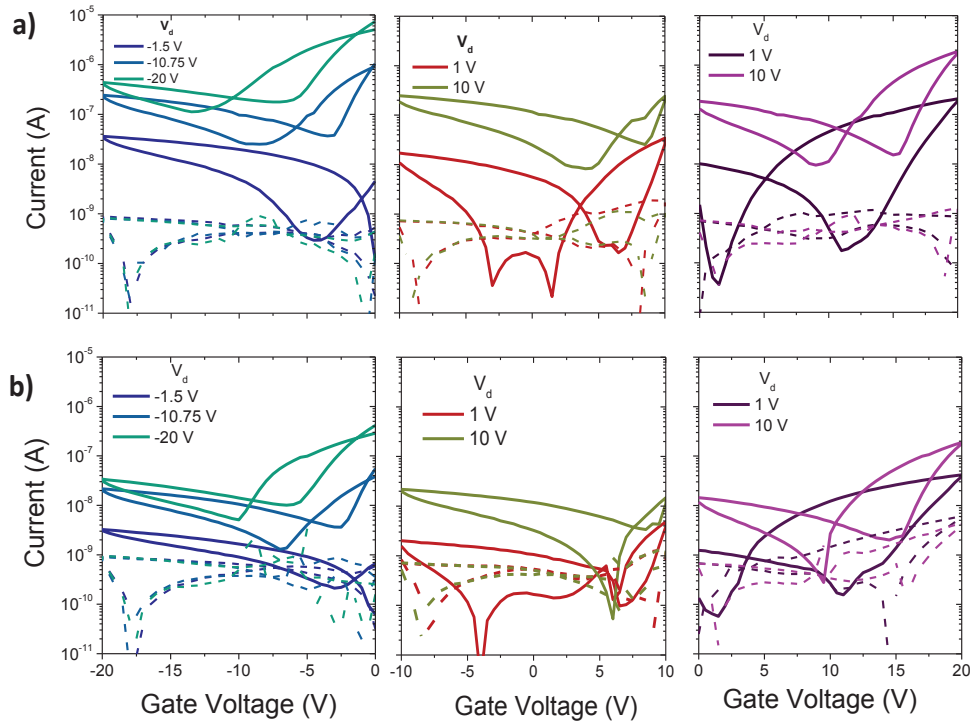
Figure 6.11. Transfer characteristics of 4layers QD based FETs at different gate voltages, (-20 – 0V), (-10 – 10V) and (0 – 20V) for FETs with channel length a) 5µm and b) 40µm. The estimated thickness of the QD layer is 125 nm. Dash lines represent the gate leakage.

Figure 6.12 shows the effect of QD film thickness to the transfer characteristics of field effect transistors. A small increase in the electron transport in negative gate voltages was observed when the QD film thickness is increased from 2 layers (60nm) to 4 and 6 layers (125 and 170 nm). However, there are no significant differences between 4 and 6 layer QD film coated FETs.

As we mentioned before, although there is a distinct "V-shape" in the transfer curves, the electron and hole transport are not equal and it means that these FETs are not certainly ambipolar. Electron transport is higher than the hole transport. It will be also shown in the light emission measurements in the next parts of this study. Figure 6.12 also shows that in the positive gate voltages the electron transport improves. This could also be count as a proof that our first generation FETs are n-type and positive gate voltages enhance the free charges – electrons as a result of an increase in the drain current.
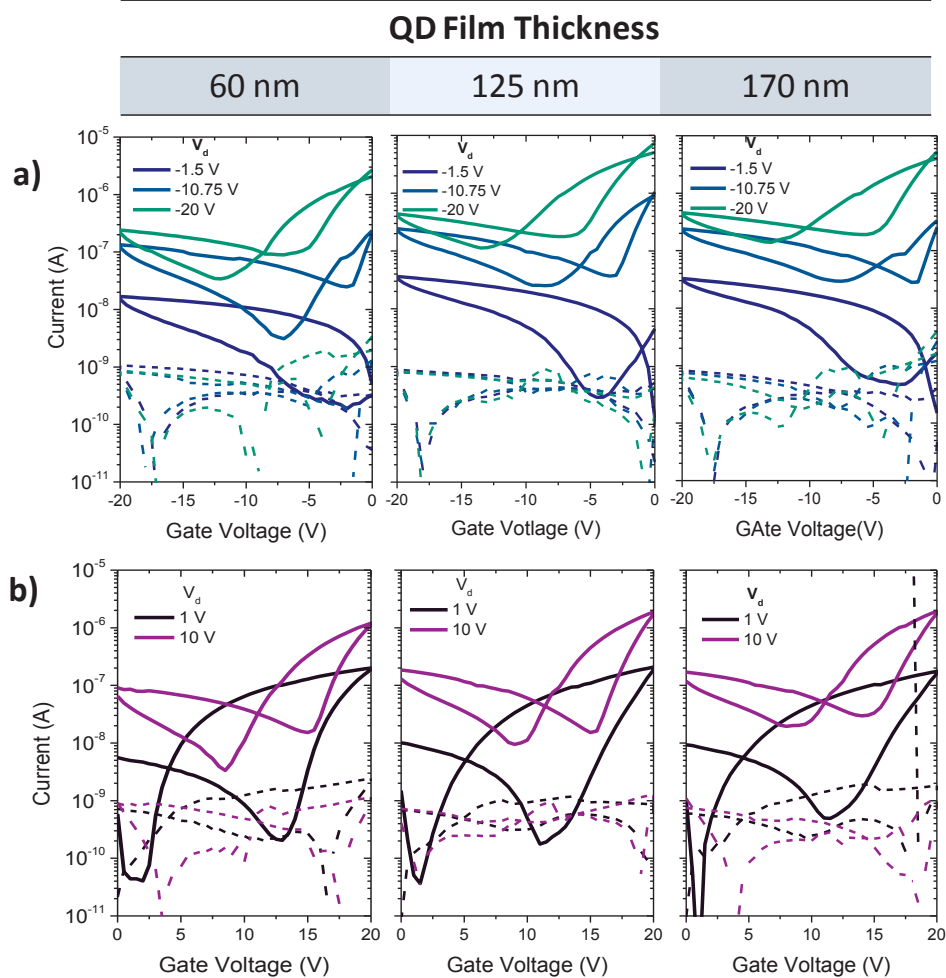
QD Film Thickness

Figure 6.12. The effect of QD film thickness on transfer characteristics in field effect transistors at both a) negative and b) positive gate voltages. Dash lines represent the gate leakage.

In order to increase the drain current and carrier charge mobility, SWNTs are also used with PbS QDS as the semiconductor layer in the same bottom contact top gate field effect transistors. The details about the fabrication are given in the previous part of this chapter (under the title of "Fabrication of FETs and LEFET").

Almost all synthesis methods of SWNTs result in a mixture of metallic SWNTs (m-SWNTs) and semiconducting SWNTs (s-SWNTs). There are some popular methods to enrich s-SWNTs but still, it is not possible to achieve both high selectivities of s-SWNTs and high yield (Schießl et al., 2015). On the other hand, for SWNT based FETs, it is very important to remove all m-SWNTs and have just s-SWNTs. Because m-SWNTs increase the off current of the channel and destroy the switching characteristics of the transistors. This is very significant for the shorter channels like 5 or 10 μm.

Figure 6.13. shows the output and transfer curves of 6,5 SWNT and 4 layers QD based FETs at negative and positive gate voltages at 5 μm channel length. It is clearly seen that there is no on/off ratio in the transfer curves. It is most probably stem from the m-SWNTs in the FETs.
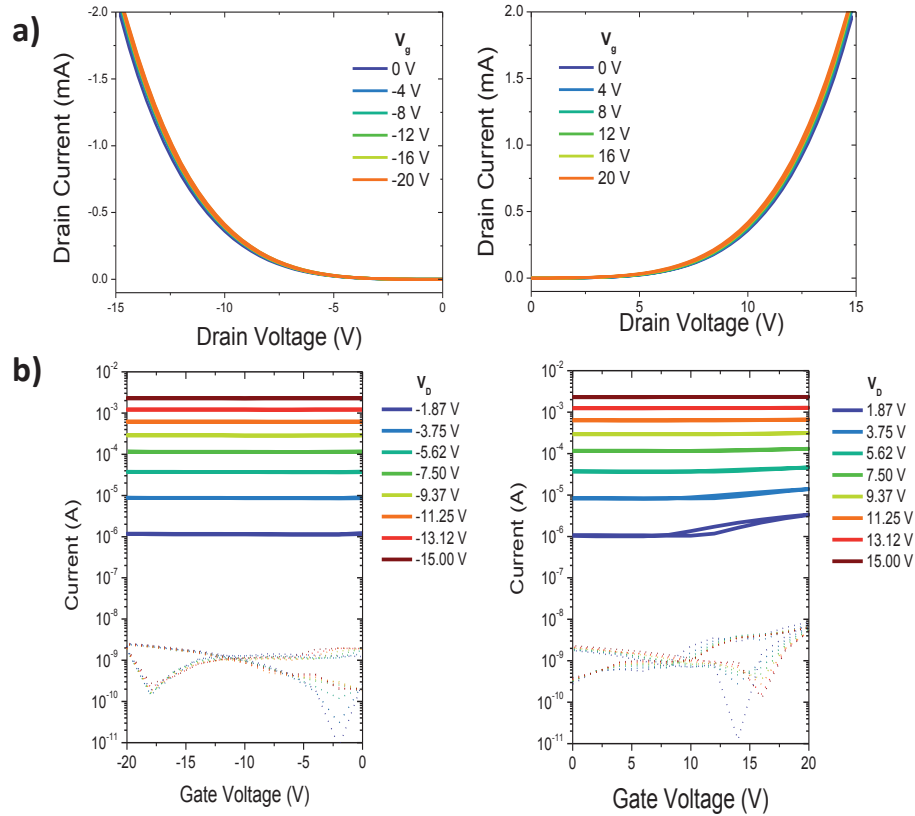
Figure 6.13. a) Output and b) transfer characteristics of 6,5 SWNT and 4layers QD based FETs at negative and positive gate voltages with channel length 5μm. The approximate SWNT and QD layer is 20 nm and 125 nm, respectively. Dots represent the gate leakage.

In the other trial, the m-SWNTs were removed more carefully by centrifugation technique. Absorption spectra of the prepared SWNTs were shown in Figure 6.14a. M_{11} and S_{22} regions show the traditional labels for nanotubes. They indicate the optical transition between valence bands and conduction bands. For example, the optical transition between $v_1 - c_1$ is labeled as E_{11}. If the conductivity of the nanotube is known or important, then it could be labeled as S_{11} or M_{11} for semiconducting or metallic nanotubes, respectively. According to the M11 region in the Figure 6.14a, m-SWNTs should be quite less, if it exists. According to the AFM image of printed SWNTs shown in Figure 6.14b the network is quite dense.
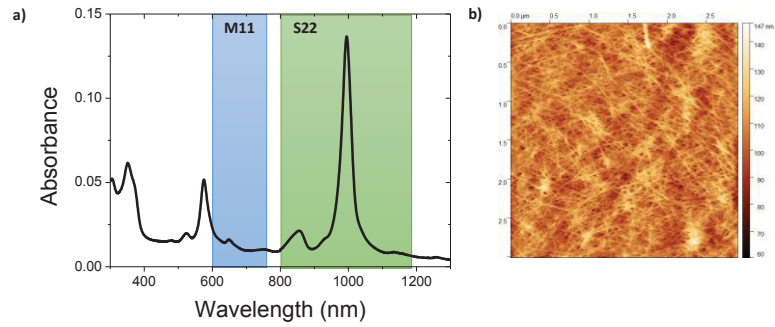
Figure 6.14. a) Absorbance spectra of 6,5 carbon nanotubes in toluene. Optical transitions related to metallic and semiconducting nanotubes are stated as blue and green regions, respectively. b) AFM image of printed 6,5 SWNTs **w**as shown.
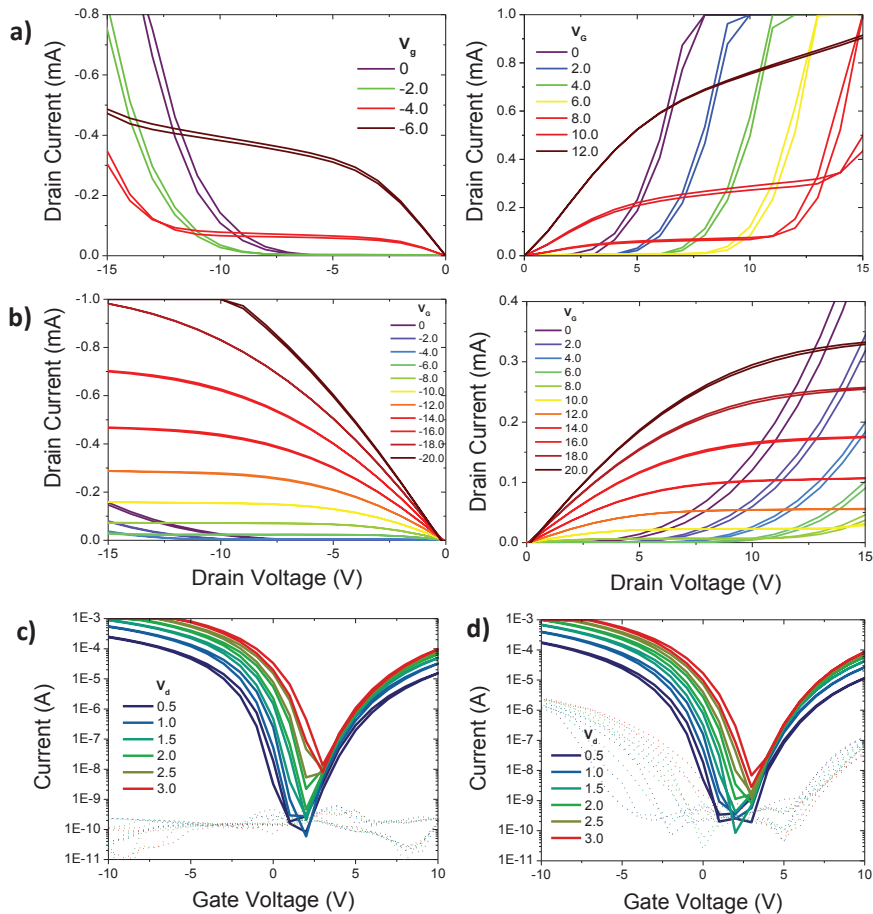
Figure 6.15. Output characteristics of 6,5 SWNT based FETs at negative and positive gate voltages with channel length a) 5μm and b) 40μm were shown. Transfer characteristics for the same transistors for c)5μm and d) 40μm channel lengths at positive drain voltages. Dash lines represent the gate leakage. The estimated thickness of SWNTs is 20 nm.
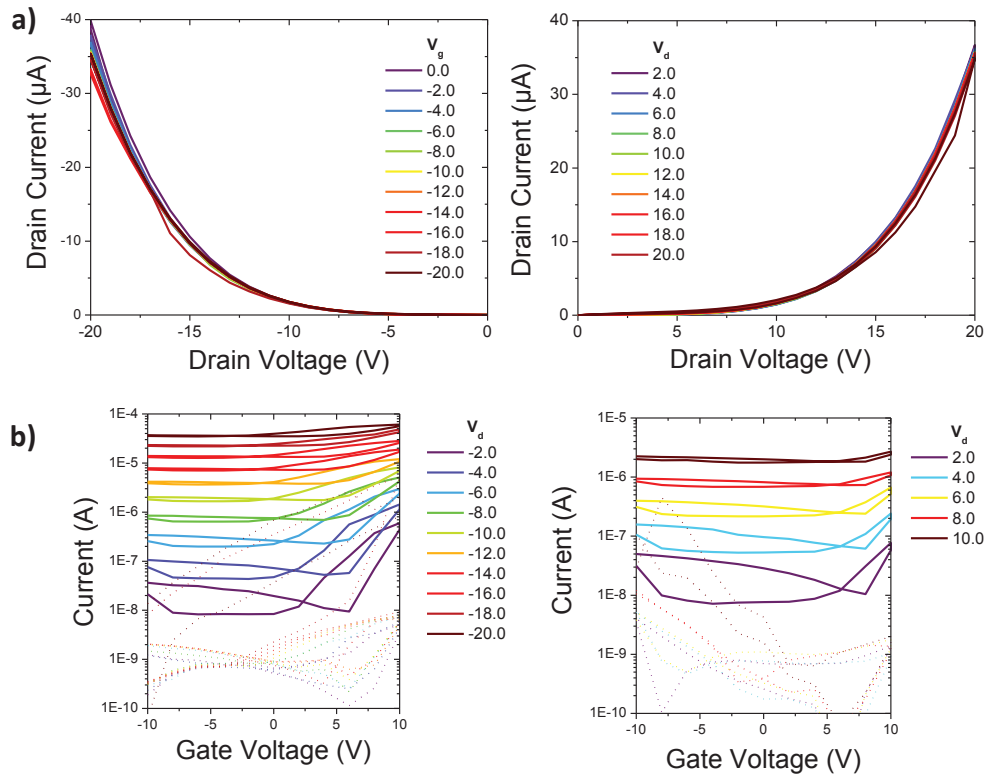
Figure 6.16. a) Output and b) transfer characteristics of 6,5 SWNT and 1 layer QD based FETs at negative and positive gate voltages with channel length 5µm. The approximate SWNT and QD layer is 20 nm and 10 nm, respectively. Dots represent the gate leakage.

As we mentioned before, in the Figure 6.14b, the linear density of the network was around 18 SWNT/µm. According to the literature (Schießl et al., 2015), this density is ideal for high effective mobilities and drive-currents. But also this high density could result in the formation of percolation paths of m-SWNTs in short channel lengths like 5 or 10µm. As we know from the reference devices and the absorption spectra prepared and used SWNTs do not indicate metallic characters, however in the hybrid semiconductor design FETs in which SWNT and PbS nanocrystals were used as semiconductor layer, in shorter channel lengths metallic character in the transfer curves were observed. As it can be seen in Figure 6.16 the on/off ratio was destroyed and the drain currents were increased. Since the electronic measurements are more convenient than the optical measurements in terms of understanding the existence of the metallic character of SWNTs, we could estimate that a few m-SWNTs remained in the solution of SWNT that we used for the FET fabrication. However for the largest channel length, we could obtain expected output and transfer curves for the FETs.
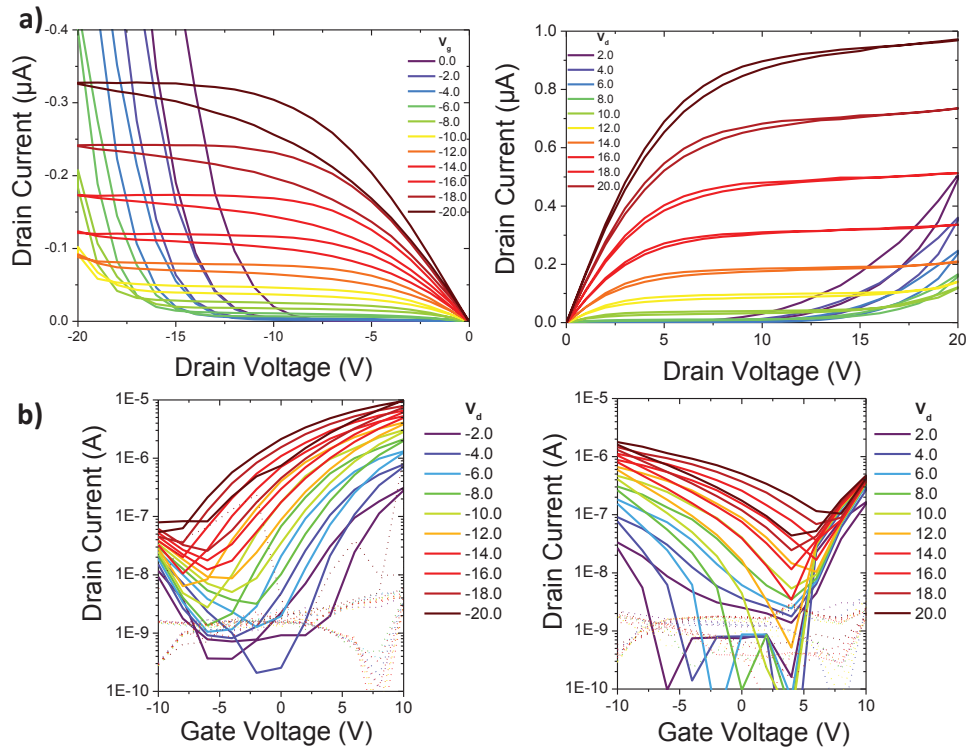
Figure 6.17. a) Output and b) transfer characteristics of 6,5 SWNT and 1 layer QD based FETs at negative and positive gate voltages with channel length 40μm. The approximate SWNT and QD layer is 20 nm and 10 nm, respectively. Dots represent the gate leakage.

The output and transfer curves are also measured for the same FETs with the largest channel lengths. Figure 6.17 shows the electronic characteristics of these FETs. If we compare the output curves with the reference devices, the drain currents are decreased, and hysteresis formed significantly. Also in the transfer curves, the on/off ratio decreased to 10^2, as in the devices which are fabricated with just PbS QDs as a semiconductor. This results showed that even there is a very thin film of QD exists on the SWNT layer, QDs are very effective in terms of electrical measurements.

In the ideal case, the electron and hole mobilities are not dependent on the applied gate voltage. That is the reason the given formulas for the charge carrier mobilities in "Characterization of FETs and LEFETs" part were used. The electron mobilities were obtained around 0.002 cm^2/Vs. The hole carrier mobilities are lower than electrons. Further optimizations could be done for the future experiments with the help of earned knowledge in Dr. Zaumseil's group. However, these mobilities are enough for obtaining electroluminescence measurements as shown in above paragraphs.

Light emission studies are also done within the scope of the proposed project. All the electrical properties were taken in the glovebox, however, the LEFET measurements are obtained in the air. Current-voltage curves did not exhibit any change in the glovebox and in the air. Even after 3 months, the I-V curves did not show significant differences in the air measurements. The transistors were very resistive to the air because HfO_x is used as a dielectric layer.It gives an effective protection of the semiconducting layer, PbS QDs. As a result, we did not observe any oxidation of PbS QDs.
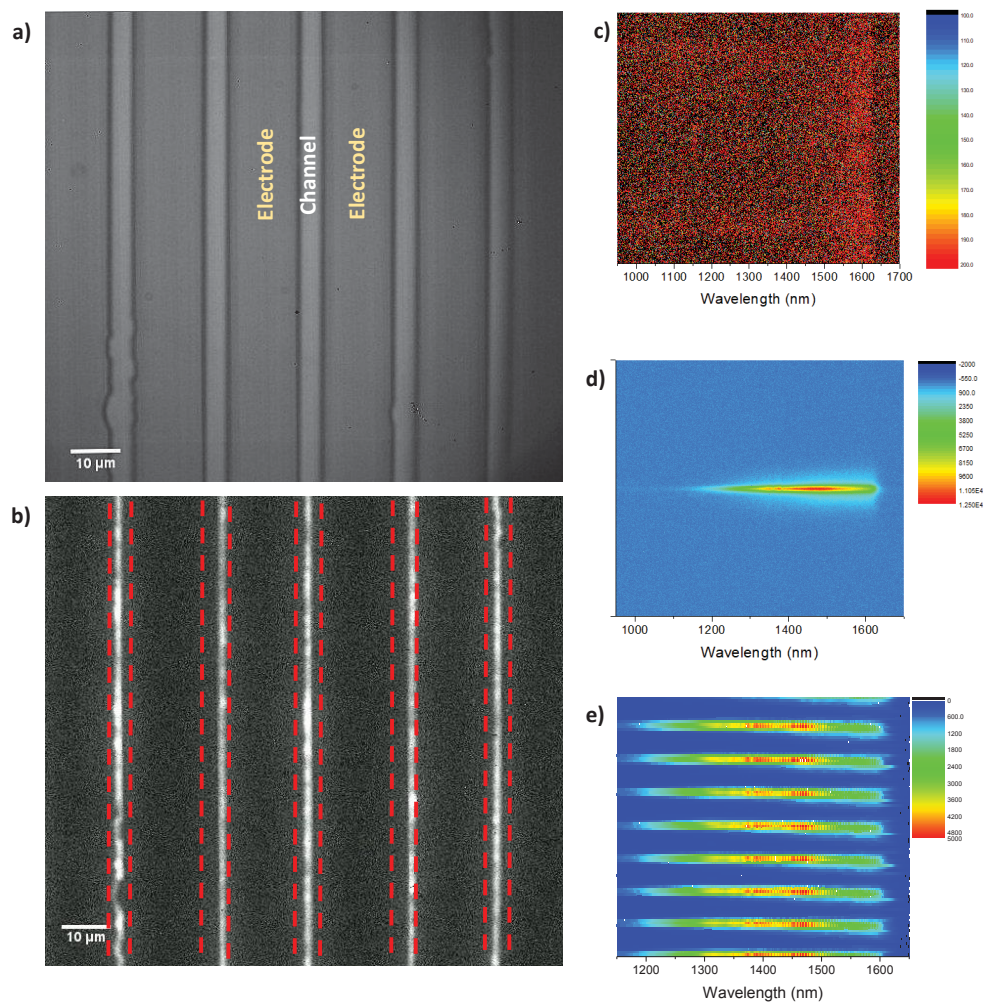
Figure 6.18. a) Image of electrodes and the channel for the PbS QD based FET in which the thickness of QD layer is 120 nm. b) NIR image (wavelength between 950 – 1600 nm) showing electroluminescence. The EL is mainly confined to the electrode which injects holes. There is no movement to the electron injecting electrode. Vg = 20V. Vd = 20V. Integration time is 30s.c)NIR and d) PL emission depending on the wavelengths. e) PL emission obtained from transistors with 765 nm laser excitation. Images show several channels.

Figure 6.18 shows the LEFET measurements of the PbS QD based FET in which the thickness of semiconducting QD layer is 120 nm. The image of electrodes and the NIR emission is shown in Figure 6.18a and b, respectively. In this example, the channel length is 5 μm. Red dash lines represent the channel length of the FETs in Figure 6.18b. If the position of the NIR emission in the channel is considered, NIR emission is confined in one of the electrodes. It can not be moved by applying different voltages. If we consider the transfer curves of the same device, we can easily specify that NIR emission confines near the electrode which injects holes. Since the electron injection of these devices is larger than the hole injection, then electrons move the hole injecting electrode faster than holes.

Independent of the position of this NIR emission, it is remarkable that the NIR emission is obtained as a uniform line without any line fragments, single dots or agglomerations. It means that there are a uniform charge injection and charge transport. This could be achieved only with a uniform, homogeneous PbS layer.

In Figure 6.18c and d, the electroluminescence and photoluminescence emission with respect to wavelengths are shown. Here it is clearly seen that the PL is much higher than the EL emission. In a sense, this is expected, because while the photoluminescence is determined by simply optical properties of the material/device, the EL is determined by various factors like optical properties, physical and chemical properties, electrical properties, optically active layers, contacts of the device etc. It means that having a high PL efficiency is not always a proof to have a high EL efficiency. Even if the whole parameters are achieved to get good EL emission, it is still expected to have much higher PL emission than EL. Because, in our device, PL is obtained from the whole channel and the excitons are generated in the whole QD layer,120 nm. However, EL is generated only at the interface between QD and dielectric PMMA. This thickness should be around 1-2 nm (Zakharko et al., 2016).

Similar measurements were done with the same design FETs but with thicker QD layer, 165 nm. TheNIR emission in the 5 μm channel could be seen in Figure 6.19. The results are comparable with the previous example that, the NIR emission is obtained uniformly and confined in one electrode in which holes are injected. These results correlate the transfer curves of the same devices in which the electron currents are higher than the hole currents. This results in the higher electron field-effect mobility than holes. As a consequence of this, these FETs could be classified as unipolar as we mentioned before.
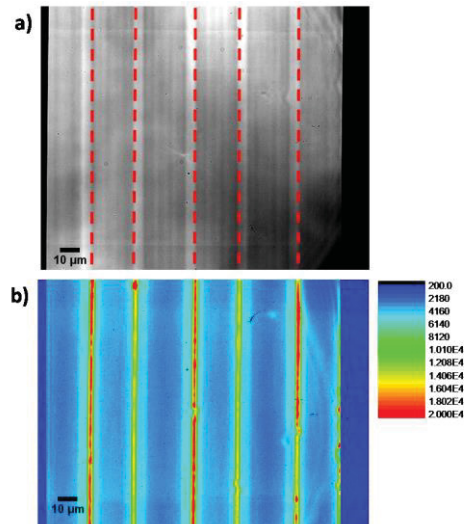
Figure 6.19. a) The image of 5µm channels The red dash lines represent the position of NIR emission. b)NIR image (wavelength between 950 – 1600 nm) showing electroluminescence from PbS QD based FET in which the thickness of QD layer is 165 nm. Electrodes could be noticeable by the color. The EL is mainly confined to the electrode which injects holes. There is no movement to the electron injecting electrode. Vg = 20V. Vd = 20V. Integration time is 20s.
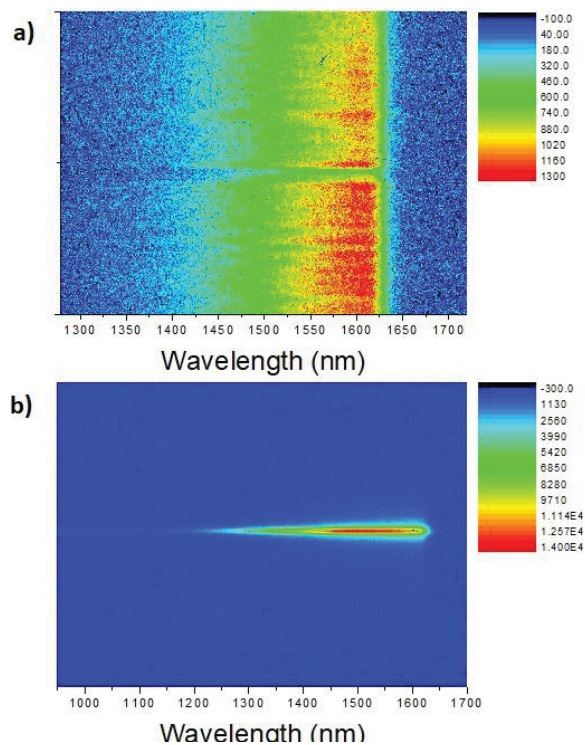
Figure 6.20. a) NIR and b) PL emission depending on the wavelengths obtained from PbS QD based FET in which the thickness of QD layer is 165 nm

Figure 6.20 shows the NIR and PL emission with respect to wavelengths obtained from the same FET. If we compare this NIR emission with the previous FET (Figure 6.18c) NIR emission is much higher when the QD layer is thicker. However, in both EL and PL, it is not possible to obtain the whole spectra because of the detection limit of the detector and the significant redshift of the QD emission. As we introduced before the PL emission of the QDs in film phase shifted to longer wavelengths than the solution phase. However, the obtained red shift in the transistors is more than expected. That enormous redshift may stem from the several steps that we did during the fabrication of the FETs. In the coating of HfO_x dielectric, the samples are heated up to 100°C under vacuum. This process takes at least 6 hours. (Details are given under "Fabrication of FETs and LEFETs" title). Also, evaporation of gate electrode may stem from the redshift because of high-temperature and vacuum requirement.

The same light emission studies are done with the other FETs in which SWNTs are also used with PbS QDs as a semiconductor. However, no EL could be obtained from these devices. As we mentioned before, EL could be obtained only for the smallest channel length, 5μm. However, the FET with the hybrid semiconductor layer, the transfer curves for 5μm channel does not proper to get good light emission. Although the transfer curves in the 40μm channel were good enough, we could not obtain electroluminescence.

6.4. Conclusion

Field effect transistors were chosen in terms of their capability of investigating charge transport. Also, the switching properties of transistors and light emitting properties of light emitting diodes could be combined in light emitting field effect transistors. This part of the Ph.D. study was carried on in Physical Chemistry Department of Heidelberg University in Germany with the help of the financial support of TUBITAK (2214/A Scholarship). Dr. Jana Zaumseil and her group (Nanomaterials for optoelectronics – NMOE) advised me in terms of design and fabrication of QD based LEFETs. PbS quantum dots were used as a semiconducting layer because of their higher bandgap and high-quality emission properties in NIR region. For the whole study "Bottom contact top-gate" transistor design was used. Since HfO_x dielectric protects to QDs from the oxidation, the measurements were taken in both glovebox and in the air

without any encapsulation requirement. The other dielectric, PMMA, protected the semiconducting layer from the HfOx deposition.

The transfer and output curves were taken for the fabricated PbS QD based FETs. The results showed that, although there is a characteristic "V-shape" in transfer curves, the electron injection is higher than the hole injection. This means that FETs are classified as unipolar rather than ambipolar. If we compare the drain current with the literature, it is necessary to increase the currents. SWNTs are used with PbS QDs as a semiconducting layer for this purpose. However, further optimizations will be helpful in order to increase the device quality.

LEFET measurements were taken in the air. We obtained nice electroluminescence from the QD based FETs. As shown in the NIR image from the electrodes there is a nice uniform EL line without any agglomeration, fragments or single dots. This is also a useful proof for the homogeneous and uniform coating of QDs after ligand exchange procedures. The obtained uniform EL line confined near the electrode which injects holes. There is no movement dependent on the voltage applied. This is also another proof for unipolar FETs.

CHAPTER 7

CONCLUSION

We developed the colloidal monodisperse and highly luminescent zinc and cadmium based nanocrystals by using different synthesis methods under an inert atmosphere. Reactant concentrations, the ratio of reactants, reaction temperature, volume and time, capping agents, pH of the medium were optimized to obtain colloidal quantum dots with narrow full width at half maximum (FWHM), high photoluminescence quantum efficiency (PL QE), and monodispersity. Several analytical techniques were used for both optical and structural characterization. Absorption and photoluminescence spectra, time-correlated single photon counting (TCSPC) measurements, fiber-optic spectrometer integrated to confocal microscope for microphotoluminescence measurements were performed for optical characterization. In order to investigate the elemental composition and crystal structure, x-ray powder diffraction (XRD), scanning electron microscopy and its x-ray energy dispersive spectroscopy detector (SEM and SEM-EDS), transmission electron microscopy (TEM), electron paramagnetic resonance (EPR) spectroscopy, dynamic light scattering (DLS), small angle x-ray scattering (SAXS), thermal gravimetric analysis (TGA) were used.

Water-dispersible ZnS_xSe_{1-x} nanoalloys were synthesized by a modified one pot aqueous method. Different Zn precursors (Zinc acetate ($ZnAc_2$), Zinc nitrate ($Zn(NO_3)_2$ and Zinc chloride ($ZnCl_2$)) were used with different capping agents thioglycolic acid (TGA), mercaptopropionic acid (MPA) and N-acetyl-L-cysteine (NAC). Results showed that capping agents are significantly effective on the optical properties of the QDs. Although all the ZnS_xSe_{1-x} nanoalloys with different capping agents have well-defined absorption spectra, only the MPA capped ZnS_xSe_{1-x} nanoalloys give an intense emission peak in the blue region of the electromagnetic spectrum with a trap state at the longer wavelengths. When the zinc precursor was changed, the trend in the emission spectra showed no difference. The optical properties were also controlled by the particle size and the alloy composition. Increasing the reaction time in a homogeneous nanoalloy, results increase in the particle size and shifts to the red (higher wavelengths – lower energetic) region. The increase in the sulfur amount in the alloy composition

results in a blue shift (lower wavelengths – higher energetic regions). The results are observed from the optical spectra and proved with the SEM-EDS and XRD analysis. Increasing in sulfur amount in the alloy composition resulted in shifts in the 2-theta angles through the ZnS binary pattern. Mn ion was doped to TGA capped ZnS_xSe_{1-x} nanoalloys in order to add magnetic susceptibility. Addition of Mn ion up to 10 % did not affect the optical spectra and the particle size. However SEM-EDS analysis proved the increase in Mn ion concentration in the alloy composition. Also, XRD diffractogram showed some shifts in (220) and (311) planes through the higher angles. On the other hand, we did not observe a significant difference in (111) plane. This results point out that Mn^{2+} ions substitutionally bound to (220) and (311) faces in the zinc blende cubic structure. In consequence of no visible emission comes from Mn ion in the PL spectra, we proposed that doped Mn ions are incorporated on the surface of ZnS_xSe_{1-x} nanoalloys. EPR measurements were performed to support the hypothesis about the surface incorporation of the Mn ion in the ZnS_xSe_{1-x} nanoalloys. Since the electronic configuration of Mn ion ends with $3d^5$ orbital, the hyperfine interaction with Mn ion results in 6-line splitting in the EPR spectra. EPR analysis for both liquid (colloidal) and powder forms was carried out. The substitutionally bound Mn ions on the surfaces interact with each other strongly and as a result, the broadening in the EPR spectra for the nanoalloys in the powder was observed. However, when the alloyed particles are in the dispersion, the doped Mn ions cannot interact (observed the hyperfine splitting even higher level of doping up to 10 %)) with each other due to fast motions of particles in aqueous dispersions.

For the first time in the literature, colloidal TOPO capped $Zn_xCd_{1-x}S_ySe_{1-y}$ quaternary nanoalloys were synthesized with the modified two-phase method at relatively low reaction temperatures. Zinc myristate (ZnMA), cadmium myristate (CdMA), thiourea and freshly synthesized NaHSe were used as Zn, Cd, S and Se precursors, respectively. We tuned the optical properties of $Zn_xCd_{1-x}S_ySe_{1-y}$ and $Zn_xCd_{1-x}S_ySe_{1-y}$/ZnCdS nanoalloys from blue to orange color by the particle size, alloy composition and the thickness of the ZnCdS shell layer. In order to control the optical properties and to form monodispersed, high-quality (high PL QE and narrow FWHM) QDs, the ratio of the reactants, reaction volume and reaction time was optimized. The alloy compositions determined by SEM-EDS were varied between 0.05 < x,y < 0.90 for $Zn_xCd_{1-x}S_ySe_{1-y}$ nanoalloys. ZnCdS shell was grown on the core of $Zn_xCd_{1-x}S_ySe_{1-y}$ nanoalloys and photophysical parameters were investigated. The relevant precursors for

the shell composition were added with different amounts. Increasing the shell layer resulted in more red shifts in the electromagnetic spectrum. Also, PL QE increased at first, however, further increase in thickness of shell layer decreased the PL QE. The PL QE and lifetime values resulted similarly for both core and core-shell $Zn_xCd_{1-x}S_ySe_{1-y}$ nanoalloys as up to 52 % and around 25 ns, respectively. TEM images and XRD analysis proved the formation of monodispersed particles with 3 – 4 nm with zinc blende cubic structure.

Microphotoluminescence measurements of spin-coated core and core/shell $Zn_xCd_{1-x}S_ySe_{1-y}$ and $Zn_xCd_{1-x}S_ySe_{1-y}/ZnCdS$ nanoalloys were carried out by fiber optic spectrometer integrated to confocal microscope. Hg lamp was used with proper filter sets to obtain continuous 365 nm light excitation. According to the measurements and calculations, 5.45×10^{-19} joule per photon energy comes from the objective to the sample. Furthermore, we estimated that there are 10^3 photons for one nanoparticle. We proposed that this number of photons may induce linear optical processes like formation of single excitons and multi-excitons (with lower probabilty) in the nanoalloys. The calibration curve of the excitation light intensity (power) with respect to PL intensity showed that collected emission from fiber optic CCD spectrometer is directly proportional with the power of the excitation light. We observed that the micro-PL measurements were collected only from the center of the image (from the circle with approximately 5 μm in diameter). During the measurements, photobleaching was observed with 5 – 6 nm of blue shift in the PL spectra. Time depending bleaching behavior of the QDs was analyzed with kinetic equation having the single exponential decay. Photobleaching rate constants and the photobleaching times were obtained as a function of excitation light intensity. Because of the excess reactants and organic ligands in the medium, unpurified $Zn_xCd_{1-x}S_ySe_{1-y}$ nanoalloys showed faster photobleaching than purified samples. The film thickness and the integration time did not affect the photobleaching rate constants significantly. Collected PL intensity increases according to the film thickness and the integration time. Since the number of $Zn_xCd_{1-x}S_ySe_{1-y}$ nanoalloys differs according to the film thickness, the intensity of the collected PL spectra changes. Similarly, increasing the integration time results in the increase in the number of photons collected which results in an enhancement in the PL spectra. On the other hand the power of the excitation light affects the photobleaching significantly. When the power was higher than 11 μW caused photobleaching in $Zn_xCd_{1-x}S_ySe_{1-y}$ nanoalloys. At 11 μW, PL emission intensity remains constant for 200 seconds but after that photobleaching

started. At 2 µW power, we did not observe any photobleaching or blueing in $Zn_xCd_{1-x}S_ySe_{1-y}$ nanoalloys. We proposed that the photobleaching and the blueing in the PL spectra after excitation at specific light power and duration time stem from two reasons: i) oxides of Cd, Zn, S and/or Se formed and leave from the surface of the QD. As a result of the particle size decreases and the PL spectra shifts to blue region. ii) formed oxides result in the changes in the alloy composition. Since Cd is more electronegative than Zn, Cd oxides are more likely to form CdO forms. The increase in the Zn amount in the alloy composition results blueing in the PL spectra.

Scale up production techniques were investigated in terms of producing a larger amount of QDs for QD based device applications. For this purpose, two different type reactors were designed and tested, the high-volume reactor and the flow reactor. High volume reactor allows setting the same experimental conditions with the standard/classical batch system. Better temperature control and mechanical stirring (instead of mixing with a magnetic bar) are the advantages of the high-volume reactor compared to flask based low volume reactors. Flow reactors provide better control on temperature, mass transport, mixing and continous production. CdTe QDs were synthesized as test experiments in both reactors. Comparison of the results with reactions carried out in the classical standard 250 ml glass reaction flask showed the adaptability of the QD synthesis for the high-volume reactor. That is the reason $Zn_xCd_{1-x}S_ySe_{1-y}$ nanoalloys were synthesized by using 500 ml, 1000 ml, and 2000 ml glass reactor vessels. SEM-EDS analysis showed that from different reaction volumes, the similar alloy composition of the QDs with the same initial mole ratios was obtained. The only difference was the growth rates of the nanoalloys. The bigger the reaction volume, the slower the reaction growth rate. The reason is most probably the mixing capability of the mechanical stirrer is not sufficient for the 2000 ml reaction volumes. Nevertheless, the absorption and PL characteristics were quite comparable with each other. Since we understood that high-volume reactor has a limitation in the amount of production, flow reactor was designed and tested again with CdTe nanocrystals. Although all the test experiments gave comparable and optimistic results for the further experiments for $Zn_xCd_{1-x}S_ySe_{1-y}$ nanoalloys in the flow reactors.

In terms of QD based device applications field effect transistors were chosen in terms of their capability of investigating charge transport. Also, the switching properties of transistors and light emitting properties of light emitting diodes could be combined in light emitting field effect transistors (LEFETs). This part of the Ph.D. study was carried

on in the Physical Chemistry Department of Heidelberg University in Germany with the help of the financial support of TUBITAK (2214/A Scholarship). Dr. Jana Zaumseil and her group (Nanomaterials for optoelectronics – NMOE) advised me in terms of design and fabrication of QD based LEFETs. Since the NIR detector existed and QDs with higher band gap were required, PbS QDs were used as an emissive layer in LEFETs. Bottom contact top-gate transistor design was used in all fabricated LEFETs. Using HfO$_x$ as a dielectric, QDs were protected from the oxidation. That is the reason the measurements were taken in both gloveboxes and in the air without any encapsulation. The other dielectric, PMMA, protected the semiconducting layer from the HfO$_x$ deposition. The transfer and output curves showed that although there was a characteristic "V-shape" in transfer curves, the electron injection was higher than the hole injection. This means that FETs were classified as unipolar rather than ambipolar. In order to increase the drain current, single wall carbon nanotubes were used as another layer before PbS QDs. LEFET measurements were taken in the air without any encapsulation. We obtained very good electroluminescence from the QD based LEFETs. NIR image obtained from the electrodes showed that there was a nice uniform EL line without any agglomeration, fragments or single dots. This was also a useful proof for the homogeneous and uniform coating of QDs after ligand exchange procedures. The obtained uniform EL line confined near the electrode which injects holes. There was no movement dependent on the voltage applied. This was also another proof for unipolar FETs.

REFERENCES

Aboulaich, A., et al. 2012. "One-pot noninjection route to CdS quantum dots via hydrothermal synthesis", *ACS applied materials & interfaces*, (4), 2561-2569.

Anikeeva, P. O., Halpert, J. E., Bawendi, M. G. and Bulovic, V. 2009. "Quantum dot light-emitting devices with electroluminescence tunable over the entire visible spectrum", *Nano Lett*, (9), 2532-2536.

Anikeeva, P. O., Halpert, J. E., Bawendi, M. G. and Bulović, V. 2007. "Electroluminescence from a Mixed Red−Green−Blue Colloidal Quantum Dot Monolayer", *Nano Letters*, (7), 2196-2200.

Baek, J., Allen, P. M., Bawendi, M. G. and Jensen, K. F. 2011. "Investigation of Indium Phosphide Nanocrystal Synthesis Using a High-Temperature and High-Pressure Continuous Flow Microreactor", *Angewandte Chemie-International Edition*, (50), 627-630.

Bailey, R. E. and Nie, S. 2003. "Alloyed Semiconductor Quantum Dots: Tuning the Optical Properties without Changing the Particle Size", *J. Amer. Chem. Soc.*, (125), 7100-7106.

Beermann, P. A. G., McGarvey, B. R., Skadtchenko, B. O., Muralidharan, S. and Sung, R. C. W. 2006. "Cationic Substitution Sites in Mn2+-doped ZnS Nanoparticles", *Journal of Nanoparticle Research*, (8), 235-241.

Berezin, M. Y. and Achilefu, S. 2010. "Fluorescence Lifetime Measurements and Biological Imaging", *Chem. Rev.*, (110), 2641-2684.

Bergin, S. D., et al. 2009. "Multicomponent Solubility Parameters for Single-Walled Carbon Nanotube−Solvent Mixtures", *ACS Nano*, (3), 2340-2350.

Borse, P. H., et al. 1999. "Effect of ${\mathrm{Mn}}^{2+}$ concentration in ZnS nanoparticles on photoluminescence and electron-spin- resonance spectra", *Physical Review B*, (60), 8659-8664.

Brichkin, S. B. and Chernykh, E. V. 2011. "Hydrophilic semiconductor quantum dots", *High Energy Chemistry*, (45), 1-12.

Brust, M., Walker, M., Bethell, D., Schiffrin, D. J. and Whyman, R. 1994. "Synthesis of thiol-derivatised gold nanoparticles in a two-phase Liquid-Liquid system", *Journal of the Chemical Society, Chemical Communications*, 801-802.

Cao, J., Xue, B., Li, H., Deng, D. and Gu, Y. 2010. "Facile synthesis of high-quality water-soluble N-acetyl-L-cysteine-capped Zn(1-x)Cd(x)Se/ZnS core/shell quantum dots emitting in the violet-green spectral range", *Journal of colloid and interface science*, (348), 369-376.

Caruge, J. M., Halpert, J. E., Wood, V., Bulović, V. and Bawendi, M. G. 2008. "Colloidal quantum-dot light-emitting diodes with metal-oxide charge transport layers", *Nature Photonics*, (2), 247.

Chan, E. M., Mathies, R. A. and Alivisatos, A. P. 2003. "Size-controlled growth of CdSe nanocrystals in microfluidic reactors", *Nano Letters*, (3), 199-201.

Chang, J., Xia, H., Wu, S. and Zhang, S. 2014. "Prolonging the lifetime of excited electrons of QDs by capping them with [small pi]-conjugated thiol ligands", *Journal of Materials Chemistry C*, (2), 2939-2943.

Chen, H.-Y., Maiti, S. and Son, D. H. 2012. "Doping Location-Dependent Energy Transfer Dynamics in Mn-Doped CdS/ZnS Nanocrystals", *ACS Nano*, (6), 583-591.

Chen, O., et al. 2013. "Compact high-quality CdSe-CdS core-shell nanocrystals with narrow emission linewidths and suppressed blinking", *Nature materials*, (12), 445-451.

Chen, W., et al. 2000. "Pressure dependence of Mn2+ fluorescence in ZnS:Mn2+ nanoparticles", *Journal of Luminescence*, (91), 139-145.

Chuang, C.-H. M., Brown, P. R., Bulović, V. and Bawendi, M. G. 2014. "Improved performance and stability in quantum dot solar cells through band alignment engineering", *Nat Mater*, (13), 796-801.

Chuang, C. H., Brown, P. R., Bulovic, V. and Bawendi, M. G. 2014. "Improved performance and stability in quantum dot solar cells through band alignment engineering", *Nature materials*, (13), 796-801.

Coe, S., Woo, W. K., Bawendi, M. and Bulovic, V. 2002. "Electroluminescence from single monolayers of nanocrystals in molecular organic devices", *Nature*, (420), 800-803.

Colvin, V. L., Schlamp, M. C. and Alivisatos, A. P. 1994. "Light-Emitting-Diodes Made from Cadmium Selenide Nanocrystals and a Semiconducting Polymer", *Nature*, (370), 354-357.

Cordero, S. R., Carson, P. J., Estabrook, R. A., Strouse, G. F. and Buratto, S. K. 2000. "Photo-Activated Luminescence of CdSe Quantum Dot Monolayers", *The Journal of Physical Chemistry B*, (104), 12137-12142.

Dai, X., et al. 2014. "Solution-processed, high-performance light-emitting diodes based on quantum dots", *Nature*, (515), 96-99.

Deng, D., Qu, L., Achilefu, S. and Gu, Y. 2013. "Broad spectrum photoluminescent quaternary quantum dots for cell and animal imaging", *Chemical Communications*, (49), 9494-9496.

Deng, Z., Yan, H. and Liu, Y. 2009. "Band Gap Engineering of Quaternary-Alloyed ZnCdSSe Quantum Dots via a Facile Phosphine-Free Colloidal Method", *J. Amer. Chem. Soc.*, (131), 17744-17745.

Dingle, R., Wiegmann, W. and Henry, C. H. 1988. "Quantum States of Confined Carriers in Very Thin AlxGa1-x As-GaAs-AlxGa1-xAs Heterostructures". Electronic Structure of Semiconductor Heterojunctions. S*pringer Netherlands*: 173-176.

Feng, B., Cao, J., Yang, J., Yang, S. and Han, D. 2014. "Characterization and photocatalytic activity of ZnSe nanoparticles synthesized by a facile solvothermal method, and the effects of different solvents on these properties", *Mater. Res. Bull.*, (60), 794-801.

Fery-Forgues, S. and Lavabre, D. 1999. "Are Fluorescence Quantum Yields So Tricky to Measure? A Demonstration Using Familiar Stationery Products", *Journal of Chemical Education*, (76), 1260.

Held, M., Schießl, S. P., Miehler, D., Gannott, F. and Zaumseil, J. 2015. "Polymer/metal oxide hybrid dielectrics for low voltage field-effect transistors with solution-processed, high-mobility semiconductors", *Applied Physics Letters*, (107), 083301.

Hofman, E., Robinson, R. J., Li, Z.-J., Dzikovski, B. and Zheng, W. 2017. "Controlled Dopant Migration in CdS/ZnS Core/Shell Quantum Dots", *Journal of the American Chemical Society*, (139), 8878-8885.

Hoyer, P., Staudt, T., Engelhardt, J. and Hell, S. W. 2011. "Quantum Dot Blueing and Blinking Enables Fluorescence Nanoscopy", *Nano Letters*, (11), 245-250.

Huang, X., et al. 2018. "Narrowing the Photoluminescence of Aqueous CdTe Quantum Dots via Ostwald Ripening Suppression Realized by Programmed Dropwise Precursor Addition", *The Journal of Physical Chemistry C*, (122), 11109-11118.

Hung, C.-C., et al. 2017. "Highly Luminescent Dual-Color-Emitting Alloyed [ZnxCd1–xSeyS1–y] Quantum Dots: Investigation of Bimodal Growth and Application to Lighting", *The Journal of Physical Chemistry C*, (121), 28373-28384.

Hurst, J. R., McDonald, J. D. and Schuster, G. B. 1982. "Lifetime of singlet oxygen in solution directly determined by laser spectroscopy", *Journal of the American Chemical Society*, (104), 2065-2067.

Igarashi, T., Isobe, T. and Senna, M. 1997. "EPR study of ${\mathrm{Mn}}^{2+}$ electronic states for the nanosized ZnS:Mn powder modified by acrylic acid", *Physical Review B*, (56), 6444-6445.

Ippen, C., et al. 2015. "Large-scale synthesis of high quality InP quantum dots in a continuous flow-reactor under supercritical conditions", *Nanotechnology*, (26).

Ithurria, S., Guyot-Sionnest, P., Mahler, B. and Dubertret, B. 2007. "Mn2+ as a radial pressure gauge in colloidal core/shell nanocrystals", *Physical review letters*, (99), 265501.

Jakubka, F., et al. 2012. "Effect of Polymer Molecular Weight and Solution Parameters on Selective Dispersion of Single-Walled Carbon Nanotubes", *ACS Macro Letters*, (1), 815-819.

Jiang, F. and Muscat, A. J. 2012. "Ligand-Controlled Growth of ZnSe Quantum Dots in Water during Ostwald Ripening", *Langmuir*, (28), 12931-12940.

Jing, L., et al. 2016. "Aqueous Based Semiconductor Nanocrystals", *Chemical Reviews*, (116), 10623-10730.

Jo, C. H., et al. 2014. "Low-temperature annealed PbS quantum dot films for scalable and flexible ambipolar thin-film-transistors and circuits", *Journal of Materials Chemistry C*, (2), 10305-10311.

Kang, B. H., et al. 2015. "Solution Processable CdSe/ZnS Quantum Dots Light-Emitting Diodes Using ZnO Nanocrystal as Electron Transport Layer", *J Nanosci Nanotechnol*, (15), 7416-7420.

Kang, X., Huang, L., Yang, Y. and Pan, D. 2015. "Scaling up the Aqueous Synthesis of Visible Light Emitting Multinary AgInS2/ZnS Core/Shell Quantum Dots", *The Journal of Physical Chemistry C*, (119), 7933-7940.

Kang, X., et al. 2015. "Large-scale synthesis of water-soluble CuInSe2/ZnS and AgInSe2/ZnS core/shell quantum dots", *Green Chemistry*, (17), 4482-4488.

Kershaw, S. V., et al. 2017. "Investigation of the Exchange Kinetics and Surface Recovery of CdxHg1–xTe Quantum Dots during Cation Exchange Using a Microfluidic Flow Reactor", *Chemistry of Materials*, (29), 2756-2768.

Kim, H., Cho, K., Kim, D.-W., Lee, H.-R. and Kim, S. 2006. "Bottom- and top-gate field-effect thin-film transistors with p channels of sintered HgTe nanocrystals", *Applied Physics Letters*, (89), 173107.

Kim, K.-J., et al. 2014. "Continuous Microwave-Assisted Gas–Liquid Segmented Flow Reactor for Controlled Nucleation and Growth of Nanocrystals", *Crystal Growth & Design*, (14), 5349-5355.

Kim, K., Jeong, S., Woo, J. Y. and Han, C.-S. 2012. "Successive and large-scale synthesis of InP/ZnS quantum dots in a hybrid reactor and their application to white LEDs", *Nanotechnology*, (23).

Koneswaran, M. and Narayanaswamy, R. 2009. "Mercaptoacetic acid capped CdS quantum dots as fluorescence single shot probe for mercury(II)", *Sensors and Actuators B: Chemical*, (139), 91-96.

Lad, A. D., et al. 2007. "Magnetic behavior of manganese-doped ZnSe quantum dots", *Journal of Applied Physics*, (101), 103906.

Lakowicz, J. R. (2006). *Principles of Fluorescence Spectroscopy* New York, Springer Science+Business Media.

Lakowicz, J. R. (2006). Time-Domain Lifetime Measurements. *Principles of Fluorescence Spectroscopy*. J. R. Lakowicz. Boston, MA, Springer US**:** 97-155.

Law, M., et al. 2008. "Structural, optical, and electrical properties of PbSe nanocrystal solids treated thermally or with simple amines", *J Am Chem Soc*, (130), 5974-5985.

Lee, S. F. and Osborne, M. A. 2007. "Photodynamics of a Single Quantum Dot: Fluorescence Activation, Enhancement, Intermittency, and Decay", *J. Amer. Chem. Soc.*, (129), 8936-8937.

Lesnyak, V., Plotnikov, A., Gaponik, N. and Eychmuller, A. 2008. "Toward efficient blue-emitting thiol-capped Zn1-xCdxSe nanocrystals", *Journal of Materials Chemistry*, (18), 5142-5146.

Li, H., Shih, W. Y. and Shih, W.-H. 2010. "Highly Photoluminescent and Stable Aqueous ZnS Quantum Dots", *Ind. Eng. Chem. Res.*, (49), 579-582.

Li, Y. Q., et al. 2005. "White organic light-emitting devices with CdSe/ZnS quantum dots as a red emitter", *J Appl Phys*, (97).

Lignos, I., Maceiczyk, R. and deMello, A. J. 2017. "Microfluidic Technology: Uncovering the Mechanisms of Nanocrystal Nucleation and Growth", *Accounts of Chemical Research*, (50), 1248-1257.

Liu, C., Ji, Y. and Tan, T. 2013. "One-pot hydrothermal synthesis of water-dispersible ZnS quantum dots modified with mercaptoacetic acid", *Journal of Alloys and Compounds*, (570), 23-27.

Liu, X., et al. 2013. "Hydrothermal Synthesis of CdSe Quantum Dots and Their Photocatalytic Activity on Degradation of Cefalexin", *Ind. Eng. Chem. Res.*, (52), 15015-15023.

Luther, J. M., et al. 2008. "Structural, optical, and electrical properties of self-assembled films of PbSe nanocrystals treated with 1,2-ethanedithiol", *ACS Nano*, (2), 271-280.

Luzio, A., Ferré, F. G., Fonzo, F. D. and Caironi, M. 2014. "Hybrid Nanodielectrics for Low-Voltage Organic Electronics", *Advanced Functional Materials*, (24), 1790-1798.

M., v. S. W. G. J. H., M., F. P. L. T., A., B. A., C., G. H. and Andries, M. 2002. "Blueing, Bleaching, and Blinking of Single CdSe/ZnS Quantum Dots", *ChemPhysChem*, (3), 871-879.

Ma, J., et al. 2013. "Phosphorescence detection of hydrochlorothiazide using Mn-doped ZnS quantum dots", *Analytical Methods*, (5), 6094-6099.

Mandal, A., Dandapat, A. and De, G. 2012. "Magic sized ZnS quantum dots as a highly sensitive and selective fluorescence sensor probe for Ag+ ions", *Analyst*, (137), 765-772.

Marre, S., et al. 2008. "Supercritical Continuous-Microflow Synthesis of Narrow Size Distribution Quantum Dots", *Advanced Materials*, (20), 4830-+.

Merino, G., Vela, A. and Heine, T. 2005. "Description of Electron Delocalization via the Analysis of Molecular Fields", *Chemical Reviews*, (105), 3812-3841.

Miao, Y., et al. 2015. "Photodegradation of Mercaptopropionic Acid- and Thioglycollic Acid-Capped CdTe Quantum Dots in Buffer Solutions", *Journal of Nanoscience and Nanotechnology*, (15), 4462-4469.

Moghaddam, M. M., Baghbanzadeh, M., Sadeghpour, A., Glatter, O. and Kappe, C. O. 2013. "Continuous-Flow Synthesis of CdSe Quantum Dots: A Size-Tunable and Scalable Approach", *Chemistry-a European Journal*, (19), 11629-11636.

Moreels, I., et al. 2009. "Size-Dependent Optical Properties of Colloidal PbS Quantum Dots", *ACS Nano*, (3), 3023-3030.

Nightingale, A. M., et al. 2013. "Large-scale synthesis of nanocrystals in a multichannel droplet reactor", *Journal of Materials Chemistry A*, (1), 4067-4076.

Nightingale, A. M. and de Mello, J. C. 2010. "Microscale synthesis of quantum dots", *Journal of Materials Chemistry*, (20), 8454-8463.

Nightingale, A. M. and deMello, J. C. 2013. "Segmented Flow Reactors for Nanocrystal Synthesis", *Advanced Materials*, (25), 1813-1821.

Nistor, S. V., Stefan, M., Nistor, L. C., Ghica, D. and Vlaicu, I. D. 2016. "Distribution and interaction of Mn2+ ions incorporated in cubic ZnS quantum dots over a broad concentration range", *Journal of Alloys and Compounds*, (662), 193-199.

Nistor, S. V., et al. 2015. "Doping Ultrasmall Cubic ZnS Nanocrystals with Mn2+ Ions over a Broad Nominal Concentration Range", *The Journal of Physical Chemistry C*, (119), 23781-23789.

Nistor, S. V., Stefan, M., Nistor, L. C., Goovaerts, E. and Van Tendeloo, G. 2010. "Incorporation and localization of substitutional ${\text{Mn}}^{2+}$ ions in cubic ZnS quantum dots", *Physical Review B*, (81), 035336.

Nistor, S. V., et al. 2016. "Aggregates of Mn2+ Ions in Mesoporous Self-Assembled Cubic ZnS:Mn Quantum Dots: Composition, Localization, Structure, and Magnetic Properties", *The Journal of Physical Chemistry C*, (120), 14454-14466.

Norberg, N. S., et al. 2004. "Synthesis of Colloidal Mn2+:ZnO Quantum Dots and High-TC Ferromagnetic Nanocrystalline Thin Films", *Journal of the American Chemical Society*, (126), 9387-9398.

Ortiz, R. P., Facchetti, A. and Marks, T. J. 2010. "High-k Organic, Inorganic, and Hybrid Dielectrics for Low-Voltage Organic Field-Effect Transistors", *Chemical Reviews*, (110), 205-239.

Pan, A., Liu, R., Sun, M. and Ning, C.-Z. 2009. "Quaternary Alloy Semiconductor Nanobelts with Bandgap Spanning the Entire Visible Spectrum", *Journal of the American Chemical Society*, (131), 9502-9503.

Pan, A., Liu, R., Sun, M. and Ning, C.-Z. 2010. "Spatial Composition Grading of Quaternary ZnCdSSe Alloy Nanowires with Tunable Light Emission between 350 and 710 nm on a Single Substrate", *ACS Nano*, (4), 671-680.

Pan, D., Wang, Q., Jiang, S., Ji, X. and An, L. 2007. "Low-Temperature Synthesis of Oil-Soluble CdSe, CdS, and CdSe/CdS Core−Shell Nanocrystals by Using Various Water-Soluble Anion Precursors", *The Journal of Physical Chemistry C*, (111), 5661-5666.

Park, S., Kim, H., Jin, C. and Lee, C. 2012. "Synthesis, structure, and photoluminescence properties of ZnSSe alloy nanorods", *Curr. Appl. Phys.*, (12), 499-503.

Pechstedt, K., Whittle, T., Baumberg, J. and Melvin, T. 2010. "Photoluminescence of Colloidal CdSe/ZnS Quantum Dots: The Critical Effect of Water Molecules", *The Journal of Physical Chemistry C*, (114), 12069-12077.

Peng, X., et al. 2000. "Shape control of CdSe nanocrystals", *Nature*, (404), 59.

Pereira, A. S., et al. 2006. "Synthesis, surface modification and optical properties of Tb 3+ -doped ZnO nanocrystals", *Nanotechnology*, (17), 834.

Phillips, T. W., Lignos, I. G., Maceiczyk, R. M., deMello, A. J. and deMello, J. C. 2014. "Nanocrystal synthesis in microfluidic reactors: where next?", *Lab on a Chip*, (14), 3172-3180.

Pradhan, N., Goorskey, D., Thessing, J. and Peng, X. 2005. "An Alternative of CdSe Nanocrystal Emitters: Pure and Tunable Impurity Emissions in ZnSe Nanocrystals", *Journal of the American Chemical Society*, (127), 17586-17587.

Proshchenko, V. and Dahnovsky, Y. (2015). Transition Metal-Doped Semiconductor Quantum Dots: Tunable Emission. Photoinduced Processes at Surfaces and in Nanomaterials, *American Chemical Society*. 1196**:** 117-135.

Protière, M. and Reiss, P. 2006. "Facile synthesis of monodisperse ZnS capped CdS nanocrystals exhibiting efficient blue emission", *Nanoscale Research Letters*, (1), 62-67.

Pshenay-Severin, E., et al. 2015. "Relaxation time mapping of single quantum dots and substrate background fluorescence", *JETP Letters*, (102), 161-166.

Qian, H., et al. 2007. "High-quality and water-soluble near-infrared photolumineseent CdHgTe/CdS quantum dots prepared by adjusting size and composition", *Journal of Physical Chemistry C*, (111), 16852-16857.

Qian, H., Qiu, X., Li, L. and Ren, J. 2006. "Microwave-Assisted Aqueous Synthesis: A Rapid Approach to Prepare Highly Luminescent ZnSe(S) Alloyed Quantum Dots", *J. Phys. Chem. B*, (110), 9034-9040.

Reed, M. A., et al. 1988. "Observation of discrete electronic states in a zero-dimensional semiconductor nanostructure", *Physical Review Letters*, (60), 535-537.

Ridley, B. A., Nivi, B. and Jacobson, J. M. 1999. "All-Inorganic Field Effect Transistors Fabricated by Printing", *Science*, (286), 746-749.

Rogach, A. L., et al. 2007. "Aqueous synthesis of thiol-capped CdTe nanocrystals: State-of-the-art", *J Phys Chem C*, (111), 14628-14637.

Rogach, A. L., et al. 2007. "Aqueous Synthesis of Thiol-Capped CdTe Nanocrystals: State-of-the-Art", *The Journal of Physical Chemistry C*, (111), 14628-14637.

Schießl, S. P., et al. 2015. "Polymer-Sorted Semiconducting Carbon Nanotube Networks for High-Performance Ambipolar Field-Effect Transistors", *ACS Applied Materials & Interfaces*, (7), 682-689.

Schlamp, M. C., Peng, X. G. and Alivisatos, A. P. 1997. "Improved efficiencies in light emitting diodes made with CdSe(CdS) core/shell type nanocrystals and a semiconducting polymer", *J Appl Phys*, (82), 5837-5842.

Schornbaum, J., et al. 2015. "Light-Emitting Quantum Dot Transistors: Emission at High Charge Carrier Densities", *Nano Letters*, (15), 1822-1828.

Schwartz, D. A., Norberg, N. S., Nguyen, Q. P., Parker, J. M. and Gamelin, D. R. 2003. "Magnetic quantum dots: synthesis, spectroscopy, and magnetism of Co2+ - and Ni2+-doped ZnO nanocrystals", *J Am Chem Soc*, (125), 13205-13218.

Senthilkumar, K., Kalaivani, T., Kanagesan, S. and Balasubramanian, V. 2012. "Synthesis and characterization studies of ZnSe quantum dots", *J. Mater. Sci. Mater. Electron.*, (23), 2048-2052.

Sergey, B. B. and Vladimir, F. R. 2016. "Colloidal quantum dots: synthesis, properties and applications", *Russian Chemical Reviews*, (85), 1297.

Sevim, S., et al. 2014. "An ultraviolet photodetector with an active layer composed of solution processed polyfluorene:Zn0.71Cd0.29S hybrid nanomaterials", *Applied Surface Science*, (305), 227-234.

Shen, H., et al. 2013. "Highly Efficient Blue–Green Quantum Dot Light-Emitting Diodes Using Stable Low-Cadmium Quaternary-Alloy ZnCdSSe/ZnS Core/Shell Nanocrystals", *ACS Applied Materials & Interfaces*, (5), 4260-4265.

Smith, A. M., Mohs, A. M. and Nie, S. 2008. "Tuning the optical and electronic properties of colloidal nanocrystals by lattice strain", *Nature Nanotechnology*, (4), 56.

Smith, A. M. and Nie, S. 2009. "Next-generation quantum dots", *Nature biotechnology*, (27), 732-733.

Sooklal, K., Cullum, B. S., Angel, S. M. and Murphy, C. J. 1996. "Photophysical Properties of ZnS Nanoclusters with Spatially Localized Mn2+", *The Journal of Physical Chemistry*, (100), 4551-4555.

Stefan, M., et al. 2011. "Substitutional and surface Mn$\{\}^{2+\}$ centers in cubic ZnS:Mn nanocrystals. A correlated EPR and photoluminescence study", *Physical Review B*, (83), 045301.

Subha, R., et al. 2013. "Efficient Photoluminescence of Mn2+-Doped ZnS Quantum Dots Excited by Two-Photon Absorption in Near-Infrared Window II", *The Journal of Physical Chemistry C*, (117), 20905-20911.

Sun, Q., et al. 2007. "Bright, multicoloured light-emitting diodes based on quantum dots", *Nature Photonics*, (1), 717.

Talapin, D. V., et al. 2001. "A Novel Organometallic Synthesis of Highly Luminescent CdTe Nanocrystals", *J. Phys. Chem. B*, (105), 2260-2263.

Talapin, D. V., Lee, J.-S., Kovalenko, M. V. and Shevchenko, E. V. 2010. "Prospects of Colloidal Nanocrystals for Electronic and Optoelectronic Applications", *Chem. Rev.*, (110), 389-458.

Talapin, D. V. and Murray, C. B. 2005. "PbSe nanocrystal solids for n- and p-channel thin film field-effect transistors", *Science*, (310), 86-89.

Tang, J., et al. 2011. "Colloidal-quantum-dot photovoltaics using atomic-ligand passivation", *Nature materials*, (10), 765-771.

The European Physical Journal B - Condensed Matter and Complex SystemsChemical Society ReviewsAbdi-Ben Nasrallah, S., Ben Afia, S., Belmabrouk, H. and

Said, M. 2005. "Optoelectronic properties of zinc blendeZnSSe and ZnBeTe alloys", *Eur Phys J B Condens Matter*, (43), 3-9.

Tian, Y., et al. 2015. "Synthesis of ZnS ultrathin nanowires and photoluminescence with Mn2+ doping", *Materials Letters*, (148), 151-154.

Tsujii, N., Kitazawa, H. and Kido, G. 2003. "Magnetic properties of Mn- and Eu-doped ZnS nanocrystals", *J. Appl. Phys.*, (93), 6957-6959.

Unlu, C., Tosun, G. U., Sevim, S. and Ozcelik, S. 2013. "Developing a facile method for highly luminescent colloidal CdSxSe1-x ternary nanoalloys", *Journal of Materials Chemistry C*, (1), 3026-3034.

Veamatahau, A., et al. 2015. "Origin of surface trap states in CdS quantum dots: relationship between size dependent photoluminescence and sulfur vacancy trap states", *Physical Chemistry Chemical Physics*, (17), 2850-2858.

Voznyy, O. and Sargent, E. H. 2014. "Atomistic model of fluorescence intermittency of colloidal quantum dots", *Physical review letters*, (112), 157401.

Wang, J. and Han, H. 2010. "Hydrothermal synthesis of high-quality type-II CdTe/CdSe quantum dots with near-infrared fluorescence", *Journal of colloid and interface science*, (351), 83-87.

Waurisch, C., Liebscher, L., Sperling, E., Hickey, S. and Eychmüller, A. (2011). New aspects in the hot injection synthesis to provide large scale high quality quantum dots. DOI: 10.1142/ 9789814343909_0078

Wei, H., et al. 2012. "One-pot synthesis of ultranarrow single crystal ZnSe nanowires", *Materials Letters*, (67), 269-272.

Wu, P. and Yan, X. P. 2013. "Doped quantum dots for chemo/biosensing and bioimaging", *Chemical Society reviews*, (42), 5489-5521.

Xie, L., Harris, D. K., Bawendi, M. G. and Jensen, K. F. 2015. "Effect of Trace Water on the Growth of Indium Phosphide Quantum Dots", *Chemistry of Materials*, (27), 5058-5063.

Xie, R., Rutherford, M. and Peng, X. 2009. "Formation of High-Quality I−III−VI Semiconductor Nanocrystals by Tuning Relative Reactivity of Cationic Precursors", *J. Amer. Chem. Soc.*, (131), 5691-5697.

Xu, S., et al. 2010. "Key Roles of Solution pH and Ligands in the Synthesis of Aqueous ZnTe Nanoparticles", *Chemistry of Materials*, (22), 5838-5844.

Xu, Y., et al. (2005). Synthesis and Characterization of Silica Coated CdSe/CdS Core/Shell Quantum Dots.

Yang, H.-J. and Tuan, H.-Y. 2014. "Efficient and scalable synthesis of quantum dots using hexane as the solvent in a non-microfluidic flow reactor system", *Rsc Advances*, (4), 51926-51934.

Yang, H., et al. 2009. "Continuous Synthesis of Full-Color Emitting Core/Shell Quantum Dots via Microreaction", *Crystal Growth & Design*, (9), 4807-4813.

Yang, W.-h., Li, W.-w., Dou, H.-j. and Sun, K. 2008. "Hydrothermal synthesis for high-quality CdTe quantum dots capped by cysteamine", *Materials Letters*, (62), 2564-2566.

Yang, Y., Chen, O., Angerhofer, A. and Cao, Y. C. 2006. "Radial-Position-Controlled Doping in CdS/ZnS Core/Shell Nanocrystals", *Journal of the American Chemical Society*, (128), 12428-12429.

Yen, B. K. H., Stott, N. E., Jensen, K. F. and Bawendi, M. G. 2003. "A continuous-flow microcapillary reactor for the preparation of a size series of CdSe nanocrystals", *Advanced Materials*, (15), 1858-1862.

Yin, Y. and Alivisatos, A. P. 2005. "Colloidal nanocrystal synthesis and the organic-inorganic interface", *Nature*, (437), 664-670.

Yu, D., Wang, C. and Guyot-Sionnest, P. 2003. "n-Type conducting CdSe nanocrystal solids", *Science*, (300), 1277-1280.

Yu, W. W., Chang, E., Drezek, R. and Colvin, V. L. 2006. "Water-soluble quantum dots for biomedical applications", *Biochemical and Biophysical Research Communications*, (348), 781-786.

Yu, W. W., Qu, L., Guo, W. and Peng, X. 2003. "Experimental Determination of the Extinction Coefficient of CdTe, CdSe, and CdS Nanocrystals", *Chemistry of Materials*, (15), 2854-2860.

Yu, Y., et al. 2012. "Hydrothermal synthesis of GSH–TGA co-capped CdTe quantum dots and their application in labeling colorectal cancer cells", *Colloids and Surfaces B: Biointerfaces*, (95), 247-253.

Yuan, M., Voznyy, O., Zhitomirsky, D., Kanjanaboos, P. and Sargent, E. H. 2015. "Synergistic Doping of Fullerene Electron Transport Layer and Colloidal Quantum Dot Solids Enhances Solar Cell Performance", *Advanced Materials*, (27), 917-921.

Yuan, Z., et al. 2012. "Effect of Mercaptocarboxylic Acids on Luminescent Properties of CdTe Quantum Dots", *Journal of Fluorescence*, (22), 121-127.

Yun, H. J., et al. 2016. "Nanocrystal Size-Dependent Efficiency of Quantum Dot Sensitized Solar Cells in the Strongly Coupled CdSe Nanocrystals/TiO2 System", *ACS Applied Materials & Interfaces*, (8), 14692-14700.

Zakharko, Y., et al. 2016. "Surface Lattice Resonances for Enhanced and Directional Electroluminescence at High Current Densities", *ACS Photonics*, (3), 2225-2230.

Zaumseil, J. and Sirringhaus, H. 2007. "Electron and Ambipolar Transport in Organic Field-Effect Transistors", *Chemical Reviews*, (107), 1296-1323.

Zhang, L., Nakamura, H., Lee, C.-G. and Maeda, H. 2012. "An investigation of heating rate effects on particle size and concentration: instruction for scale-up", *Rsc Advances*, (2), 3708-3713.

Zhang, L. and Xia, Y. 2014. "Scaling up the Production of Colloidal Nanocrystals: Should We Increase or Decrease the Reaction Volume", *Advanced Materials*, (26), 2600-2606.

Zhang, W. J., Li, Y., Zhang, H., Zhou, X. G. and Zhong, X. H. 2011. "Facile Synthesis of Highly Luminescent Mn-Doped ZnS Nanocrystals", *Inorganic Chemistry*, (50), 10432-10438.

Zhao, T., et al. 2016. "Advanced Architecture for Colloidal PbS Quantum Dot Solar Cells Exploiting a CdSe Quantum Dot Buffer Layer", *ACS Nano*, (10), 9267-9273.

Zhou, D., et al. 2011. "Simple Synthesis of Highly Luminescent Water-Soluble CdTe Quantum Dots with Controllable Surface Functionality", *Chem. Mater.*, (23), 4857-4862.

Zhu, H., Song, N. and Lian, T. 2013. "Charging of Quantum Dots by Sulfide Redox Electrolytes Reduces Electron Injection Efficiency in Quantum Dot Sensitized Solar Cells", *J. Amer. Chem. Soc.*, (135), 11461-11464.

Zukas, B. G. and Gupta, N. R. 2017. "Interphase Synthesis of Zinc Oxide Nanoparticles in a Droplet Flow Reactor", *Industrial & Engineering Chemistry Research*, (56), 7184-7191.

VITA

PERSONAL INFORMATION
Surname, Name: SEVİM ÜNLÜTÜRK, Seçil
Nationality: Turkish (T.C.)
Date and Place of Birth: 15.09.1987, İzmir
Marital Status: Married
Phone: (+90) 55 258 5992
E-mail: sclsvm@gmail.com

EDUCATION

Degree	Institution	Year
PhD	İzmir Institute of Technology	2018
Visiting Reseacher	Ruprecht-Karls Heidelberg University	2017
MSc	İzmir Institute of Technology	2012
BSc	İzmir Institute of Technology	2010

PUBLICATIONS

1. Görkem Aşkın, Volkan Çeçen, Secil Sevim Ünlütürk, Serdar Özçelik , Mustafa M. Demir "Enthalpy-driven selective loading of CdSe0.75S0.25nanoalloys in triblock copolymer polystyrene-b-polyisoprene-b-polystyrene" Materials Today Communication **2016**, 8, 91-99
2. Seçil Sevim, Görkem Memişoğlu, Canan Varlıklı, Leyla Eral Doğan, Didem Taşcıoğlu, Serdar Özçelik "An ultraviolet photodetector with an active layer composed of solution processed polyfluorene:Zn0.71Cd0.29S hybrid nanomaterials" Applied Surface Science 2014, 305, 227–234
3. Caner Ünlü, Gülçin Ünal Tosun, Seçil Sevim and Serdar Özçelik "Developing a facile method for highly luminescent colloidal CdS_xSe_{1-x} ternary nanoalloys" J. Mater. Chem. 2013, 1, 3026

CONFERENCES

1. The 11th National Conference On Nanoscience And Nanotechnology – NanoTR11, June 2015, Middle East Technical University METU, Ankara, TÜRKİYE (Oral presentation)
2. International Semiconductor Science Technology Conference – ISSTC2015, May 2015, Gediz University, Kuşadası, İzmir, TÜRKİYE (Oral presentation)
3. International Semiconductor Science Technology Conference – ISSTC2015, May 2015, Gediz University, Kuşadası, İzmir, TÜRKİYE
4. The 10th National Conference On Nanoscience And Nanotechnology– NanoTR10, June 2014, Hacettepe Universtiy, Ankara, TÜRKİYE (Oral presentation)
5. Advanced Materials World Congress, September 2013, İzmir TURKEY. (Poster Presentation)
6. The 8th National Conference On Nanoscience And Nanotechnology – NanoTR8, June 2012, Ankara, TÜRKİYE (Two Poster Presentations)
7. "International Summer School and Workshop on Physics and Chemistry of Solar Energy Institute of Theoretical and Applied Physics (ITAP), 24-30/08/2013, Turunç/Marmaris, Türkiye